

UNIVERSITA' VITA-SALUTE SAN RAFFAELE

CORSO DI DOTTORATO DI RICERCA

INTERNAZIONALE IN MEDICINA MOLECOLARE

Curriculum in Neuroscience and Experimental Neurology

**CLINICAL AND SURGICAL VALIDATION
OF ADVANCED NEUROIMAGING FOR
ENHANCED ASSESSMENT OF BRAIN
TUMORS**

DoS: Prof. Andrea Falini

Second Supervisor: Prof. Cesare Colosimo

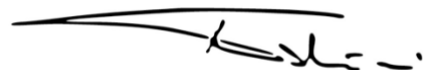
Tesi di DOTTORATO di RICERCA di Michele Bailo

Matr. 013915

Ciclo di Dottorato XXXIV

SSD MED/27 e MED/37

Anno Accademico 2020/2021

A handwritten signature in black ink, appearing to be 'M. Bailo', located at the bottom right of the page.

CONSULTAZIONE TESI DI DOTTORATO DI RICERCA

Il sottoscritto / I **Michele Bailo**

Matricola / registration number **013915**

nato a / born at **Bergamo (BG), Italia**

il / on **22/12/1986**

autore della tesi di Dottorato di ricerca dal titolo / author of the PhD Thesis titled

CLINICAL AND SURGICAL VALIDATION OF ADVANCED NEUROIMAGING FOR ENHANCED ASSESSMENT OF BRAIN TUMORS

• AUTORIZZA la Consultazione della tesi / AUTHORIZES the public release of the thesis

X NON AUTORIZZA la Consultazione della tesi per **12** mesi / DOES NOT AUTHORIZE the public release of the thesis for **12** months

a partire dalla data di conseguimento del titolo e precisamente / from the PhD thesis date, specifically

Dal / from **24/01/2022** Al / to **24/01/2023**

Poiché /because:

l'intera ricerca o parti di essa sono potenzialmente soggette a brevettabilità/ The whole project or part of it might be subject to patentability;

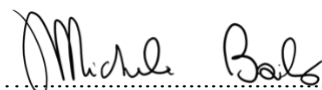
X ci sono parti di tesi che sono già state sottoposte a un editore o sono in attesa di pubblicazione/ Parts of the thesis have been or are being submitted to a publisher or are in press;

la tesi è finanziata da enti esterni che vantano dei diritti su di esse e sulla loro pubblicazione/ the thesis project is financed by external bodies that have rights over it and on its publication.

E' fatto divieto di riprodurre, in tutto o in parte, quanto in essa contenuto / Copyright the contents of the thesis in whole or in part is forbidden

Data /Date **24/01/2022**

Firma /Signature



DECLARATION

This thesis has been composed by myself and has not been used in any previous application for a degree. Throughout the text I use both 'I' and 'We' interchangeably.

All the results presented here were obtained by myself, except for:

- 1) *technical processing of dMRI (from raw DWI and DTI MR acquisitions) and PWI (from raw DSC and, DCE MR acquisitions) maps utilized in the present research was performed in collaboration with Dr. **Antonella Castellano** (Vita-Salute San Raffaele University, Neuroradiology department of IRCCS San Raffaele Hospital, Milan, Italy); Medical doctor and Neuroradiologist, PhD in Neuroscience*
- 2) *The Matlab script utilized in experiment 1 to perform the OTSU algorithm and the generation of the HYPERDirect clusters was performed in collaboration with Ing. **Nicolò Pecco** (Centro Eccellenza Risonanza Magnetica ad Alto Campo, IRCCS San Raffaele Hospital, Milan, Italy); degree in Biomedical engineering*
- 3) *VERDICT maps analysis (experiment 2) was part of an international multi-center project and was performed in collaboration with the following figures:*
 - ***Dr. Matteo Figini** (Centre for Medical Image Computing, Department of Computer Science, University College London, London, United Kingdom); degree in Biomedical engineering, PhD in Bioengineering*
 - ***Prof. Mara Cercignani** (Clinical Imaging Sciences Centre, Brighton and Sussex Medical School, Brighton, United Kingdom); degree in Medical Physics, PhD in Neuroscience*
 - ***Dr. Eleftheria Panagiotaki** (Cardiff University Brain Research Imaging Centre (CUBRIC), School of Psychology, Cardiff University, Cardiff, United Kingdom); degree in mathematics, PhD in medical imaging*
- 4) *The review of histopathology slides was performed in collaboration with Dr. **Marcella Callea** (Pathology department, IRCCS San Raffaele Hospital, Milan, Italy); medical doctor and Neuropathologist*
- 5) *The statistical assumptions to be met for the multivariate analysis in experiment 3 were also reviewed in collaboration with Dr. **Gianluca Nocera** (Vita-Salute San Raffaele University, Milan, Italy); medical doctor and PhD student*

All sources of information are acknowledged by means of reference.

Abstract

Advanced neuroimaging techniques have been introduced in the last years to overcome the limits of conventional magnetic resonance (MR) and computed tomography (CT) modalities for an enhanced assessment and surgical management of brain tumors. Preliminary studies showed extremely promising results for modern techniques of perfusion (PWI), diffusion (dMRI), blood-oxygen-level-dependent (BOLD), and spectroscopic MR acquisition, as well as for PET with a multitude of innovative radiotracers. However, many *uncertainties and controversies* still abound for most of these sophisticated techniques, preventing their systematic introduction as a standard for clinical practice, and *further validation in the setting of brain tumors* is required.

The general **aim** of this thesis was to *corroborate the application of advanced neuroimaging* in the preoperative assessment and surgical management of brain tumors, with a particular focus on intra-axial neoplasms. Since, indeed, this represents an extremely vast field, we specifically focused on their validation in terms of:

- *characterization of tumor biological heterogeneity* and ability to guide the neurosurgeon in a *more accurate target definition* for bioptic sampling and surgical resection, allowing a more comprehensive diagnosis of tumor biological and molecular characteristics and a more appropriate treatment.
- *increase of the rate of maximum safe resection, patient's quality of life, and eventual survival.*

In the **first experiment**, we presented an innovative PET and MRI approach, defined *HYPERDirect*, for the evaluation of *HYpoxia*, *PERfusion*, and *DIffusion* in high-grade gliomas to derive combined *habitats* representing intra-tumor biologic heterogeneity. Our preliminary analyses in 17 patients confirmed that quantitative imaging features from metabolic maps of PWI, dMRI, and 18F-FAZA-PET, expressing vascularization, cellularity, and hypoxia, respectively, may reflect this heterogeneity non-invasively and can consistently divide malignant gliomas into some small number of clusters. We were able to identify the unique corresponding morphological and physiological MR characteristics and histopathologic correlate (in the ten patients subjected to stereotactic sampling) of each cluster, observing an outstanding reproducibility in pattern distribution among different cases and allowing us to even speculate about the possible evolution over the time of one habitat into each other.

In the **second experiment**, we investigated “*VERDICT*” MR imaging, a pioneering computational multi-compartment modeling framework originally developed for the extraction of quantitative maps from advanced dMRI acquisitions in body tumors, representing their vascular, extracellular and restricted component. We optimized this model for the assessment of brain neoplasms, which entail a variable surrounding infiltration and therefore a higher complexity, eventually obtaining a four-compartment model without extra free parameters, showing its improved fitting performance, especially for peritumoral areas. The results from our *VERDICT* model were validated against PWI parameters (rCBV and Vp) and histopathology from corresponding stereotactic sampling, noting a good correlation. In particular, we observed higher intracellular and vascular fractions and lower extracellular fractions in more malignant histologies and tumor areas, an extremely high free water fraction in radionecrosis, and a trend towards higher free water fraction and extracellular diffusivity in purely vasogenic edemas (compared to infiltrative ones).

In the **third experiment**, we investigated the clinical application of advanced *Diffusion Tensor Imaging (DTI)* tractography and *BOLD functional MRI (fMRI)*, as well as the generation of detailed *3D-rendered anatomic-functional-pathological models* for virtual reality, in the preoperative and intraoperative management of 234 brain gliomas undergoing surgical resection. The role of modern modalities of image-guided surgery, such as intraoperative *neuronavigation* and *ultrasound*, was also investigated. All these imaging techniques generally proved advantageous in terms of extent of resection and functional outcome. In particular, the availability of DTI and fMRI was found significantly correlated with a longer survival at multivariate analysis; the former was also significantly associated with a lower chance of postoperative morbidity and a higher chance of recovering preexisting deficits.

Conclusively, we presented, for the *first time*, innovative approaches for enhanced brain tumor characterization (*HYPERDirect* approach and optimized *VERDICT* model) and evaluated *DTI* and *fMRI* techniques, together with pioneering *anatomic-functional-pathological 3D models*, for virtual reality in a large surgical series. We demonstrated that advanced neuroimaging techniques could represent a formidable tool to increase maximum safe resection and patient survival and to assess tumor heterogeneity, histopathologic/molecular characteristics, and expected behavior, possibly guiding the surgical sampling to the most aggressive cluster and perhaps, in the next future, even representing a valid alternative to invasive diagnostic procedures.

Table of contents

| | | |
|----------|--|------------------|
| 1 | <i>INTRODUCTION.....</i> | <i>12</i> |
| 1.1 | Brain Gliomas..... | 12 |
| 1.2 | The role and limits of surgery in glioma management | 14 |
| 1.3 | Conventional Imaging for Brain Gliomas..... | 17 |
| 1.4 | Advanced neuroimaging for enhanced assessment of brain gliomas..... | 20 |
| 1.5 | Application of Advanced neuroimaging in glioma surgery | 39 |
| 1.6 | General considerations regarding advanced neuroimaging in the setting of treatment response monitoring..... | 51 |
| 1.7 | Radiomics and Habitat analysis | 52 |
| 2 | <i>AIM OF THE THESIS.....</i> | <i>55</i> |
| 3 | <i>DECODING THE HETEROGENEITY OF MALIGNANT GLIOMA BY PET AND MRI FOR SPATIAL HABITAT ANALYSIS OF HYPOXIA, PERFUSION AND DIFFUSION IMAGING: A PRELIMINARY ANALYSIS FOR THE HYPERDIRECT STUDY.</i> | <i>56</i> |
| 3.1 | Introduction | 56 |
| 3.2 | Aims..... | 58 |
| 3.3 | Materials and Methods | 58 |
| 3.4 | Results | 66 |
| 3.5 | Discussion | 88 |
| 3.6 | Conclusions | 94 |
| 3.7 | Final considerations | 95 |
| 4 | <i>COMPREHENSIVE BRAIN TUMOR CHARACTERIZATION WITH VERDICT-MRI: EVALUATION OF CELLULARITY AND VASCULARITY MEASURES VALIDATED BY HISTOLOGY AND PERFUSION MRI.....</i> | <i>96</i> |

| | | |
|----------|--|-------------------|
| 4.1 | Introduction | 96 |
| 4.2 | Aims..... | 99 |
| 4.3 | Materials and methods | 99 |
| 4.4 | Results | 103 |
| 4.5 | Discussion | 114 |
| 5 | <i>CLINICAL VALIDATION OF ADVANCED FUNCTIONAL IMAGING IN A LARGE GLIOMA SERIES.....</i> | <i>117</i> |
| 5.1 | Introduction | 117 |
| 5.2 | Aims..... | 119 |
| 5.3 | Materials and Methods | 120 |
| 5.4 | Results | 130 |
| 5.5 | Discussion | 154 |
| 5.6 | Conclusions | 176 |
| 6 | <i>FINAL REMARKS.....</i> | <i>178</i> |
| 7 | <i>REFERENCES.....</i> | <i>180</i> |
| | <i>Appendix: Supplementary material to Experiment III</i> | <i>211</i> |

Acronyms and abbreviations

| | |
|------------|---|
| 11C-MET: | 11C-Methionine |
| 18F-FAZA: | 18F-Fluoroazomycin arabinoside |
| 18F-FDG: | 18F-Fluorodeoxyglucose |
| 18F-FDOPA: | 18F-Fluorodihydroxyphenylalanine |
| 18F-FET: | 18F-Fluoroethyltyrosine |
| 18F-FLT: | 18F-Fluorothymidine |
| 18F-FMISO: | 18F-Fluoromisonidazole |
| 1H-MRS: | Proton Magnetic Resonance Spectroscopy |
| 2D: | Two-dimensional |
| 2HG: | 2-Hydroxyglutarate |
| 3D: | Three-dimensional |
| AA: | Anaplastic Astrocytoma |
| AAAIR: | Age-Adjusted Incidence Rate |
| ADC: | Apparent Diffusion Coefficient |
| AED: | Anti-Epileptic Drug |
| AF: | Arcuate Fasciculus |
| AIC: | Akaike's Information Criterion |
| AIFA: | Italian Medicines Agency |
| aMRI: | advanced Magnetic Resonance Imaging |
| AO: | Anaplastic Oligodendroglioma |
| ASL: | Arterial Spin Labeling |
| ATRX: | Alpha Thalassemia/mental Retardation syndrome X-linked |
| AXR: | Apparent exchange Rate |
| BBB: | Blood-Brain Barrier |
| BOLD: | Blood-oxygen-level-dependent |
| CBF: | Cerebral Blood Flow |
| CBV: | Cerebral Blood Volume |
| CDKN2A/B: | Cyclin Dependent Kinase Inhibitor 2A/B |
| CE: | Contrast-Enhanced |
| CERMAC | Centro Eccellenza Risonanza Magnetica ad Alto Campo |
| CFARI: | Crossing Fiber Angular Resolution Intra-voxel structure |
| Cho: | Choline-containing compounds |
| ChT: | Chemotherapy |
| cMAPs: | Muscle Action Potential |
| cMRI: | Conventional Magnetic Resonance Imaging |
| CNS: | Central Nervous System |
| Cr: | Creatine |
| CSD: | Constrained Spherical Deconvolution |
| CSF: | Cerebrospinal Fluid |
| CST: | Corticospinal Tract |

| | |
|------------------|---|
| CT: | Computed Tomography |
| DCE: | Dynamic Contrast-Enhanced |
| DES: | Direct Electrical Stimulation |
| DICOM: | Digital Imaging and Communications in Medicine |
| DKI: | Diffusion Kurtosis Imaging |
| dMRI: | Diffusion Magnetic Resonance Imaging |
| DSC: | Dynamic Susceptibility-Weighted Contrast-Enhanced |
| DSI: | Diffusion Spectrum Imaging |
| DTI: | Diffusion Tensor Imaging |
| DWI: | Diffusion Weighted Imaging |
| EANO: | European Association of Neuro-Oncology |
| ECOG: | Eastern Cooperative Oncology Group |
| EGFR: | Epidermal Growth Factor Receptor |
| EOR: | Extent of Resection |
| EPI: | Echo-Planar Imaging |
| FA: | Fractional Anisotropy |
| FAZA: | Fluoroazomycin arabinoside |
| FDOPA: | Fluorodihydroxyphenylalanine |
| FECV: | Extracellular Volume Fraction |
| FICV: | Intracellular Volume Fraction |
| FISO: | Fraction of Isotropic Gaussian Diffusion |
| FLAIR: | Fluid-Attenuated Inversion Recovery |
| FLIRT: | FMRIB's Linear Image Registration Tool |
| FMISO: | Fluoromisonidazole |
| fMRI: | Functional Magnetic Resonance Imaging |
| FOV: | Field of View |
| FS: | Fat-Saturation |
| FU: | Follow-Up |
| FWE: | Free Water Elimination |
| GBL: | Glioblastoma |
| GD: | Gadolinium |
| GE-EPI: | Gradient Echo Echo-Planar Imaging |
| GE: | Gradient Echo |
| GTR: | Gross Total Removal |
| H&E: | Hematoxylin and Eosin |
| HARDI: | High Angular Resolution Diffusion Imaging |
| HGG: | High-Grade Glioma |
| HIF-1 α : | Hypoxia-Inducible Factor 1 α |
| HYPERDirect: | Hypoxia, PERfusion and tissue DIffusion |
| IDH1: | Isocitrate Dehydrogenase 1 |
| IDH2: | Isocitrate Dehydrogenase 2 |
| iDTI: | Intraoperative Diffusion Tensor Imaging |

| | |
|------------|--|
| IONM: | Intraoperative Neuromonitoring |
| IR: | Inversion Recovery |
| IRCCS: | Scientific Institute for Research Hospitalization and Healthcare |
| ITSS: | Intra-Tumoral Susceptibility Signal |
| IVIM: | Intra-Voxel Incoherent Motion |
| KPS: | Karnofsky Performance Status |
| Ktrans: | Volume transfer constant |
| Lac: | Lactate |
| LGG: | Low-Grade Glioma |
| Lip: | Mobile lipids |
| MD: | Mean Diffusivity |
| MGMT: | O6-methylguanine-DNA methyltransferase |
| MK: | Mean Kurtosis |
| MP: | Mag Prepared |
| MR: | Magnetic Resonance |
| MRI: | Magnetic Resonance Imaging |
| MRS: | Magnetic Resonance Spectroscopy |
| MRSI: | Magnetic Resonance Spectroscopic Imaging |
| N/A: | Not Available / Not Applicable |
| NAA: | N-Acetyl-Aspartate |
| NODDI: | Neurite Orientation Dispersion and Density Imaging |
| OR: | Optic Radiations |
| OS: | Overall survival |
| PET: | Positron Emission Tomography |
| PFS: | Progression Free Survival |
| PWI: | Perfusion Weighted Imaging |
| R132: | Arginine 132 |
| RANO: | Response Assessment in Neuro-Oncology |
| rCBF: | relative Cerebral Blood Flow |
| rCBV: | relative Cerebral Blood Volume |
| rMTT: | relative Mean Transit Time |
| ROI: | Region of Interest |
| RT: | Radiotherapy |
| SD: | Standard Deviation |
| SE: | Spin Echo |
| SENSE | SENSitivity Encoding |
| SK: | Segmented k-space |
| SLF: | Superior Longitudinal Fasciculus |
| SPECT: | Single Photon Emission Computerized Tomography |
| SUV: | Standardized Uptake Value |
| SWI: | Susceptibility Weighted Imaging |
| T/N ratio: | Tumor-to-Normal brain uptake ratio |

| | |
|----------|--|
| TE: | Echo Time |
| TERT: | Telomerase Reverse Transcriptase |
| TI: | Time of inversion |
| TP53: | Tumor Protein p53 |
| TR: | Repetition Time |
| US: | Ultrasound |
| VEGF: | Vascular-Endothelial Growth Factor |
| VERDICT: | Vascular Extracellular and Restricted Diffusion for Cytometry in Tumors |
| VOI: | Volume of Interest |
| Vp: | Plasma Volume |
| VR: | Volume Rendering |
| WHO: | World Health Organization |
| WT: | Wild Type |

List of figures

| | |
|--|----|
| Figure 1.1 - Illustrative cases, showing the four most common glioma subtypes on conventional MRI..... | 13 |
| Figure 1.2 - Integration of direct volume rendering for 3D preplanning (A and B), intraoperative neuronavigation with DTI and fMRI elaborations (C) and awake surgery (D) in order to achieve maximum safe resection. | 15 |
| Figure 1.3 - Illustrative case of a highly heterogeneous tumor..... | 17 |
| Figure 1.4 - Complementary information offered from different conventional and advanced imaging modalities on the same tumoral lesion..... | 19 |
| Figure 1.5 - Two illustrative cases of high-grade gliomas are presented to show the relevance of integrating DTI tractography in surgical preplanning and in candidate selection. | 27 |
| Figure 1.6 - An illustrative case of Susceptibility-weighted imaging (SWI)..... | 31 |
| Figure 1.7 - Integration of advanced MRI sequences in a Gamma Knife radiosurgical planning for a recurrent WHO grade III astrocytoma..... | 32 |
| Figure 1.8 - Illustrative case of a patient undergoing stereotactic biopsy for a high-grade glioma complicated by postoperative bleeding..... | 40 |
| Figure 1.9 - Illustrative case of a stereotactic biopsy performed in a highly heterogeneous tumor. | 40 |
| Figure 1.10 - Illustrative case of a stereotactic biopsy planning with no definite contrast-enhancement identifiable on T1-weighted imaging post gadolinium administration..... | 41 |
| Figure 1.11 - Illustrative case where advanced neuroimaging was integrated with conventional MRI to select the (possibly) most aggressive region inside the contrast-enhancement tumor components as the target for stereotactic biopsy..... | 42 |
| Figure 1.12 - Illustrative case of DTI integration in surgical and radiosurgical stereotactic procedures. | 44 |
| Figure 1.13 - Illustrative case of integrating DTI tractography into the preoperative planning and the intraoperative setting, as guidance for cortical and subcortical mapping. | 45 |
| Figure 1.14 - Modern intraoperative neuroimaging tools: neuronavigated ultrasound (US).. | 46 |
| Figure 1.15 - Brain-shift correction using modern combined ultrasound-neuronavigation systems. | 47 |
| Figure 1.16 - Fusion of different imaging modalities | 49 |
| Figure 1.17 - Main differences between direct (left) and geometric/surface (right) volume rendering | 50 |

| | |
|--|-----|
| Figure 1.18 - Illustrative case of preplanning, integrating functional data, performed with combined direct and geometric rendering techniques | 51 |
| Figure 1.19 - Illustrative case of habitat analysis from the combination of three diverse imaging modalities (dMRI, PWI, and 18F-FAZA PET)..... | 54 |
| Figure 3.1 - FLAIR-tumor and CE-tumor segmentations on different MRI sequences..... | 61 |
| Figure 3.2 - OTSU algorithm and cluster intersection. | 63 |
| Figure 3.3 - Habitats volumetric representation. | 69 |
| Figure 3.4 - Four different illustrative cases (A, B, C, and D) showing habitats distribution and reproducibility of HYPERDIrect maps. | 78 |
| Figure 3.5 - Habitats' representation (% of total tumor volume) according to IDH-1 status. | 81 |
| Figure 3.6 - Habitats' representation (% of total tumor volume) according to WHO 2016 grade. | 82 |
| Figure 3.7 - Illustrative case of a 57-year-old female patient (case 16 in Table 3.1) who underwent stereotactic biopsy. | 84 |
| Figure 3.8 - Illustrative case of a 58-year-old male patient (case 2 in Table 3.1) who underwent stereotactic biopsy. | 85 |
| Figure 3.9 - Illustrative case of a 41-year-old male patient (case 13 in Table 3.1), who underwent a stereotactic biopsy for a large parieto-temporo-occipital lesion without a clear core of contrast enhancement. | 88 |
| Figure 4.1 - Compartments models | 101 |
| Figure 4.2 - FLAIR and T1w images in representative cases | 105 |
| Figure 4.3 - Ambiguity between free water and pseudo-diffusion (vascularity). | 108 |
| Figure 4.4 - VERDICT results in the tumor core in the whole patients' sample, according to histopathological classification | 109 |
| Figure 4.5 - VERDICT results in the peritumoral areas..... | 110 |
| Figure 4.6 - VERDICT results in the tumor core in the whole patients' sample, according to IDH molecular status,..... | 111 |
| Figure 4.7 - Correlation between VERDICT fvasc and PWI metrics in the tumor core..... | 111 |
| Figure 4.8 - Comparison between VERDICT maps and histology from gross resection. ... | 112 |
| Figure 4.9 - Comparison between VERDICT maps and histology from stereotactic biopsies. | 113 |
| Figure 5.1 - Workaround utilized to extrapolate volumes-of-interest from DTI and fMRI outputs to be integrated into neurosurgical 3D preplanning and neuronavigation systems. | 124 |
| Figure 5.2 - Generation of the different volumes-of-interest for 3D representation in virtual reality..... | 127 |

| | |
|---|-----|
| Figure 5.3 - Survival estimates according to preoperative DTI and fMRI acquisition among higher grade gliomas close to motor functional areas..... | 140 |
| Figure 5.4 - Survival estimates according to preoperative DTI and fMRI acquisition among higher grade gliomas close to language functional areas..... | 141 |
| Figure 5.5 - Survival estimates according to advanced 3D imaging preplanning adoption in WHO grade IV gliomas close to motor (left) language (right) functional areas. | 144 |
| Figure 5.6 - Survival estimates in WHO grade III-IV tumors according to the adoption of intraoperative neuronavigation (left) and ultrasound (right)..... | 148 |
| Figure 5.7 - Survival estimates in WHO grade III-IV tumors according to the adoption of intraoperative neuro-monitoring (IONM). | 148 |
| Figure 5.8 - Illustrative case showing the aid provided by morphological and advanced imaging (fMRI and DTI) in identifying the critical functional areas..... | 157 |
| Figure 5.9 - Illustrative case of an advanced 3D preoperative planning of a thalamic lesion integrating direct and geometric rendering techniques. | 170 |

List of tables

| | |
|---|-----|
| Table 3.1 - Characteristics of the sequences acquired with the 1.5 T MR scanner..... | 60 |
| Table 3.2 - Characteristics of the sequences acquired with the 3 T MR scanner..... | 60 |
| Table 3.3 - Patient demographic, histopathologic, and survival data..... | 67 |
| Table 3.4 - Habitats' characteristics and volumetric representation. | 69 |
| Table 3.5 - Vp, FAZA and MD maps voxel absolute values among different habitats. | 72 |
| Table 3.6 - Vp, FAZA and MD maps "normalized" voxel intensities among different habitats. | 73 |
| Table 3.7 - The semi-quantitative histopathologic description is reported for each bioptic sample obtained..... | 79 |
| Table 3.8 - Mean and median representation of the 8 different habitats according to IDH-1 status and WHO 2016 grade..... | 80 |
| Table 4.1 - Acquisition parameters for the dMRI protocol..... | 100 |
| Table 4.2 - Summary of patients' sample characteristic | 104 |
| Table 4.3 - Details of patients' characteristics..... | 104 |
| Table 4.4 - Ranking of two- and three-compartment models fitted on high-b signals, based on the average AIC across patients. | 106 |
| Table 4.5 - AIC of the considered models with and without FWE, averaged across patients. | 106 |
| Table 4.6 - Pearson correlation coefficient between the mean FA of the extracellular compartment of each model and the mean ODI from NODDI in the same area (core or periphery). | 107 |
| Table 5.1 - Tumors' grade according to WHO 2016 classification..... | 131 |
| Table 5.2 - Distribution of different tumor subtypes..... | 132 |
| Table 5.3 - Symptoms/signs assessed at hospital admission according to WHO grade..... | 133 |
| Table 5.4 - Signs/symptoms assessed at hospital admission, early postoperatively (within 24 hours from surgery), and at hospital discharge. | 133 |
| Table 5.5 - Preoperative tumor volume according to WHO grade..... | 134 |
| Table 5.6 - Extent of resection rate according to WHO grade..... | 134 |
| Table 5.7 - Extent of resection according to tumor proximity to eloquent areas and WHO grade. | 135 |
| Table 5.8 - Extent of resection (EOR) in tumors close to motor functional areas according to preoperative DTI and fMRI acquisition. | 137 |
| Table 5.9 - Extent of resection in tumors close to language functional areas..... | 138 |

| | |
|---|-----|
| Table 5.10 - DTI and fMRI impact on motor clinical outcome, stratified by the presence of a preoperative deficit..... | 139 |
| Table 5.11 - DTI and fMRI impact on language clinical outcome, stratified according to the presence of a preoperative deficit. | 140 |
| Table 5.12 - Tumor and procedure characteristics of patients to advanced 3D imaging preplanning availability..... | 142 |
| Table 5.13 - Achievement of 90% and 75% FLAIR-tumor EOR cutoffs according to advanced 3D imaging preplanning availability in low grade gliomas. | 143 |
| Table 5.14 - Achievement of 90% and gross total resection of CE-tumor EOR cutoffs according to advanced 3D imaging preplanning availability in WHO grade III-IV tumors. | 143 |
| Table 5.15 - Advanced 3D preplanning impact on motor clinical outcome, stratified according to the presence of a preoperative deficit. | 145 |
| Table 5.16 - Advanced 3D preplanning impact on language clinical outcome, stratified according to the presence of a preoperative deficit..... | 145 |
| Table 5.17 - Number of cases where Neuronavigation, Ultrasound, and Intraoperative neuromonitoring were adopted according to tumor location proximity to critical eloquent (motor and/or language) areas..... | 146 |
| Table 5.18 - Mean degree of FLAIR and CE-tumor extent of resection with and without neuroimaging and neuromonitoring tools. | 147 |
| Table 5.19 - Number of cases achieving different cut-off values for extent of resection according to intraoperative neuroimaging and neuromonitoring tools usage. | 147 |
| Table 5.20 - Number of clinical functions worsened postoperatively according to intraoperative neuroimaging and neuromonitoring tools adoption. | 149 |
| Table 5.21 - Impact of intraoperative neuroimaging and neuromonitoring tools on postoperative motor function as assessed at hospital discharge..... | 150 |
| Table 5.22 - Impact of intraoperative neuroimaging and neuromonitoring tools on postoperative language function as assessed at hospital discharge..... | 150 |
| Table 5.23 - Duration of surgical procedures according to intraoperative neuroimaging and neuromonitoring tools usage. | 151 |
| Table 5.24 - Preoperative status of white matter fibers among different published series. ... | 158 |

1 INTRODUCTION

1.1 Brain Gliomas

Gliomas constitute the vast majority of primary tumors arising within the brain parenchyma, the annual incidence rate of 6 per 100 000 (age-adjusted) in the United States (Ostrom *et al*, 2018a; Ostrom QT, 2014). Despite the relatively lower incidence (compared to other body cancers), they are responsible for significant morbidity and mortality, mainly related to the critical location (imbedded with functional brain areas) and the intrinsic inoperability of most of them. Moreover, only small improvements in survival have been accomplished in the last decade and treatment options are still limited, especially if compared to other cancers (e.g., breast and lung). Glioma incidence differs considerably according to histopathology, patient's age, gender, ethnicity, and living environment. Usually, these tumors have a higher frequency among older persons, males and white (non-Hispanic) individuals (Ostrom *et al*, 2018b; Ostrom QT & JL, 2014).

These tumors are classified into several specific subtypes and four malignancy grades according to the World Health Organization (WHO) Classification of Tumors of the Central Nervous System (CNS) histopathological criteria, with astrocytic (WHO grades I-IV) and oligodendroglial (WHO grades II-III) cellular subtypes being the most frequent, followed by ependymal tumors (Louis *et al*, 2016; Ostrom *et al.*, 2018b) (**Figure 1.1**). The recently published WHO 2021 classification introduced some differences in nomenclature (e.g., arabic number will be used instead of roman) and grading (neoplasms are now graded within types, rather than across different tumor types), and it emphasizes the importance of integrated diagnoses and layered reports (Louis *et al*, 2021). Glioblastoma (GBL, WHO grade IV), in particular, is the most frequent histology (60% of cases); it has the highest incidence in individuals over 60 years old and, despite developments in surgical procedures and techniques, its multimodal approach still achieves a median overall survival (OS) of only 12-15 months (Ostrom *et al.*, 2018a; Ostrom *et al.*, 2018b; Young *et al*, 2015). Incidence rate, age at diagnosis and mortality rate at a fixed time-point of the other subtypes reduce progressively along with the lowering of the WHO grade (Ostrom *et al.*, 2018a; Ostrom *et al.*, 2018b). From a historical point of view, WHO grades I and II lesions,

have been denoted “low-grade gliomas” (LGGs) due to the slower-growing attitude; LGGs can be further distinguished in diffuse and more circumscribed ones. Conversely, the term high-grade glioma (HGG) was designed for rapidly progressing lesions. However, these terms amass together extremely diverse tumor histologies, each characterized by different behavior in clinical/radiological progression and response to therapies (Louis *et al.*, 2016).

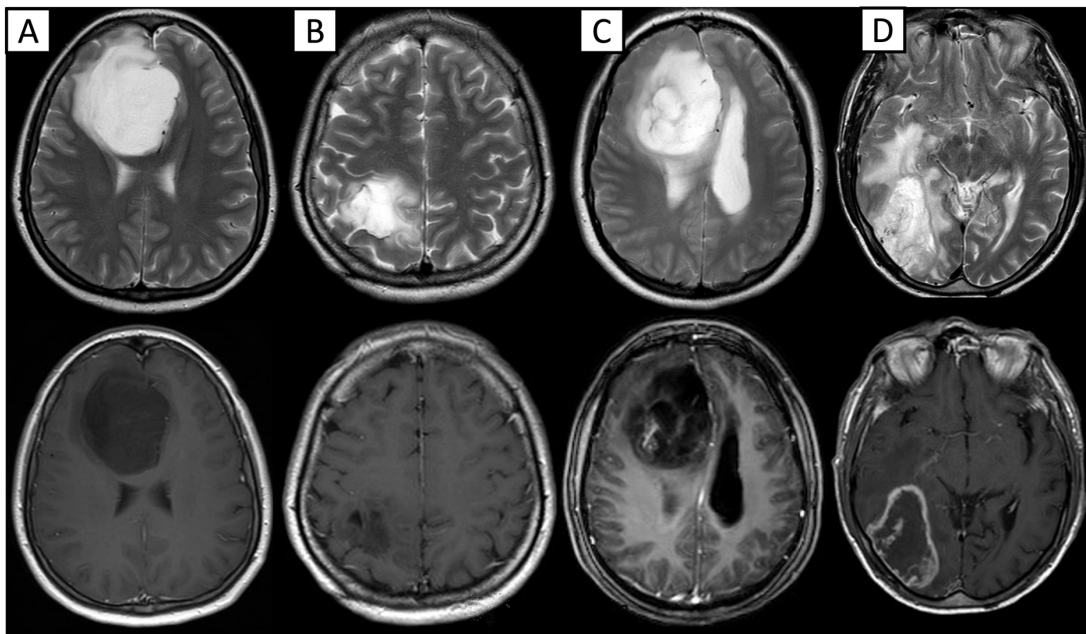


Figure 1.1 - Illustrative cases, showing the four most common glioma subtypes on conventional MRI. T2-weighted and contrast-enhanced T1-weighted images are reported for the following glioma histologies. (A) WHO grade II astrocytoma (IDH-1 mutated). (B) WHO grade II oligodendroglioma (IDH-1 mutated, 1p19q-codeleted). (C) WHO grade III astrocytoma (IDH-1 wild-type). (D) WHO grade IV glioblastoma (IDH-1 wild-type).

The WHO CNS classification of 2016 introduced, for the first time, a new a multilayered approach that broke with the traditional standard of diagnosis grounded merely on histologic criteria (such as mitotic index, necrosis, microvascular proliferation), combining molecular features to conventional histologic one in order to form an “integrated diagnosis” (Louis *et al.*, 2016; Masui *et al.*, 2016). Currently, the most relevant molecular biomarkers in adult brain gliomas can be considered the *isocitrate dehydrogenase 1* or *2* (IDH1/IDH2) gene mutation, *1p/19q* co-deletion and the *O6-methylguanine-DNA methyltransferase* (MGMT) promoter methylation; although many other markers have been described having a role in tumorigenesis and prognosis (as *TERT* promoter mutation, *ATRX* gene mutation, *TP53* mutation,

CDKN2A/B deletion, *EGFR* gene amplification and *chromosomes +7/-10* copy number changes) (Louis *et al.*, 2016; Louis *et al.*, 2021; Masui *et al.*, 2016). These alterations are able to stratify tumors, across and inside different WHO grades, in entities denoted by specific clinical behavior, sensitivity to therapies and prognosis (Komori *et al.*, 2018; Louis *et al.*, 2016; Louis *et al.*, 2021). *IDH1/IDH2* status currently represents the most important feature for prognostic stratifications; mutations of these genes are identified in 70-80% of WHO grades II and III oligodendrogliomas and astrocytomas and among 10% of GBL and are significantly correlated to better survival (Brat *et al.*, 2015; Louis *et al.*, 2021; Sanvito *et al.*, 2021). IDH-mutation is contemplated as a precocious event in tumorigenesis, and it causes an overproduction of oncometabolite *2HG* (*2-hydroxyglutarate*), that influences cellular metabolism and genetic stability (Sanvito *et al.*, 2021). The co-deletion of *1p/19q* is the principal characteristic of oligodendrogliomas from a molecular perspective and is linked to positive prognostic value and may foresee response to ChT (Kristensen *et al.*, 2019). MGMT promoter methylation is an additional factor correlating with a better prognosis and foreseeing effectiveness of alkylating chemotherapy (Yu *et al.*, 2019).

1.2 The role and limits of surgery in glioma management

In the current brain tumors management, surgery remains, when feasible, the primary option, having the advantage to provide both histopathological diagnosis and cytoreduction prior to following therapies. Neurosurgical removal of cerebral neoplasms relies on a strict balance between achievement of maximum tumor resection and maximum functional preservation since they are both related to treatment success and patient's prognosis (Dubey *et al.*, 2018). Tumor gross total removal (GTR) lower the risk of recurrence and allows a higher efficacy for subsequent chemo-radiotherapy; moreover, it is able to reduce symptoms related to mass effect and cortical irritation, directly ameliorating patient's quality of life (Chaichana *et al.*, 2014b; de Leeuw & Vogelbaum, 2019; Duffau, 2016, 2019; Eyupoglu *et al.*, 2016; Fujii *et al.*, 2018; Incekara *et al.*, 2020a; Karschnia *et al.*, 2021; Keles *et al.*, 2006; Li *et al.*, 2016; Marko *et al.*, 2014; Molinaro *et al.*, 2020; Nuno *et al.*, 2013; Oppenlander *et al.*, 2014; Orringer *et al.*, 2012; Pessina *et al.*, 2017; Sales *et al.*, 2019; Sanai *et al.*, 2011; Smith *et al.*, 2008; Stummer *et al.*, 2008; Wijnenga *et al.*, 2018). On the other hand, the concurrent

preservation of eloquent areas, such as those related to motor, language, cognitive or visual functions is an additional variable significantly affecting patient's performance status and well-being and are therefore correlated too with overall survival (OS) and successful treatment (Dubey *et al.*, 2018; Hervey-Jumper & Berger, 2014; Mandonnet *et al.*, 2007; Shalan *et al.*, 2021; Talos *et al.*, 2006). The definite goal of neurosurgical management in brain gliomas is therefore represented by obtaining maximum *safe* resection (an illustrative case of integration of different preoperative and intraoperative modalities in order to achieve maximum safe resection is depicted in **Figure 1.2**).

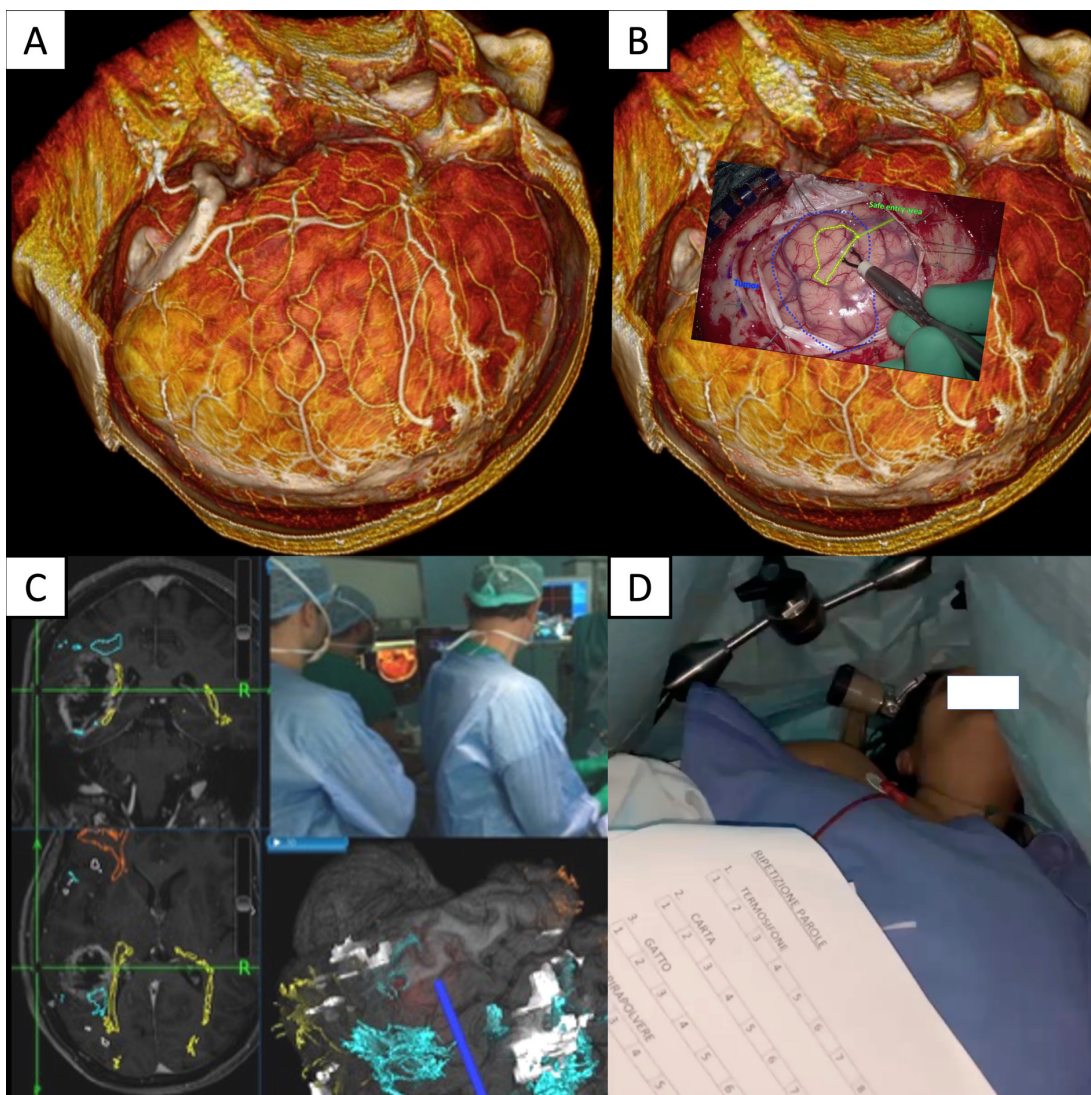


Figure 1.2 - Integration of direct volume rendering for 3D preplanning (A and B), intraoperative neuronavigation with DTI and fMRI elaborations (C) and awake surgery (D) in order to achieve maximum safe resection.

At present, the gold standard to distinguish between functional brain areas and tumoral tissue relies on invasive techniques as cortical and subcortical mapping via direct electrical stimulation (DES) and histological analysis (multiple bioptic sampling), respectively. Unfortunately, being available only during a surgical procedure, not only these techniques are quite invasive (with possible related risks for the patients, such as seizures or intraoperative bleedings and neurological deficits) and time-consuming (since they do not provide a simultaneous, all-encompassing approach, rather requiring an interruption of the resective procedure to perform a data collection, centimeter per centimeter, along the surgical margins), but they are also unable to provide information at the time of decision making, when the surgical approach is about to be planned and the indications for resection have to be balanced with the perioperative risks (Conti Nibali *et al*, 2019; Costabile *et al*, 2019; Duffau, 2007; Szelenyi *et al*, 2010).

Moreover, besides the extent of safe resection, patient's outcome critically depends on tumor histopathological and molecular classification and grading (***Komori et al., 2018; Louis et al., 2016; Louis et al., 2021***). Intra-tumoral heterogeneity has been noted both histologically and genetically in brain glioma, and augmented grades of diversity are related to therapy resistance and treatment failure (***Sottoriva et al, 2013***). At the individual patient level, the heterogeneous biology of malignant gliomas challenges the reliability of, limited, needle biopsy sampling (such as in the case of patients not amenable to tumor removal) for making disease-wide assessments and poses a problem in planning effective subsequent treatments (**Figure 1.3**). It must also be considered that even in the case of microsurgical resection, the extensive use of suction tools or the inability to reach complete removal might significantly reduce the amount of viable specimen for the pathologist, which, therefore, not necessarily represents the complete heterogeneity of the neoplasm (Lasocki *et al*, 2015; Mikkelsen *et al*, 2021). As such, an *in vivo*, non-invasive, and all-encompassing detection of malignant glioma heterogeneity may be extremely precious in predicting prognosis, personalizing treatment and following-up patients.



Figure 1.3 - Illustrative case of a highly heterogeneous tumor.

A 56-year-old patient presented with epileptic seizures and was discovered harboring an extremely heterogeneous lesion in the left parietal lobe, with the presence of cystic components and areas of various grades of contrast enhancement and T2/FLAIR hyperintensity. Considering the uncertain radiological diagnosis and the impossibility of performing a gross total resection due to the infiltration of eloquent structures (language, motor, and corpus callosum), the patient was proposed a stereotactic biopsy. However, in this case, the marked heterogeneity of the lesion could challenge the reliability of a limited number of small specimens from stereotactic biopsy for making a disease-wide assessment, particularly if not adequately guided to the most representative tumor areas.

1.3 Conventional Imaging for Brain Gliomas

The development of Computer Tomography (CT) and Magnetic Resonance Imaging (MRI) revolutionized the management of intracranial pathologies and the whole neurosurgical field allowing a non-invasive comprehensive representation and characterization of CNS disorders (Mishra & Singh, 2010; Ono *et al.*, 2018). Currently, CT and, in particular, MRI takes a decisive part in the first diagnosis of intracranial gliomas, planification of surgical approaches, selection of the best postoperative treatments, and patient's follow-up (FU) over time to monitor disease behavior (Ono *et al.*, 2018; Villanueva-Meyer *et al.*, 2017). The following sequences embody the mainstay of Conventional magnetic resonance imaging (cMRI) and should always be performed (level B recommendation) when evaluating an individual affected from a brain lesion: plain T1- and T2-weighted MRI, FLAIR (Fluid-attenuated inversion recovery), and T1-weighted sequences acquired after Gadolinium (Gd) administration (Castellano & Falini, 2016; Ono *et al.*, 2018; Villanueva-Meyer *et al.*, 2017). The first two sequences are pivotal for anatomical and structural assessment (Ricci & Dungan, 2001; Villanueva-Meyer *et al.*, 2017). The FLAIR sequence can better characterize areas of T2 prolongation thanks to its ability to suppress cerebrospinal fluid (CSF) signal and the creation of a higher contrast between the lesion border and the unaffected surrounding brain (Villanueva-Meyer *et al.*, 2017). Ultimately, T1-

weighted sequences post-contrast injection are able to enhance areas of abnormal blood-brain barrier thanks to Gd extravasation (Ono *et al.*, 2018).

Conventional MRI offers much information, suggesting a correct basic diagnosis in about 80% of the cases (Villanueva-Meyer *et al.*, 2017), however, it provides insufficient biological specificity. For instance, T2/FLAIR hyperintensity may be present in multiple situations as neoplastic infiltration, edema, ischemia, demyelination, infection, or modifications caused by therapies (Ono *et al.*, 2018; Villanueva-Meyer *et al.*, 2017). Gadolinium-enhanced areas do not necessarily define glioma's borders, neither they denote its most aggressive components, and they may be due to different causes as lesion hypervascularization or increased BBB permeability induced by various factors (i.e., ischemia, toxicity, infection/inflammation, etc.). Additionally, cMRI sequences are not able to provide significant details about the metabolism or the function of the assessed region (Ono *et al.*, 2018; Villanueva-Meyer *et al.*, 2017).

Due to these limitations, many advanced MRI (aMRI) acquisition and processing methods have been introduced over time (**Figure 1.4**) to complement cMRI, as diffusion MRI and its derivatives (dMRI), perfusion-weighted imaging (PWI), magnetic resonance spectroscopy (MRS) and Blood-oxygen-level-dependent (BOLD) functional MRI (fMRI). These aMRI techniques, together with nuclear medicine imaging modalities, like positron emission tomography (PET) with different radiotracers, are expected to provide metabolic, hemodynamic and even functional information about the tumor and the surrounding cerebral areas, allowing an assessment and quantification of tumoral architecture, aggressiveness, and heterogeneity in the time and space, as well as its relationship with the surrounding functional cortical and subcortical areas (Mabray *et al.*, 2015; Ono *et al.*, 2018; Villanueva-Meyer *et al.*, 2017). Preliminary studies published during the past years have shown promising results about the ability of advanced neuroimaging to provide a non-invasive, holistic assessment of both the characteristics and boundaries of tumor tissue to be confronted surgically and the location of the functional areas to be preserved during the procedure; particularly, they showed a better capacity over cMRI in the assessment of treatment response. However, despite multiple results published, many uncertainties and controversies still abound for most of these advanced

techniques preventing their systematic introduction in guidelines for clinical practice, and further validation in the setting of primary brain tumor is still required.

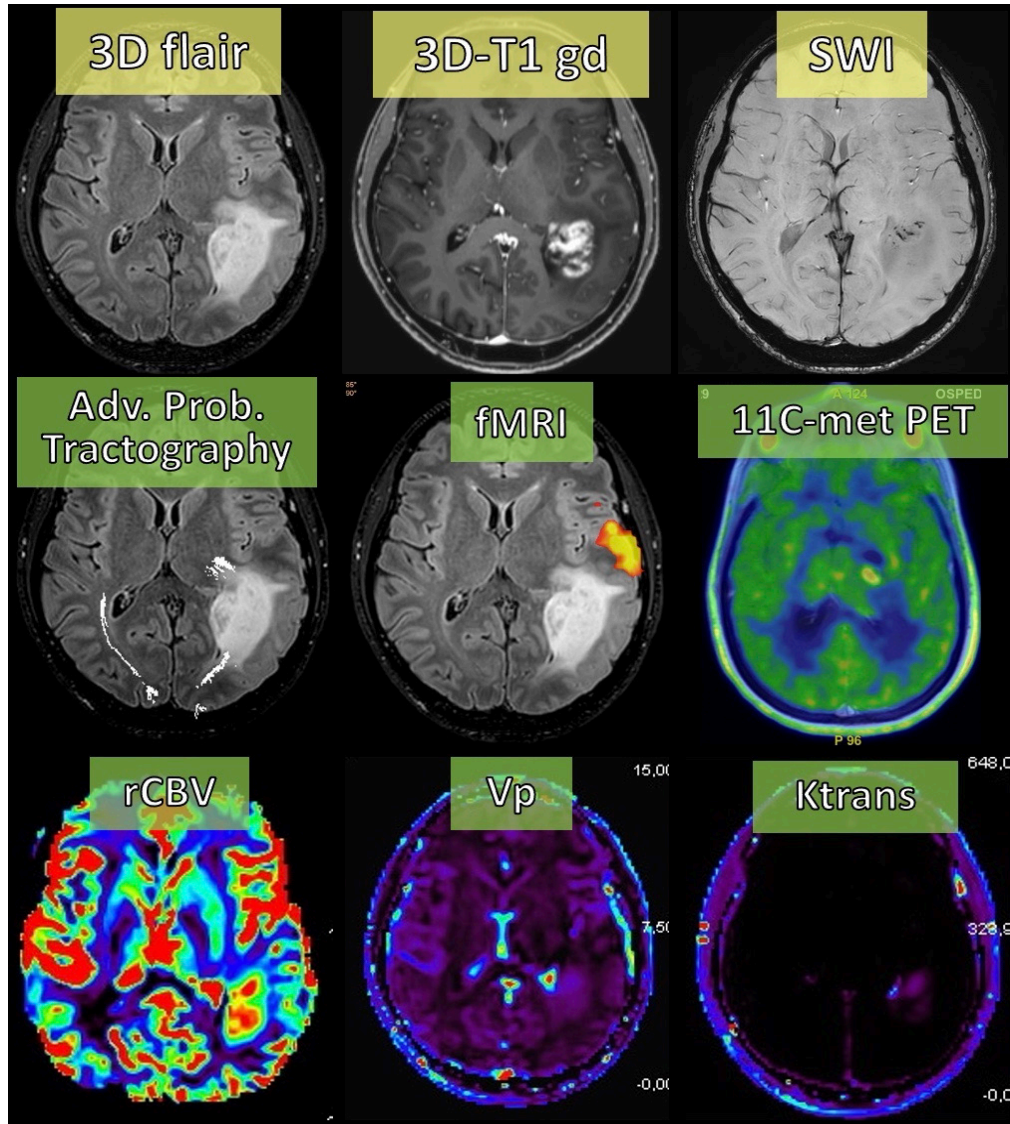


Figure 1.4 - Complementary information offered from different conventional and advanced imaging modalities on the same tumoral lesion.

The integration of both functional and physiological/metabolic imaging techniques in surgical planning can enhance target definition for stereotactic biopsies and surgical resection, and, at the same time, provide precious information about the functional areas to be preserved.

In the following paragraphs, a synthetic introduction to the most relevant advanced imaging techniques will be provided.

1.4 Advanced neuroimaging for enhanced assessment of brain gliomas

1.4.1 Diffusion-weighted MRI (dMRI)

Diffusion MRI (dMRI) is an imaging technique in which the contrast mechanism is determined by the microscopic motility of water molecules (Bastiani & Roebroeck, 2015). An image acquired with diffusion encoding gradients is called a **diffusion-weighted image (DWI)**; the latter is founded on echo-planar imaging with applied motion probe gradients and is a technique extensively used in brain tumors assessment. A restriction in water diffusivity is visualized as an augmented DWI signal and a reduced *apparent diffusion coefficient (ADC)*, which measures the water molecules' mean diffusivity (expressed in mm²/s) within each voxel. A known drawback of DWI is the T2 hyperintensity “shining through” in its acquisition sequences (the so-called “T2 shine-through effect”); however, this is not associated to an ADC signal decrease (Gatidis *et al.*, 2016).

Water diffusion in the extra-cellular space remains characteristically restricted when high cellularity impedes its motion, as in the case of tumoral cells proliferating and packing the normal tissue architecture with their membranes (Castellano & Falini, 2016). ADC, in particular, has been proved to be correlated to cellularity and histopathological grade of the tumor, as well as some molecular biomarkers: higher ADC values have been encountered in *IDH-mutated*, lower ADC in *EGFR* alterations, while data about *1p/19q codeleted* and *MGMT-methylated* tumors predictions appears conflicting (Ahn *et al.*, 2014; Bulakbasi & Paksoy, 2019; Castellano & Falini, 2016; Latysheva *et al.*, 2019; Leu *et al.*, 2017; Maier *et al.*, 2010; Miloushev *et al.*, 2015; Rundle-Thiele *et al.*, 2015; Sanvito *et al.*, 2021; Young *et al.*, 2013). Another possible utilization of DWI techniques is the thorough assessment of the tumor-related edema/necrosis/cysts and infiltration of the adjacent brain; additionally, ADC, thanks to its relative insensitivity to corticosteroids, consent a reliable assessment of response to therapies (Young, 2007). Ultimately, DWI (and FLAIR sequences) can also identify acute hemorrhagic components (although a CT scan is generally preferred for this purpose) (Xu *et al.*, 2017).

An acquisition b-value (degree of diffusion weighting) of 1000 s/mm² is generally considered the “standard” (Castellano *et al.*, 2021). However, previous works have shown that by increasing the b-value (therefore the sensitivity to tinier water

movements), this technique can intensify its own strength (Pramanik *et al.*, 2015). As such, the adoption of higher b-values (3000-4000 s/mm²) can recognize hypercellular sub-volumes in HGGs, extending inside the regions of FLAIR abnormality, or even beyond it, possibly predicting PFS (Castellano *et al.*, 2021; Ono *et al.*, 2018; Pramanik *et al.*, 2015).

1.4.1.1 Diffusion tensor imaging (DTI)

Water motion is frequently highly directional inside of biological tissues and particularly in the white matter, where the kinesis of water protons is relatively unimpeded along the dominating axonal direction, while critically hampered by the numerous myelin coatings over the axon when perpendicular to the fibers' long axis (Castellano & Falini, 2016). A particular dMRI technique termed **Diffusion tensor imaging (DTI)** can appraise these phenomena consenting a depiction of the orientation and quantification of water diffusion along white matter tracts (Castellano & Falini, 2016). An ellipsoid is generated for each voxel to estimate diffusivity in the three-dimensional space, and each dimension (or aggregate of dimensions) can infer data about the properties of the tissue (Costabile *et al.*, 2019). DTI can provide various parameters, including *fractional anisotropy (FA)*; that measures the amount of anisotropic diffusion along a distinct direction in comparison to others), *pure anisotropic diffusion (q)*; that measures diffusion with a preferential direction), *pure isotropic diffusion (p)*, that measures diffusion lacking a preferential direction), and *mean diffusivity (MD)* (Sanvito *et al.*, 2021). The main difference between DTI and DWI acquisition is that the former has motion probe gradients in multiple (at least six) directional acquisitions, which better characterize the preferential water movement along the axons' long axes (Pierpaoli *et al.*, 1996). The principal purpose of DTI in neuro-oncology is, indeed, to offer datasets for tracking the fibers of eloquent tracts (a process named fiber-tracking) to be utilized for surgical planning (Bello *et al.*, 2008; Castellano *et al.*, 2012). However, numerous papers pointed out the possible role of this technique also in the characterization of neoplastic tissue and the demarcation of tumor borders. *MD* assesses the mean motility of water molecules (averaged over all the directions obtained) in the tissue, a parameter comparable to the ADC generated from DWI acquisitions (Sanvito *et al.*, 2021). On the contrary, the directionality of

diffusion is generally represented by FA (Castellano & Falini, 2016), which is also an important diagnostic tool, since it allows the depiction of fiber tracts, reporting density, compression or tumor infiltration (Ono *et al.*, 2018; Sanvito *et al.*, 2021).

HGGs, when compared with LGGs, generally show a decreased MD (and ADC) value and an increased FA (Miloushev *et al.*, 2015). More specifically, the minimum MD seems to diverge considerably according to the WHO grade (Miloushev *et al.*, 2015). Nevertheless, the molecular and expression profiles characteristics of each neoplasm can create further heterogeneity among the LGG and HGG groups; this may have significant effects on DTI parameters and should be addressed in next future investigations (Sanvito *et al.*, 2021). Numerous papers have been published on the possibility of discerning gliomas from diverse neoplasms, and recognizing different WHO grades, with variegated results (Costabile *et al.*, 2019). The absence of agreement might be related to the dissimilarities in DTI acquisition, procedures of pre- and post-processing, positioning of the region of interest (ROI), and the dimension of the sample analyzed (Costabile *et al.*, 2019; Ono *et al.*, 2018).

Since DTI reflects the infiltration and disruption of the microstructure composed of glia, axons and extracellular matrix, it might be able to evaluate, in a quantitative manner, the amount of tumor invasion beyond the GADOLINIUM-enhanced area (and perhaps even beyond apparent borders defined on T2/FLAIR-weighted images), because of subtle white matter changes, by decomposing the diffusion tensor into an isotropic component (p) and an anisotropic component (q), proving higher specificity compared to T2/FLAIR hypertense signal alone (Sternberg *et al.*, 2014; Castellano *et al.*, 2016; Sanvito *et al.*, 2021). Increased q and decreased p values in areas of tumor infiltration have been suggested to reflect greater cellularity coexisting with undamaged axons (Aliotta *et al.*, 2019a). This information could be a precious support in the segmentation of tumor perimeters (Aliotta *et al.*, 2019a), since their correct identification has considerable implications in the preoperative surgical planning and the radiation treatment planning (Bonm *et al.*, 2020; Bulakbasi & Paksoy, 2019; Sanvito *et al.*, 2021). More aggressive removal of these abnormalities identified on DTI has been associated with a higher probability of PFS and OS (Yan *et al.*, 2017).

Moreover, higher FA -values have been reported in IDH wild type gliomas (Aliotta *et al.*, 2019b; Suh *et al.*, 2019; Tan *et al.*, 2014), possibly representing microvascular

structures (Tan *et al.*, 2014; Xiong *et al.*, 2016) or cell atypia (Aliotta *et al.*, 2019b; Sanvito *et al.*, 2021); conversely, the same molecular status was associated with lower MD values (Hempel *et al.*, 2017).

However, controversies still abound in the present literature and uncertainties exist about the clinical value of DTI in the assessment of the peritumoral area, mainly due to the lacking tissue histopathology confirmation of the results in most of these studies (Castellano & Falini, 2016; Sternberg *et al.*, 2014). Moreover, DTI's role in the analysis of the peritumoral region could be reinforced by more innovative measures compared to only *FA* and *MD* (Sanvito *et al.*, 2021).

1.4.1.2 Diffusion kurtosis imaging (DKI)

Diffusion kurtosis imaging (DKI) is an innovative and more sophisticated addition to the basic DTI model. Whereas water displacement is assumed to follow a Gaussian distribution in classic DWI and DTI, DKI measures the amount of deviation of diffusion behavior from a Gaussian distribution and permits direction-dependent assessment of ADC (Hempel *et al.*, 2017; Wu & Cheung, 2010), resulting in an enhanced representation of the restricted component of diffusion in the brain tissue (Chu *et al.*, 2021). The non-Gaussian displacement of water correlates in a positive manner with a more complex microstructural architecture caused by organelles, cell membranes, axons, or vascular structures hindering diffusion (Castellano & Falini, 2016). The parameters originating from DKI reflect a non-Gaussian diffusion along the main orientation (*axial kurtosis, Ka*), the secondary one (*radial kurtosis, Kr*), and as an average of the three directions (*mean kurtosis, MK*) (Sanvito *et al.*, 2021). Lower *MK* values suggest a more homogeneous and less dense cytological architecture, while an *MK* increase is usually detected in regions of highly cellulated tissues, with the presence of heterogeneity, necroses, hemorrhages, and microvascular proliferation (Ono *et al.*, 2018); lower *MK* values have been associated with *IDH-mutation* and loss of *ATRX* function (Hempel *et al.*, 2017). Early publications have proposed that parameters originating from *DKI* might offer supplementary data, in comparison to *DTI*, regarding WHO grading (Bai *et al.*, 2016; Tietze *et al.*, 2015); a recently published meta-analysis described a good ability for *MK* in discriminating LGG from HGG (Abdalla *et al.*, 2020). Conversely, *Ka* appears to be the most qualified marker in the

identification of *IDH* status (Chu *et al.*, 2021; Zhao *et al.*, 2019). In addition, a positive and negative correlation of *DKI*-metrics and *MD*, respectively, was found with *Ki-67* proliferation marker, whereas no correlation was identified with *FA*, suggesting that non-Gaussian diffusion parameters might be superior in depicting cellular density (Zhao *et al.*, 2019). It has been hypothesized that *Ka* may represent axonal density and integrity, entailing lower values when dealing with tumor infiltration (Chu *et al.*, 2021; Ono *et al.*, 2018; Tariq *et al.*, 2016).

1.4.1.3 *Neurite orientation dispersion and density imaging (NODDI)*

New techniques that assume “a priori” an underlying tissue model are able to calculate the relative ‘weight’ of the diffusion from every compartment (free water, intracellular, extracellular), and therefore to measure definite microstructural factors, as the volume fraction that each compartment occupies, or the orientation and size of the structures hindering the diffusion of water molecules (Pieri *et al.*, 2021; Sanvito *et al.*, 2021). *Neurite orientation dispersion and density imaging (NODDI)* is an innovative model of diffusion that permits a quantitative assessment of the microstructural characteristics of a specific tissue segregating the diffusion signal from free water (*fraction of isotropic Gaussian diffusion, FISO*), extra-neurite (*extracellular volume fraction, FECV*), and intra-neurite (*intracellular volume fraction, FICV*) compartments (Jelescu *et al.*, 2020; Ono *et al.*, 2018; Pieri *et al.*, 2021; Sanvito *et al.*, 2021; Tariq *et al.*, 2016).

While the NODDI model was not originally built using a neoplastic environment, its metrics are nonetheless able to evaluate tumor cellular density, and, for this reason, may complement DTI information (Caverzasi *et al.*, 2016b; Figini *et al.*, 2018; Sanvito *et al.*, 2021; Wen *et al.*, 2015). Quantitative NODDI-parameters extrapolated along the path of peritumoral fiber tracts were found entailing a higher sensitivity than DTI-parameters in the identification of microstructural alterations in the white-matter and, for this reason, NODDI has been proposed having a role in the discrimination among vasogenic and infiltrative edema (Caverzasi *et al.*, 2016b; Kadota *et al.*, 2020; Pieri *et al.*, 2021), with the evidence of a higher FECV in infiltrative edema when compared to vasogenic one (Kadota *et al.*, 2020; Sanvito *et al.*, 2021; Wen *et al.*, 2015).

1.4.1.4 Vascular, extracellular, and restricted diffusion for cytometry in tumors (VERDICT)

Differently from NODDI, other models, as vascular, extracellular, and restricted diffusion for cytometry in tumors (VERDICT), were elaborated for the precise purpose of representing a tumoral environment (Sanvito *et al.*, 2021). VERDICT was initially adjusted for the assessment of prostate tumors, but it has further been tested in the glioma setting over the last few years (Zaccagna *et al.*, 2019). VERDICT evaluates the following compartments: *vascular* (anisotropic), *extracellular* (with isotropic diffusion hampered), and an *intracellular* compartment (with restricted diffusion) (Panagiotaki *et al.*, 2014; Sanvito *et al.*, 2021). VERDICT is also able to describe an estimate of *cell radius*, which could see a major potential application in the evaluation of the response to therapies (based on the concept the cell shrinkage represents an early indicator for its death), as previously verified with VERDICT using animal models (Panagiotaki *et al.*, 2014; Roberts *et al.*, 2020; Sanvito *et al.*, 2021).

1.4.1.5 DTI Tractography

Tractography, which represents the current primary application of DTI, is a procedure that incorporates axonal orientations into a path connecting distant cerebral areas (Chanraud *et al.*, 2010; Dubey *et al.*, 2018). This is done by pursuing the orientation of the highest water diffusion from a specific voxel to a contiguous one till the ending criteria previously set are encountered (Chanraud *et al.*, 2010; Dubey *et al.*, 2018). Such is the case of deterministic streamline tractography, that is nowadays widely accepted as a part of the neurosurgical pre- and intra-operative management of patients harboring cerebral neoplasms, mainly to represent the principal eloquent fiber tracts (with corticospinal tract (CST), arcuate fasciculus (AF) and optic radiations (OR) being the most represented) close or inside a brain lesion (Arfanakis *et al.*, 2006; Basser *et al.*, 2000; Berman, 2009; Bucci *et al.*, 2013; Chanraud *et al.*, 2010; Dubey *et al.*, 2018; Kamada *et al.*, 2005; Karimi *et al.*, 2006; Provenzale *et al.*, 2006; Yu *et al.*, 2005).

The fiber tracts representation can prove beneficial in the preoperative planning for candidate selection (an illustrative case is depicted in **Figure 1.5**), identifying those patients that could profit the most from resective surgery, and the selection of the

optimal surgical strategy (to limit the risk of damaging eloquent areas), but also providing an anatomical correlate in the intraoperative setting that can be used as guidance during DES or a limit for safe resection when functional monitoring in awake surgery is not amenable due to patients contraindications (Bello *et al.*, 2008; Castellano *et al.*, 2012; Castellano & Falini, 2016; Ohue *et al.*, 2012). More recent studies suggested that the visualization of eloquent fibers not only in the preplanning phase but also intraoperatively, integrating them into neuronavigation systems, might diminish postoperative morbidity, particularly in the case of lesions close to the CST (Bello *et al.*, 2010; Bello *et al.*, 2008; Costabile *et al.*, 2019; Sang *et al.*, 2018; Vassal *et al.*, 2013).

The elaboration of the eloquent fiber tracts and the indirect assessment of axons integrity have generated algorithms able to predict the neurological morbidity that surgical removal could create on language, motor, and visual function (Costabile *et al.*, 2019). Motor impairments after surgery have been associated with a distance ≤ 8 mm between tumor and CST and to a greater *MD* and lesser *FA* averages in the involved CST (Rosenstock *et al.*, 2017a; Rosenstock *et al.*, 2017b). The likelihood to preserve the superior longitudinal fasciculus (SLF) and the arcuate fasciculus (AF) were related to an absence of language impairment in the long term, whereas the inability of completely preserving these fiber tracts (as elaborated by DTI) implied language morbidity even in the long-term (Caverzasi *et al.*, 2016a). Another risk factor for post-surgical language dysfunction was identified in the inter-hemispheric connectivity as determined preoperatively with tractography (Sollmann *et al.*, 2017). Lastly, a linear relationship between postoperative visual field deficits and OR injury or distance between the tumor and OR elaborated with DTI has been reported; visual morbidity was also documented as lessened with OR tracts being displayed intraoperatively (Anderson *et al.*, 1989; Chen *et al.*, 2009; Costabile *et al.*, 2019; James *et al.*, 2015; Krolak-Salmon *et al.*, 2000; Taoka *et al.*, 2008). Some studies even reported the capability of tractography to predict the EOR achievable prior to surgery, therefore providing information about patient prognosis and possible surgical outcome (Castellano *et al.*, 2012; Dubey *et al.*, 2018).

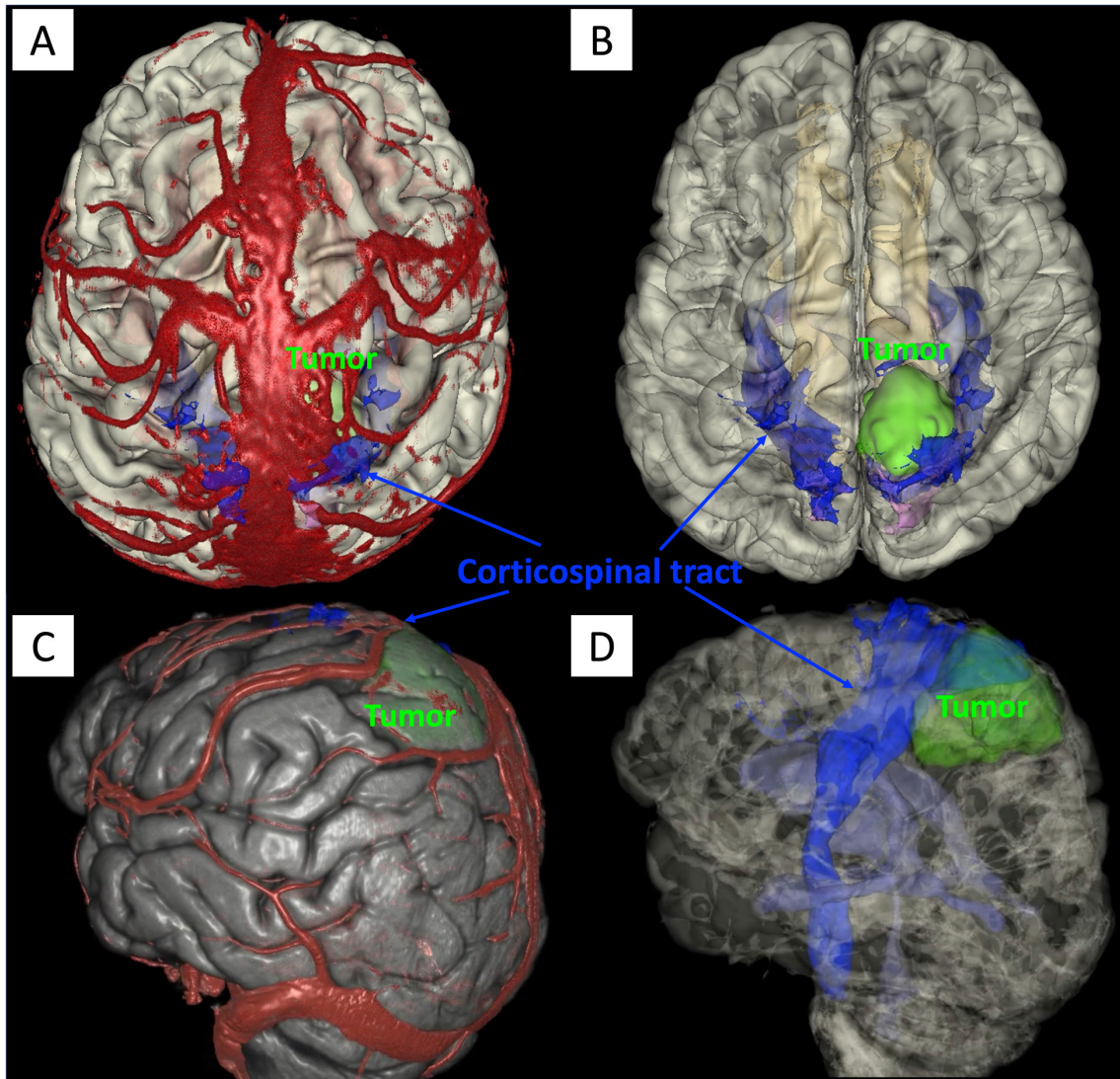


Figure 1.5 - Two illustrative cases of high-grade gliomas are presented to show the relevance of integrating DTI tractography in surgical preplanning and in candidate selection.

In the first case (A and B), the tumor is located inside the anterior component of the left corticospinal tract. In the second case (C and D), the tumor is located posteriorly to the corticospinal tract and the latter seems unaffected from tumor invasion. In the first case, the patient is undoubtedly at a much higher risk of postoperative motor deficit, therefore the indication for surgical resection needs to be carefully evaluated, balancing the potential benefits and risks derived by clinical and radiologic characteristics of the patient and tumor.

In (A) and (C), the geometric volume rendering of the segmented brain surface, tumor (green), and corticospinal tract (blue) are represented, together with the cortical vascular anatomy generated from the direct volume rendering of a skull-stripped contrast-enhanced 3D T1-weighted sequence. In the images on the right (B and D), only the semi-transparent shells generated from geometric volume rendering are shown in order to visualize better and understand the deep-located relationships between tumor and surrounding functional and anatomical structures.

Nevertheless, DTI entails some limitations. Despite intraoperative DES for subcortical mapping has demonstrated sensitivity >90% and high specificity for tractography-reconstructed CST, with scores proved consistent even when edema or tumor infiltration is present, there is still a risk of artifacts in sites where a high number

of crossing fibers meet (Krivosheya *et al.*, 2016). This drawback might be overwhelmed by the adoption of innovative methods to evaluate the white matter, such as *HARDI (high angular resolution diffusion imaging)* and *DSI (diffusion spectrum imaging)*, together with the use of probabilistic algorithms (Castellano & Falini, 2016; Krivosheya *et al.*, 2016). Particularly, cutting-edge models of diffusion MRI concentrated on the evaluation of the direction of numerous fibers as *Constrained Spherical Deconvolution* and *Q-ball* imaging have been proved to ameliorate tractography resolution in areas with elevated complexity of the microstructural tissue because of manyfold crossing fibers (Castellano & Falini, 2016). These novel tracking modalities, when applied to surgical planning, allow a great improvement in the accuracy and reliability compared to conventional DTI-based methods (Castellano & Falini, 2016; Caverzasi *et al.*, 2016a; Kuhnt *et al.*, 2013; Mormina *et al.*, 2015).

Unlike CST, fiber tracts involved in the language function are extremely inconstant among different patients, and therefore they prove hard to be accurately depicted (Costabile *et al.*, 2019). However, the visualization of these fiber tracts along the procedure has been reported to help in the preservation of the language function in cases of lesions close to the SLF, particularly when tractography is used in synergy with navigated transcranial magnetic stimulation (Costabile *et al.*, 2019; Negwer *et al.*, 2017; Sollmann *et al.*, 2018).

Another relevant drawback for DTI reliability is caused by the modification of the intracranial anatomy (“brain shift”) that occurs after dura opening (Nimsky *et al.*, 2006; Nimsky *et al.*, 2005a). This can be overcome by acquiring its sequences intraoperatively (iDTI) (Nimsky & Carl, 2015). In operations where iDTI is adopted, a marked increase in EOR rate (from 44% to 89%) and PFS at 6 months (39% to 73%) has been described (Marongiu *et al.*, 2017). An additional advantage gathered from the upsurge of fiber tracking reliability with iDTI, is the possibility to perform a higher rate of surgeries under general anesthesia (Costabile *et al.*, 2019). Published studies had revealed that a mean of >95% resection under general anesthesia close to language eloquent areas is conceivable conjoining fMRI and iDTI (D'Andrea *et al.*, 2016), although the acquisition of imaging intraoperatively necessitates supplementary preparation and a longer surgical time (Costabile *et al.*, 2019; Nimsky *et al.*, 2005c). However, in the next future, the introduction of robust advanced elastic-coregistration

algorithms, able to update the preoperative DTI dataset according to freshly acquired intraoperative imaging (e.g., intraoperative CT or ultrasound), will hopefully overcome the drawbacks related to iDTI acquisition (Riva *et al.*, 2020).

1.4.2 Functional BOLD MRI (fMRI)

A non-invasive modality able to identify the activation of specific cerebral areas is represented by **functional MRI (fMRI)** (Weng *et al.*, 2018). The most common method relies on signal modifications in *BOLD (blood oxygen level-dependent)* MR imaging, recognized as a hemodynamic response, that is due to the rise of cerebral blood flow locally while performing a specific task (neurovascular coupling) (Castellano *et al.*, 2017; Ogawa *et al.*, 1990). The activation of cortical areas ends in local alterations of the relative levels of deoxyhemoglobin (paramagnetic) and oxyhemoglobin (diamagnetic), that have different magnetic properties (Ogawa *et al.*, 1990). Throughout the hemodynamic response, a rise in the oxyhemoglobin/deoxyhemoglobin ratio can be observed using an Echo-planar imaging pulse sequence, ending in a higher homogeneity of the local magnetic field and growth of the fMRI signal (Ogawa *et al.*, 1990; Castellano *et al.*, 2017) The aforementioned procedure has been extensively adopted for the evaluation of numerous cerebral functions, but the principal aim in the clinical setting is recognition of the cortical areas involved in the speech and motor functions; the preservation of which is of paramount importance during the surgical removal of brain gliomas (Castellano *et al.*, 2017; Iseki *et al.*, 2008; Weng *et al.*, 2018). Tasks adopted to assess motor cortex activation generally comprise repeated finger movements or hand grasping; motor cortex localization with fMRI is easily reproducible, offering accuracy close to 95%; instead, verbal tasks used to assess the activation of language-related cortical regions (naming, verb generation and word chain games, are more challenging for the patient, particularly when language disturbances are already present (Ono *et al.*, 2018). Ishikawa *et al.* (Ishikawa *et al.*, 2017) reported an efficacy of 71.6% in language-dominant hemisphere identification with BOLD fMRI as opposed to the 98.6% obtained with the Wada test. The exact localization of Broca's and, particularly, Wernicke's areas is frequently unreliable with a broad spectrum of sensitivity (37-91%) and specificity (64-97%), although a vaguely higher diagnostic accuracy can be

obtained when joining multiple tasks (Castellano *et al.*, 2017; Ono *et al.*, 2018; Roux *et al.*, 2003). Either false-negative or false-positive cortical activations may be witnessed, mostly due to neurophysiological and hemodynamic changes produced by the neoplasm and its surrounding cerebral edema (Krivosheya *et al.*, 2016; Ono *et al.*, 2018; Pak *et al.*, 2017), not completely understood or predictable to date.

Noteworthy, in more recent years, BOLD has also been successfully employed in the detection of areas of neurovascular uncoupling and hypoxia present in tumoral tissue, in the identification of areas of neoplastic infiltration outside cMRI-defined boundaries, and it was even explored for potential insights in tumor molecular features (as IDH-mutation and EGFR-amplification) (Englander *et al.*, 2018; Pillai & Zaca, 2012; Sanvito *et al.*, 2021; Stadlbauer *et al.*, 2018a; Stadlbauer *et al.*, 2018b; Stadlbauer *et al.*, 2017).

1.4.3 Susceptibility-weighted imaging (SWI)

Susceptibility-weighted imaging (SWI) is a recently developed technique that uses the differences in magnetic susceptibility among several compounds, such as blood, iron, and diamagnetic calcium, as a new source of contrast for MRI (Halefoglou & Yousem, 2018). The heterogeneity in the local magnetic field generating a shortening in T2 can be provoked by diamagnetic, paramagnetic, and ferromagnetic elements and ends in signal loss on T2* weighted gradient-echo acquisitions (Halefoglou & Yousem, 2018); the latter sequences can be obtained by exploiting gradient-echoes with a relative protracted echo time in order to reduce the “apparent” T2 relaxation time and highlight local magnetic homogeneity effects (Hsu *et al.*, 2016). SWI is exceptionally good in the recognition of deoxygenated blood (particularly within the veins), blood products (microhemorrhages), neoangiogenic vessels, and calcifications enhancing the assessment of tissue architecture and heterogeneity (Halefoglou & Yousem, 2018). *Intratumoral susceptibility signal (ITSS)* is referred to as dot-like or linear hypointensity regions (probably correlated to neovascularity) or condensed and conglomerated areas (possibly representing necroses and hemorrhagic components) (Hsu *et al.*, 2016); the latter can be easily identified in the right image of **Figure 1.6**. An additional potential application of T2* imaging is the generation of T2’ maps (maps of T2 relaxation time), which reproduce local concentrations of

deoxyhemoglobin, that could correspond to higher oxygen consumptions due to great metabolic requests; although further studies are necessary to validate this application (Hsu *et al.*, 2016; Ono *et al.*, 2018).

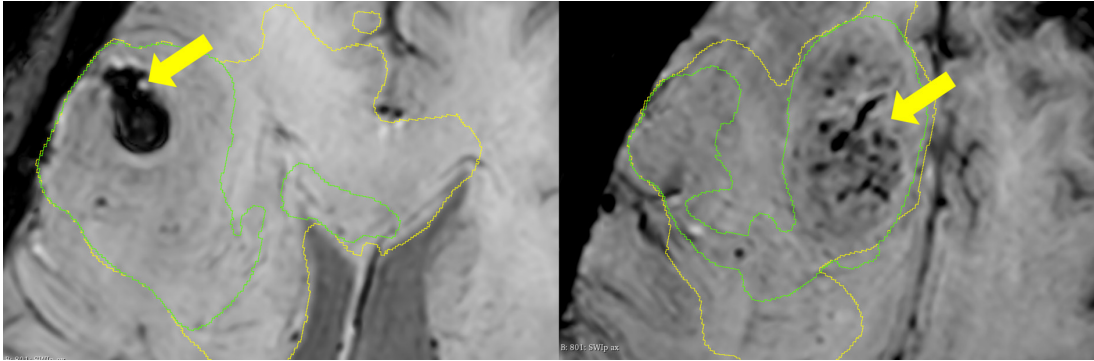


Figure 1.6 - An illustrative case of Susceptibility-weighted imaging (SWI)

The green segmentation represents the tumoral areas of contrast-enhancements, while the yellow segmentation depicted the area of hyperintensity as defined by T2/FLAIR imaging. A larger intratumoral hemorrhagic focus can be identified on the left panel (yellow arrow). In contrast, conglomerated areas (possibly representing necroses and hemorrhagic components) can be spotted inside the contrast-enhancing core of a glioblastoma (on the right panel).

1.4.4 Perfusion-weighted imaging (PWI)

Perfusion MRI (PWI) is now recognized as an important technique in the neuro-oncological field because of its capacity to measure the microvessel proliferation and permeability in the neoplasm, and therefore to assess modifications related to neoangiogenesis, correlating to higher malignancy (Castellano & Falini, 2016). PWI has been extensively investigated for the grading, prognostic assessment, and differentiation between post-treatment changes and recurrent tumors in the follow-up of brain tumors (Castellano & Falini, 2016; Griffith & Jain, 2015) (**Figure 1.7**).

Numerous methods can be adopted to obtain **perfusion-weighted imaging (PWI)**, and multiple single-center reports have proved the reliability of its derived maps in answering clinically relevant questions (Castellano & Falini, 2016).

1.4.4.1 DSC-PWI (Dynamic Susceptibility Contrast PWI)

DSC-PWI is the most utilized and validated PWI technique for the analysis of cerebral diseases. It is based on susceptibility variations during the first pass of a gadolinium-based contrast agent bolus through the tumor microvasculature; the

resulting T2*-weighted dynamic data are elaborated to extract parameters as *rCBV* (relative cerebral blood volume), *rCBF* (relative cerebral blood flow), and *rMTT* (relative mean transit time) (Castellano & Falini, 2016). Utilization of spin-echo EPI acquisitions allows for improved sensitivity to microvascular alterations at the capillary level, while gradient-echo EPI is desirable when assessing the volume of blood inside larger vessels, consequently, it is more appropriate for histopathological grading (Ono *et al.*, 2018; Sugahara *et al.*, 2001). *rCBV* has been proved to reliably correlate with findings of neoangiogenesis at histopathology and able to correctly predict the WHO grade and the outcome of patients in brain gliomas (Castellano & Falini, 2016; Law *et al.*, 2008); higher values have also been associated to *1p/19q-codeletion* and *IDH-wild type* status (Latysheva *et al.*, 2019; Suh *et al.*, 2019; Whitmore *et al.*, 2007). Nevertheless, DSC-PWI doesn't allow absolute quantification of perfusion values (Okuchi *et al.*, 2019).

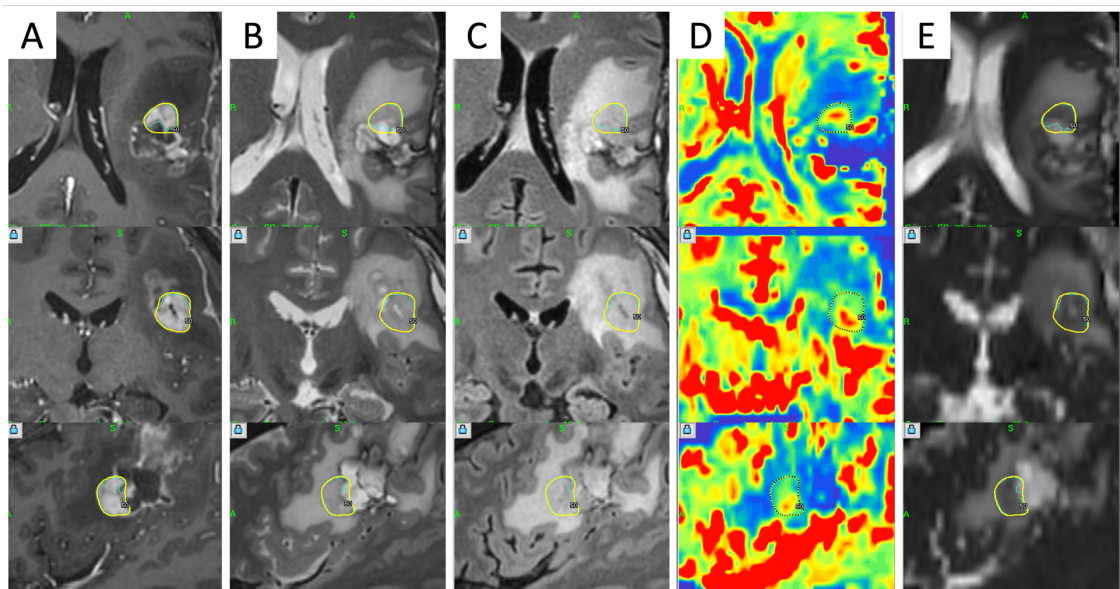


Figure 1.7 - Integration of advanced MRI sequences in a Gamma Knife radiosurgical planning for a recurrent WHO grade III astrocytoma

(A) contrast-enhanced T1-weighted (B) T2-weighted (C) FLAIR (D) relative cerebral blood volume (*rCBV*) and (E) apparent diffusion coefficient (*ADC*) map are portrayed. The patient had a recurrence of a WHO grade III astrocytoma after multimodal first-line therapy and recent redo-surgery with maximum safe resection. Contrast enhancement was present along most of the surgical cavity and target definition was challenging. The treatment was mainly defined based on elevated perfusion values on the *rCBV* map and low-intensity values in *ADC* maps. Partially adapted from images published in (Castellano, Bailo *et al.*, 2021).

1.4.4.2 DCE-PWI (Dynamic Contrast-Enhanced PWI)

DCE (Dynamic contrast-enhanced) is a PWI method founded on the increase of the T1 signal generated by the shortening tissue T1 relaxation time from the passage of gadolinium (Castellano & Falini, 2016). Due to its intrinsic technique, some advantages of DCE over DSC are: not being affected by susceptibility artifacts, having an additional insight on BBB integrity, enhanced spatial resolution and better temporal resolution (allowing better estimation of blood volume) (Anzalone *et al.*, 2018b; Castellano & Falini, 2016). A comprehensive study of its signal intensity-time curve permits manifold quantifications indicating the tumoral tissue perfusion, microvessel permeability (from BBB integrity) and the extracellular extravascular volume, thus permitting a multiparametric assessment of the tumor microvasculature (Anzalone *et al.*, 2018b; Castellano & Falini, 2016; Heye *et al.*, 2014; Okuchi *et al.*, 2019). In fact, by fitting pharmacokinetic models to DCE-MRI perfusion data, multiple maps can be obtained: K_{trans} (volume transfer coefficient), V_p (plasma volume or fractional volume of the intra-vascular compartment), V_e (fractional volume of the extravascular-extracellular space, an index of leakage) and K_{ep} (rate transfer constant between the extracellular extravascular space and the plasma) (Anzalone *et al.*, 2018b; Castellano & Falini, 2016; Heye *et al.*, 2014; Okuchi *et al.*, 2019). The principal interest on DCE-derived measures was firstly focused on K_{trans} , a marker of permeability that correlates with BBB alteration (Heye *et al.*, 2014) and malignancy (Anzalone *et al.*, 2018b; Li *et al.*, 2015; Patankar *et al.*, 2005). By introducing two-compartment pharmacokinetic models to fit DCE data, the V_p , a marker for tumor neoangiogenesis, was also investigated for prediction of tumor grading (Alcaide-Leon *et al.*, 2015; Nguyen *et al.*, 2016), and V_e was explored as a possible predictor of mitotic index (Anzalone *et al.*, 2018b; Mills *et al.*, 2016). Nonetheless, published works supporting DCE validation are much scarcer compared to DSC-technique, and standardization of acquisition and postprocessing protocols in a multicenter setting and precise assessment of the reliability of all DCE-derived maps is still lacking, and, therefore, the value of utilizing either marker or the combination is still unclear (Anzalone *et al.*, 2018b).

1.4.4.3 Other techniques of perfusion assessment in brain tumors

Arterial spin labeling (ASL) is a novel PWI technique adopting magnetically tagged arterial blood water molecules as an endogenous tracer, with no need for gadolinium injection (Castellano & Falini, 2016). ASL consents measurement of *cerebral blood flow (CBF)* (Herholz *et al.*, 2007); however full benefits of this technique in the setting of brain glioma still need to be completely elucidated (Castellano & Falini, 2016).

CT and PET can also be adopted to assess perfusion; the former entails the advantage of linear association among signal intensity and iodine-based contrast media concentration, therefore offering superior possibilities for absolute measurement of obtained hemodynamic parameters; however, MRI-based modalities entail a higher temporal and spatial resolution, with no need of ionizing radiation or radiotracer production (Hatzoglou *et al.*, 2016; Johnson *et al.*, 2020; Ono *et al.*, 2018).

1.4.4.4 Current limitations of PWI application in the assessment of brain gliomas

PWI still suffers from some limitations and possible errors. Unrealistically augmented values are often observed in the proximity of larger vessels. Occurrence of hemorrhagic components, cysts, melanin deposits, interstitial edema compression the smaller vessels, or marked contrast media extravasation may generate susceptibility artifacts and reduce *CBV* measurements (Jain *et al.*, 2011; Jain *et al.*, 2010; Jain *et al.*, 2007; Okuchi *et al.*, 2019). Tumoral perfusion can be significantly masked by normal brain *rCBV*, particularly when dealing with less aggressive tumors (Zach *et al.*, 2015). Moreover, perfusion studies can be considerably disturbed by corticosteroids or antiangiogenic therapies (Jain *et al.*, 2010; Young, 2007). Finally, standardization of protocols of PWI acquisition and a comparative assessment of the postprocessing techniques in prospective studies still lacks (Castellano & Falini, 2016). For instance, different centers adopt diverse preload (at different dosages), countermeasures for leakage-effects, lowering of flip angle, and/or post-processing leakage correction: this contributes to the *CBV*-estimation inconsistencies (Anzalone *et al.*, 2018b; Sanvito *et al.*, 2021) that limit its full validation in the assessment of brain tumors.

Reaching a conclusive multicentric consensus on DSC-*rCBV* (which is at present the most validated MRI metric to differentiate treatment effects, as radiation-induced injury or pseudoprogression, from disease progression) would hypothetically permit

the inclusion of PWI in the assessment of treatment response for clinical trials, which currently exclusively relies on cMRI findings and measurements, according to the 2010 Response Assessment in Neuro-Oncology (RANO) criteria (Sanvito *et al.*, 2021; Wen *et al.*, 2010). Finally, a joint usage of DSC and DCE MRI, partially compensating limitations of each technique, can definitely provide much stronger data and should be advocated when dealing with brain neoplasms (Anzalone *et al.*, 2018b; Wang *et al.*, 2020).

1.4.5 MR spectroscopy (MRS)

MR spectroscopy (MRS) is a diagnostic tool that can noninvasively obtain qualitative, quantitative, and/or semi-quantitative assessment of numerous metabolites of the brain, analyzing their alterations as part of the clinical history of the disease or as consequences of treatments. Because of the large quantity of proton nuclei in all tissues and biologically relevant molecules, their relatively easy processing and high signal-to-noise ratio, ¹H-MRS (proton magnetic resonance spectroscopy) has received a very high acknowledgment in neuro-oncology for its ability to identify and measure a multitude of cellular metabolites (Castellano & Falini, 2016; Chaumeil *et al.*, 2015). It is possible to obtain ¹H-MRS either as a single- or multi-voxel investigation. Moreover, when integrating the acquisition of MRS with techniques using spatial localization, analogous to those adopted when producing morphological MR sequences, a bigger volume can be designated in order to perform 2D or 3D signal acquisition from numerous voxels, this can produce semi-quantitative maps of the deviations in levels of the diverse metabolites and is also defined MRSI (MR spectroscopic imaging) or “chemical shift”; it consents concurrent acquisition of spectra from extensive tissue areas, offering the so-termed “metabolite maps” (Castellano *et al.*, 2021; Roy *et al.*, 2013; Wilson *et al.*, 2019). With contemporary MR systems, the acquisition of clinically-adapted 3D whole-brain MRSI takes about 5-10 minutes, achieving a voxel spatial resolution of typically 5-10 mm³ (Castellano *et al.*, 2021; Ozhinsky *et al.*, 2013).

The following are the most relevant metabolites identified in vivo in the healthy and pathological brain: Cr (creatine and phosphocreatine), Cho (choline-containing compounds, mainly represented by phosphocholine and glycerophosphocholine),

NAA (N-acetyl-aspartate), Lip (mobile lipids) and Lac (lactate) (Castellano *et al.*, 2021; Chaumeil *et al.*, 2015; Krivosheya *et al.*, 2016). These molecules reflect different tissues, and their modifications correspond to definite histopathological and pathophysiological features, possibly aiding in the diagnosis and differentiation of a specific brain lesion (Ono *et al.*, 2018). Since the absolute measure of the metabolites identified via MRS is technically difficult in clinical practice, semi-quantitative evaluation adopting ratios (usually setting Cr as reference) is often preferred (Castellano *et al.*, 2021). Typical spectroscopic features of brain gliomas include Cho increase, NAA reduction and inconstant deviations of Cr, which ends in an increase of the ratio Cho/Cr and a fall of NAA/Cho and NAA/Cr proportions (Castellano *et al.*, 2021). An anomalous increase of Cho is noticed together with the increase of glioma malignancy and grade because of the prominent turnover of phospholipids in the membrane of actively proliferating tumor cells, while it is detected a reduction of the Cr, a marker of bioenergy storage, and the NAA peaks, a marker for neuronal integrity (Dowling *et al.*, 2001; Guo *et al.*, 2012; Howe *et al.*, 2003; McKnight *et al.*, 2002). HGGs frequently display the presence of Lac (from tissue hypoxia and anaerobic glycolysis) and Lip peaks (byproducts of cell death and necrosis) (Howe *et al.*, 2003; Krivosheya *et al.*, 2016; Ono *et al.*, 2018; Ricci & Dungan, 2001). Nonetheless, differences in the spectroscopic profile among brain tumors are frequent and diverse arrangements might be spotted. The principal drawbacks of ¹H-MRS comprise the use of a rather large voxel volume (generally ≥ 10 mm³), the substantial measurement variability of metabolite ratios (at minimum 10-15%), and the technical disparities in the approaches used to process and post-process data, that considerably hamper comparison of results acquired on diverse scanners (Herholz *et al.*, 2007; Hollingworth *et al.*, 2006; Ono *et al.*, 2018). Lastly, presence of hemorrhagic components within the explored tissue and lesion location close to brain ventricles or bones may generate important impediments for a trustworthy analysis (Majós *et al.*, 2004; Ono *et al.*, 2018; Verma *et al.*, 2016).

The prospect of noninvasively detecting intratumoral accretion of metabolite 2HG (2-hydroxyglutarate) in cerebral gliomas embodied one of the principal developments of the recent years in the ¹H-MRS setting (Andronesi *et al.*, 2012; Castellano & Falini, 2016; Choi *et al.*, 2012). Mutations of arginine 132 (R132) inside the *IDH1* gene end in a redundant production of 2HG that can be utilized as a marker to identify *IDH-*

mutated tumors (Castellano & Falini, 2016). In a recent meta-analysis including 14 studies (Suh *et al.*, 2018), 2HG-MRS constantly quantified an increased 2HG level in gliomas harboring IDH mutation (Sanvito *et al.*, 2021). In addition, since 2HG-levels decline following effective ChT, while it rises abruptly in the event of tumor progression, a hypothetical utilization in the assessment of response to therapies has been suggested for 2HG-MRS (Choi *et al.*, 2016b) in IDH mutant gliomas, particularly in the event of IDH-targeted drugs utilization (i.e. vorasidenib and ivosidenib) (Lombardi *et al.*, 2020; Sanvito *et al.*, 2021). Nevertheless, MRS capability in detecting 2HG accumulation has been shown to rely on both tumor volume (de la Fuente *et al.*, 2015) and cellularity (Choi *et al.*, 2016a), and 2HG-MRS is a technique difficult to implement, mainly because of spectral overlap among 2HG and various other metabolites that confound results (Bai *et al.*, 2020; Sanvito *et al.*, 2021). A “modified” MEGA-PRESS 2HG-MRS sequence could represent a potential solution; this has been recently suggested for the quantification of a different peak of 2HG (located at 4.02 ppm), which show lesser concentration but also a reduced overlapping with other metabolites (Branzoli *et al.*, 2018; Nguyen *et al.*, 2021; Sanvito *et al.*, 2021).

1.4.6 Positron Emission Tomography (PET)

PET is founded on i.v. injection of several radiolabeled tracers and assessment of tumor assimilation. When concerning gliomas, the largest clinical practice has been obtained with the use of ^{18}F -fluorodeoxyglucose (^{18}F -FDG) and ^{11}C -methionine (^{11}C -MET) (Galldiks *et al.*, 2019; Treglia *et al.*, 2019). Nevertheless, normal cerebral cortex, basal ganglia and thalamus normally present diffuse ^{18}F -FDG uptake and corticosteroids therapy can considerably decrease its SUV (standardized uptake value) and T/N ratio (tumor-to-normal brain uptake ratio); ^{18}F -FDG is therefore much less adopted nowadays compared to the past (Albert *et al.*, 2016; Herholz *et al.*, 2007). Conversely, *aminoacidic tracers* entail way more advantages in the diagnostic setting thanks to their considerably superior tumor uptake compared to healthy cerebral tissue (although some uptake can be still detected inside the pons, pituitary gland and choroid plexus) (Castellano *et al.*, 2021; Galldiks *et al.*, 2019; Treglia *et al.*, 2019). Latest suggestions from the RANO (Response Assessment in Neuro-Oncology) and the EANO (European Association of Neuro-Oncology) working groups emphasize the

aminoacidic PET efficacy when assessing gliomas, particularly in the discernment between neoplastic and non-neoplastic pathology, histopathological tumor grading, lesion delineation for surgical or RT planning, determination of the region with the highest metabolism inside the tumor (that can be used, for instance, as a target for tissue sampling or a RT boost), clinical course prognostication, evaluation of response to treatments, and discernment between treatment-induced effects and tumor relapse (Albert *et al.*, 2016; Castellano *et al.*, 2021; Law *et al.*, 2019). Especially, $^{11}\text{C-MET}$ PET exhibited great diagnostic accuracy in the assessment of cerebral neoplasms (Galldiks *et al.*, 2019). The reasons of intratumoral accumulation of $^{11}\text{C-MET}$ are not entirely understood; this could be connected to an augmented synthesis of protein by multiplying cells, active aminoacidic transport throughout cell membrane, BBB alteration, and high concentration of vessels (Ono *et al.*, 2018). A poorer T/N ratio and maximal SUV on $^{11}\text{C-MET-PET}$ has been associated with *IDH-mutation*, while the contrary has been associated with *1p/19q co-deleted Oligodendrogliomas* (Lopci *et al.*, 2017; Saito *et al.*, 2013). Lately, increasing attention has been focused on different radioisotope tracers as $^{18}\text{F-fluorodihydroxyphenylalanine}$ ($^{18}\text{F-FDOPA}$), $^{18}\text{F-fluorothymidine}$ ($^{18}\text{F-FLT}$) and $^{18}\text{F-fluoroethyltyrosine}$ ($^{18}\text{F-FET}$) (Albert *et al.*, 2016; Galldiks *et al.*, 2019; Krivosheya *et al.*, 2016; Weber *et al.*, 2010).

Whereas PET entails rather modest spatial resolution (about 0.5 cm with present clinical scanners), this can be surmounted by co-registering PET series with CT or MR images (Ono *et al.*, 2018). The adoption of hybrid PET/MRI appears advantageous as it permits simultaneous (time-saving) acquisition of the two long-lasting, but clinically relevant, exams and direct voxel-by-voxel comparison of several sequences (Ferda *et al.*, 2017; Juhasz & Bosnyak, 2016; Ono *et al.*, 2018). A drawback of $^{11}\text{C-}$ constructed radiotracers, like $^{11}\text{C-MET}$, is their brief half-life (about twenty minutes), that restricts the implementation of these tracers only to hospitals equipped with a cyclotron (Krivosheya *et al.*, 2016; Ono *et al.*, 2018). Conversely, $^{18}\text{F-FLT}$ accumulation in the neoplasm relies on its penetrability of the BBB; for this reason, it entails lower effectiveness in gliomas not showing contrast enhancement, while normal accumulation of FDOPA in basal ganglia can generate problems in the identification of tumoral borders (Ono *et al.*, 2018). The accuracy of PET, especially to discern between different cerebral neoplasms, can be augmented with the utilization of

dynamic studies, where numerous sequential acquisitions are executed at various timings after the administration of the radiotracer (Aki *et al.*, 2012; Albert *et al.*, 2016; Ferda *et al.*, 2017; Galldiks *et al.*, 2019; Treglia *et al.*, 2019).

1.5 Application of Advanced neuroimaging in glioma surgery

1.5.1 Adoption of physiologic and metabolic information from advanced neuroimaging

1.5.1.1 Tumor margin delineation and Biopsy Target selection

Accurate delimitation of the tumor margins grounded on advanced imaging (PWI, DWI, PET, 1H-MRS) can prove beneficial to discern among infiltrating tumor and edematous brain inside regions of non-specific high T2/FLAIR signal intensity. Adoption of such data throughout surgery could implicate a superior extent of resection (EOR) while improving safety, particularly when dealing with relapsing tumors sited in proximity to eloquent cerebral structures. Likewise, the adoption of metabolic demarcation of tumoral margins during RT or stereotactic radiosurgery could permit higher precision in the treatment planning, although its effect on clinical and radiological outcomes is yet to be established (Castellano *et al.*, 2021; Herholz *et al.*, 2007).

On the other end, identification of the tumoral region with the highest metabolic activity, that generally matches with the area of uppermost tumor proliferation, is extremely relevant to guide tissue biptic sampling, especially when performing stereotactic needle biopsy in patients where microsurgical resection is not indicated (Moussazadeh *et al.*, 2016). Conventionally, the planning of stereotactic biopsies generally lean on the identification of the gadolinium-enhancing region; however, contrast enhancement alone does not provide sufficient specificity about underlying time biology, and choosing this region as a target might result in not comprising the part of the tumor characterized by the greatest aggressiveness in the sample, particularly in relapsing lesions after previous treatments (Upadhyay & Waldman, 2011). Some illustrative cases regarding the possible application of advanced neuroimaging in tumor sampling are reported in **Figure 1.8**, **Figure 1.9**, **Figure 1.10** and **Figure 1.11**.

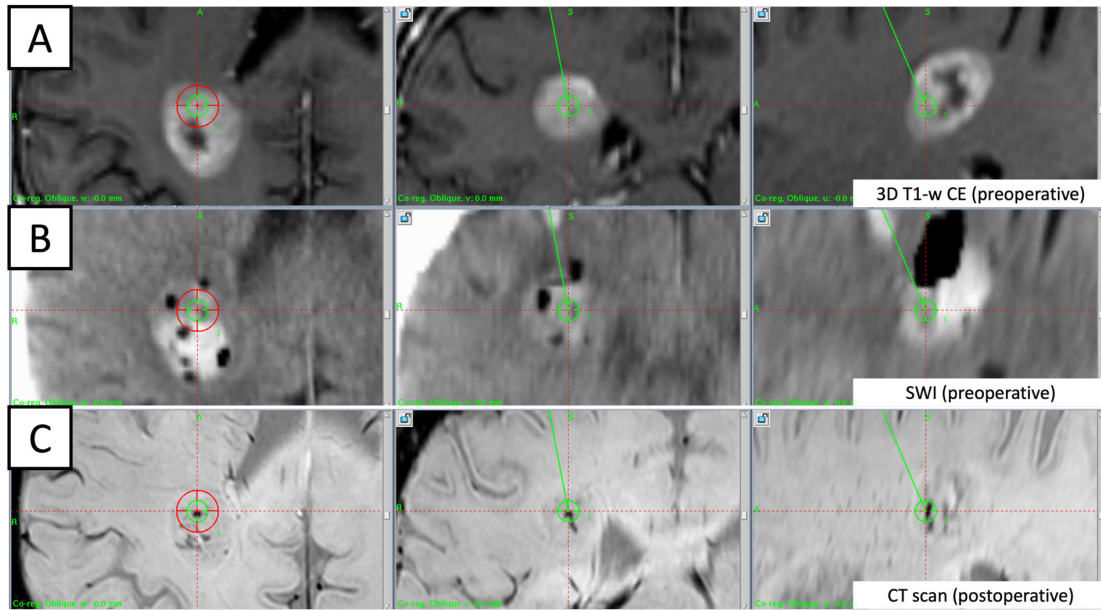


Figure 1.8 - Illustrative case of a patient undergoing stereotactic biopsy for a high-grade glioma complicated by postoperative bleeding.

(A) The neurosurgeon defined the target solely based on the contrast-enhancing component visible on 3D T1-weighted imaging acquired after gadolinium injection. The procedure (performed with the patient awake under local anesthesia) was aborted due to significant bleeding after the first specimen collection. The patient rapidly developed a left hemiparesis. (B) The immediate postoperative CT scan showed bleeding at the site of the sampling. (C) Retrospectively reviewing the complete preoperative imaging dataset acquired, a structure resembling a large vessel was identified at the targeting site on Susceptibility weighted imaging (SWI), while it was not visible on conventional MRI sequences. This case points out the advisability of introducing advanced neuroimaging techniques into standard neurosurgical practice.

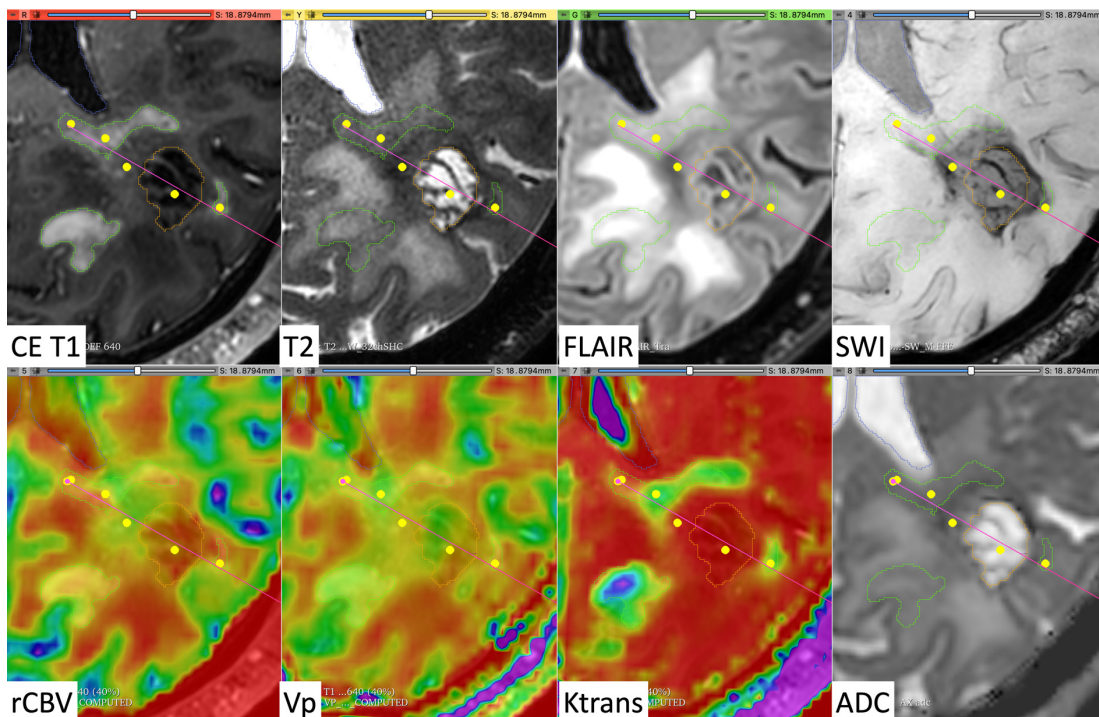


Figure 1.9 - Illustrative case of a stereotactic biopsy performed in a highly heterogeneous tumor.

The stereotactic biopsy of the same patient reported in Figure 1.3 is here represented. The trajectory was planned in order to sample multiple different areas (yellow dots) of the tumor according to data provided by morphological and advanced MRI. The final diagnosis was anaplastic astrocytoma WHO grade III, IDH-1 wild-type.

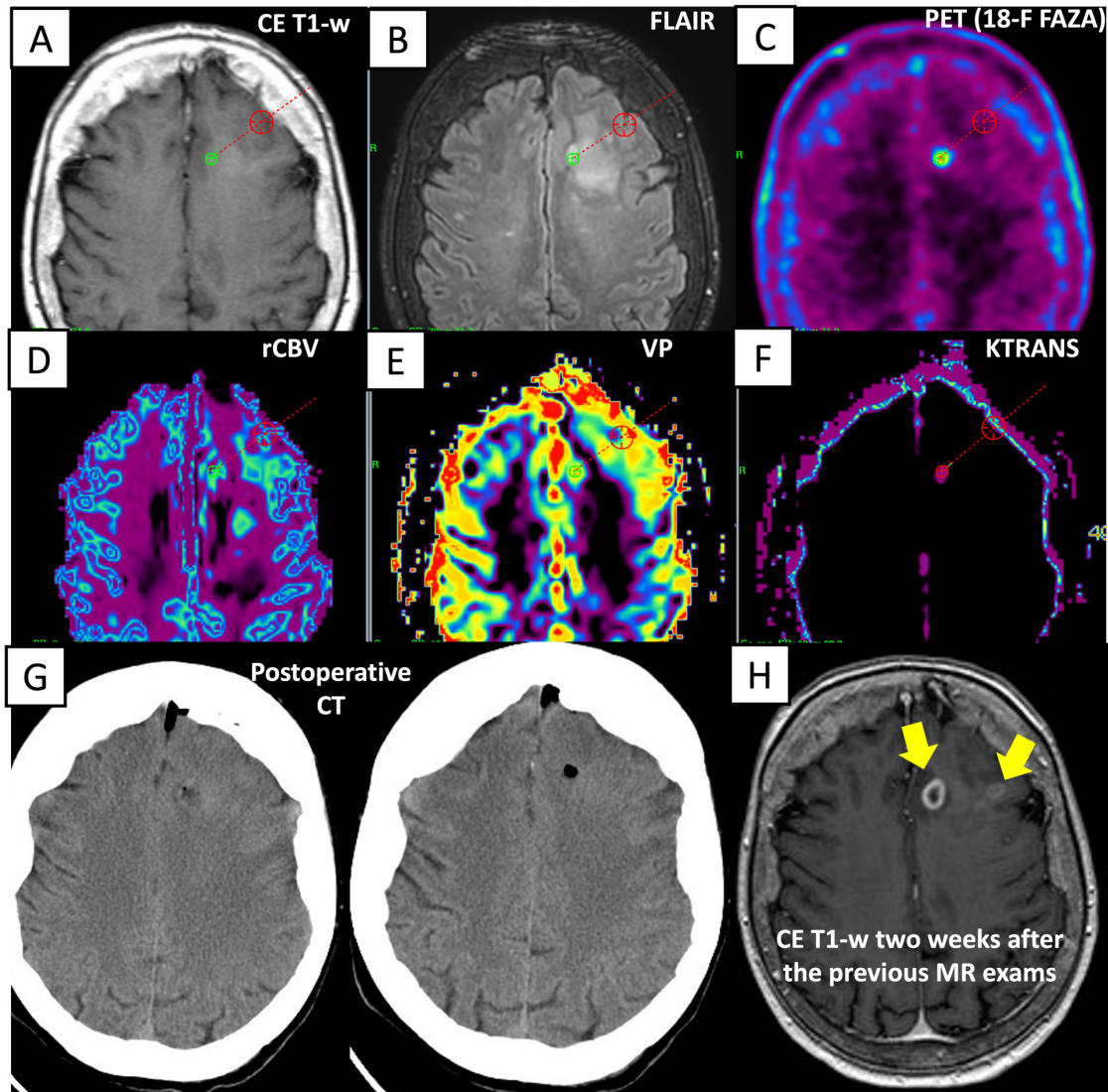


Figure 1.10 - Illustrative case of a stereotactic biopsy planning with no definite contrast-enhancement identifiable on T1-weighted imaging post gadolinium administration.

Vp, Ktrans, rCBV, and 18-F FAZA PET maps were imported in the stereotactic planning system (Surgiplan, Elekta, Sweden). A small area characterized by high perfusion on rCBV and Vp maps and high hypoxia according to 18F FAZA PET was set as the final target for the bioptic sampling; the eventual diagnosis was glioblastoma IDH-1 wild type. The immediate postoperative plain CT scan showing an air bubble at the sampling site is reported in (G). The contrast-enhanced T1 weighted MRI acquired two weeks after the previous MRI exam (H) showed the appearance of areas of contrast enhancement (yellow arrows) in sites already exhibiting increased perfusion and hypoxia values at the initial advanced imaging acquisition.

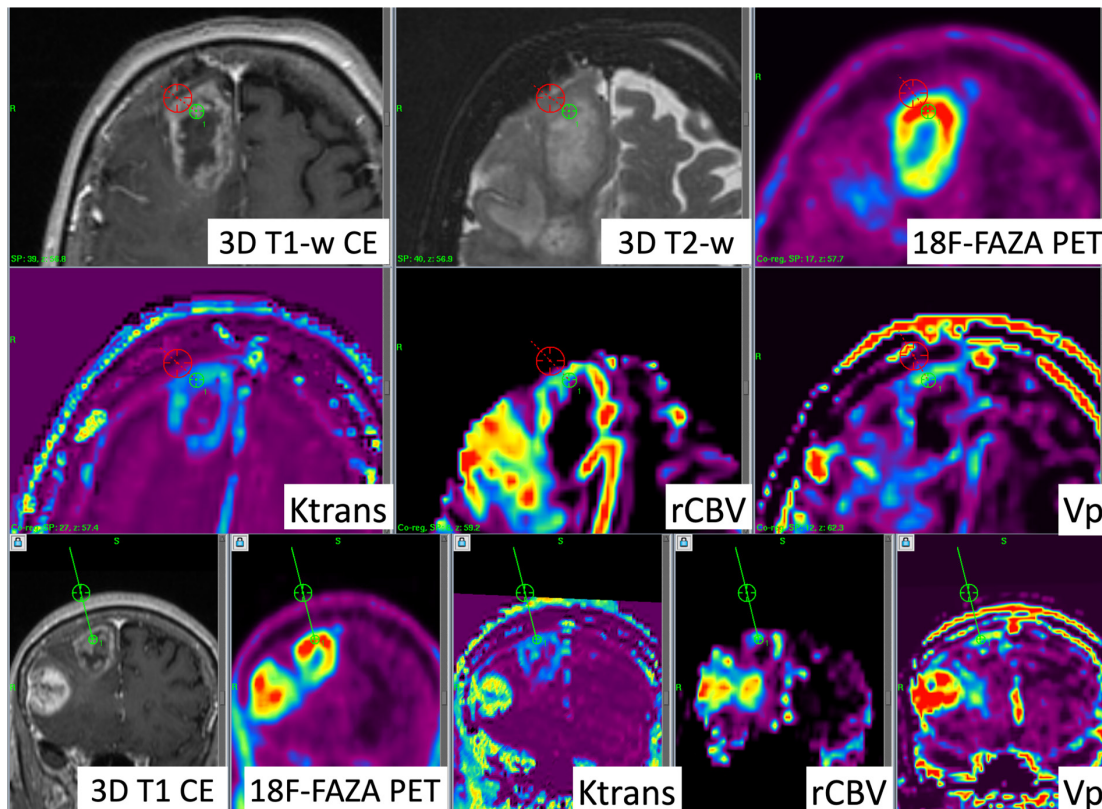


Figure 1.11 - Illustrative case where advanced neuroimaging was integrated with conventional MRI to select the (possibly) most aggressive region inside the contrast-enhancement tumor components as the target for stereotactic biopsy.

Stereotactic contrast-enhanced 3D T1-weighted imaging is coregistered, inside the neurosurgical planning software (Surgeplan, Elekta, Sweden), with DCE (Vp and Ktrans) and DSC (rCBV) MR perfusion techniques and 18F-FAZA PET (a hypoxia radiomarker). The final path and sampling sites are chosen inside an area of increased perfusion and hypoxia after balancing surgical risks and technical limits (from a procedural point of view) of the different possible alternatives.

1.5.2 Adoption of functional information from advanced neuroimaging in glioma surgery

The techniques of advanced neuroimaging considerably ease the achievement of higher tumor removal, that is powerfully related with patient prognosis. Comprehensive presurgical brain mapping obtained with DTI and fMRI permits proper identification of those individuals that could bear extensive tumor resection with a negligible hazard of neurological complications (Conti Nibali *et al.*, 2019) (illustrative case in **Figure 1.12**). Preoperative documentation of the eloquent fibers through DTI has been proved to reduce surgery-related morbidity, being related with longer OS in individuals harboring HGGs (Bello *et al.*, 2010; Conti Nibali *et al.*, 2019; Krivosheya *et al.*, 2016). Noteworthy, the adoption of preoperative imaging as a guide for tumor removal always necessitates a combination with intraoperative

neuroimaging techniques (as neuronavigation systems) and DES for cortical and subcortical mapping (Illustrative case in **Figure 1.13**) in order to prevent errors of localization generated by potential geometrical deformations on high-field MRI, errors in coregistration to the patient's coordinates and the so-called “brain shift” phenomenon that occurs during intracranial surgery (Costabile *et al.*, 2019; Iseki *et al.*, 2008). Nevertheless, inaccuracy of the coordinate system can be quantified and correct with intraoperative neuroimaging techniques as intraoperative MRI, CT, or ultrasound.

1.5.3 Advanced processing of neuroimaging modalities for an enhanced preplanning and image-guided surgery in brain gliomas

1.5.3.1 Image-guided surgery in neurosurgery

The concept of image-guided surgery was introduced in neurosurgery in the 1940-1950s, when stereotactic approaches were performed for the first time (Gosal *et al.*, 2021; Spiegel *et al.*, 1947; Thomas & Sinclair, 2015). The original attempts to use ultrasound (US) and CT during neurosurgical interventions to determine the EOR were made during the 1980s (Nimsky & Carl, 2015). In the years 1990s, intraoperative US and neuronavigation systems started to become largely available, boosting a much wider adoption of image-guiding tools among neurosurgeons (Barnett *et al.*, 1993; Gosal *et al.*, 2021; Koivukangas *et al.*, 1993; LeRoux *et al.*, 1989; Watanabe *et al.*, 1991; Watanabe *et al.*, 1987; Zinreich *et al.*, 1993). In the same decade, intraoperative MRI proved to augment GTR and progression-free survival rates in glioma patients in many randomized studies (Ganslandt *et al.*, 2002; Gosal *et al.*, 2021; Napolitano *et al.*, 2014; Roder *et al.*, 2014; Senft *et al.*, 2011a; Senft *et al.*, 2011b; Yrjana *et al.*, 2007; Zhang *et al.*, 2015). These intraoperative neuroimaging modalities revolutionized neurosurgery; however, each one of them still entails some limitations, the main being intraprocedural loss of accuracy (due to brain shift) for neuronavigation of preoperatively-acquired imaging, difficulty in interpretation of acquired intraoperative imaging for ultrasound, and extremely high cost and time loss in the case of intraoperative MRI. Nevertheless, the combination of two different techniques, such as neuronavigation and ultrasound, have been explored in recent years showing significant advantages in limiting the drawbacks specific to the single technique (see **Figure 1.14** and **Figure 1.15**).

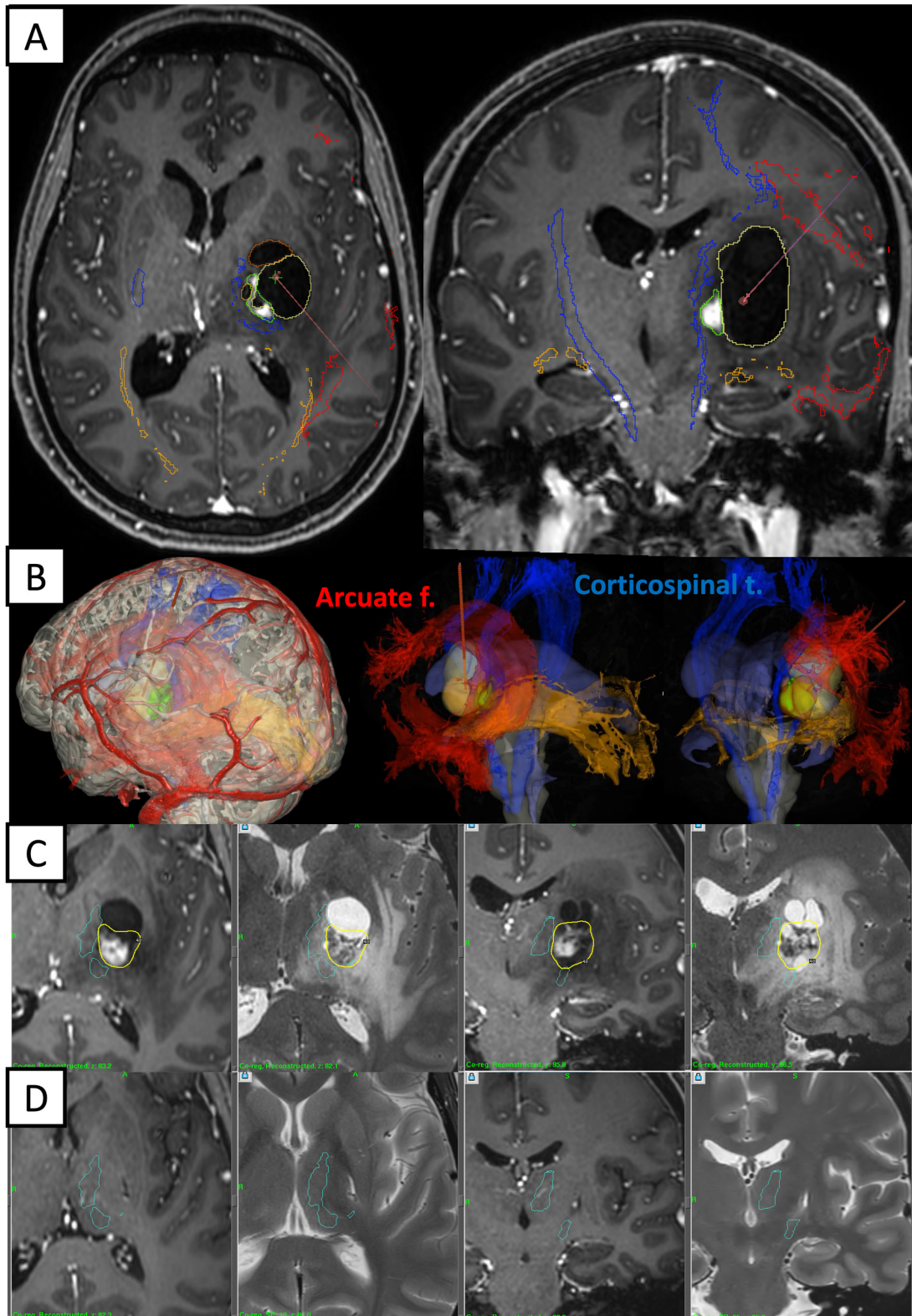


Figure 1.12 - Illustrative case of DTI integration in surgical and radiosurgical stereotactic procedures.
 (A and B) A 26-year-old female harbored a deep-seated tumor with mixed components (cystic parts and contrast-enhancing mural nodules). The lesion was located in the posterior arm of the left internal capsule; at DTI tractography, the corticospinal tract appeared split by the tumor in an anterior and a posterior section; in light of this functional information, the lesion was considered inoperable unless incurring in an unacceptable risk of

morbidly. In consideration of the progressive enlargement of the cystic components and surrounding edema at radiological follow-up, stereotactic drainage of the cystic components and concurrent biopsy of the solid part were carefully planned after integrating DTI data in the stereotactic planning. The main difficulties of the procedure were related to the adjacent corticospinal tract and left arcuate fasciculus and the possible shifting of the bioptic target following drainage of the cystic content. The final diagnosis was pilocytic astrocytoma. (C) A Gamma Knife radiosurgery was performed on the solid components, integrating the volume of the corticospinal tract in the treatment planning as an organ-at-risk. (D) The last radiological follow-up (20 months) showed complete regression of the contrast-enhancing nodules and the surrounding T2/FLAIR hyperintensity.

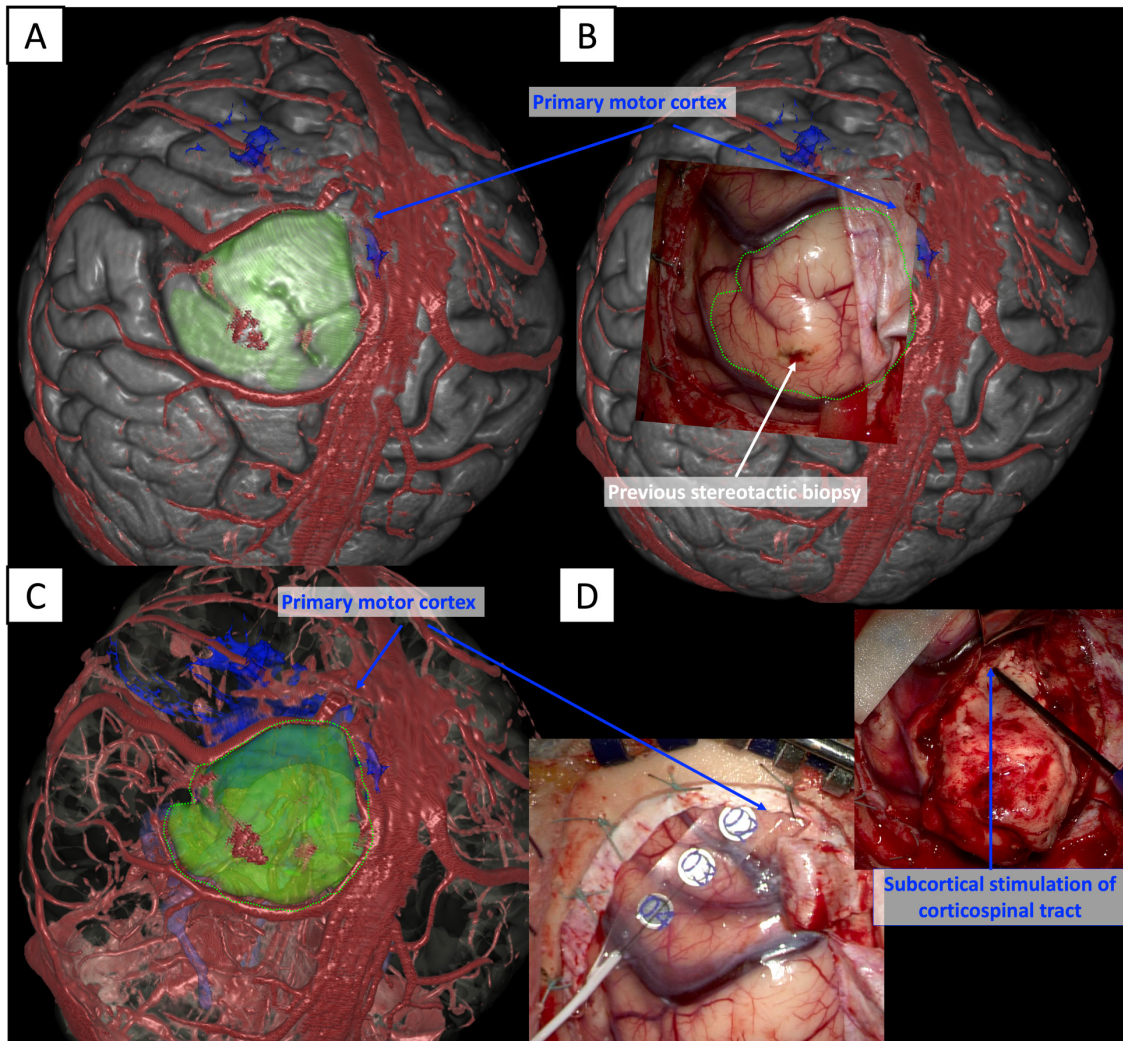


Figure 1.13 - Illustrative case of integrating DTI tractography into the preoperative planning and the intraoperative setting, as guidance for cortical and subcortical mapping.

A patient previously subjected to a stereotactic biopsy, with a diagnosis of IDH-wild type glioblastoma, was offered a surgical resection after preoperative DTI acquisition and preplanning with advanced 3D reconstruction. Data from the 3D anatomic-functional-pathological model were pivotal for the straightforward identification of the primary motor cortex and the tumor cortical margins immediately after dura opening; functional neuronavigation was then used as a guidance for cortical and subcortical motor mapping with direct electrical stimulation to complete the safe tumor removal.

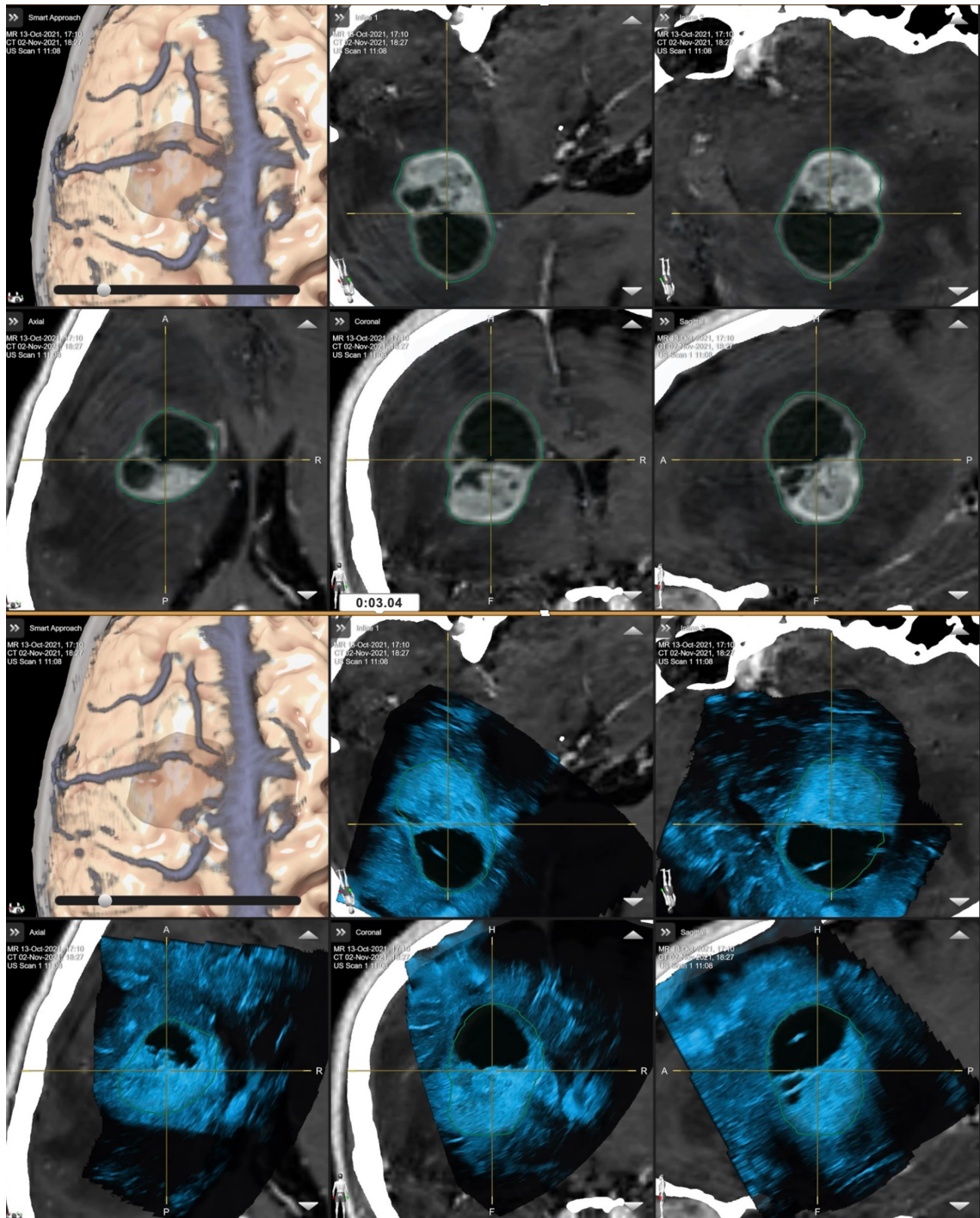


Figure 1.14 - Modern intraoperative neuroimaging tools: neuronavigated ultrasound (US)

A combined ultrasound neuronavigation can conjoin the benefits (while overcoming specific limitations) of both the techniques: the real-time visualization from the US can compensate the possible “brain-shift” affecting neuronavigation accuracy; conversely, the easier understanding of magnetic resonance imaging visualized in the neuronavigation system can aid in the (often challenging) interpretation of the anatomy depicted by the ultrasounds probe.

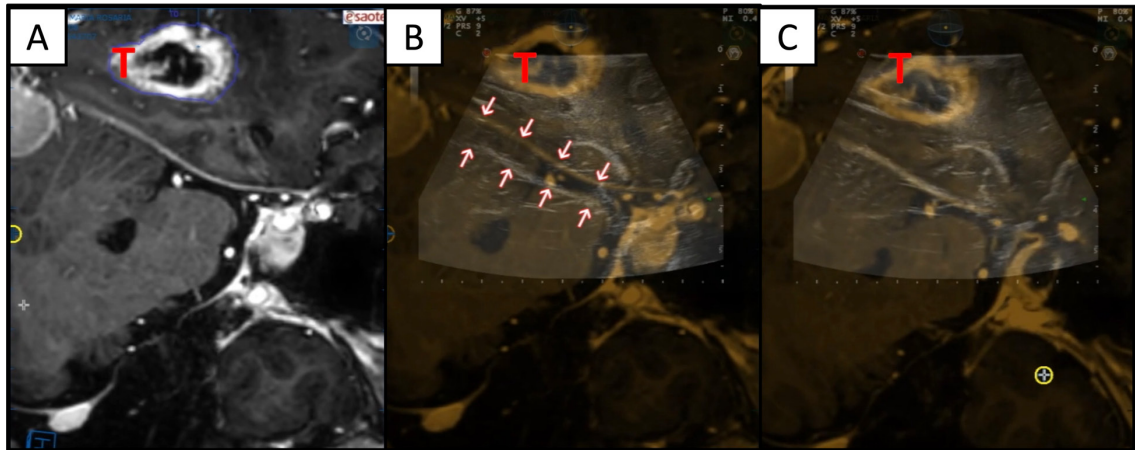


Figure 1.15 - Brain-shift correction using modern combined ultrasound-neuronavigation systems.
 (A) Orthogonal reconstruction of the contrast-enhanced (CE) 3D T1-weighted sequence generated according to the position and direction of the ultrasound (US) probe. (B) The superimposition of US imaging acquired in real-time on the preoperative CE 3D-T1-weighted images stored in the neuronavigation systems can disclose the presence of a certain degree of brain-shift (red arrows). (C) The image position can be corrected to a new coordinates system using real-time US imaging as a reference. This process is particularly relevant to reupdate the position of preoperative DTI and fMRI datasets since it is rather unpractical (and impossible in the case of task-based fMRI) to reacquire them during the surgical procedure.

Today image-guided neurosurgery is part of the neurosurgical standard when resecting intracranial lesions, as long as for many other different procedures (Gerganov *et al*, 2009; Gosal *et al.*, 2021; Miner, 2017; Willems *et al*, 2006). However, each of the aforementioned systems has its practical limitations and can prove quite expensive. Consequently, most of these tools are still not widely available, especially in resource-constrained countries (de Oliveira Santos *et al*, 2018; Gosal *et al.*, 2021; Malilay *et al*, 2021).

1.5.3.2 3D volume rendering and virtual reality in brain glioma surgery

The 3D volume-rendering is a technique that allows to interactively explore, in a three-dimensional virtual space and with high-quality texture, multiple imaging modalities, providing precious information for surgical planning (Gosal *et al.*, 2021; Malilay *et al.*, 2021). The clinical application of the 3D reconstruction technique in neurosurgery was preliminary demonstrated in the late 1990s (Chabrierie *et al*, 1998; Gosal *et al.*, 2021). Since then, several studies have described its clinical application in different neurosurgical subspecialties, as neurooncological, vascular, skull-base, reparative/reconstructive and degenerative spinal surgery (de Notaris *et al*, 2014; Gong *et al*, 2008; Gosal *et al.*, 2021; Jha *et al*, 2019; Oishi *et al*, 2011b; Rotariu *et al*, 2017;

Wang *et al.*, 2010). Computer hardware (particularly for what concerns working memory and central and graphics processing units) and virtual reality software and technologies have drastically advanced over the past ten years, boosting the output's quality while reducing processing time and economic investment required (Kin *et al.*, 2017). Thanks to these advances, the application of neuroimaging to virtual reality is increasing in both the research and clinical settings, and it is beginning to occupy an important position also commercially.

Many different software solutions have been implemented for neurosurgical simulation, with a large diversity of functions, usability levels, availability on the market, and prices, despite not being officially certified for clinical purpose in most cases and therefore limited to research application only (Kin *et al.*, 2017). Volume rendering techniques are readily available as an incorporated tool in numerous DICOM viewer programs, as OsiriX (Pixmeo SARL, Switzerland), Horos (horosproject.org), and RadiAnt (Medixant, Poland) (Aydin *et al.*, 2006; Beyer *et al.*, 2007; de Oliveira Santos *et al.*, 2018; Gosal *et al.*, 2021; Jha *et al.*, 2019; Lovato *et al.*, 2019; Malilay *et al.*, 2021; Spiriev *et al.*, 2017). However, many other dedicated platforms, including StealthViz (Medtronic, USA), Elements (Brainlab, Germany), Dextroscope® (Volume Interactions, Singapore), MRicro (www.mricro.com) and 3D Slicer (www.slicer.org), have also been implemented over the years (Kin *et al.*, 2017).

OsiriX was the adopted software in the majority of the published studies on virtual reality, using conventional volumetric MR imaging as input (Harput *et al.*, 2014; Jaimovich *et al.*, 2014; Kim *et al.*, 2012; Lovato *et al.*, 2019; Rotariu *et al.*, 2017; Spiriev *et al.*, 2017; Wang *et al.*, 2010). Esposito *et al.* reported for the first time in 2006 the utilization of a three-dimensional virtual reconstruction in the trans-sulcal removal of a left insular cavernous angioma (Esposito *et al.*, 2006), using cortical sulci as landmarks for intraoperative orientation. Later, Harput *et al.*, suggested the adoption of cortical veins in the place of sulcal anatomy to navigate around subcortical lesions (Harput *et al.*, 2014). More recently, Fernandes de Oliveira Santos *et al.* emphasized the importance of both the cortical surface and venous anatomy in the identification of cortical projection of subcortical lesions (de Oliveira Santos *et al.*, 2018). These authors (de Oliveira Santos *et al.*, 2018), and subsequently Gosal *et al.* (Gosal *et al.*, 2021), introduced the usage of volumetric FLAIR sequences for better visualization of

the cortical surface, instead of the plain 3D T1-weighted sequences adopted in the preceding studies (Esposito *et al.*, 2006; Gong *et al.*, 2008; Harput *et al.*, 2014; Lovato *et al.*, 2019)). Direct volume rendering from volumetric FLAIR images was also described as ideal for 3D visualization of non-enhancing diffuse LGGs (WHO grade II) (Gosal *et al.*, 2021). Conversely, contrast-enhanced volumetric T1-weighted sequences were advocated for 3D assessment of enhancing HGGs, since they provided a better identification of the lesion abutting to the cerebral surface, together with a good representation of the cortical vascularity (Gosal *et al.*, 2021).

Most of the previously published series employed **direct volume rendering** methods on fused 3D conventional neuroimaging datasets (i.e., a new single sequence is created from the sum of voxel intensity of a 3D-Flair and a co-registered contrast-enhanced 3D-T1, in order to conjoin unique information provided by each technique, and then rendered in 3D) (Harput *et al.*, 2014; Jaimovich *et al.*, 2014; Kim *et al.*, 2012; Lovato *et al.*, 2019; Rotariu *et al.*, 2017; Spiriev *et al.*, 2017; Wang *et al.*, 2010) (see **Figure 1.16**).

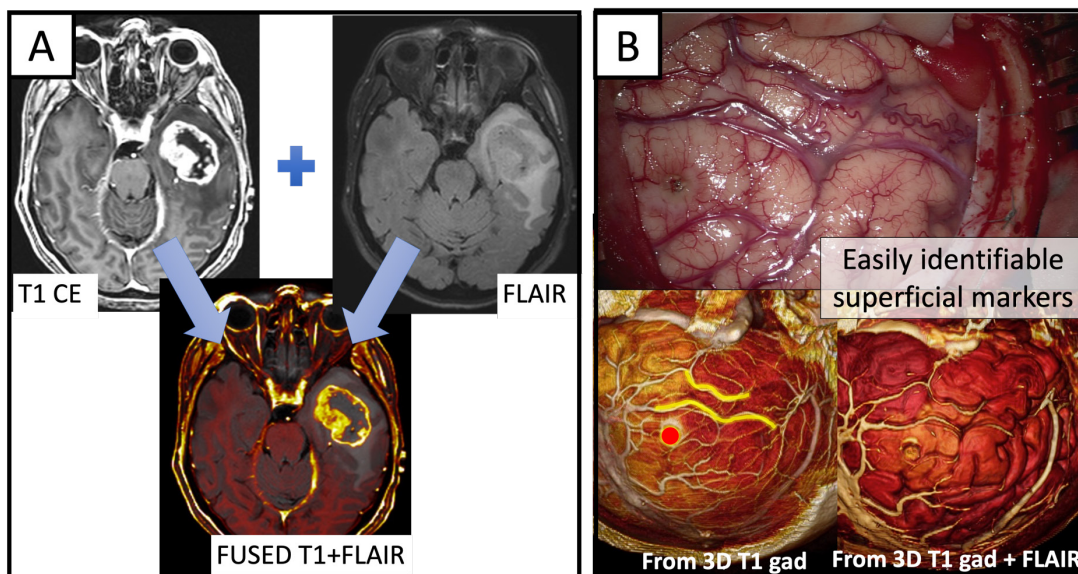


Figure 1.16 - Fusion of different imaging modalities

(A) An example of the fusion of different imaging datasets (here contrast-enhanced (CE) 3D T1 + 3D FLAIR) is represented in the case of a left temporal high-grade glioma. (B) Direct volume rendering techniques showing the reconstruction based solely on the CE 3D T1 exam (bottom left) and the 3D rendering of the fused dataset (CE 3D T1 + 3D FLAIR). The first one is more indicated if cortical vascular anatomy alone must be assessed; the second one entails a better representation of the sulci and gyri while still depicting the larger vessels.

However, the overall visibility and anatomical discrimination of overlaid images displayed with this technique tend to drop when multiple imaging sequences are fused together for surgical simulation. To overcome this problem, the user needs to manually modify a higher number of parameters, which increases the complexity in the software utilization (Kin *et al.*, 2017).

Surface (or geometric) rendering techniques have become clinically available in more recent years to overcome these limitations (Kin *et al.*, 2017). Surface rendering algorithms rely on polygonal modeling of a segmented volume and are the principal modality adopted in computer graphics (i.e., videogames and movies) (see **Figure 1.17**). However, notwithstanding the amount of image analysis programs granting the combination of direct and surface volume rendering techniques in the same 3D view (an example of the benefits of combining both the two techniques in clinical practice is reported in **Figure 1.18**), are increasingly available, only a few authors, to date, reported the usage of both technologies combined (Kin *et al.*, 2017; Kin *et al.*, 2011).

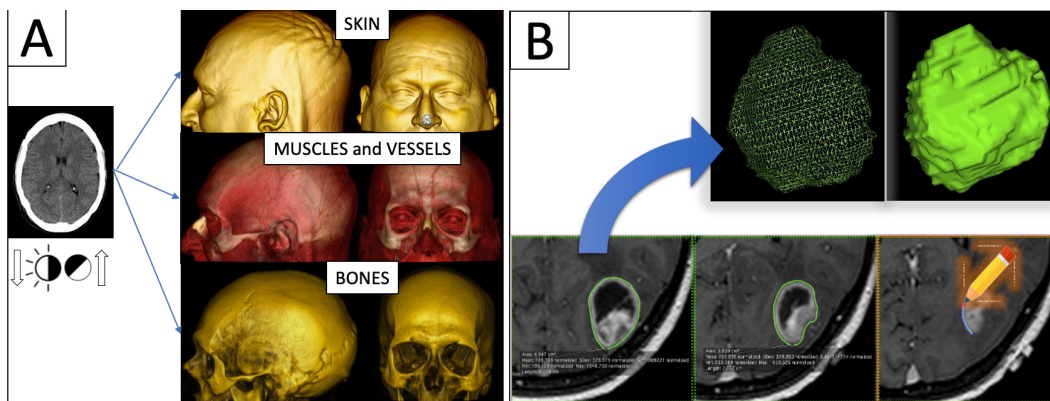


Figure 1.17 - Main differences between direct (left) and geometric/surface (right) volume rendering
 (A) With direct volume rendering, applying different windowing in the parameters, it is possible to select and cast different anatomical details in 3D in a straightforward manner; the main advantage of this technique is being easily and rapidly available (it does not require previous segmentation), and the extremely high anatomical detail obtained. (B) In surface (or geometric) volume rendering, the surface is extracted from a region-of-interest previously segmented on planar images; then, it is represented in 3D using a lot of simple geometric primitives (e.g., triangles). The main advantages of geometric rendering are that surfaces can be made transparent, allowing visualization of structures located deep from the surface (as it is the case of fiber tracts running below the cortical surface); moreover, the color of each volume/structure displayed can be set arbitrarily, easing the interpretation of different structure portrayed in the final anatomic-functional-pathological model.

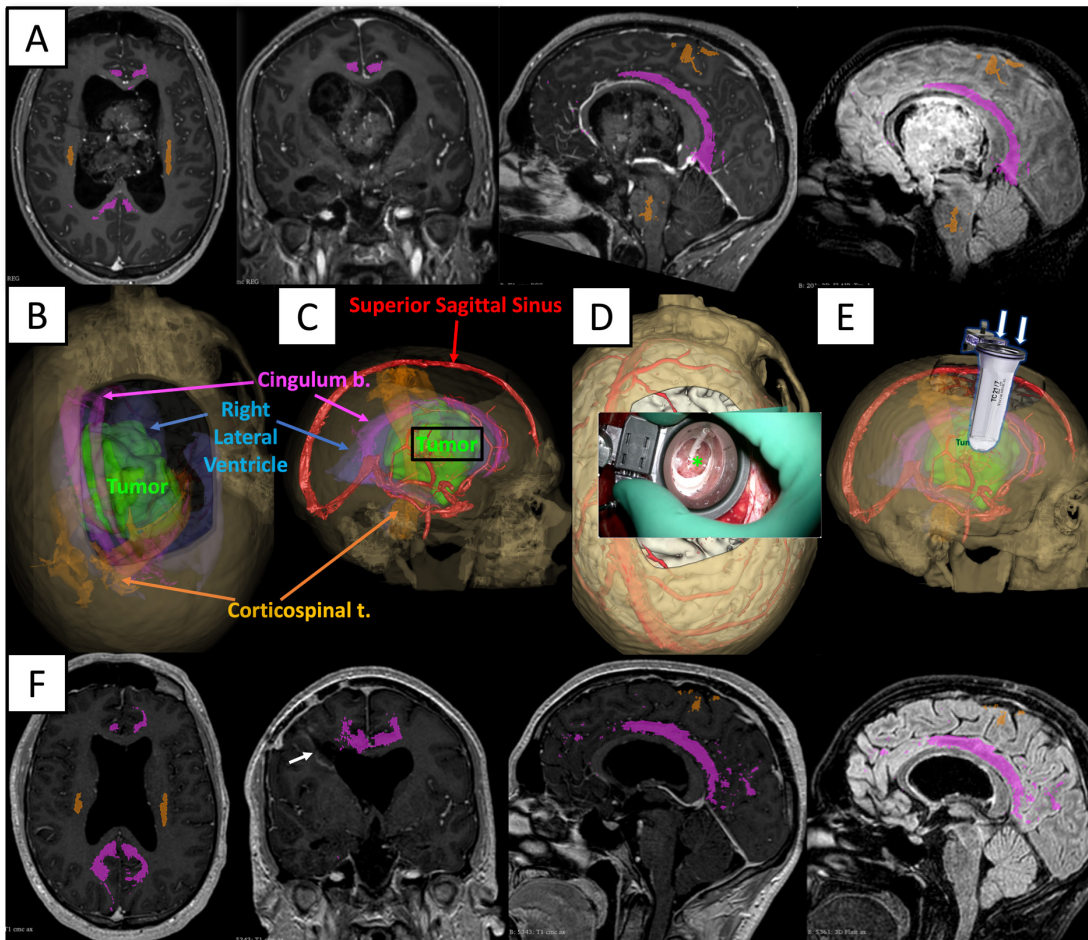


Figure 1.18 - Illustrative case of preplanning, integrating functional data, performed with combined direct and geometric rendering techniques

(A) After suffering from symptomatic hydrocephalus, a young patient is diagnosed with a large tumor occupying the third and lateral ventricles and compressing the adjacent structures. (B and C) A preplanning integrating DTI information was performed to identify the ideal surgical corridor toward the deeply located tumor with a careful assessment of morphological and functional anatomy (with particular attention to the cortical and deep-seated vessels and critical functional structures) using a virtual reality approach. The integration of direct volume rendering (for vascular anatomy) and geometric volume rendering (for the tumor, brain, ventricles, and fiber tracts) allowed the best visual representation possible. (D and E) A corticectomy was performed at the chosen site (right frontal lobe), and a tubular retractor was gently inserted through the white matter till reaching the top of the tumor (the latter can be spotted in the image at the bottom of the tubular retractor, green asterisk). The lesion is therefore removed through the portal system using a minimally-invasive approach. (F) Postoperative MRI shows complete tumor resection (a white arrow the surgical corridor adopted).

1.6 General considerations regarding advanced neuroimaging in the setting of treatment response monitoring

The adoption of sequential functional and metabolic examinations along FU could offer comprehensive data on the neoplasm pathophysiology: hypothetically, successful therapy in gliomas should progressively lead to normalization of the spectroscopic configuration (reduction of Cho, Lac, Lip and elevation of the NAA/Cho proportion),

higher water diffusion, and declining of PWI values inside the tumoral tissue with potential regularization of vessels permeability, while the opposite modifications might portray tumor progression (Thust *et al*, 2018c).

PWI, dMRI and 1H-MRS, appear especially attractive, as they might be handily acquired at the same time of routine MRI scanning; metabolic evaluations using SPECT or PET radiotracers are more challenging since dedicated equipment is required, radioactive isotopes need to be administered, and they are expensive exams (Ono *et al.*, 2018). Nonetheless, compared to cMRI, PET with aminoacidic radiotracers seems to provide an earlier and superior appraisal of tumoral treatment response; a constant reduction of tumoral radiotracer uptake (particularly with *11C-MET*) is generally noticed following successful RT, ChT, and antiangiogenic treatment (Dhermain *et al*, 2010; Hutterer *et al*, 2015; Nagane *et al*, 2014; Ono *et al.*, 2018; Ribom *et al*, 2002).

The adoption of advanced neuroimaging to evaluate subtle response not complemented by volumetric modification in cMRI might consent the precocious assessment of the effectiveness of therapies conducting to confirmation of the chosen treatment or its appropriate diversion to a possibly more successful one (Hutterer *et al.*, 2015; Shaikh *et al*, 2020). Nonetheless, additional studies are needed to validate the appropriateness of such longitudinal functional and metabolic examining and its potential utility in the clinical setting.

1.7 Radiomics and Habitat analysis

Qualitative assessment of diverse imaging sequences at the naked eye is fundamentally the most widely adopted process to date. Nonetheless, the intricate characteristics of gliomas' morphology and their frequently narrow modifications among different exams are often arduous to perceive accurately at direct visual inspection (Lohmann *et al*, 2021; Upadhyay & Waldman, 2011; Zhou *et al*, 2018). Apart from the introduction of novel imaging acquisition modalities and map elaborations, another approach to increment brain neoplasms' characterization relies on the adoption of advanced mathematical models to extract existing "deep-seated" data, not easily identifiable at common clinical observation, from available cMRI and aMRI sequences (Lohmann *et al.*, 2021). Radiomics, as the aforementioned method is

termed, quantifies textural information throughout computations extrapolation of the spatial distribution of signal intensities and pixel interrelations, applying methods of analysis from the field of artificial intelligence. The former is a multi-step procedure comprising image acquisition and reconstruction, image pre-processing, manual, or semi- and fully-automated identification of regions of interest, extraction of features and quantification, feature selection, and finally, generation of predictive models utilizing machine learning (Singh *et al*, 2021; Zhou *et al.*, 2018). Radiomic features founded on first-order statistics generally implicate the calculation of cumulative statistics of voxel values and their histograms throughout the entire tumor. Second-order texture features, instead, are utilized to assess the probability of detecting spatially related voxels within the tumor. Altogether, the extrapolation of these data from radiological images generates mineable databases that can be utilized for diagnosis, prognosis characterization, and to assess or predict response to specific treatments (Kotrotsou *et al*, 2016; Singh *et al.*, 2021).

Furthermore, with the application of advanced mathematical modeling, it is also possible to divide neoplasms into definite subregions comprehending clusters of voxels with comparable radiomics features (**Figure 1.19**). This method is defined as 'habitat imaging' and is considered a way to characterize and measure the heterogeneity of the tumoral microenvironment (Gatenby *et al*, 2013), which is strictly associated with patients' prognosis and overall survival (Barajas *et al*, 2012; Dextraze *et al*, 2017; Eder & Kalman, 2014). Additionally, monitoring/tracking the progression of aggressive habitat sub-volumes can offer a more profound understanding of disease evolution/recurrence over time and space, compared to the mere assessment of the tumor volume modifications conventionally performed (Dextraze *et al.*, 2017). Habitat imaging has been currently mainly employed on cMRI sequences, although it could hypothetically be applied to any neuroimaging method, comprising aMRI techniques such as PWI and dMRI as well as PET imaging with different radiotracers, providing relevant information for surgical procedures, radiotherapy planning, disease monitoring, and prognosis estimation.

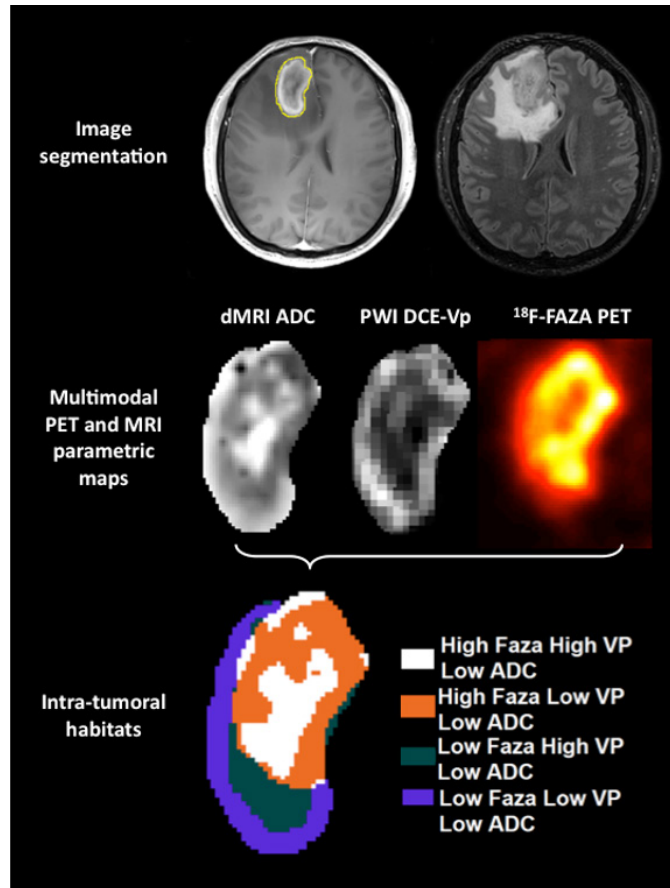


Figure 1.19 - Illustrative case of habitat analysis from the combination of three diverse imaging modalities (dMRI, PWI, and 18F-FAZA PET).

According to the combination of the three different parametric maps, the tumor is subdivided into a definite number of clusters, possibly identifying areas characterized by different metabolic and molecular statuses.

2 AIM OF THE THESIS

The **aim** of this thesis was to *validate the application of advanced neuroimaging techniques* in the preoperative assessment and surgical management of brain gliomas, focusing on their derived:

- A. *characterization of tumor biological heterogeneity* and ability to guide the neurosurgeon in a *more accurate target definition* for bioptic sampling and surgical resection, allowing a more comprehensive diagnosis of tumor biological and molecular characteristics and a more appropriate treatment. This goal will be assessed through:
 - I. generation of metabolic tumor habitats combining radiomic features from perfusion and diffusion magnetic resonance imaging (MRI) techniques with those of ¹⁸F-FAZA positron emission tomography (a radio-marker for hypoxia). These clusters will be validated against the corresponding morphologic characteristics at conventional MRI sequences and histopathology from bioptic sampling (**Experiment I**)
 - II. optimization for brain gliomas' microenvironment of the pioneering Vascular, Extracellular, and Restricted Diffusion for Cytometry in Tumors (*VERDICT*) MRI technique, a computational multi-compartment modeling framework originally developed for the extraction of quantitative maps from advanced dMRI acquisitions in body tumors, representing their vascular, extracellular and restricted component. The results from our VERDICT model will be validated against Perfusion weighted imaging parameters (relative cerebral blood volume (DSC-rCBV) and plasma volume (DCE-Vp)) and histopathology from corresponding stereotactic sampling (**Experiment II**)
- B. *increase of the rate of maximum safe resection, patient's quality of life, and eventual survival.*
 - III. To validate this aim, we will investigate the clinical application of advanced *Diffusion Tensor Imaging (DTI)* tractography and *BOLD functional MRI (fMRI)*, as well as the generation of detailed *3D-rendered anatomic-functional-pathological models* for virtual reality, in the preoperative and intraoperative management of 234 brain gliomas undergoing surgical resection (**Experiment III**)

3 DECODING THE HETEROGENEITY OF MALIGNANT GLIOMA BY PET AND MRI FOR SPATIAL HABITAT ANALYSIS OF HYPOXIA, PERFUSION AND DIFFUSION IMAGING: A PRELIMINARY ANALYSIS FOR THE HYPERDIRECT STUDY.

In the first experiment of this thesis, a preliminary study was performed to validate the clinical potential of spatial tumor habitat imaging combining radiomic features from perfusion and diffusion magnetic resonance imaging (MRI) techniques with those of 18F-FAZA positron emission tomography (a radio-marker for hypoxia). This approach aimed at assessing HYpoxia, PERfusion, and tissue DIffusion in a retrospective series of HGGs where 18F-FAZA-PET/CT and advanced MRI were available, and deriving a combined HYPERDIrect map for clustering of intra-tumor heterogeneity. Habitat clusters were validated against the corresponding morphologic characteristics at conventional MRI sequences and histopathology from stereotactic bioptic sampling.

The abstract of this study was pre-accepted by the journal *Frontiers in Neuroscience* as part of a special issue "Advanced Imaging and Mapping in Brain Tumors" and the final manuscript has been submitted.

3.1 Introduction

Tumor heterogeneity poses a major clinical challenge in brain tumors and its enhanced assessment probably represents the key for the understanding treatment failure in high grade gliomas (HGGs) (O'Connor *et al.*, 2015; Stadlbauer *et al.*, 2018b). Indeed, in HGGs, the regional diversity both at the level of DNA mutation and gene expression profiles may ultimately alter phenotype by influencing tumor cell metabolism, apoptosis, and angiogenesis processes (Komori *et al.*, 2018; Louis *et al.*, 2016). At the individual patient level, the heterogeneous biology of malignant gliomas challenges tools that rely on single biopsy criteria for making disease-wide assessments and poses a problem in planning effective subsequent treatments.

Furthermore, tumor heterogeneity is reflected in differential and also dynamical responses during therapy, eventually causing the failure of previously effective alkylating drugs or targeted therapies, as resistant clones invariably emerge and proliferate (Sottoriva *et al.*, 2013; Stadlbauer *et al.*, 2018b).

Noninvasive imaging can provide multiple biomarkers with insight into malignancy and biology of gliomas. Conventional magnetic resonance imaging (cMRI) is routinely employed in the diagnosis and clinical management of malignant gliomas: besides the tumor features described by cMRI sequences, advanced physiological MRI techniques such as diffusion MRI (dMRI) and perfusion-weighted imaging (PWI) add important structural, physiological and hemodynamic information to measure biological properties quantitatively and non-invasively and correlate with patients' outcome (Castellano & Falini, 2016). Similarly, positron emission tomography (PET) imaging reflects fundamental metabolic patterns throughout the tumor. In particular, PET using tracers from nitroimidazoles family, such as [18F]fluoromisonidazole (18F-FMISO) or [18F]-Fluoroazomycin arabinoside (18F-FAZA), identifies areas of hypoxic tissue that have been shown as related to treatment resistance, thus negatively impacting on patient outcome and survival (Abdo *et al.*, 2019; Preibisch *et al.*, 2017).

Furthermore, with the application of advanced mathematical modeling, it is also possible to divide neoplasms into definite subregions comprehending clusters of voxels with comparable radiomics features. This method is defined as 'habitat imaging' and is considered a way to characterize and measure the heterogeneity of tumoral microenvironment (Gatenby *et al.*, 2013). Habitat imaging has been currently mainly employed on cMRI sequences, although it could hypothetically be applied to any neuroimaging method, comprising aMRI techniques such as PWI and dMRI as well as PET imaging with different radiotracers (Beig *et al.*, 2020; Cui *et al.*, 2016; Del Mar Alvarez-Torres *et al.*, 2020; Dextraze *et al.*, 2017; Fathi Kazerooni *et al.*, 2018; Fuster-Garcia *et al.*, 2018; Hu *et al.*, 2015; Ismail *et al.*, 2018; John *et al.*, 2019; Juan-Albarracin *et al.*, 2019; Juan-Albarracin *et al.*, 2018; Kim & Gatenby, 2017; Kim *et al.*, 2021a, b; Lee *et al.*, 2015a; Lee *et al.*, 2015b; Li *et al.*, 2019a; Li *et al.*, 2018a; Li *et al.*, 2018b; O'Connor *et al.*, 2015; Park *et al.*, 2021; Sauwen *et al.*, 2016; Stringfield *et al.*, 2019; Verma *et al.*, 2020; Wang *et al.*, 2019; Wei *et al.*, 2019; Wu *et al.*, 2020; Zhang *et al.*, 2019; Zhou *et al.*, 2017; Zhou *et al.*, 2014).

To date, the spatial relationship between hypoxic areas, as depicted by PET, high vascular endothelial proliferation and angiogenesis, as depicted by PWI, and increment of cellularity and tumor invasion, as depicted by dMRI, in malignant brain gliomas has not been completely elucidated.

3.2 Aims

The aim of the present study is to evaluate an innovative PET / MRI approach for the assessment of HYpoxia, PERfusion and tissue DIffusion in HGG and derive a combined HYPERDIrect map for clustering of intra-tumor heterogeneity. To the best of our knowledge, this represents the first study combining the aforementioned parameters to define tumor habitats.

3.3 Materials and Methods

3.3.1 Patients

Twenty patients harboring brain MRI features evocative for high grade glioma (HGG) were prospectively recruited at San Raffaele Scientific Institute from April 2016 to October 2017. Patients' enrollment commenced after the authorization of the Institute's Ethics Committee and the patient's informed consent. All the registered individuals were subjected to an advanced MRI acquisition and 18F-FAZA PET/CT before surgery, except for 2 patients that were withdrawn from the study due to technical problems related to radiotracer synthesis. Another patient was eventually excluded from the analysis since the final histopathological diagnosis was brain metastases from lung cancer.

3.3.2 PET/CT image acquisition

The procedure of ¹⁸F-FAZA radiotracer production followed the technique previously reported by Savi et al. (Savi *et al*, 2017b). Every recruited patient had an intravenous administration of about 372±17 (minimum 340, maximum 407) MBq of ¹⁸F-FAZA. The PET/CT scan acquisition and analysis was conducted as previously reported by Mapelli et al. (Mapelli *et al*, 2021; Mapelli & Picchio, 2020)

3.3.3 Advanced MR acquisition

Preoperative MRI datasets were acquired (1-5 days prior to the surgical procedure) on a 1.5 T scanner (Philips Achieva - Philips Healthcare, Best, Netherlands) in 12/17 cases, while on a 3.0 T (Ingenia CX scanner, Philips Healthcare, Best, The Netherlands) on 5/17 patients.

Imaging acquisition included the following sequences:

- 3D-FLAIR and Contrast-enhanced (CE) 3D-T1 weighted images, for morphological evaluation and tumor segmentation;

- dMRI (DWI and DTI), to detect microstructural differences within the tumor tissue (Castellano *et al*, 2016; Castellano & Falini, 2016; Steven *et al*, 2014). DWI analysis was performed to calculate Apparent Diffusion Coefficient (ADC) maps using the MRI scanner software. DTI acquisition was also performed to calculate Mean Diffusivity (MD) maps using FMRIB Diffusion Toolbox (FDT tool, FMRIB Software Library [FSL] version 6.0.0, <https://fsl.fmrib.ox.ac.uk/>) software after correction of raw DTI images for head motion and eddy currents.

- PWI, including dynamic susceptibility contrast enhanced (DSC) and dynamic contrast-enhanced (DCE) MRI, to characterize tumor vascularization and neoangiogenic processes (Santarosa *et al*, 2016). PWI analysis was performed with Olea Sphere (v 3.0, Olea Medical Solutions, France) to obtain the parametric maps of volume transfer constant (Ktrans) and plasma volume (Vp), derived from DCE, and relative cerebral blood volume (rCBV), derived by DSC, as described in Anzalone *et al*. (Anzalone *et al*, 2018a). Pre-processing steps included automatic motion correction by a rigid-body registration, automatic spatial smoothing, and background segmentation.

The acquisition parameters of the sequences acquired are reported in **Table 3.1** and **Table 3.2**.

| | Scanning sequence and options | TR (ms) | TE (ms) | FOV (mm) | Acquisition matrix (mm) | Slice thickness (mm) | Reconstructed voxel (mm) | Acquisition time (seconds) |
|----------|--|---------|---------|----------|-------------------------|----------------------|--------------------------|----------------------------|
| 3D T1 CE | Axial 3D spoiled gradient echo T1 weighted | 25 | 5 | 256 | 256x256 | 1 | 1x1x1 | 512 |
| 3D FLAIR | Axial 3D FLAIR (TI = 1700) | 4800 | 320 | 240 | 240x240 | 1 | 1x1x1 | 240 |

| | | | | | | | | |
|-----|--|------|-----|-----|--------|-----|---------------|-----|
| DWI | GE-EPI, b-values of 0 and 1000 s/mm ² , 3 directions | 4000 | 65 | 240 | 120x94 | 4.4 | 0.72x0.72x4.4 | 52 |
| DTI | GE-EPI, b-values of 0 and 1000 s/mm ² , 15 directions | 3733 | 99 | 224 | 92x90 | 2.5 | 1.75x1.75x2.5 | 694 |
| DCE | Axial DCE 3D spoiled gradient echo T1 weighted, 70 dynamics | 4 | 1.9 | 230 | 96x96 | 5 | 2.05x2.05x2.5 | 466 |
| DSC | Axial DSC FFE-EPI T2* weighted, 80 dynamics | 1650 | 40 | 230 | 76x61 | 5 | 2.05x2.05x5 | 137 |

Table 3.1 - Characteristics of the sequences acquired with the 1.5 T MR scanner.

The scanner was a Philips Achieva (Philips Healthcare, Best, Netherlands). GE = gradient eco, EPI = Echo Planar Imaging, IR = inversion recovery, SE = Spin Echo., CE = contrast-enhanced, TI = Time of inversion.

| | Scanning sequence and options | TR (ms) | TE (ms) | FOV (mm) | Acquisition matrix (mm) | Slice thickness (mm) | Reconstructed voxel (mm) | Acquisition time (seconds) |
|----------|--|---------|---------|----------|-------------------------|----------------------|--------------------------|----------------------------|
| 3D T1 CE | Axial 3D spoiled gradient echo T1 weighted | 11 | 5 | 256 | 284x190 | 0.9 | 0.8x0.8x0.9 | 321 |
| 3D FLAIR | Axial 3D FLAIR (TI = 1700) | 9000 | 300 | 230 | 204x204 | 1.2 | 0.7x0.7x0.7 | 486 |
| DWI | GE-EPI, b-values of 0 and 1000 s/mm ² , 3 directions | 3000 | 90 | 230 | 152x138 | 3 | 0.96x0.96x3 | 99 |
| DTI | GE-EPI, b-values of 0 and 1000 s/mm ² , 32 directions | 3200 | 80 | 240 | 96x94 | 2.5 | 0.94x0.94x2.5 | 215 |
| DCE | Axial DCE 3D spoiled gradient echo T1 weighted, 70 dynamics | 4 | 1.8 | 230 | 96x96 | 5 | 2.05x2.05x2.5 | 382 |
| DSC | Axial DSC FFE-EPI T2* weighted, 80 dynamics | 1500 | 40 | 230 | 96x78 | 5 | 2.05x2.05x5 | 124 |

Table 3.2 - Characteristics of the sequences acquired with the 3 T MR scanner.

The scanner was an Ingenia CX (Philips Healthcare, Best, Netherlands). GE = gradient eco, EPI = Echo Planar Imaging, IR = inversion recovery, SE = Spin Echo, CE = contrast-enhanced, TI = Inversion Time

3.3.4 Image processing

For each patient, all the radiological studies and maps were imported, coregistered to the reference 3D-T1 CE sequence (two consecutive automatic rigid registration

processes, with 6 degrees of freedom and 0.1 percentage of samples, were performed after initial manual adjustment, then carefully checked for the eventual necessity of minor manual correction) and reformatted to the same matrix (voxel 1x1x1 mm) in the image processing software 3D Slicer (<http://www.slicer.org>) (Fedorov *et al*, 2012), creating a single dataset for each patient. Two different tumor masks were segmented: one including only the enhancing tissue and necrotic core on the post-gadolinium 3D-T1 images (CE-tumor, green contour in **Figure 3.1C**), the second including, additionally, the peritumoral infiltrative edema as identified on 3D-FLAIR images (FLAIR-tumor, orange contour in **Figure 3.1F**). Care was taken while comparing data from multiple coregistered sequences (e.g., Susceptibility-weighted imaging, T2-weighted, PWI maps, ADC/MD, T1-weighted Spin-echo with and without contrast enhancement, CT) not to include non-tumoral structures that could jeopardize subsequent analyses (e.g., subarachnoid cisterns, sulci, ventricular space, choroid plexus, ependyma, significant vascular structures, dural folds, calcifications).

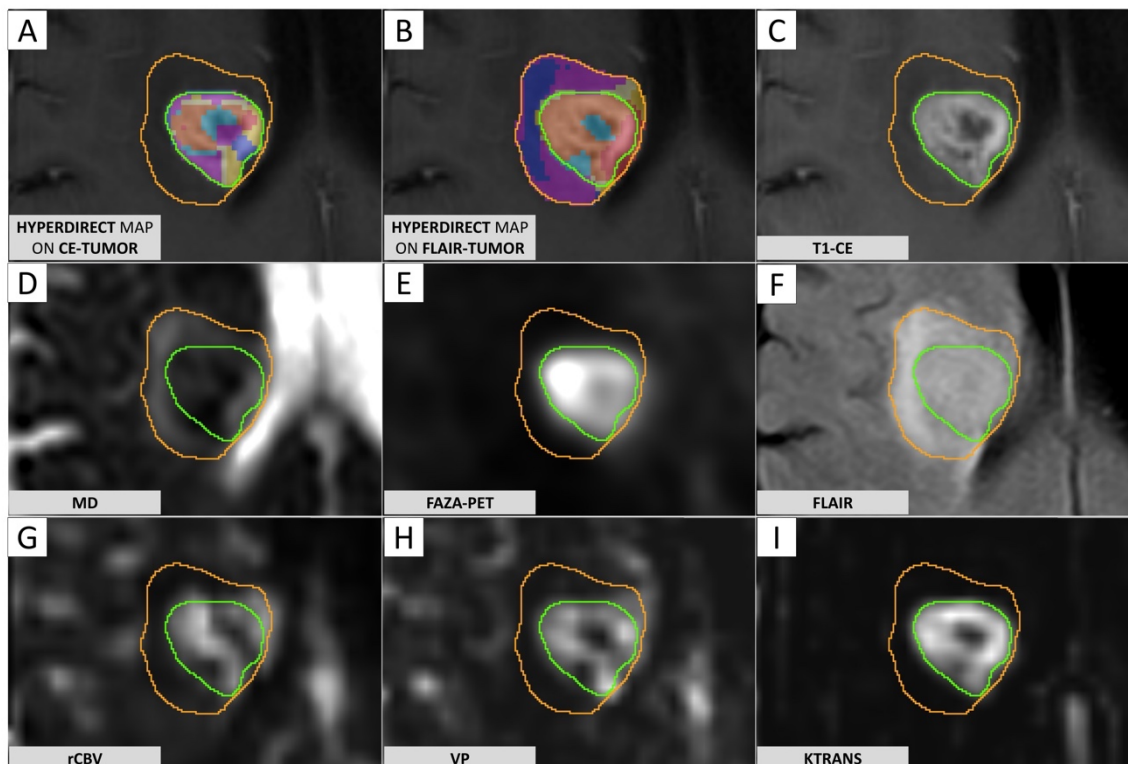


Figure 3.1 - FLAIR-tumor and CE-tumor segmentations on different MRI sequences.

(A) Prototype of clusters resulting from the application of the HYPERDirect algorithm only to the contrast-enhanced tumor volume (CE-tumor); clusters obtained from CE-tumor volume were considered too small and fragmented in order to be reliably correlated to histology, and therefore not suitable for the purpose of the present study. (B) Habitats obtained applying the HYPERDirect algorithm to the FLAIR-tumor volume (which included the

contrast-enhanced tumor core along with the surround FLAIR hyperintensity) were able to divide the whole tumor in a more reproducible way, with larger clusters amenable to a reliable histological correlation with the bioptic samples obtained. (C) T1-weighted contrast-enhanced imaging: the CE-tumor volume is contoured in green, including only the enhancing tissue and necrotic core. (D) MD map elaborated from DTI acquisition. (E) FAZA-PET uptake showing hypoxic areas (F) FLAIR images: FLAIR-tumor is contoured in orange, including both the CE-tumor and the peritumoral hyperintensity. (E) rCBV map elaborated from DSC MR perfusion acquisition. (F) VP map elaborated from DCE MR perfusion acquisition (H) Ktrans map elaborated from DCE MR perfusion acquisition.

The feasibility of deriving a combined HYPERDIrect map was then exploited by using the following method. Clustering analysis in the tumoral region-of-interest of each coregistered map (perfusion, diffusion, and hypoxia) was performed: each map was clustered in 2 disjointed regions by grouping together voxels with high and low-intensity values via an automatic OTSU thresholding algorithm method developed in Matlab2019a. Therefore, given three MRI sequences D_1 , D_2 and D_3 , they were clustered as follows:

$$D_1 \rightarrow [D_{1L}, D_{1H}], D_2 \rightarrow [D_{2L}, D_{2H}] \text{ and } D_3 \rightarrow [D_{3L}, D_{3H}]$$

$$D_{1L} \cap D_{1H} = \emptyset, D_{2L} \cap D_{2H} = \emptyset \text{ and } D_{3L} \cap D_{3H} = \emptyset$$

In this way, 2 clusters for each map ('high' and 'low' expression of a parameter) were obtained (see **Figure 3.2A**). Then, HYPERDIrect habitat maps were composed in each patient by defining as a different 'habitat' each possible combination of clusters (see **Figure 3.2B**). Thus, the cluster which groups together all high intensity cluster sequences (HHH) is defined as:

$$\text{Habitat } (HHH) : [D_{1H} \cap D_{2H} \cap D_{3H}]$$

The different habitats, represented with different colors to ease visual identification, yield regions with different combinations of perfusion, diffusion, and hypoxia, supposedly reflecting different physiological microenvironments within the tumor.

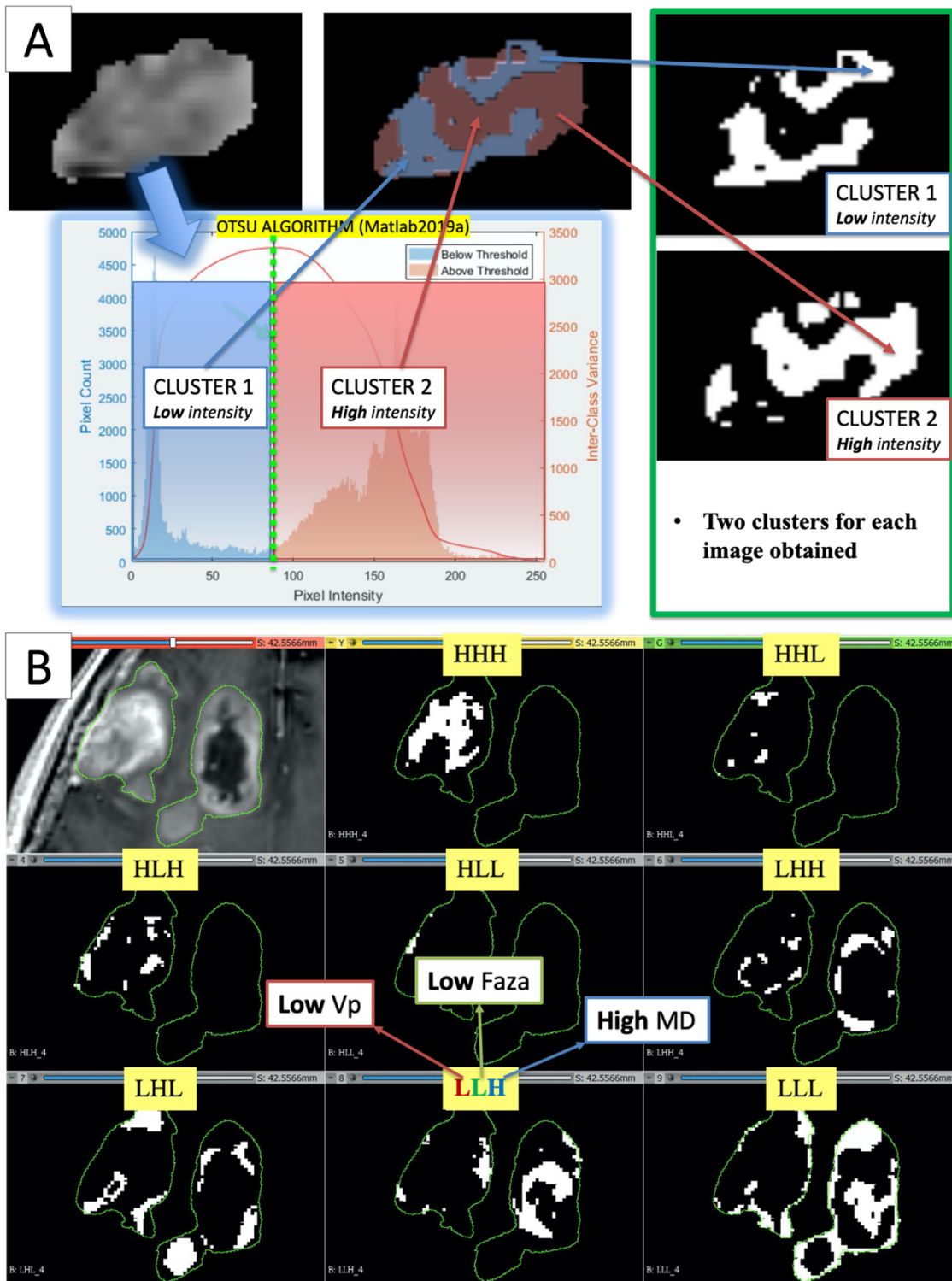


Figure 3.2 - OTSU algorithm and cluster intersection.

(A) The OTSU algorithm was adopted to identify the best cut-off able to divide voxels in two clusters of intensity while preserving the highest possible amount of information. Each tumor-masked parametric map then underwent an automatic OTSU binary clustering in 2 disjointed regions by grouping together voxels with HIGH and LOW intensity values (B). The 8 combinations (cluster intersection) were then generated by combining all possible high (H) and low (L) regions of each map (e.g., Vp + FAZA + MD) obtained from the OTSU algorithm.

3.3.5 *Surgical procedure and Histopathology*

All patients underwent the surgical procedure at the Neurosurgery Department of the IRCCS San Raffaele Hospital (Milan, Italy). Patients were considered for maximum safe resection or stereotactic needle biopsy according to tumor location/extension and patient characteristics (e.g., age, comorbidities, and performance status).

In the case of stereotactic biopsy, the procedure commenced with the fixation of the MRI-compatible Leksell stereotactic frame to the patient's skull (Model G, Elekta, Stockholm, Sweden), under mild intravenous sedation (midazolam) and local anesthesia (lidocaine and mepivacaine). The patient then underwent the acquisition of an axial 3D-T1 MRI after gadolinium administration (Voxel 1 x 1 mm, slice thickness 1 mm without gap, Matrix 256x256 mm) using the appropriate fiducial system on a Philips Achieva 1.5 Tesla MR scanner (Philips Medical Systems, Best, the Netherlands). In most of the cases, a 3D T2-weighted series was also obtained. All the relevant imaging and parameter maps were then imported into the stereotactic planning software Leksell SurgiPlan® (Elekta Instruments AB, Stockholm, Sweden) and co-registered to the newly acquired stereotactic images.

Since the final HYPERDIrect habitats were not available to the neurosurgeon preoperatively, the designation of target sites for biopsy sites and the needle path were planned according to the best clinical practice in order to maximize patient's safety while ensuring final diagnosis. During the procedure, a Sedan needle (2.5 mm diameter and 10 mm of bioptic window) was used to acquire a minimum of two cylindrical bioptic samples, according to the size and macroscopical aspect of the tissue obtained and procedure-related risks. The accuracy of the bioptic sampling was eventually verified in all cases with the co-registration of the preoperative imaging and planned trajectory with the postoperative CT images inside the SurgiPlan software; the stereotactic coordinates of the exact, final sites of the biopsy were therefore imported in the 3D Slicer Dataset.

The tissue samples obtained were directly fixed in a 10% formalin solution and referred to the pathology department, where they were processed the same day or the following one if the procedures were performed in the late afternoon. The final diagnosis was established according to 2016 WHO classification (Louis *et al.*, 2016).

A descriptive analysis of the microscopic morphology of each sample was performed by an expert neuropathologist (M.C.) with the assistance of a neurosurgeon (M.B.), repeating the whole evaluation at three distant time points (blinded from previously reported values and patient's case) in order to enhance the reproducibility of the results. Additionally, to address the issue of the length variability among different bioptic specimens and to maximize the correspondence with the target point set on the stereotactic planning system, only the central portion (extending 5 mm along the greatest axis of the specimen in its largest section available) was analyzed in each sample.

The following parameters were semi-quantitatively graded similarly to a previously reported work (Mikkelsen *et al*, 2018), despite the adoption of a higher number of classes dividing each feature in the present analysis: cellularity, extent of necrosis, and the number of hyperplastic vessels counted. Cellularity was graded with a score from 1 (seemingly normal representation) to 5 (extremely high cellular density). Classes considered for necrosis (expressed as a rate over the whole area considered for each specimen) were the following: 0 (0%), 1 ($\leq 10\%$), 2 (11-25%), 3 (26-50%), 4 (51-75%) and 5 (76-100%).

3.3.6 Statistical analysis

Statistical analysis was performed with IBM SPSS Statistics, version 23.0 (IBM Corp., Armonk, New York, USA) and Matlab2019a (MathWorks, Natick, Massachusetts, USA). The threshold of statistical significance was defined as two-sided $p=0.05$. Distribution normality was assessed with the Kolmogorov-Smirnov test. Categorical variables were compared with the Pearson χ^2 test or Fisher's exact tests and continuous variables with either the Student t-test or the Mann-Whitney U test (according to whether the distribution was normal or not).

The following variables were tested for possible associations: voxel intensities of each parametric map across different habitats, CE-tumor volume, FLAIR-tumor volume, representation of the different habitats (absolute volume, rate over total), patient's age, which tumor grading, MGMT methylation, 1p19q codeletion, IDH-1 status, overall survival.

A Kruskal-Wallis test was conducted to determine if there were differences in voxel intensity, for each parametric map, between different habitats. The shape of distributions of voxel intensity was then assessed by boxplots' visual inspection. Subsequently, pairwise comparisons were performed using Dunn's (1964) procedure with a Bonferroni correction for multiple comparisons.

3.4 Results

3.4.1 Patients and Tumors

The study population (data summarized in **Table 3.3**) was composed of 5 female and 13 male patients, with ages ranging from 41 to 81 years old (mean 66 years).

| Nº | Age (yrs) | Sex | Tumor vol. CE (cm ³) | Tumor vol. Flair (cm ³) | N ° of distinct lesions | Surgical procedure | Histology | p53 | ATRX | GFAP | KI-67 | MGMT methylation | IDH-1 status | OS (wks) |
|----|-----------|-----|----------------------------------|-------------------------------------|-------------------------|--------------------|--------------|-------|------|------|-------|------------------|--------------|----------|
| 1 | 71 | F | 23.4 | 67.8 | 1 | Resection | GBL (IV WHO) | 20% | + | + | 10% | + | - | 40 |
| 2 | 58 | M | 4.4 | 10.2 | 1 | Biopsy | GBL (IV WHO) | 15% | + | + | 20% | N/A | + | 76 |
| 3 | 56 | M | 25.0 | 111.6 | 1 | Resection | GBL (IV WHO) | 5% | + | + | 25% | + | - | 214 |
| 4 | 61 | M | 1.1 | 10.9 | 1 | Resection | AA (III WHO) | 5% | - | + | 30% | + | - | 71 |
| 5 | 73 | F | 61.4 | 130.2 | 1 | Biopsy | GBL (IV WHO) | 5-10% | + | + | 7% | N/A | - | 21 |
| 6 | 77 | M | 56.1 | 184.0 | 1 | Resection | GBL (IV WHO) | 0 | + | + | 15% | + | - | 16 |
| 7 | 79 | M | 79.1 | 185.4 | 1 | Resection | GBL (IV WHO) | 10% | - | + | 20% | + | - | 26 |
| 8 | 69 | F | 1.6 | 50.1 | 5 | Biopsy | AA (III WHO) | 5% | + | + | 3% | N/A | - | 13 |
| 9 | 64 | M | 2.6 | 91.1 | 3 | Biopsy | GBL (IV WHO) | 10% | + | + | 35% | N/A | - | 21 |
| 10 | 81 | M | 34.4 | 98.1 | 4 | Biopsy | AO (III WHO) | 0 | + | ++ | 15% | N/A | + | 10 |
| 11 | 65 | M | 30.3 | 136.5 | 1 | Resection | GBL (IV WHO) | 0 | + | + | 15% | + | - | 44 |
| 12 | 77 | M | 5.4 | 23.4 | 1 | Biopsy | GBL (IV WHO) | N/A | + | N/A | 5% | N/A | - | 13 |
| 13 | 41 | M | 0.0 | 146.5 | 1 | Biopsy | AA (III WHO) | 3% | + | + | 10% | + | + | 10 |
| 14 | 64 | M | 53.0 | 70.8 | 1 | Biopsy | AA (III WHO) | < 1% | + | -- | 20% | - | - | 8 |

| | | | | | | | | | | | | | | |
|----|----|---|------|-------|---|-----------|--------------|------|---|---|-----|-----|---|-----|
| 15 | 61 | M | 26.8 | 102.9 | 1 | Resection | GBL (IV WHO) | 40% | + | + | 40% | N/A | - | 88 |
| 16 | 57 | F | 8.0 | 18.8 | 1 | Biopsy | GBL (IV WHO) | < 5% | + | + | 5% | N/A | - | 222 |
| 17 | 44 | F | 16.8 | 162.3 | 1 | Biopsy | GBL (IV WHO) | 70% | - | + | 25% | N/A | - | 9 |

Table 3.3 - Patient demographic, histopathologic, and survival data.

Immunohistochemical analysis displayed was performed on a single sample considered chosen as the most representative by the referring neuropathologist. Abbreviations: AA= anaplastic astrocytoma, AO = anaplastic oligodendroglioma, GBL = glioblastoma, N/A = not available.

A single contrast enhancing (CE) lesion was detected in 13/17 patients; 3/17 patients harbored multiple CE lesions, while in one patient no definite CE tumor core was detectable. The average cumulative CE-tumor volume (per patient) was 25.3 ± 24.4 cm³ (range 0-79.1 cm³). Mean cumulative FLAIR-tumor volume (per patient) was 94.2 ± 58.7 cm³ (range 10.2-185.4 cm³). The mean rate between CE-tumor and FLAIR-tumor volume was 0.30 ± 0.20 (range 0-0.7).

Maximum surgical resection was performed in 7/17, while a stereotactic biopsy was obtained in 10/17 patients.

Four/17 individuals harbored an anaplastic astrocytoma (WHO grade III), one had an anaplastic oligodendroglioma (1p/19q co-deleted, WHO grade III), and 12/17 patients had grade IV glioblastoma, according to 2016 WHO classification. Three tumors retained an IDH-1 mutation. Histopathological and molecular data are summarized in **Table 3.3**.

3.4.2 Maps selection

The ideal number of maps to be included simultaneously in the algorithm was thoroughly evaluated. The possible complementary information gathered by adding a higher number of maps had to be balanced with the exponential increase in the number of significantly smaller and fragmented clusters, resulting in unreliable surgical targeting. For the aforementioned reasons, after several simulations, “8” (from the combination of 3 different maps) was identified as the ideal number of clusters for the purpose of the project. Among the considered perfusion MR maps, the intra-vascular plasma volume (Vp), which quantify tumor microvessel proliferation similarly to rCBV, was found as the most appropriate for the purpose of the study due to the lower susceptibility artifacts, absolute quantification, better evaluation close to large vessels,

cortex and hemorrhagic foci, higher spatial resolution compared to rCBV and a more informative representation of the FLAIR-tumor outside of the contrast-enhancing compared to Ktrans (Anzalone *et al.*, 2018b; Callewaert *et al.*, 2021; Gordon *et al.*, 2014; Zhang *et al.*, 2017).

3.4.3 Habitats' analysis

Eight habitats were generated from cluster intersection by combining all possible HIGH (H) and LOW (L) intensity regions of each map (Vp + FAZA + MD), and the final HYPERDirect map was composed. Since MD is inversely correlated to cellularity, for the pursuit of clarity and linearity, we decided to refer, in the majority of cases, to the concept of “cellularity” (instead of MD value) and to reverse the corresponding values accordingly.

The same algorithm was applied, separately, to either CE-tumor and FLAIR-tumor volume. Clusters obtained from CE-tumor volume alone were considered too small and fragmented in order to be reliably correlated to histology, and therefore they were not deemed suitable for the purpose of the present study (**Figure 3.1A**). On the contrary, habitats obtained from FLAIR-tumor (which included the contrast-enhanced region along with the surrounding FLAIR hyperintensity) were able to divide the whole tumor in a more reproducible way, with larger clusters amenable to a reliable histological correlation with the bioptic samples obtained. (**Figure 3.4B**). The radiological characteristics of the 8 clusters, and their volumetric representation, are summarized in **Table 3.4** and depicted in **Figure 3.3**.

| Habitats' characteristics | | | | Habitats representation among cases (% of total tumor volume) | | | | | | | | | | | | | | | | | |
|---------------------------|-----------------|--------------------|--------------------|---|------|------|------|------|------|------|------|------|------|-----|------|------|------|------|------|------|--------------|
| n | Perfus (↑Vp) | Hypoxia (↑FAZA) | Cellular (↓MD)* | Patient number | | | | | | | | | | | | | | | | | Row Aver. |
| | | | | 1 | 2 | 3 | 4 | 5 | 6 | 7 | 8 | 9 | 10 | 11 | 12 | 13 | 14 | 15 | 16 | 17 | |
| 1 | High | High | Low* | 0.2 | 11.1 | 2.0 | 1.3 | 8.0 | 6.7 | 4.8 | 1.9 | 2.6 | 1.7 | 5.4 | 1.9 | 4.4 | 6.7 | 11.1 | 6.4 | 0.7 | 4.5 |
| 2 | High | High | High* | 25.1 | 10.2 | 13.6 | 9.1 | 7.4 | 11.6 | 16.0 | 3.1 | 2.1 | 23.6 | 3.1 | 16.2 | 11.7 | 6.8 | 6.7 | 25.8 | 14.5 | 12.1 |
| 3 | High | Low | Low* | 2.0 | 4.8 | 3.5 | 16.8 | 1.4 | 1.1 | 1.4 | 10.6 | 9.5 | 2.1 | 3.3 | 2.6 | 6.6 | 5.2 | 1.7 | 2.4 | 1.3 | 4.5 |
| 4 | High | Low | High* | 5.0 | 12.9 | 2.2 | 4.9 | 1.5 | 1.4 | 2.6 | 9.4 | 12.0 | 5.1 | 6.0 | 3.1 | 7.1 | 4.3 | 2.3 | 7.2 | 1.6 | 5.2 |
| 5 | Low | High | Low* | 0.3 | 5.7 | 1.9 | 1.2 | 10.4 | 3.7 | 6.2 | 0.6 | 0.9 | 2.1 | 4.3 | 0.4 | 8.5 | 12.4 | 7.1 | 5.6 | 0.3 | 4.2 |

| | | | | | | | | | | | | | | | | | | | | | |
|----------|-----|------|-------|------|------|------|------|------|------|------|------|------|------|------|------|------|------|------|------|------|------|
| 6 | Low | High | High* | 6.3 | 3.7 | 4.1 | 2.8 | 23.0 | 4.6 | 8.1 | 0.7 | 1.0 | 7.7 | 3.4 | 5.9 | 11.8 | 18.6 | 2.2 | 7.0 | 9.3 | 7.1 |
| 7 | Low | Low | Low* | 45.3 | 7.0 | 54.8 | 34.3 | 21.2 | 37.0 | 31.4 | 41.5 | 28.9 | 15.4 | 12.8 | 35.1 | 33.9 | 21.1 | 37.7 | 18.0 | 43.2 | 30.5 |
| 8 | Low | Low | High* | 15.7 | 44.7 | 17.8 | 29.6 | 27.2 | 33.8 | 29.3 | 32.1 | 43.1 | 42.2 | 61.7 | 34.7 | 15.9 | 24.7 | 31.2 | 27.7 | 29.1 | 31.8 |

Table 3.4 - Habitats' characteristics and volumetric representation.

* Since MD is inversely related to cellularity, for the pursuit of clarity and linearity, we are referring here to the concept of "cellularity" (instead of MD value), reversing the corresponding values accordingly. Abbreviations: Aver = average row value, Cellular = cellularity, Perfus = perfusion

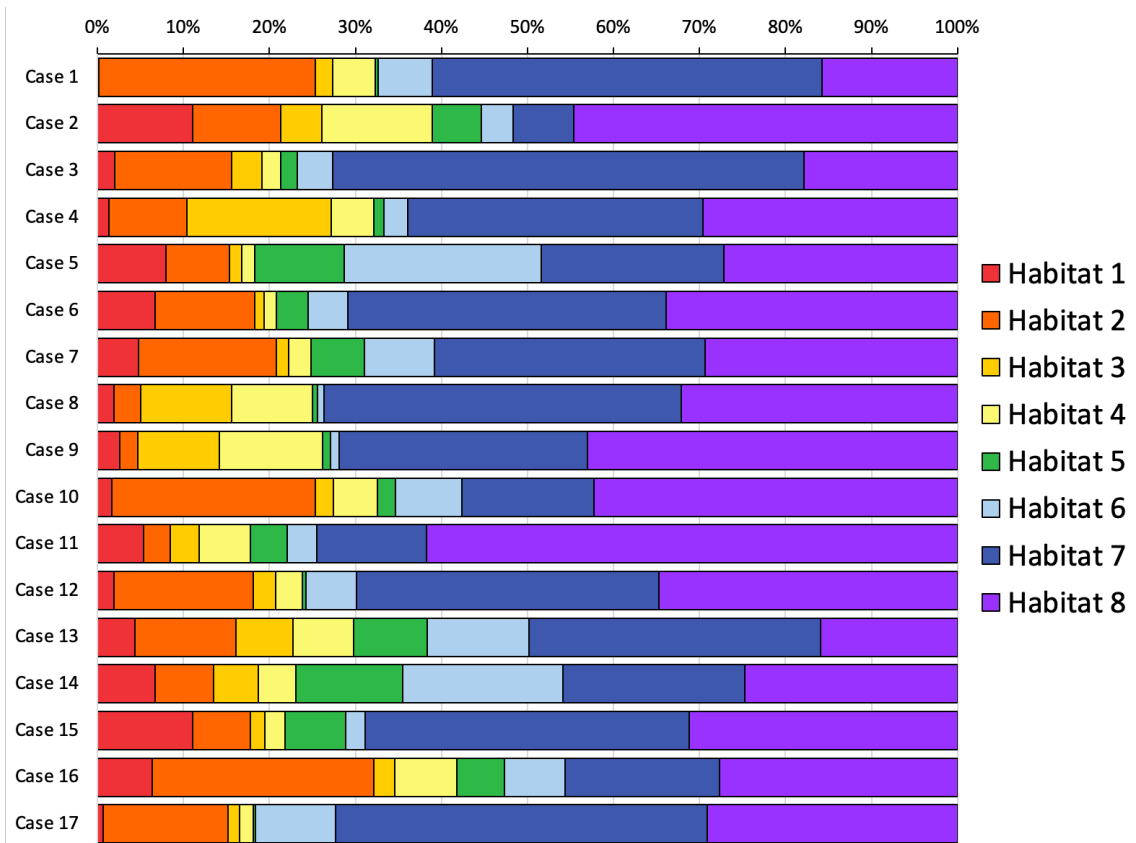


Figure 3.3 - Habitats volumetric representation.

Figure 3.4 depicts habitats distribution in 4 different cases of the present series. Habitats' description and characteristics are analyzed below.

Habitat 1, characterized by high perfusion (the highest Vp values among all clusters), high hypoxia, and high MD (low cellularity), corresponded to areas of mild hyperintensity on T2/FLAIR sequences and intense enhancement on T1-CE sequences; Habitat 1 voxels were localized inside of GD-tumor segmentation in 92% of the cases overall. No areas of necrosis were identifiable on cMRI sequences inside this cluster. This cluster was often located at the periphery of the CE-tumor, leaving other aggressive clusters more internally in the tumor core.

Habitat 2 corresponded, hypothetically, to the most aggressive tumor habitat since it was denoted by elevated perfusion, hypoxia and cellularity, representing, alone, about half of contrast-enhancing tumor volume overall. On cMRI it was denoted by a mild hyperintensity on T2/FLAIR sequences and no visible necrosis. Similarly to Habitat 1, this cluster was localized inside of GD-tumor segmentation in 89% of the cases overall, usually in close proximity to the previous one; however, when compared to the first cluster, Habitat 2 was much more represented (12.1% vs. 4.5%), harboring a less intense contrast enhancement on T1-CE sequences, lower perfusion values, but higher cellularity (lower MD) and, generally (in 12/17 patients), higher hypoxia (FAZA-uptake).

Habitat 3 and **4**, both sharing low hypoxia and high perfusion, but different degree of cellularity, were extremely fragmented and poorly represented among all cases (4.5% and 5.2% of the tumor volume, respectively). They are mostly grouped together, often located either at the interface between tumor CE core and FLAIR-hyperintense not contrast-enhancing area, adjacent to large vessels or close to the cerebral cortex. Only about 25% of the voxels of these clusters were located inside of GD-tumor segmentation.

Habitat 5 was characterized by high hypoxia, low perfusion and low cellularity, and co-localized, predominantly, with necrotic areas (as identifiable on cMRI) inside of GD-tumor segmentation (93% of cases). This was the least represented habitat, with an average among considered tumors of 4.2%, and a range between 0.3 of 12.4%.

Habitat 6 (low perfusion, but high hypoxia and cellularity) had a relatively high representation compared to the aforementioned clusters (average 7.1%, range 0.7-23%), being mostly localized inside of GD-tumor segmentation (75% of the cases). It was predominantly identified as areas of less intense CE inside the tumor core, in close relation to Habitat 5 (located more internally) and Habitat 2 (located more externally), as well perceivable in **Figure 3.4C** and **Figure 3.4D**. In other cases, this cluster was identified as areas of shaded CE outside the main tumor cores, as one could appreciate in **Figure 3.4A** and **Figure 3.4B**.

The remaining two clusters had the largest volumetric representation (each one representing over 30% of the total FLAIR-tumor volume) and were both found in areas with no contrast enhancement in roughly 95% of the cases. **Habitat 7** was, possibly, the least aggressive one inside the tumor mask due to its low values in all parametric maps; it was characterized by low cellularity (harboring the highest absolute MD values among

all clusters) and it was located in areas of markedly hyper-intense FLAIR signal (**Figure 3.4B** and **Figure 3.4D**). **Habitat 8** was characterized, on the contrary, by higher cellularity (lower MD); moreover, also perfusion values and hypoxia values were significantly higher ($p < 0.001$) than those of Habitat 7. **Habitat 8** was also identified in the setting of hemorrhagic foci or necrotic areas with micro-hemorrhagic components (as identified on susceptibility weighted imaging, SWI) or viscous mucinous components, due to low ADC/MD values resulting from extravascular blood components or liquefactive necrosis (Chen *et al.*, 2018; Kang *et al.*, 2001; Ono *et al.*, 2018) (white arrow on **Figure 3.4A** and **Figure 3.4B**). Additionally, as easily noticeable in **Figure 3.4C** and **Figure 3.4D**, the localization of Habitat 8 in cortical areas distant from the tumor core is likely related to the markedly lower MD values of the cerebral cortex, compared to underlying edematous white matter.

| Map | Habitat * | Case 1 | Case 2 | Case 3 | Case 4 | Case 5 | Case 6 | Case 7 | Case 8 | Case 9 | Case 10 | Case 11 | Case 12 | Case 13 | Case 14 | Case 15 | Case 16 | Case 17 | Row Average | Total voxels | | |
|------|----------------|--------|--------|--------|--------|--------|--------|--------|--------|--------|---------|---------|---------|---------|---------|---------|---------|---------|-------------|--------------|------|------|
| | | MD | MD | MD | MD | MD | MD | MD | MD | MD | MD | MD | MD | MD | MD | MD | MD | MD | | MD | MD | MN |
| Vp | 1- <u>H</u> HH | 5.90 | 8.80 | 3.72 | 0.98 | 7.67 | 7.04 | 5.85 | 2.86 | 6.42 | 2.32 | 4.90 | 2.00 | 1.28 | 9.25 | 7.51 | 6.60 | 5.95 | 5.24 | 6.09 | 7.33 | 4.97 |
| | 2- <u>H</u> HL | 5.39 | 8.43 | 3.40 | 1.16 | 5.14 | 5.15 | 6.55 | 2.63 | 5.36 | 2.27 | 4.47 | 1.91 | 1.36 | 7.48 | 8.45 | 6.71 | 6.67 | 4.85 | 4.84 | 5.62 | 3.88 |
| | 3- <u>H</u> LH | 4.79 | 8.16 | 2.66 | 1.22 | 5.20 | 4.37 | 5.45 | 1.72 | 3.14 | 2.07 | 3.52 | 1.75 | 1.08 | 7.80 | 5.95 | 5.91 | 4.77 | 4.09 | 3.02 | 3.82 | 3.28 |
| | 4- <u>H</u> LL | 4.74 | 7.46 | 2.84 | 1.10 | 4.82 | 4.41 | 5.25 | 1.69 | 2.97 | 1.91 | 3.25 | 1.55 | 1.10 | 7.04 | 6.18 | 6.12 | 4.59 | 3.94 | 3.19 | 3.86 | 2.84 |
| | 5- <u>L</u> HH | 2.65 | 4.90 | 1.28 | 0.68 | 2.18 | 0.92 | 2.48 | 1.13 | 1.21 | 0.97 | 1.22 | 0.65 | 0.24 | 2.40 | 2.69 | 3.06 | 2.36 | 1.82 | 1.57 | 1.75 | 1.30 |
| | 6- <u>L</u> HL | 2.79 | 5.76 | 1.45 | 0.71 | 2.71 | 2.08 | 2.96 | 1.20 | 1.16 | 1.28 | 1.26 | 0.71 | 0.34 | 2.47 | 2.96 | 3.71 | 2.86 | 2.14 | 2.14 | 2.08 | 1.23 |
| | 7- <u>L</u> LH | 0.86 | 4.44 | 0.64 | 0.51 | 1.26 | 0.01 | 1.17 | 1.03 | 1.03 | 0.65 | 0.94 | 0.11 | 0.18 | 1.77 | 0.47 | 1.30 | 1.16 | 1.03 | 0.73 | 0.88 | 0.80 |
| | 8- <u>L</u> LL | 1.66 | 4.80 | 0.66 | 0.47 | 1.75 | 0.15 | 1.46 | 0.99 | 1.02 | 0.91 | 1.07 | 0.21 | 0.33 | 1.92 | 0.84 | 2.15 | 1.72 | 1.30 | 0.99 | 1.18 | 0.95 |
| | Whole mask | 1.94 | 5.89 | 0.83 | 0.64 | 2.32 | 0.25 | 1.88 | 1.14 | 1.40 | 1.14 | 1.23 | 0.31 | 0.43 | 2.81 | 1.15 | 3.84 | 1.67 | 1.70 | - | - | - |
| FAZA | 1- <u>H</u> HH | 0.77 | 1.55 | 1.26 | 0.73 | 1.97 | 1.73 | 2.08 | 1.38 | 1.06 | 1.52 | 0.84 | 1.38 | 0.41 | 3.45 | 1.48 | 1.43 | 1.05 | 1.42 | 1.60 | 1.64 | 0.80 |
| | 2- <u>H</u> HL | 1.00 | 1.26 | 1.86 | 1.13 | 1.95 | 1.87 | 2.48 | 1.14 | 1.90 | 1.76 | 0.83 | 2.00 | 0.44 | 3.45 | 1.38 | 1.48 | 1.38 | 1.61 | 1.62 | 1.68 | 0.78 |
| | 3- <u>H</u> LH | 0.30 | 0.70 | 0.69 | 0.33 | 1.03 | 0.81 | 1.04 | 0.42 | 0.37 | 0.61 | 0.31 | 0.46 | 0.26 | 1.28 | 0.54 | 0.84 | 0.47 | 0.62 | 0.39 | 0.53 | 0.35 |
| | 4- <u>H</u> LL | 0.45 | 0.70 | 0.65 | 0.34 | 1.12 | 0.88 | 0.99 | 0.39 | 0.37 | 0.65 | 0.30 | 0.78 | 0.26 | 1.21 | 0.57 | 0.83 | 0.66 | 0.66 | 0.40 | 0.53 | 0.33 |
| | 5- <u>L</u> HH | 0.73 | 1.69 | 1.64 | 0.66 | 1.81 | 1.66 | 1.92 | 0.74 | 0.69 | 1.76 | 0.64 | 1.22 | 0.37 | 3.46 | 1.33 | 1.27 | 0.87 | 1.32 | 1.58 | 1.62 | 0.97 |
| | 6- <u>L</u> HL | 0.84 | 1.29 | 1.97 | 0.77 | 1.75 | 2.21 | 2.09 | 0.73 | 0.88 | 1.68 | 0.65 | 1.52 | 0.40 | 3.44 | 1.15 | 1.38 | 0.97 | 1.40 | 1.59 | 1.65 | 0.93 |
| | 7- <u>L</u> LH | 0.13 | 0.43 | 0.12 | 0.27 | 0.56 | 0.16 | 0.23 | 0.37 | 0.33 | 0.31 | 0.25 | 0.22 | 0.25 | 0.44 | 0.15 | 0.40 | 0.30 | 0.29 | 0.24 | 0.29 | 0.23 |
| | 8- <u>L</u> LL | 0.22 | 0.46 | 0.16 | 0.26 | 0.88 | 0.21 | 0.28 | 0.36 | 0.32 | 0.33 | 0.20 | 0.29 | 0.26 | 0.56 | 0.19 | 0.56 | 0.45 | 0.35 | 0.28 | 0.36 | 0.27 |
| | Whole mask | 0.24 | 0.63 | 0.18 | 0.31 | 1.31 | 0.25 | 0.47 | 0.38 | 0.34 | 0.45 | 0.24 | 0.35 | 0.30 | 1.79 | 0.26 | 0.92 | 0.42 | 0.52 | - | - | - |
| MD | 1- <u>H</u> HH | 1.60 | 1.05 | 1.54 | 1.22 | 0.97 | 1.49 | 1.64 | 0.49 | 1.26 | 1.24 | 1.45 | 1.28 | 1.48 | 1.46 | 1.70 | 1.24 | 0.95 | 1.30 | 1.48 | 1.48 | 0.35 |
| | 2- <u>H</u> HL | 0.99 | 0.85 | 1.13 | 0.86 | 0.81 | 1.13 | 1.15 | 0.40 | 1.03 | 0.90 | 1.08 | 0.95 | 1.19 | 1.12 | 1.20 | 0.88 | 0.76 | 0.97 | 1.01 | 1.01 | 0.20 |
| | 3- <u>H</u> LH | 1.68 | 1.05 | 1.65 | 1.33 | 1.04 | 1.45 | 1.65 | 0.50 | 1.20 | 1.30 | 1.40 | 1.39 | 1.51 | 1.46 | 1.64 | 1.27 | 0.99 | 1.32 | 1.42 | 1.35 | 0.37 |
| | 4- <u>H</u> LL | 1.10 | 0.79 | 1.15 | 1.02 | 0.73 | 1.14 | 1.23 | 0.40 | 0.98 | 0.93 | 1.01 | 1.03 | 1.21 | 1.15 | 1.20 | 0.89 | 0.81 | 0.99 | 1.02 | 1.00 | 0.25 |
| | 5- <u>L</u> HH | 1.51 | 1.28 | 1.61 | 1.20 | 0.95 | 1.57 | 1.70 | 0.51 | 1.23 | 1.29 | 1.71 | 1.27 | 1.50 | 1.42 | 1.84 | 1.31 | 0.95 | 1.34 | 1.50 | 1.50 | 0.37 |
| | 6- <u>L</u> HL | 0.98 | 0.83 | 1.25 | 0.89 | 0.78 | 1.09 | 1.21 | 0.41 | 0.98 | 0.92 | 1.04 | 0.92 | 1.22 | 1.15 | 1.30 | 0.97 | 0.71 | 0.98 | 0.99 | 0.99 | 0.23 |
| | 7- <u>L</u> LH | 1.85 | 1.04 | 1.72 | 1.26 | 1.01 | 1.53 | 1.63 | 0.49 | 1.17 | 1.36 | 1.40 | 1.37 | 1.56 | 1.46 | 1.61 | 1.31 | 0.99 | 1.34 | 1.51 | 1.44 | 0.36 |
| | 8- <u>L</u> LL | 1.22 | 0.78 | 1.30 | 1.00 | 0.72 | 1.15 | 1.27 | 0.41 | 1.00 | 0.95 | 0.96 | 1.06 | 1.26 | 1.13 | 1.23 | 0.97 | 0.83 | 1.01 | 1.01 | 1.01 | 0.23 |
| | Whole mask | 1.41 | 0.84 | 1.58 | 1.14 | 0.84 | 1.33 | 1.39 | 0.46 | 1.07 | 0.97 | 1.02 | 1.13 | 1.41 | 1.27 | 1.50 | 1.01 | 0.88 | 1.13 | - | - | - |

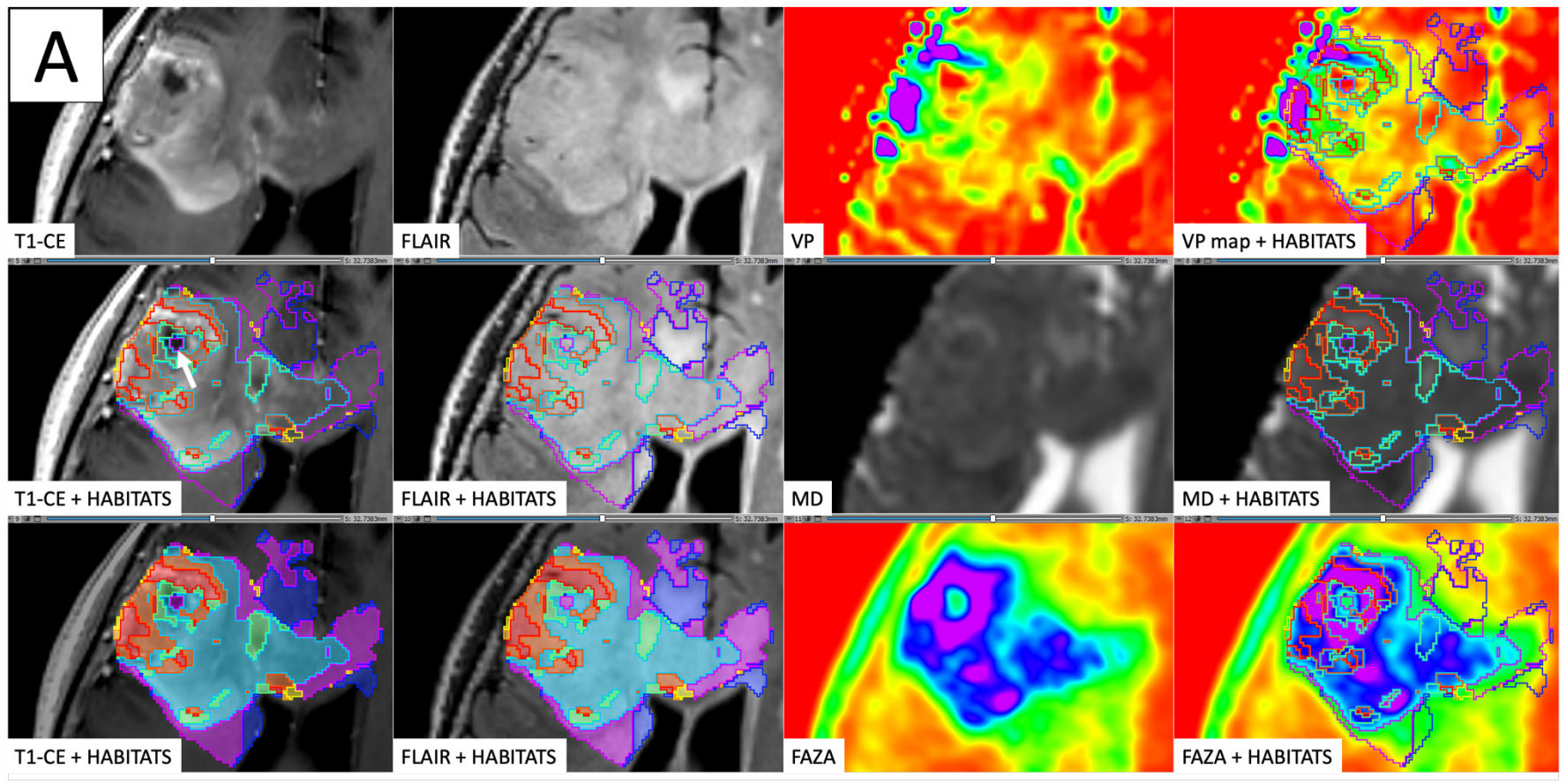
Table 3.5 - Vp, FAZA and MD maps voxel absolute values among different habitats.

In order to analyze voxel intensity values, the third parameter is here referred to MD value (not to the, inversely related, “cellularity”); MD Values are here reported with a multiplication factor of 10^3 . * “H” and “L” correspond, respectively to the High and Low intensity cluster of the considered parametric maps. Abbreviation list: MD = median; MN = mean; SD = standard deviation

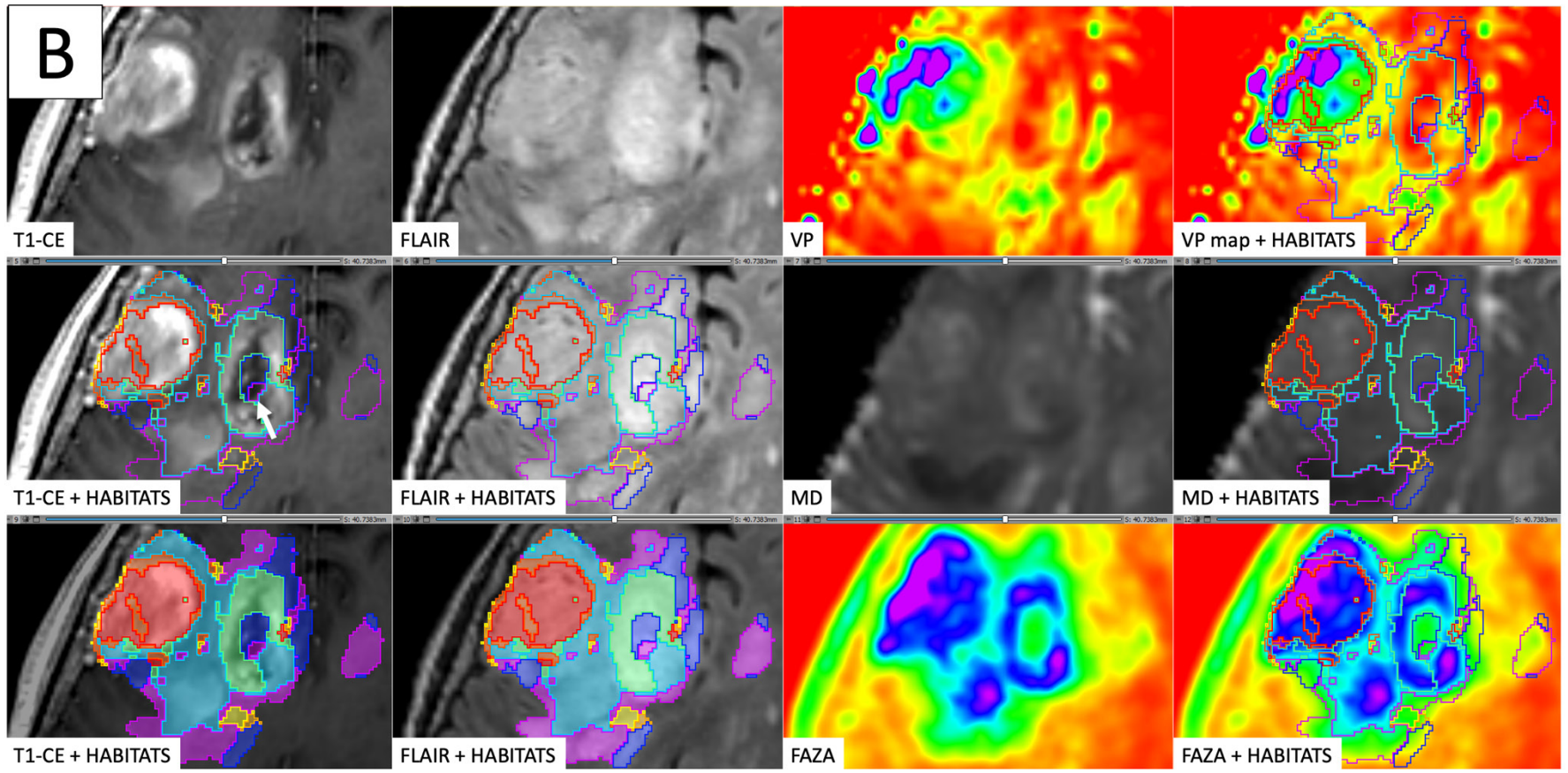
| Map | Habitat * | Case 1 | Case 2 | Case 3 | Case 4 | Case 5 | Case 6 | Case 7 | Case 8 | Case 9 | Case 10 | Case 11 | Case 12 | Case 13 | Case 14 | Case 15 | Case 16 | Case 17 | Row Average | Total voxels | | |
|------|----------------|--------|--------|--------|--------|--------|--------|--------|--------|--------|---------|---------|---------|---------|---------|---------|---------|---------|-------------|--------------|------|------|
| | | MD | MD | MD | MD | MD | MD | MD | MD | MD | MD | MD | MD | MD | MD | MD | MD | MD | | MD | MD | MN |
| Vp | 1- <u>H</u> HH | 2.08 | 1.43 | 2.80 | 1.31 | 2.51 | 4.14 | 1.82 | 2.22 | 3.49 | 1.69 | 2.81 | 2.91 | 2.05 | 2.40 | 2.68 | 1.56 | 2.33 | 2.37 | 2.56 | 3.18 | 1.90 |
| | 2- <u>H</u> HL | 1.90 | 1.37 | 2.55 | 1.55 | 1.68 | 3.03 | 2.03 | 2.04 | 2.91 | 1.65 | 2.56 | 2.78 | 2.18 | 1.94 | 3.02 | 1.58 | 2.62 | 2.20 | 2.17 | 2.59 | 1.36 |
| | 3- <u>H</u> LH | 1.69 | 1.33 | 2.00 | 1.63 | 1.70 | 2.57 | 1.69 | 1.33 | 1.71 | 1.51 | 2.02 | 2.54 | 1.72 | 2.02 | 2.13 | 1.40 | 1.87 | 1.82 | 1.78 | 2.03 | 0.97 |
| | 4- <u>H</u> LL | 1.67 | 1.21 | 2.14 | 1.47 | 1.58 | 2.59 | 1.63 | 1.31 | 1.62 | 1.39 | 1.86 | 2.26 | 1.75 | 1.83 | 2.21 | 1.44 | 1.80 | 1.75 | 1.70 | 1.94 | 0.87 |
| | 5- <u>L</u> HH | 0.94 | 0.80 | 0.96 | 0.91 | 0.71 | 0.54 | 0.77 | 0.88 | 0.66 | 0.71 | 0.70 | 0.94 | 0.38 | 0.62 | 0.96 | 0.72 | 0.93 | 0.77 | 0.69 | 0.69 | 0.40 |
| | 6- <u>L</u> HL | 0.98 | 0.94 | 1.09 | 0.96 | 0.89 | 1.23 | 0.92 | 0.93 | 0.63 | 0.93 | 0.72 | 1.03 | 0.54 | 0.64 | 1.06 | 0.88 | 1.12 | 0.91 | 0.90 | 0.85 | 0.37 |
| | 7- <u>L</u> LH | 0.30 | 0.72 | 0.48 | 0.69 | 0.41 | 0.00 | 0.36 | 0.80 | 0.56 | 0.47 | 0.54 | 0.15 | 0.29 | 0.46 | 0.17 | 0.31 | 0.46 | 0.42 | 0.37 | 0.42 | 0.33 |
| | 8- <u>L</u> LL | 0.59 | 0.78 | 0.49 | 0.63 | 0.57 | 0.09 | 0.45 | 0.77 | 0.56 | 0.66 | 0.61 | 0.31 | 0.52 | 0.50 | 0.30 | 0.51 | 0.68 | 0.53 | 0.52 | 0.54 | 0.35 |
| FAZA | 1- <u>H</u> HH | 1.68 | 1.89 | 2.26 | 1.78 | 1.48 | 2.52 | 1.99 | 3.10 | 2.54 | 1.77 | 2.67 | 1.92 | 1.30 | 1.73 | 2.68 | 1.48 | 1.73 | 2.03 | 2.03 | 2.20 | 0.87 |
| | 2- <u>H</u> HL | 2.21 | 1.53 | 3.33 | 2.75 | 1.47 | 2.73 | 2.38 | 2.56 | 4.55 | 2.05 | 2.65 | 2.78 | 1.40 | 1.73 | 2.50 | 1.53 | 2.28 | 2.38 | 2.19 | 2.32 | 0.87 |
| | 3- <u>H</u> LH | 0.66 | 0.85 | 1.23 | 0.82 | 0.78 | 1.19 | 1.00 | 0.93 | 0.89 | 0.72 | 0.99 | 0.64 | 0.84 | 0.64 | 0.99 | 0.86 | 0.78 | 0.87 | 0.88 | 0.89 | 0.28 |
| | 4- <u>H</u> LL | 1.00 | 0.85 | 1.17 | 0.84 | 0.84 | 1.28 | 0.95 | 0.87 | 0.88 | 0.75 | 0.97 | 1.09 | 0.82 | 0.61 | 1.04 | 0.85 | 1.09 | 0.94 | 0.89 | 0.89 | 0.27 |
| | 5- <u>L</u> HH | 1.60 | 2.05 | 2.94 | 1.61 | 1.37 | 2.42 | 1.85 | 1.66 | 1.66 | 2.05 | 2.02 | 1.69 | 1.19 | 1.73 | 2.40 | 1.31 | 1.45 | 1.82 | 1.69 | 1.83 | 0.63 |
| | 6- <u>L</u> HL | 1.85 | 1.56 | 3.52 | 1.89 | 1.32 | 3.22 | 2.00 | 1.64 | 2.12 | 1.96 | 2.08 | 2.11 | 1.28 | 1.73 | 2.08 | 1.43 | 1.60 | 1.96 | 1.62 | 1.84 | 0.71 |
| | 7- <u>L</u> LH | 0.28 | 0.52 | 0.21 | 0.66 | 0.42 | 0.24 | 0.22 | 0.83 | 0.78 | 0.37 | 0.80 | 0.30 | 0.80 | 0.22 | 0.28 | 0.41 | 0.49 | 0.46 | 0.39 | 0.48 | 0.30 |
| | 8- <u>L</u> LL | 0.48 | 0.56 | 0.28 | 0.63 | 0.67 | 0.30 | 0.27 | 0.81 | 0.77 | 0.38 | 0.63 | 0.40 | 0.84 | 0.28 | 0.34 | 0.58 | 0.75 | 0.53 | 0.52 | 0.56 | 0.30 |
| MD | 1- <u>H</u> HH | 1.12 | 1.19 | 1.01 | 1.07 | 1.13 | 1.12 | 1.16 | 1.08 | 1.16 | 1.21 | 1.29 | 1.10 | 1.06 | 1.13 | 1.15 | 1.18 | 1.07 | 1.13 | 1.14 | 1.19 | 0.19 |
| | 2- <u>H</u> HL | 0.69 | 0.97 | 0.74 | 0.76 | 0.94 | 0.85 | 0.81 | 0.88 | 0.95 | 0.87 | 0.97 | 0.82 | 0.85 | 0.87 | 0.81 | 0.83 | 0.86 | 0.85 | 0.84 | 0.83 | 0.12 |
| | 3- <u>H</u> LH | 1.17 | 1.19 | 1.08 | 1.17 | 1.21 | 1.09 | 1.17 | 1.09 | 1.11 | 1.26 | 1.25 | 1.19 | 1.08 | 1.14 | 1.10 | 1.20 | 1.11 | 1.15 | 1.12 | 1.16 | 0.15 |
| | 4- <u>H</u> LL | 0.76 | 0.90 | 0.76 | 0.89 | 0.85 | 0.86 | 0.87 | 0.87 | 0.90 | 0.91 | 0.90 | 0.89 | 0.87 | 0.89 | 0.81 | 0.85 | 0.92 | 0.86 | 0.88 | 0.86 | 0.11 |
| | 5- <u>L</u> HH | 1.05 | 1.45 | 1.06 | 1.05 | 1.11 | 1.18 | 1.21 | 1.11 | 1.14 | 1.25 | 1.53 | 1.09 | 1.07 | 1.10 | 1.23 | 1.25 | 1.07 | 1.17 | 1.14 | 1.21 | 0.22 |
| | 6- <u>L</u> HL | 0.68 | 0.94 | 0.82 | 0.79 | 0.91 | 0.82 | 0.85 | 0.90 | 0.91 | 0.90 | 0.93 | 0.79 | 0.87 | 0.89 | 0.88 | 0.92 | 0.80 | 0.86 | 0.87 | 0.86 | 0.11 |
| | 7- <u>L</u> LH | 1.28 | 1.17 | 1.13 | 1.11 | 1.18 | 1.15 | 1.15 | 1.08 | 1.08 | 1.33 | 1.25 | 1.18 | 1.12 | 1.13 | 1.08 | 1.24 | 1.12 | 1.16 | 1.14 | 1.17 | 0.14 |
| | 8- <u>L</u> LL | 0.85 | 0.89 | 0.85 | 0.88 | 0.84 | 0.86 | 0.90 | 0.90 | 0.93 | 0.92 | 0.85 | 0.91 | 0.90 | 0.88 | 0.83 | 0.92 | 0.93 | 0.88 | 0.89 | 0.87 | 0.11 |

Table 3.6 - Vp, FAZA and MD maps “normalized” voxel intensities among different habitats.

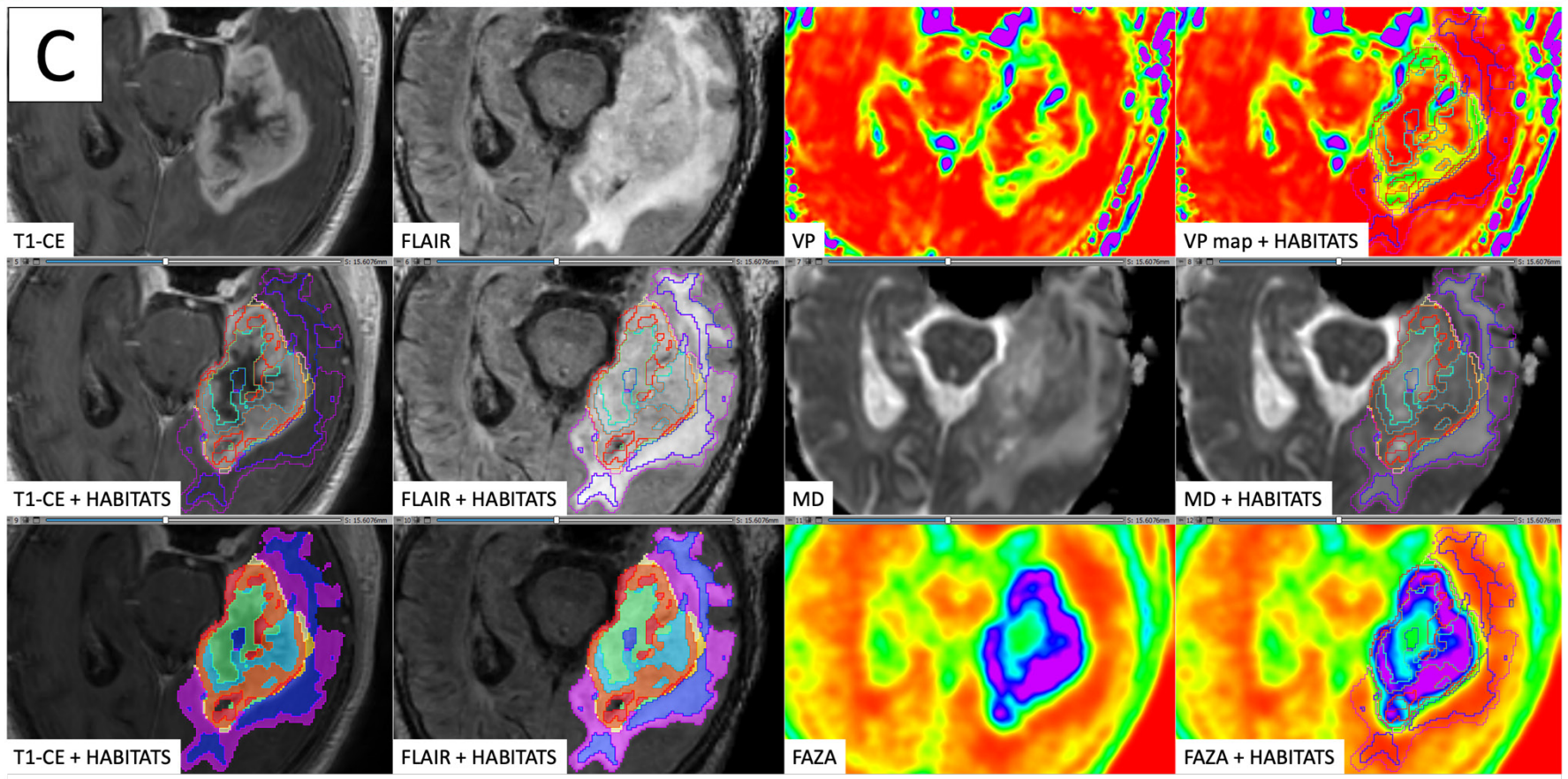
Values are expressed as a ratio to the median tumor mask intensity of each map. In order to analyze voxel intensity values, the third parameter is here referred to MD value (not to the, inversely related, “cellularity”). * “H” and “L” correspond, respectively to High and Low intensity clusters of the considered parametric maps. Abbreviation list: MD = mean; MN = mean; SD = standard deviation



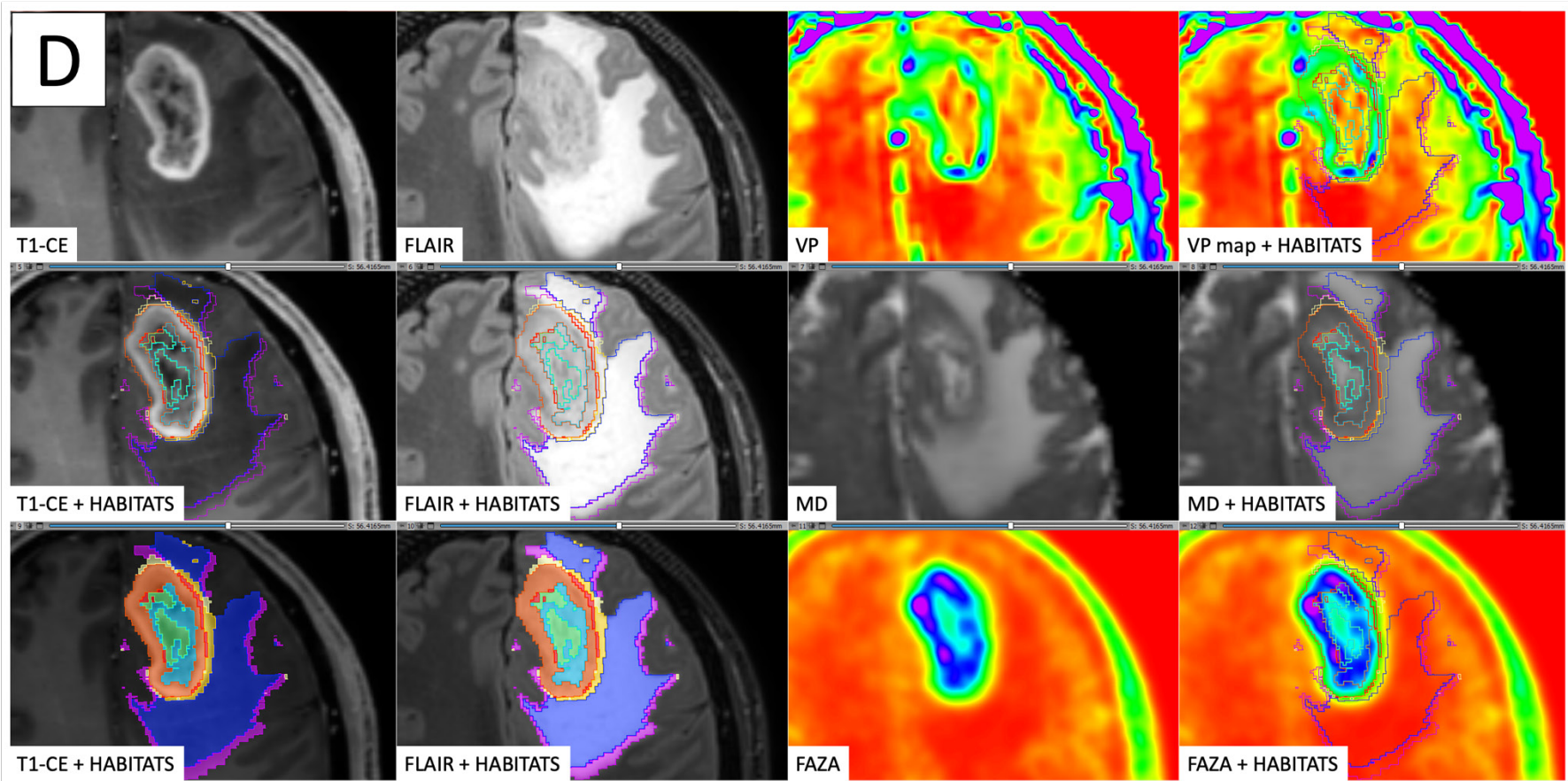
(Continued on the next page)



(Continued on the next page)



(Continued on the next page)



(Continued on the next page)

Figure 3.4 - Four different illustrative cases (A, B, C, and D) showing habitats distribution and reproducibility of HYPERDIrect maps.

A table listing the key colors (1 - red, 2 - orange, 3 - gold, 4 - yellow, 5 - aquamarine, 6 - light blue, 7 - dark blue, 8 - violet) assigned to each habitat is reported in Figure 3.7.

3.4.4 Radiomic correspondence in stereotactic biopsies

In the 10/17 patients who underwent needle biopsy, the stereotactic coordinates of the sampling sites were imported in the 3D Slicer Dataset as a 5 mm diameter spherical volume, similarly to what was previously described by other authors (Barajas *et al.*, 2012; Gates *et al.*, 2019; Jun *et al.*, 2006; Rotkopf *et al.*, 2020), in order to take into account the maximum reported accuracy error in Euclidean distance reported in the literature (Roth *et al.*, 2018). Each histopathological specimen, labeled according to the order of resection, was then analyzed in comparison to the corresponding voxels and habitats in the 3D Slicer Dataset. Considering the macroscopical aspect and size of the sample obtained and the procedure-related risks/complications, at least two (median 3, range 2-4) cylindrical tissue biopsies (range 4-11 mm, median length 8 mm) were obtained. The microscopic semi-quantitative analysis (cellularity, extent of necrosis, number of hyperplastic vessels) of each sample and the corresponding Habitats on imaging are reported in **Table 3.7**.

Figure 3.7 and **Figure 3.8** present illustrative cases showing how microscopic morphology of the tissue was found consistent with the corresponding functional habitat identified.

| Case number | Sample | Cellularity ⁱ (1-5) | Class of necrosis ⁱⁱ (0-5) | Number of hyperplastic vessels counted (n) | Habitats involved (ordered by prevalence inside VOI) ⁱⁱⁱ |
|-------------|-----------------|-----------------------------------|--|--|---|
| 2 | A | 1 | 0 | 0 | 7, 8 |
| | B | 4 | 0 | 43 | 2 |
| | A | 4 | 1 | 21 | 5 |
| 5 | A | 3 | 2 | 1 | 6 |
| | B | 4 | 4 | 1 | 2, 5 |
| | C | 3 | 5 | 3 | 5, 7, 8 |
| | D ^{iv} | 3 | 3 | 6 | 5, 6 |
| 8 | A | 2 | 0 | 0 | 1 |
| | B | 2 | 0 | 0 | 1 |
| | C | 2 | 0 | 1 | 1 |
| | D | 2 | 0 | 0 | 1 |
| 9 | A | 5 | 2 | 20 | 1 |
| | B | 5 | 2 | 19 | 1 |
| 10 | A | 1 | 0 | 0 | 7, 8 |
| | B | 3 | 1 | 8 | 2 |
| 12 | A | 1 | 0 | 4 | 8, 2, 6 |
| | B | 3 | 2 | 4 | 2, 6 |
| | C | 4 | 1 | 8 | 2 |
| 13 | A | 1 | 0 | 0 | 7 |

| | | | | | |
|----|---|------------------|---|-------------------|-------|
| | B | 1 | 0 | 0 | 5 |
| | C | 3 | 0 | 0 | 3 |
| | D | 3 | 0 | 2 | 1,3 |
| 14 | A | 3 | 0 | 5 | 7,8,6 |
| | B | 4 | 0 | 11 | 6 |
| 16 | A | 1 | 0 | 0 | 7, 8 |
| | B | 3 | 0 | 28 | 1 |
| | C | 5 | 1 | 11 | 2 |
| | D | N/A ^v | 5 | N/A ^{vi} | 5, 7 |
| 17 | A | 4 | 0 | 6 | 2 |
| | B | 4 | 1 | 7 | 2 |
| | C | 4 | 0 | 4 | 6, 2 |

Table 3.7 - The semi-quantitative histopathologic description is reported for each bioptic sample obtained.

Features assessed in the present analysis were: cellularity, extent of necrosis and the number of hyperplastic vessels counted. To address the issue of length variability among different bioptic specimens and to maximize the correspondence with the target point set on the stereotactic planning system, only the central portion (extending 5 mm along the greatest axis of the specimen in its largest section available) was analyzed in each sample. The corresponding HYPERDirect habitats involved are reported in the last column, ordered accordingly to their relative prevalence inside of the 5 mm diameter volume of interest. N/A = not applicable

i Cellularity was graded with a score from 1 (seemingly normal representation) to 5 (extremely high cellular density).

ii Classes considered for necrosis (expressed as a rate over the whole area considered for each specimen) were the following: 0 (0%), 1 ($\leq 10\%$), 2 (11-25%), 3 (26-50%), 4 (51-75%), 5 (76-100%).

iii A 5 mm diameter volume of interest (VOI) was drawn according to the exact stereotactic coordinates of each target and needle window orientation, then carefully verified also in the coregistered in the early postoperative CT scan. In this column the included habitats are reported. Since the HYPERDirect maps were not available at the time of planning, final sampling VOI ended at the intersection of multiple clusters in many cases; in the latter case cluster are listed in order of maximum volumetric representation inside of the VOI.

iv This sample was only 4 mm long.

v It was not possible to calculate these features since the sample was completely represent by necrosis.

vi It was not possible to calculate these features since the sample was completely represent by necrosis.

3.4.5 Patients' prognosis

Mean overall survival (**Table 3.1**) was 53.1 ± 67 weeks (median 21 weeks, range 8-222 weeks). Two patients were still alive at the last follow-up assessment (49 and 51 months, respectively). The remaining 15 patients died during follow-up due to causes directly (e.g., tumor progression increasing mass effect on cerebral structures) or indirectly (e.g., aspiration pneumonia) associated with the disease.

In this small and heterogeneous series, we were not able to obtain sufficient data to prove statistically significant correlations between the intra-patient habitats representation and tumor histological diagnosis (type, grading, immunohistochemical and molecular characteristics) and patient prognosis. Nevertheless, the distribution of the most aggressive clusters was higher (although not in a statistically significant way) among

WHO grade IV compared to III: **Habitat 1** (5.1% vs. 1.9%) and **Habitat 2** (12.6% vs. 9.1%), possibly representing the tumor vital core, and **Habitat 5** (4% vs. 2.1%), which mostly colocalized in necrotic areas of the tumor. Conversely, the distribution of **Habitat 7** was found significantly higher (mean 33.03% vs. 18.8%, median 34.7% vs. 15.4%, $p=0.05$, independent sampled Mann-Whitney U test) in IDH-1 wild-type tumor compared to IDH-1 mutated.

| Habitats characteristics | | | | Habitats' representation (% of total tumor volume) according to | | | | | | | |
|--------------------------|-------------|----------------|----------------|---|------------|----------|------------|------------------|------------|----------|------------|
| | | | | IDH-1 status | | | | WHO 2016 Grading | | | |
| | | | | Wild-type | | Mutated | | III | | IV | |
| n | Perf. (↑Vp) | Hypox. (↑FAZA) | Cellul. (↓MD)* | Mean (%) | Median (%) | Mean (%) | Median (%) | Mean (%) | Median (%) | Mean (%) | Median (%) |
| 1 | High | High | Low* | 4.3 | 3.7 | 5.8 | 4.4 | 3.2 | 1.9 | 5.1 | 5.1 |
| 2 | High | High | High* | 11.5 | 10.3 | 15.2 | 11.7 | 10.9 | 9.1 | 12.7 | 12.6 |
| 3 | High | Low | Low* | 4.5 | 2.5 | 4.5 | 4.8 | 8.3 | 6.6 | 2.9 | 2.2 |
| 4 | High | Low | High* | 4.6 | 3.7 | 8.4 | 7.1 | 6.2 | 5.1 | 4.8 | 2.9 |
| 5 | Low | High | Low* | 4.0 | 2.8 | 5.4 | 5.7 | 4.9 | 2.1 | 3.9 | 4.0 |
| 6 | Low | High | High* | 6.9 | 5.3 | 7.8 | 7.7 | 8.3 | 7.7 | 6.6 | 5.3 |
| 7 | Low | Low | Low* | 33.0 | 34.7 | 18.8 | 15.4 | 29.3 | 33.9 | 31.0 | 33.2 |
| 8 | Low | Low | High* | 31.3 | 29.5 | 34.2 | 42.2 | 28.9 | 29.6 | 33.0 | 30.3 |

Table 3.8 - Mean and median representation of the 8 different habitats according to IDH-1 status and WHO 2016 grade.

Data are expressed as a percentage of the cumulative tumor volume of the whole series

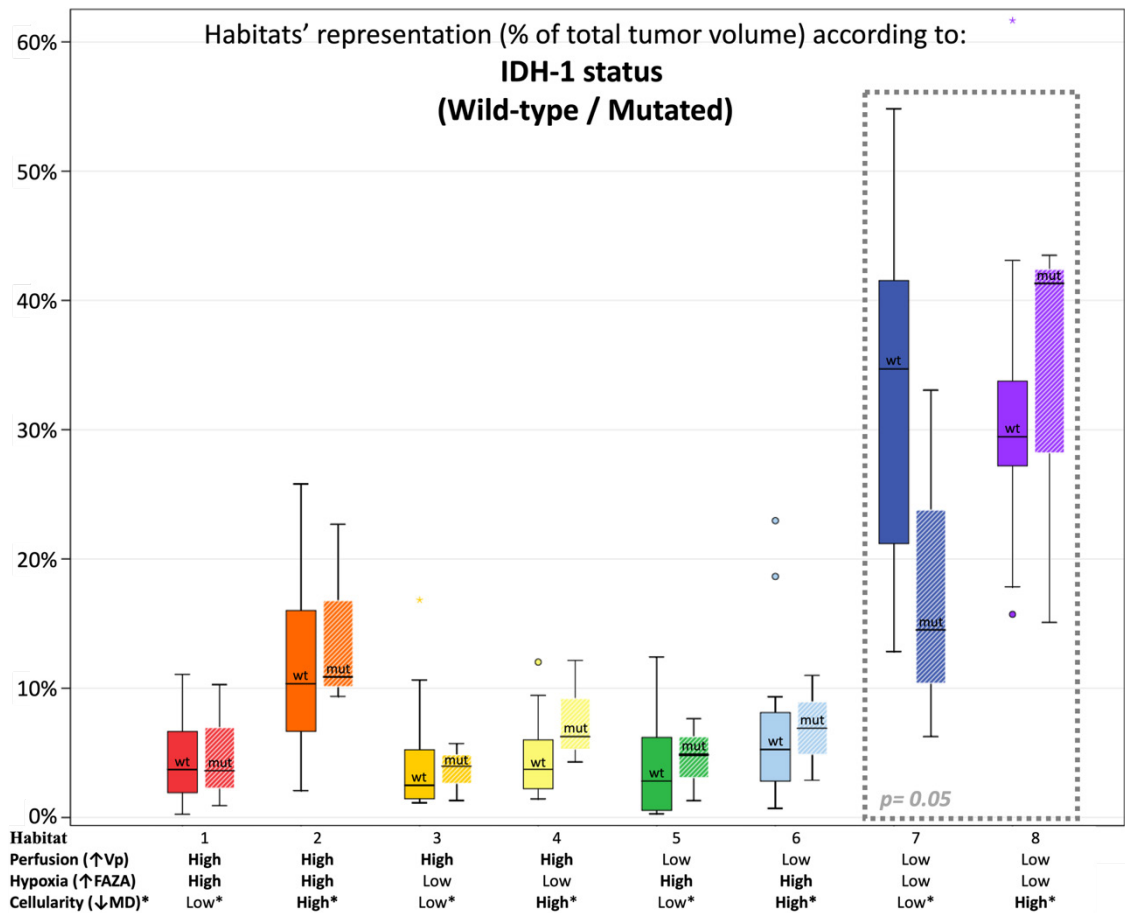


Figure 3.5 - Habitats' representation (% of total tumor volume) according to IDH-1 status.

Wild-type (boxplot on the left with filled colors) or Mutated (boxplot on the right with oblique white stripes). IDH-1 mutated tumors had a statistically significantly lower representation of Habitat 7 (low perfusion, hypoxia, and cellularity), while (not statistically significant) higher representation of Habitat 8 (low perfusion and hypoxia, but high cellularity). Main differences were found in the representation of Habitat 7 (possibly embodying pure vasogenic edema) and 8 (possibly representing infiltrative edema). The former was significantly ($p = 0.05$) higher in IDH wild-type tumors, while the latter was higher (not significantly) in IDH-mutated lesions.

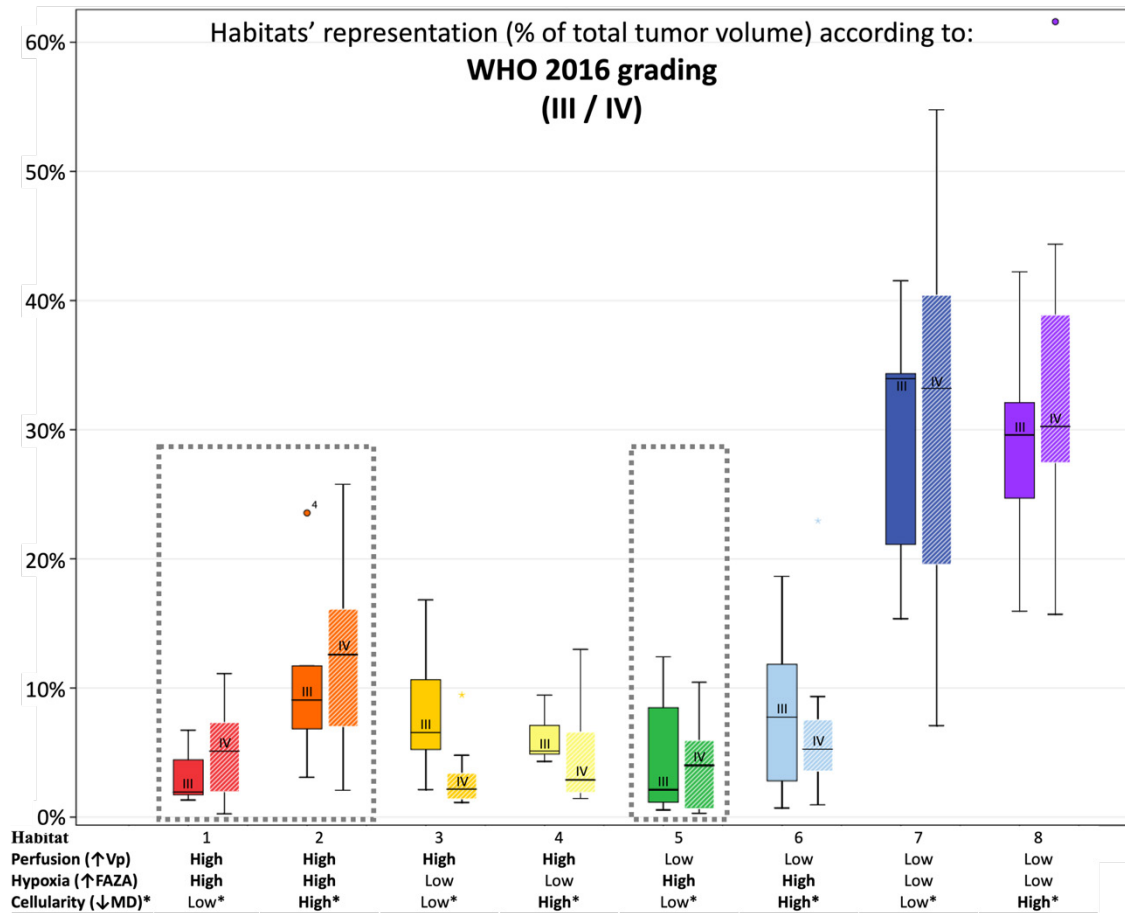


Figure 3.6 - Habitats' representation (% of total tumor volume) according to WHO 2016 grade.
 Grade III (boxplot on the left with filled colors) or grade IV (boxplot on the right with oblique white stripes). WHO grade IV gliomas had a higher (although not statistically significant) representation of Habitat 1 and 2 (considered the most aggressive clusters from a metabolic point of view) and Habitat 5 (mostly associated with necrotic areas).

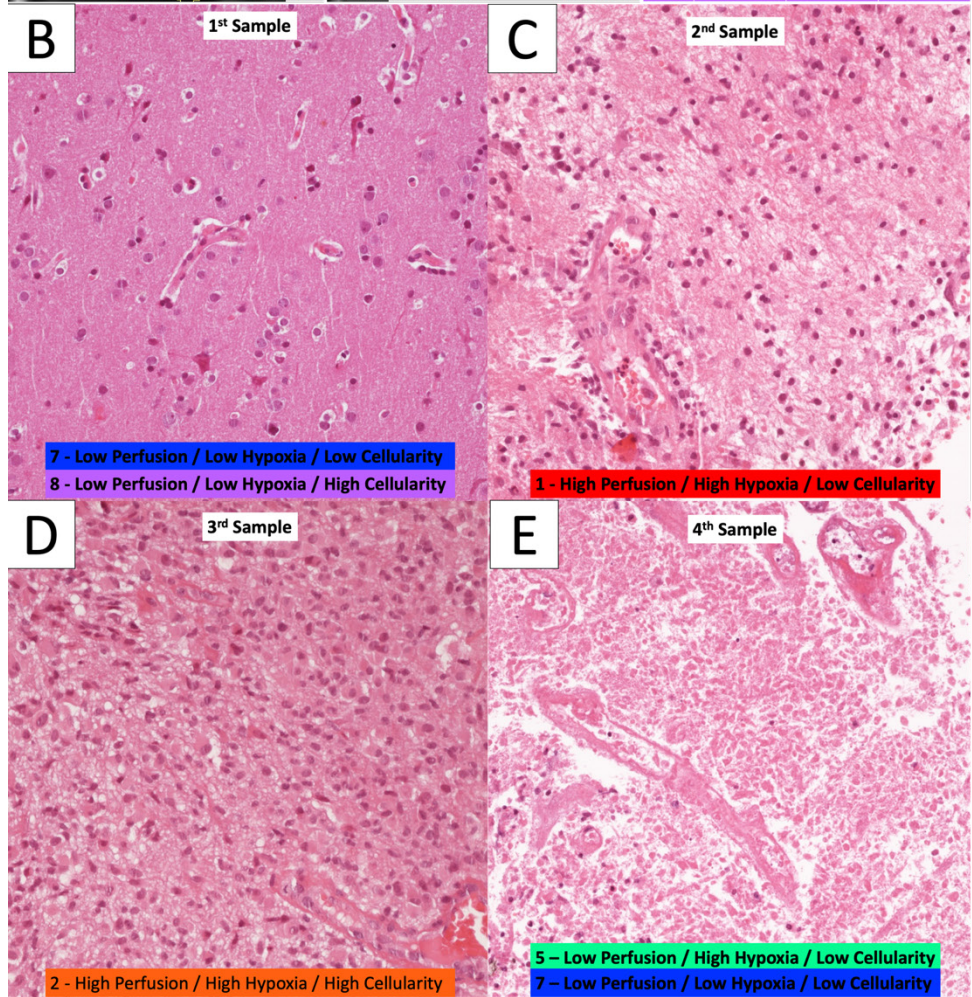
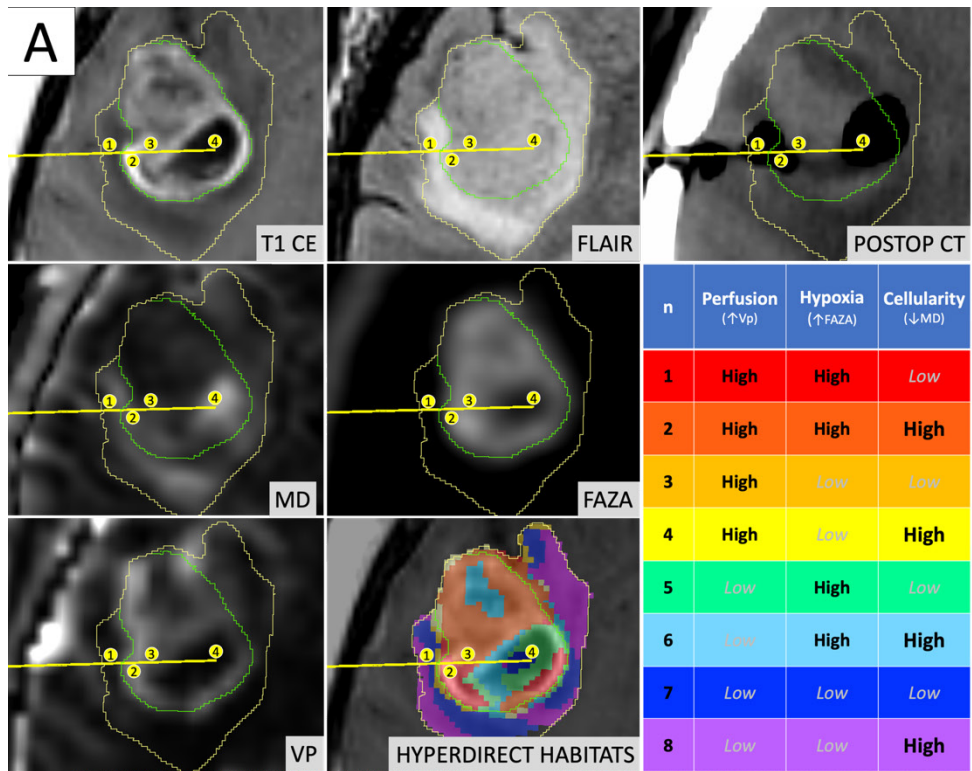


Figure 3.7 - Illustrative case of a 57-year-old female patient (case 16 in Table 3.1) who underwent stereotactic biopsy.

(A) The trajectory path (yellow line) and the four consecutive sampling sites (enumerated in the yellow circles) are displayed in axial formatted T1-CE, FLAIR, MD, FAZA, Vp and postoperative CT images; the spatial distribution of the identified habitats and the assigned key colors are also displayed (1 - red, 2 - orange, 3 - gold, 4 - yellow, 5 - aquamarine, 6 - light blue, 7 - dark blue, 8 - violet). Since MD is inversely related to cellularity, for the pursuit of clarity and linearity, we referred here to the concept of “cellularity” (instead of MD value), and we reversed the corresponding High and Low values accordingly. **(B)** Microscopic slide (20x magnification, Hematoxylin and Eosin (H&E) from the first sampling (corresponding to Habitat 7 - Low Perfusion / Low Hypoxia / Low Cellularity and Habitat 8 - Low Perfusion / Low Hypoxia / High Cellularity) showing a cortical/subcortical area with normal tissue architecture, presence of normal vessel and no significant increase in cellularity, but rather mild reactive gliosis. **(C)** Microscopic slide (20x magnification, H&E) from the second sampling (Habitat 1 - High Perfusion / High Hypoxia / Low Cellularity) showing a clearly pathological area of white matter with increased cellularity, disruption of the physiological tissue architecture, and abnormal vessels. **(D)** Microscopic slide (20x magnification, H&E) from the third sampling (Habitat 2 - High Perfusion / High Hypoxia / High Cellularity) showing neoplastic tissue with cytoarchitecture disruption, elevated cellularity with the presence of gemistocytic astrocytes, nuclear atypia, abundant eosinophilic cytoplasm, abnormal vascularization. **(E)** Microscopic slide (20x magnification, H&E) from the fourth sampling (Habitat 5 - Low Perfusion / High Hypoxia / Low Cellularity and Habitat 7 - Low Perfusion / Low Hypoxia / Low Cellularity) showing tissue with extensive necrosis.

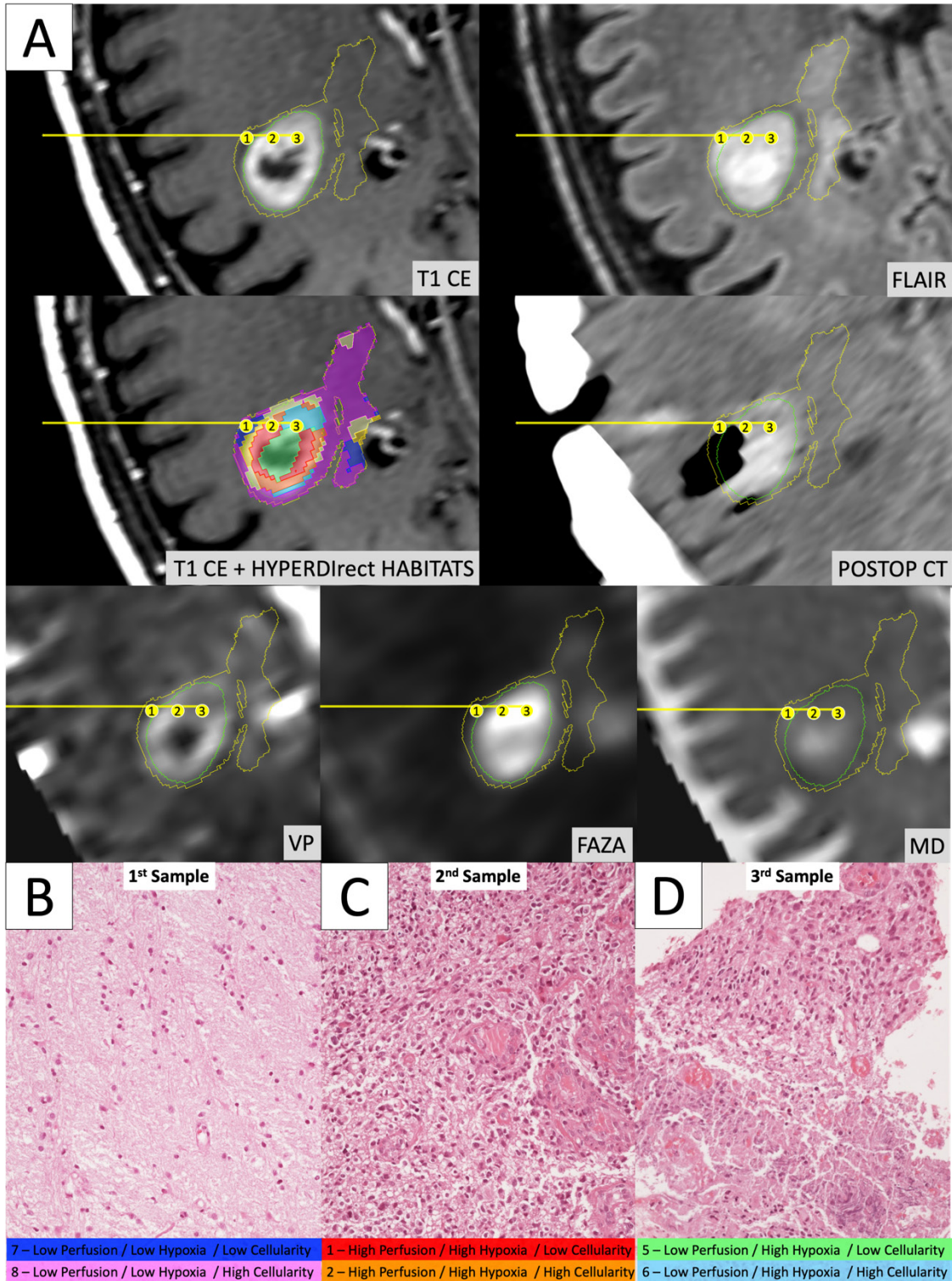


Figure 3.8 - Illustrative case of a 58-year-old male patient (case 2 in Table 3.1) who underwent stereotactic biopsy. (A) The trajectory path (yellow line) and the four consecutive sampling sites (enumerated in the yellow circles) are displayed in axial formatted T1-CE, FLAIR, MD, FAZA, Vp and postoperative CT images; habitats were identified using the same key-color described in Figure 3.7. (B) Microscopic slide (20x magnification, Hematoxylin and Eosin (H&E)) from the first sampling (Habitat 7 - Low Perfusion / Low Hypoxia / Low Cellularity and Habitat 8 - Low Perfusion / Low Hypoxia / High Cellularity) showing a seemingly normal white matter architecture. (C) Microscopic slide (20x magnification, H&E) from the second sampling (Habitat 1 - High Perfusion / High Hypoxia / Low Cellularity

and Habitat 2 - High Perfusion / High Hypoxia / High Cellularity) showing evident hypercellularity with nuclear atypias and marked vascular proliferation. **(D)** Microscopic slide (20x magnification, H&E) from the third sampling (Habitat 5 - Low Perfusion / High Hypoxia / Low Cellularity and Habitat 6 - Low Perfusion / High Hypoxia / High Cellularity) areas of vital tumoral tissue (on the upper part) mixed with areas of necrosis (on the lower part).

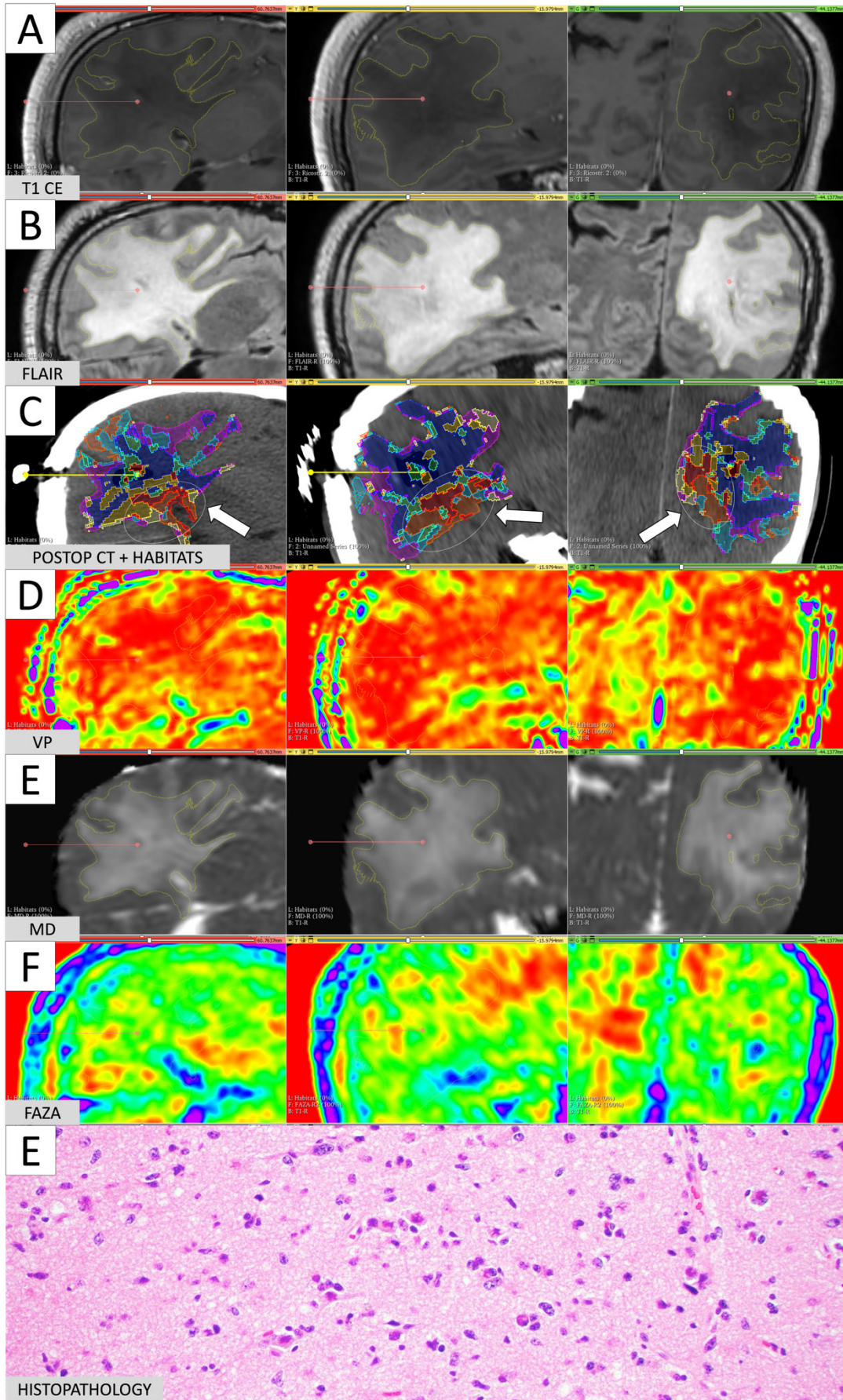


Figure 3.9 - Illustrative case of a 41-year-old male patient (case 13 in Table 3.1), who underwent a stereotactic biopsy for a large parieto-temporo-occipital lesion without a clear core of contrast enhancement.

Axial, sagittal, and coronal slices of (A) T1-CE, (B) FLAIR, (C) early postoperative CT scan with superimposed HYPERDirect maps, (D) Vp, (E) MD, (F) FAZA are reported. The bioptic trajectory is depicted in each slide; in this case, the neurosurgeon targeted the sampling on a small area of dubious, mild contrast enhancement on T1-CE sequences located in the parietal lobe white matter. From the HYPERDirect maps shown in panel C, a more aggressive tumor component, composed by Habitat 1 (red; high perfusion, high hypoxia, low cellularity) and Habitat 2 (orange; high perfusion, high hypoxia, high cellularity), is clearly identifiable (also indicated by the white arrow) in the deep periventricular white matter and splenium of the corpus callosum. The geographic pattern previously described in the text, with Habitat 2 mainly occupying a more internal part of the tumor core (here the periventricular area), Habitat 1 the more peripheral part and Habitat 3 and 4 being at the interface between the tumor core and the remaining FLAIR-tumor volume, can be somehow recognized also in this non-enhancing lesion. The presence of fragmented aggressive habitats (red, orange, light blue and green) in the remaining FLAIR-tumor volume is mainly attributable to the close proximity to cortical gyri and vessels, since median values of parametric maps (0.43 for Vp, 0.3 for FAZA, 0.0014 for MD) inside of the FLAIR-tumor mask were not remarkably altered, in this patient, compared to normal brain. The site where the four samplings were performed is approximated by a small yellow circle at the end of the yellow path, showing that the specimens were collected in an area outside of the HYPERDirect-defined tumor vital core, that was mainly composed by Habitat 7, with multiple fragments of Habitat 1, 3, 4 and 5. (E) At histological diagnosis most of the areas analyzed corresponded to low grade astrocytoma with a KI-67 of 2%, only the 4th and last biotic sample (showed in the panel) contained islands of more aggressive tumor areas (with a KI-67 of 10%, some nuclear atypia and a few proliferating vessels) that made possible the final diagnosis of Anaplastic astrocytoma (III grade WHO 2016) IDH-1 mutated. Despite the diagnosis and young age, patient's overall survival was extremely short (10 weeks), suggesting that a higher grade malignancy could have seemingly been identified if the biopsy had involved the tumor "vital" core as identified on the identified habitats (Habitat 1, red, and Habitat 2, orange).

3.5 Discussion

Tumor heterogeneity poses a major clinical challenge in high grade gliomas (HGGs), since the regional diversity at the level of both DNA mutation and gene expression profiles may ultimately alter phenotype by influencing tumor cell metabolism, apoptosis and angiogenesis processes (Komori *et al.*, 2018; Louis *et al.*, 2016). Habitat imaging has been currently mainly employed on cMRI sequences, although it could hypothetically be applied to any neuroimaging method, comprising aMRI techniques such as PWI and dMRI as well as PET imaging with different radiotracers (Beig *et al.*, 2020; Cui *et al.*, 2016; Del Mar Alvarez-Torres *et al.*, 2020; Dextraze *et al.*, 2017; Fathi Kazerooni *et al.*, 2018; Fuster-Garcia *et al.*, 2018; Hu *et al.*, 2015; Ismail *et al.*, 2018; John *et al.*, 2019; Juan-Albarracin *et al.*, 2019; Juan-Albarracin *et al.*, 2018; Kim & Gatenby, 2017; Kim *et al.*, 2021a; Lee *et al.*, 2015a; Lee *et al.*, 2015b; Li *et al.*, 2019a; Li *et al.*, 2018a; Li *et al.*, 2018b; O'Connor *et al.*, 2015; Park *et al.*, 2021; Sauwen *et al.*, 2016; Stringfield *et al.*, 2019; Verma *et al.*, 2020; Wang *et al.*, 2019; Wei *et al.*, 2019; Wu *et al.*, 2020; Zhang *et al.*, 2019; Zhou *et al.*, 2017; Zhou *et al.*, 2014). In the current study, we presented an innovative PET and MRI multi-parametric approach for the assessment of Hypoxia, Perfusion, and tissue Diffusion in HGG and derived combined habitats for clustering of

intra-tumor heterogeneity in a series of 17 patients affected from HGG. To the best of our knowledge, this represents the first study combining the aforementioned parameters to define tumor habitats.

3.5.1 *Habitats*

A reproducible pattern in intra-tumoral habitats distribution (in relation to each other and to the morphological features identified on cMRI) was found among different patients. Of the 8 habitats identified, we speculated that the first two could identify the “vital” core of the tumor, with the second cluster being, hypothetically, the most aggressive component. Interestingly, **Habitat 1**, characterized by the highest Vp values, was often located more peripherally than **Habitat 2**, which is in line with the fact that perfusion values tend to be higher at the periphery of the tumor core (Ponte *et al.*, 2017). These two habitats also showed the highest hypoxia values, data in accordance with previously reported studies (Ponte *et al.*, 2017). The fact that the tumor “vital core” represents, at the same time, the most perfused and most hypoxic area, although paradoxical-seeming, is likely related to the functionally and structurally abnormal vascularity that characterize HGGs, unable to provide sufficient perfusion and oxygen supply (Ponte *et al.*, 2017; Rosinska & Gavard, 2021). The higher hyperintensity on T1-weighted contrast enhanced sequences noticed inside **Habitat 1** could be related to higher perfusion and/or vascular permeability, as confirmed by the significantly higher Vp, but also rCBV and Ktrans, values noted in this cluster. **Habitat 1** was also characterized, when compared to **Habitat 2**, by a higher MD value; the latter could imply lower tissue cellularity but also the presence of stronger vasogenic edema due to Blood-brain barrier leakage. As somehow expected, the distribution of these habitats, together with the other most “aggressive” biologic cluster representing areas of tumor necrosis (Habitat 5), was higher in WHO grade IV tumors compared to WHO III.

The poor representation of **Habitat 3** and **4** (both have high perfusion and low hypoxia values, while different cellularity) might be related to the fact that there are very few well-oxygenated areas inside the tumor core (mainly present in close proximity to larger vessels) and that, on the other hand, a certain degree of hypoxia is required to trigger neoangiogenesis and increased perfusion: it is, therefore, unlikely to find the second parameter without the first one inside a HGGs (Huang *et al.*, 2016; Ponte *et al.*, 2017).

Habitat 5 (high hypoxia, low perfusion, and low cellularity) was considered representing necrotic areas still including some degree of vital tissue, since the FAZA-PET tracer needs hypoxic, yet vital, cells in order to be reduced to reactive oxygen radicals and remain locally trapped (Halmos *et al*, 2014; Mapelli & Picchio, 2020). This habitat likely represents the region where pseudopalisading takes place (Stadlbauer *et al.*, 2018b).

Habitat 6, when colocalizing with areas of shaded contrast enhancement outside the tumor “vital” and necrotic cores, was interpreted by the authors as new tumoral seeds progressing toward higher malignancy (perhaps close to turning, later on, into the more aggressive **Habitats 1 or 2**), since it harbored increased cellularity and hypoxia, but not yet a significantly augmented vascularization. On the contrary, when **Habitat 6** was identified inside of the tumor core, it was interpreted as regions where tumor growth exceeded vascularization and that were close to undergoing a necrotizing process.

Finally, we speculated that **Habitat 8**, due to its increased cellularity (but low perfusion and hypoxia), might identify areas of tumor infiltration beyond the CE vital core, while **Habitat 7** (low cellularity, perfusion, and hypoxia) areas of vasogenic edema (with no, or less significant, tumor infiltration). Interestingly, the relative volume of pure edema (Habitat 7) was significantly higher in IDH-1 wild-type tumors compared to IDH-1 mutated lesions, in accordance with what was recently described by Dubinski *et al.* (Dubinski *et al*, 2021); on the contrary, no association was found with the non-enhancing tumoral infiltrative component (Habitat 8).

3.5.2 Spatio-temporal evolution of the Habitats

The broadly recognized model of glioblastoma progression comprises the following steps (Brat *et al*, 2002; Hardee & Zagzag, 2012; Holash *et al*, 1999; Stadlbauer *et al.*, 2018b). Initially, neoplastic cells infiltrate through the cerebral tissue, receiving nutrients and oxygen supplies through vascular co-option of intact native blood vessels (Hardee & Zagzag, 2012; Stadlbauer *et al.*, 2018b). Neoplastic cells then commence to migrate away from the growing hypoxia around the vascular pathology and generate a peripherally moving wave (known as pseudopalisades) with central necrosis (Stadlbauer *et al.*, 2018b). Hypoxic and necrotic regions enlarge and the migrating hypoxic pseudopalisading glioma cells produce hypoxia-inducible factor 1 α (HIF-1 α) and

Vascular-Endothelial Growth Factor (VEGF,) leading to neovascularization and, in further consequence, to an accelerated outward expansion of neoplastic cells toward a new vasculature (Stadlbauer *et al.*, 2018b).

Considering the known models of tumor progression, we are able to speculate about the, possible, evolution over the time of the identified HYPERDIrect: areas of tumor infiltration in the white matter (**Habitat 8**: increased cellularity), might eventually develop some degree of hypoxia (**Habitat 6**: increased cellularity and hypoxia), which, in turn, trigger neovascularization (through tumor cells secretion of mediators such as HIF-1 α and VEGF (Stadlbauer *et al.*, 2018b)) and increased perfusion values, becoming a tumor “vital core”: **Habitat 1** and (perhaps subsequently) **Habitat 2**, both characterized by extremely high perfusion and hypoxia. In due course, the tumor growth in the vital core will overwhelm its abnormal vascularization, leading toward areas of pre-necrotic state (**Habitat 6**: low perfusion, high hypoxia and high cellularity); as the necrotizing process progresses, cellularity will decrease (**Habitat 5**: low perfusion, high hypoxia and low cellularity) eventually turning into liquefactive necrosis, with no remaining vital cells and showing, consequently, a concomitant drop in hypoxia signaling and FAZA-tracer uptake (**Habitat 7**: low perfusion, low hypoxia and low cellularity). The aforementioned “habitat progression” is easily perceivable in **Figure 3.4C** and **Figure 3.4D**, where a somehow concentric distribution of the clusters is identifiable.

3.5.3 *Potential clinical applications*

The heterogeneous biology of HGGs challenges the reliability of limited needle biopsy sampling for making disease-wide characterization. Nevertheless, needle biopsies are utilized, to date, in about a third of cases to define HGG diagnosis. The rate of non-diagnostic (to be repeated) stereotactic biopsies is 7-10% (Lu *et al.*, 2015; Sciortino *et al.*, 2019), and complete diagnostic accuracy has been reported as low as 33-64% of cases (compared to pathologic analysis obtained with the subsequent gross-total resection of the same lesion) (Jackson *et al.*, 2001; Muragaki *et al.*, 2008; Reithmeier *et al.*, 2013). Integrating HYPERDIrect habitats into a bioptic planning system might better guide the neurosurgeon in sampling the most relevant functional regions of the tumor, especially by virtue of the much easier perception of the colored maps of these 8 habitats, compared to the thorough expertise in advanced neuroimaging needed to interpret multiple

coregistered parametric maps elaborated from dMRI, PWI or PET tracers. This might be particularly valuable in those gliomas showing poor or no enhancement on T1-CE sequences, since about one-third of non-enhancing gliomas entail malignant islands that, if correctly included in the pathologic analysis, can classify the lesion into a higher-grade tumor, with consequently remarkable differences on treatment management and patient prognosis [Jin, 2019]. In these cases, the few samples achievable via needle biopsy might easily underestimate the actual tumor grade, if not adequately guided to the most aggressive areas (an explicative case is reported in **Figure 3.9**). Moreover, it must be considered that even in the case of surgical resection, the extensive use of suction tools or the inability to reach complete removal might significantly lessen the amount of viable specimen for the pathologist, which, therefore, does not necessarily represent the wide heterogeneity of the neoplasm (Lasocki *et al.*, 2015; Mikkelsen *et al.*, 2021).

We believe that further exploration of hypoxia, perfusion and diffusion derived habitats might provide precious, holistic information about intra-tumor heterogeneity, unveiling regional diversity both at the level of DNA mutation and gene expression profiles, helping in prognosis stratification and, perhaps, in future, treatment selection. The precise identification of the most perfused, cellulated and hypoxic regions inside and outside the tumor contrast enhancement component could represent an enormous aid in surgical and radiotherapy planning. Radiation dose painting with a boost on the most aggressive and resistant clusters represents one of the most appealing perspectives for the next future (Castellano *et al.*, 2021). Finally, the identified habitats could represent a precious tool in monitoring the dynamical spatio-temporal modification in glioma heterogeneity during therapies and follow-up and could identify more clearly areas of tumor response or progression.

3.5.4 Limitations and future work

One main drawback of the present work is the limited number of cases analyzed and their heterogeneity (e.g., tumor histology, grading, molecular characteristics, volume, location, patient's age, comorbidities, type of surgery) which have likely hampered the achievement of conclusive associations between the variables involved (parametric map values, habitats, histopathological data and patient outcome/survival).

In the subgroup of 10 patients undergoing a stereotactic biopsy, we were able to identify a qualitative correlation between the expected microenvironment of the different habitats and the actual histopathologic morphology, although only a preliminary analysis was possible in this small and heterogeneous series and no definite, statistically significant, conclusions could be drawn. The designation of biopsy target spots and path was planned in order to maximize patient's safety while ensuring final diagnosis, according to the best clinical practice, by means of the minimum amount of sampling deemed necessary (due to ethical concerns). This, along with the fact that the HYPERDIrect habitats were not available to the neurosurgeon preoperatively, prevented the acquisition of a sufficient variety of sampled habitats in the same lesion and frequently ended in sampling over multiple clusters at one, therefore limiting the possibility of direct associations.

Considerable processing and analyses were required initially for the generation of the final HYPERDIrect habitats, which demanded intensive labor and both imaging clinical scientist and informatics/engineering expertise. This requirement could be particularly critical in clinical practice, when a short time in-between imaging and surgery is available. However, we believe that this could be overcome in the future via dedicated flowcharts with automated algorithms, providing the benefit of a much easier data interpretation for the neurosurgeon in charge of planning the procedure.

A limitation of the applied algorithm was the possible colocalization of the same radiological habitat in different tumor microenvironments as the case of Habitat 8 (which was thought to mainly represent areas of augmented cellularity due to tumor infiltration of the surrounding white matter) in proximity to microhemorrhagic foci, liquefactive necrosis including viscous mucinous components or cerebral vessels and cortex. A possible solution to this issue could be to leave a larger margin from these regions while segmenting tumor mask, to identify different cut-offs for the clustering analysis or to add/modify the parametric maps utilized in the algorithm.

Since this represents a preliminary analysis, a study with prospectively and systematically collected data is clearly necessary. The systematic use of a combined PET/MR scan with a high (3 Tesla) magnetic resonance field could further enhance the quality and spatial discrimination of the data obtained from dMRI and PWI, while optimizing scanning time and image coregistration. The alternative adoption of novel advanced MR techniques capable of assessing tissutal hypoxia could represent another

extremely appealing eventuality since it would avoid the need for PET hypoxia tracers (such as FMISO or FAZA) that can be difficult to be gathered from specialized manufacturers or produced locally, expensive, time-consuming, and still problematic to be implemented in common practice due to the lack of a thorough clinical validation and institutional authorization. Indeed, in more recent years, resting-state blood oxygen level-dependent (BOLD) acquisitions have been successfully employed in the detection of areas of neurovascular uncoupling and hypoxia inside of tumoral tissue (Englander *et al.*, 2018; Pillai & Zaca, 2012; Stadlbauer *et al.*, 2011; Stadlbauer *et al.*, 2018a; Stadlbauer *et al.*, 2018b). These maps could be easily acquired in the same MR sessions together with morphological sequences, dMRI and PWI, can be eventually integrated into our algorithm to generate HYPERDIrect habitats.

Conclusively, future goals will be to link the identified clusters with histopathological, immunohistochemical and molecular biomarkers, as well as clinical information such as survival and recurrence, in a larger, prospective clinical series. Moreover, it would be interesting to follow up patients over the course of the disease with the HYPERDIrect maps, in order to monitor spatio-temporal changes and be able to validate the hypothesis formulated in the present study.

3.6 Conclusions

In the current study, we presented an innovative PET and MRI approach for the assessment of Hypoxia, Perfusion and Diffusion in HGGs and to derive combined habitats for the clustering of intra-tumor heterogeneity. Our preliminary analyses in a series of 17 HGGs confirmed that quantitative imaging features related to these biological processes may reflect this heterogeneity non-invasively and that malignant gliomas can be consistently divided into some small number of clusters based on the combinations of quantitative parameters from PWI, dMRI, and 18F-FAZA PET metabolic maps. Prospectively and systematically collected data, including a more detailed immunohistochemical and molecular analysis through image-guided sampling, in a larger population will be further necessary.

3.7 Final considerations

The student was one of the co-investigators in the research group (guided by Dr. Antonella Castellano) that won a 450.000€ grant (“Bando Giovani Ricercatori - Ricerca Finalizzata 2018”, Italian Ministry of Health) for a project aiming at investigating and validating a novel approach based on fully hybrid PET/MR images with specific HYpoxia tracers and advanced PERfusion (PWI) and DIffusion (dMRI) MR techniques in high grade gliomas (HGG): the HYPERDIrect study. In this study, quantitative data from a PET/MRI exam acquired in over 30 prospectively-enrolled patients with a new diagnosis of high grade glioma, were to be combined in a unique HYPERDIrect map, with the aim to identify discrete radiomic “habitats”, possibly reflecting diverse genetic and biological features, to be proven by image-guided tissue sampling. The final aim was to investigate intra-tumoral heterogeneity depicted by HYPERDIrect map as a predictor of clinical outcome. Unfortunately, the project was still awaiting to start at the present time, due to significant delays due to lacking authorization of the use of nitroimidazoles hypoxia tracers from the Italian Medicines Agency (AIFA) in human subjects. The latter institution, after recently changing its own regulations over the matter of clinical studies, requested an amount and type of supportive documentation that the (few) companies manufacturing these niche radiotracers precursors, were not able to provide within reasonable time and costs; this despite multiple clinical studies using the same [18F]-Fluoroazomycin arabinoside (18F-FAZA) radiotracer have been already authorized by AIFA, completed and published in our center in the previous years, proving the safety and incredible potential of this PET marker of hypoxia (Capitanio *et al*, 2020; Mapelli *et al*, 2018; Mapelli *et al.*, 2021; Mapelli *et al*, 2020; Mapelli *et al*, 2017a; Mapelli & Picchio, 2020; Mapelli *et al*, 2017b; Savi *et al*, 2017a).

4 COMPREHENSIVE BRAIN TUMOR CHARACTERIZATION WITH VERDICT-MRI: EVALUATION OF CELLULARITY AND VASCULARITY MEASURES VALIDATED BY HISTOLOGY AND PERFUSION MRI

In the second experiment of this thesis, the potential applicability of Vascular, Extracellular, and Restricted Diffusion for Cytometry in Tumors (VERDICT) MR imaging in brain tumors was investigated. VERDICT represents a pioneering computational multi-compartment modeling framework originally developed for the extraction of quantitative maps from advanced dMRI acquisitions in body tumors, representing their vascular, extracellular and restricted component. Our teamwork successfully optimized this model for the assessment of brain neoplasms, which entail a variable surrounding infiltration and therefore a higher complexity, eventually obtaining a four-compartment model without extra free parameters, showing its improved fitting performance, especially for peritumoral areas. The results from our VERDICT model were validated against PWI parameters (rCBV and Vp) and histopathology from corresponding stereotactic sampling.

This study was part of an international multi-center project and was performed in collaboration with diverse professional figures from the University College of London (UK), Clinical Imaging Sciences Centre of Brighton, (UK) and Cardiff University Brain Research Imaging Centre (UK).

4.1 Introduction

Characterizing the microstructure of brain tumors and peritumoral region is essential to reach an accurate preoperative diagnosis and to select the most appropriate treatment option in every patient, pointing at tailoring individualized therapies. This should be ideally performed in a non-invasive manner, nevertheless, this still results challenging in the present clinical practice. Particularly, what still remains not thoroughly understood is the reliability of non-invasive Magnetic Resonance Imaging (MRI) methods to disentangle micro-structural and biological tumoral tissue features in a consistent manner (Ellingson *et al*, 2014). As not all patients are suitable for surgical resection or needle biopsy, which are currently still necessary to obtain a complete histopathological and

molecular diagnosis, it is crucial to enforce techniques able to corroborate diagnostic and predictive MRI biomarkers for brain tumors noninvasively (Sanvito *et al*, 2021). Moreover, by a non-invasive definition of microscopic tissue modifications over time, surrogate indicators of disease response or progression could be disclosed, avoiding the intrusive need for repeated biopsies during patients' follow-up (Shah & Kochar, 2018).

Numerous multiparametric MR studies aimed at characterizing and differentiating brain neoplasms utilizing advanced MRI techniques as diffusion MRI (dMRI) and perfusion-weighted imaging (PWI), that add important structural, hemodynamic and physiological information to the routinely-employed morphological MRI protocols (Castellano & Falini, 2016). In particular, the microstructure of cerebral neoplasms can be non-invasively evaluated using diffusion-weighted MRI (dMRI) (Nilsson *et al*, 2018a): diffusion appears intensely reduced in hypercellular regions. The Apparent Diffusion Coefficient (ADC) generated with dMRI has been proved to inversely correlate with tissue cellularity (Chen *et al*, 2013; Doskaliyev *et al*, 2012; Sugahara *et al*, 1999), despite the presence in literature of some conflicting findings (Jenkinson *et al*, 2010) and considerable overlapping of tumor-specific ranges of ADC values (Maier *et al*, 2010). The inconsistency probably derives from the fact that ADC is a gross measurement that conjoins several physiologic parameters, including cell density, shape, size, permeability, subcellular microstructure, and vascular perfusion effects. These biophysical mechanisms affect the ADC in diverse manners that can compete and even neutralize one another, invalidating overall specificity (Panagiotaki *et al*, 2014). Model-based dMRI approaches can hypothetically segregate these effects, providing estimations of specific histological characteristics, therefore providing a considerably plentiful characterization of the investigated tissue on which to base a diagnosis or grade assessment.

The Mean Kurtosis is a Diffusion Kurtosis Imaging (DKI) parameter related to diffusional variance, that has been reported as a more accurate and sensitive higher-order dMRI analysis when dealing with histological differentiation and grading of cerebral neoplasms (Raab *et al*, 2010; Raja *et al*, 2016). Recently, MK has been decomposed into two measures related to microscopic anisotropy and tissue heterogeneity, respectively, using valued diffusion encoding MRI acquisitions. These two metrics have been applied in the histopathological differentiation of cerebral lesions (Nilsson *et al*, 2020; Szczepankiewicz *et al*, 2016). An additional approach is represented by fitting a multi-

compartment model (Panagiotaki *et al*, 2012), segregating the contributions that different tissue compartments provide to the MR signal; these models require a certain degree of complexity to acquire a biological significance, but this infers a considerable danger of degeneracy (Jelescu *et al*, 2016). Fixing or constraining certain parameters of the model constitute a frequently adopted solution; this is the case of the NODDI (Zhang *et al*, 2012) technique application in the analysis of cerebral neoplasms (Figini *et al*, 2018; Qiuting *et al*, 2015), despite its presuppositions are not appropriate for the whole tumor area. The acquisition of a richer dataset might prove a better option, for instance, using several oscillating gradients or diffusion times, allowing the quantification of cellular size and density (Jiang *et al*, 2017).

All the aforementioned dMRI modalities concentrate their analysis on the cellular component of cerebral neoplasms overlooking the vascular features. By modeling perfusion in vessels as pseudo-diffusion (with very high diffusivity) as in the Intra-Voxel Incoherent Motion (IVIM) model it is possible for dMRI to characterize micro-vascularity (Le Bihan, 2019). This technique, as opposed to classic perfusion MRI methods as dynamic susceptibility contrast (DSC) and dynamic contrast enhanced (DCE), do not necessitate the administration of contrast media (Svolos *et al*, 2014; Villanueva-Meyer *et al*, 2017). The IVIM technique has been employed in the brain tumors assessment (as described by Federau *et al*. and Jabehdar Maralani *et al*. (Federau *et al*, 2014; Jabehdar Maralani *et al*, 2021)); its representation of the tissue's non-vascular components relies on simple ADC measure; however, it is not able to provide restriction or other complex features that frequently characterize brain tumors.

VERDICT-MRI (Vascular, Extracellular, and Restricted Diffusion for Cytometry in Tumors) is an imaging and computational modeling framework, relying on dMRI acquisitions with multiple diffusion times and weightings, using multi-compartment models, that permits a quantitative analysis of the vascular, extracellular and restricted component of tumoral lesions (Panagiotaki *et al*., 2014). VERDICT has already proved a diagnostic value and high repeatability in other cancers located outside the central nervous system (CNS), particularly prostatic tumors (Johnston *et al*, 2019; Panagiotaki *et al*, 2015) and metastases (Bailey *et al*, 2018). Nevertheless, the implementation of VERDICT among CNS neoplasms is demanding since the brain tissues' microstructure is particularly intricate. Notwithstanding that the main part of most cerebral tumors is

comparable to other cancer outside the CNS from a microstructural point of view, features not adequately modeled by VERDICT (in a formulation designed for body tumors) might still be present, such as anisotropic areas of peritumoral edema and neoplastic infiltration.

4.2 Aims

The aim of this study is to adopt the VERDICT framework to identify a microstructural model suitable for cerebral neoplasm. The research will concentrate on the investigation of clinically relevant features provided by VERDICT measures: vascularity, cellularity, neoplastic infiltration, and edemas. The VERDICT model will be validated by comparing its measures with independent estimates obtained from MR perfusion, such as cerebral blood volume or plasma volume. Additionally, we will provide a comparison of VERDICT estimates to qualitative histopathological findings of the corresponding tumor both in cases undergoing surgical removal than in those undergoing bioptic sampling, with the latter permitting a more precise comparison inside different voxels of heterogeneous lesions.

4.3 Materials and methods

4.3.1 Subjects and MRI acquisition

Data were collected from 21 patients admitted at the Department of Neurosurgery and Gamma Knife Radiosurgery of San Raffaele Hospital (Milan, Italy) harboring an intracerebral lesion, suspected for either a primary or secondary brain tumor. All the patients included were considered for maximum safe resection or stereotactic needle biopsy according to tumor location/extension and patient characteristics (e.g., age, comorbidities, and performance status) and gave their consent to undergo advanced MRI acquisition and to use their data, anonymously, for scientific studies.

MRI was performed preoperatively on a 3.0T Ingenia CX scanner (Philips Healthcare, Best, The Netherlands) at the Neuroradiology Unit and CERMAC, IRCCS Ospedale San Raffaele (Milan, Italy). Conventional MRI including 3D-FLAIR images (TE/TI/TR = 285/2500/9000 ms, isotropic resolution 0.7 mm) and post-contrast 3D T1-weighted images (TE/TR = 5.27/11.12 ms, flip angle 8°, isotropic resolution 0.5 mm) were acquired.

dMRI scans were acquired according to the scheme in **Table 4.1** and with an isotropic voxel size of 2 mm. Nineteen of the patients also had perfusion MRI including dynamic contrast enhanced (DCE) 3D spoiled gradient echo sequences (TE/TR = 1.8/3.9 ms, flip angle 15°, in-plane resolution 2x2 mm², slice thickness 2.5 mm, 70 repetitions) and dynamic susceptibility contrast (DSC) fast field echo EPI sequences (TE/TR = 31/1500 ms, flip angle 75°, in-plane resolution 2x2 mm², slice thickness 5 mm, 80 repetitions).

| b (s/mm²) | 50 | 70 | 90 | 110 | 350 | 1000 | 1500 | 2500 | 3000 | 3500 | 711 | 3000 |
|-----------------------------|----|----|----|-----|-----|------|------|------|------|------|-----|------|
| TE (ms) | 45 | 53 | 43 | 43 | 54 | 78 | 118 | 88 | 103 | 123 | 78 | 78 |
| δ (ms) | 5 | 5 | 5 | 5 | 10 | 10 | 10 | 20 | 15 | 15 | 20 | 20 |
| Δ (ms) | 22 | 30 | 20 | 20 | 26 | 50 | 90 | 50 | 70 | 90 | 42 | 42 |
| Ndir | 3 | 3 | 3 | 3 | 3 | 3 | 3 | 3 | 3 | 3 | 38 | 63 |

Table 4.1 - Acquisition parameters for the dMRI protocol.

Abbreviations: *b* = *b*-value (degree of diffusion weighting), *TE* = echo time, *δ* = diffusion gradient duration, *Δ* = diffusion gradient separation, *Ndir* = number of diffusion gradient directions

4.3.2 Processing of Diffusion and perfusion MRI

We performed denoising, removal of Gibbs artifacts and motion correction of dMRI data using MRtrix3(Tournier *et al*, 2019) and distortion correction using MD-dMRI (Nilsson *et al*, 2018b).

Perfusion MRI data were analyzed with Olea Medical software (v 3.0, Olea Medical Solutions, La Ciotat, France) to obtain parametric maps of plasma volume (*V_p*) and relative blood volume (rCBV). These maps were registered to the first B₀ volume of the dMRI data using the FMRIB's Linear Image Registration Tool (FLIRT) (Jenkinson *et al*, 2002) from the FMRIB Software Library (FSL v 6.0, FMRIB, Oxford, UK).

Regions of interest (ROI) masks were segmented on 3D FLAIR images for the whole tumor and on post-contrast 3D T1-weighted images for the tumor core. Both anatomical images were registered to the first B₀ volume using FLIRT, and the periphery mask was obtained as the difference between the whole tumor and tumor core. To minimize misregistration issues, both core and periphery masks were eroded, visually checked in all patients, and manually corrected where necessary, especially in heterogeneous lesions.

4.3.3 Tissue Models

We fit multiple three-compartment models to the data (Matlab MathWorks, Natick, MA, USA) from compartment model combinations (**Figure 4.1**). Using the terminology

in (Panagiotaki *et al.*, 2012), we use the Sphere to model intracellular restriction in tumor cells, as in (Palombo *et al.*, 2020; Panagiotaki *et al.*, 2014); we consider Zeppelin, Tensor, Cylinder, Stick, and Watson-distributed Sticks for the extracellular compartment, accounting for the extracellular space and possibly white matter fibers and/or areas of edema; and Ball and AstroSticks for the vascular compartment. We constrain the pseudo-diffusivity (dv) in the vascular compartment to be at least $3 \cdot 10^{-9} \text{ m}^2/\text{s}$ when using Ball or $9 \cdot 10^{-9} \text{ m}^2/\text{s}$ when using AstroSticks. The name of each multi-compartment model is formed first by the extracellular compartment, then the vascular compartment, and finally the restricted compartment.

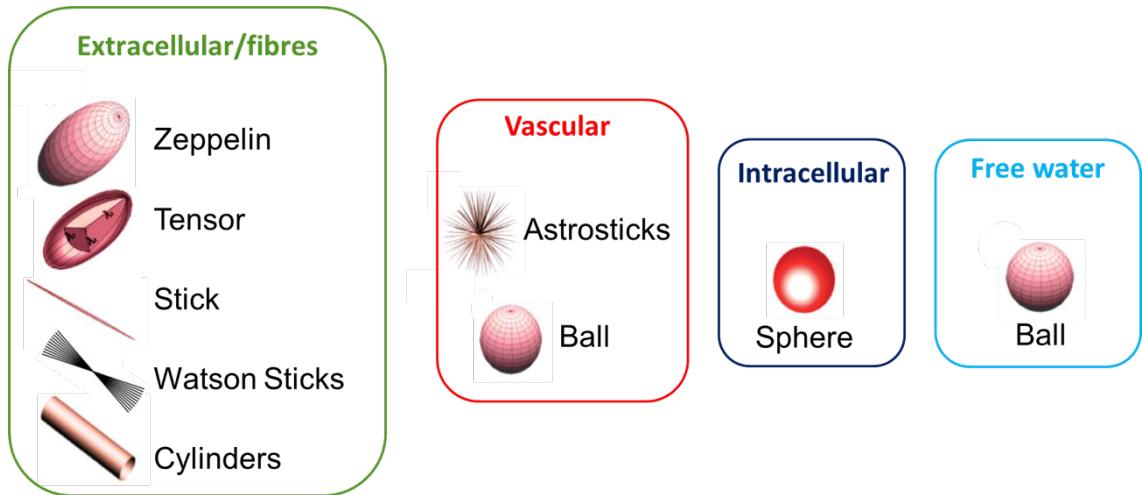


Figure 4.1 - Compartments models

Given the complexity of the brain tissue, a three-compartment model may possibly be insufficient to capture all the effects we may see in the dMRI signal in some cases. In particular, it would be useful to have a free water compartment to characterize areas of necrosis, cysts or edema, but adding a fourth compartment with additional free parameters would most likely result in model degeneracy and unreliable estimates. For this reason, we tested a Free Water Elimination (FWE) procedure based on a preliminary fitting of the NODDI model to the data in the last two shells (see **Table 4.1**). Our FWE approach consists in adding a Ball compartment to the model, with the diffusivity fixed to $3 \cdot 10^{-9} \text{ m}^2/\text{s}$ and the signal fraction constrained to the value estimated by NODDI for the isotropic compartment (fiso). This effectively results in four-compartment models with the same number of free parameters as the corresponding three-compartment models with no FWE.

4.3.4 *Model selection*

Starting from all the possible combinations of compartments listed in the previous section, we followed a stepwise model selection procedure including the following evaluations:

1) To select the best extracellular compartment model without the confounding effect of low- b dMRI signal that is mainly related to pseudo-diffusion, we used the Akaike's Information Criterion (AIC) to evaluate the fitting performance of two- and three-compartment models on high- b data ($b > 200$ s/mm², excluding the first four shells in **Table 4.1**)

2) To assess the fitting performance on the full signal, we evaluated the AIC again on the best-performing models from 1) with the addition of the vascular compartment (Ball or AstroSticks), and with and without FWE.

3) We evaluated anisotropy measures in the extracellular compartment of the same models as in 2), fitted to the full signal. ODI from NODDI is considered as the gold standard.

4) To highlight issues of ambiguity between pseudo-diffusion and diffusion with high diffusivity, we investigated estimates of the vascular fraction (f_v) from the same models as in 2), fitted to the full signal, in areas where NODDI provided $f_{iso} > 0.5$ and we don't expect any significant vascularity.

4.3.5 *Histology*

The tissue samples obtained were directly fixed in a 10% formalin solution and referred to the pathology department, where they were processed the same day or the following one if the procedure was performed in the late afternoon. The final diagnosis was established according to the 2016 WHO classification (Louis *et al*, 2016).

In the case of stereotactic biopsy, the procedure commenced with the fixation of the MRI-compatible Leksell stereotactic frame to the patient's skull (Model G, Elekta, Stockholm, Sweden), under mild intravenous sedation (midazolam) and local anesthesia (lidocaine and mepivacaine). The patient then underwent the acquisition of an axial 3D-T1 MRI after gadolinium administration (Voxel 1 x 1 mm, slice thickness 1 mm without

gap, Matrix 256x256 mm) using the appropriate fiducial system on a Philips Achieva 1.5 Tesla MR scanner (Philips Medical Systems, Best, the Netherlands). In most of the cases, a 3D T2-weighted series was also obtained. During the procedure, a Sedan needle (2.5 mm diameter and 10 mm of bioptic window) was used to acquire a minimum of two cylindrical bioptic samples, according to the size and macroscopical aspect of the tissue obtained and procedure-related risks. The accuracy of the bioptic sampling was eventually verified in all cases with the co-registration of the preoperative imaging and planned trajectory with the postoperative CT images inside the SurgiPlan software; the stereotactic coordinates of the exact, final sites of the biopsy were exported from the Surgiplan software and transferred to VERDICT maps by using the transformations obtained when registering T1-weighted images to dMRIs.

4.3.6 Statistical analysis

Shapiro-Wilk's test was used to test the normality of the data. To assess clinical utility, we evaluated the parameters from the model that performed best according to our model selection procedure, and we compared their values between different histotypes in tumor core and periphery using one-way ANOVA with Tukey's multiple comparisons test or Kruskal-Wallis and Dunn multiple pairwise comparison tests, the latter when data were non-normally distributed, with a significance level of $P < 0.05$.

The Pearson correlation coefficient (r) was used to assess the relationships between the vascular fraction and PWI-derived V_p and $rCBV$ in order to verify if the correlations found at low b -values with two-compartment models still hold with the full model fitted on the full signal.

4.4 Results

4.4.1 Patients' population

The patients' cohort included 21 adult patients with suspected brain tumors (16 M, 5 F; mean age, 52 years; range, 19-77 years), whose histopathological and molecular data are summarized in **Table 4.2** and **Table 4.3**. Of them, 16 patients had a gross tumor resection (GTR) and 5 underwent a stereotactic biopsy.

| Variable | Value |
|---|--|
| Age | mean age 52 yrs (range 19-77 yrs) |
| Sex | |
| Male | 16 |
| Female | 5 |
| Histopathology | |
| Glioma | |
| Lower-grade glioma (WHO 2-3) | 11 |
| <i>IDH1/2 mutated</i> ^a | 4 (1 WHO 2, 3 WHO 3) |
| <i>IDH1/2 wild type</i> ^a | 7 (3 WHO 2, 4 WHO 3) |
| Glioblastoma (WHO 4) | 4 |
| <i>IDH1/2 wild type</i> | 4 |
| Other glial tumors (ependymal)^a | 2 (1 subependymoma WHO 1, 1 ependymoma WHO 3) |
| Metastasis | 2 (melanoma) |
| Other | 1 radiation necrosis, 1 focal cortical dysplasia |

Table 4.2 - Summary of patients' sample characteristic

| Patient code | Age | Sex | Biopsy/surgery | Histology diagnosis | WHO grade | IDH mutation |
|--------------|-----|-----|----------------|---------------------------------------|-----------|--------------|
| 01 | 69 | F | Biopsy | Astrocytoma | 3 | wild-type |
| 02 | 61 | M | Surgery | Astrocytoma | 3 | wild-type |
| 03 | 65 | M | Biopsy | Glioblastoma | 4 | wild-type |
| 04 | 71 | M | Surgery | Melanoma metastasis | / | - |
| 05 | 41 | M | Biopsy | Astrocytoma | 3 | mutated |
| 06 | 24 | M | Surgery | Astrocytoma | 2 | wild-type |
| 07 | 57 | M | Surgery | Radionecrosis (Pulmonary AdenoCa Met) | / | / |
| 08 | 74 | M | Surgery | Glioblastoma | 4 | wild-type |
| 09 | 73 | M | Surgery | Astrocytoma | 2 | wild-type |
| 10 | 20 | M | Surgery | Ependymoma | 3 | / |
| 11 | 31 | F | Biopsy | Astrocytoma | 2 (3)* | wild-type |
| 12 | 58 | M | Biopsy | Astrocytoma | 3 | wild-type |
| 13 | 77 | M | Surgery | Glioblastoma | 4 | wild-type |
| 14 | 65 | M | Surgery | Melanoma metastasis | / | / |
| 15 | 32 | F | Surgery | Subependymoma | 1 | / |
| 16 | 51 | M | Surgery | Astrocytoma | 3 | mutated |
| 17 | 65 | M | Surgery | Glioblastoma | 4 | wild-type |
| 18 | 64 | F | Surgery | Astrocytoma | 3 | mutated |
| 19 | 19 | M | Surgery | Astrocytoma | 2 | mutated |
| 20 | 42 | M | Surgery | Focal cortical dysplasia | - | - |
| 21 | 37 | F | Surgery | Astrocytoma | 2 | wild-type |

Table 4.3 - Details of patients' characteristics.

* biopsy-confirmed WHO 2 with foci of radiological progression

The histopathological analysis resulted in 11/21 patients having a lower grade astrocytoma (4 WHO 2, 7 WHO 3), 4/21 patients having a glioblastoma WHO 4. Two patients had ependymal tumors (1 subependymoma WHO 1, 1 ependymoma WHO 3), two had brain metastases from melanoma, one had a pathology-proven radionecrosis after a previous radiosurgical treatment of a solitary brain metastasis from lung adenocarcinoma. One had a focal cortical dysplasia, resembling a low-grade glial neoplasm on preoperative imaging.

WHO 2 gliomas tend to be more homogeneous on FLAIR images and to have no contrast enhancement on T1-weighted images, whereas most of WHO 3 gliomas showed discrete foci of enhancement; glioblastomas and metastases present as large lesions with central heterogeneous enhancement surrounding necrosis, and peripheral edema on FLAIR images (**Figure 4.2**).

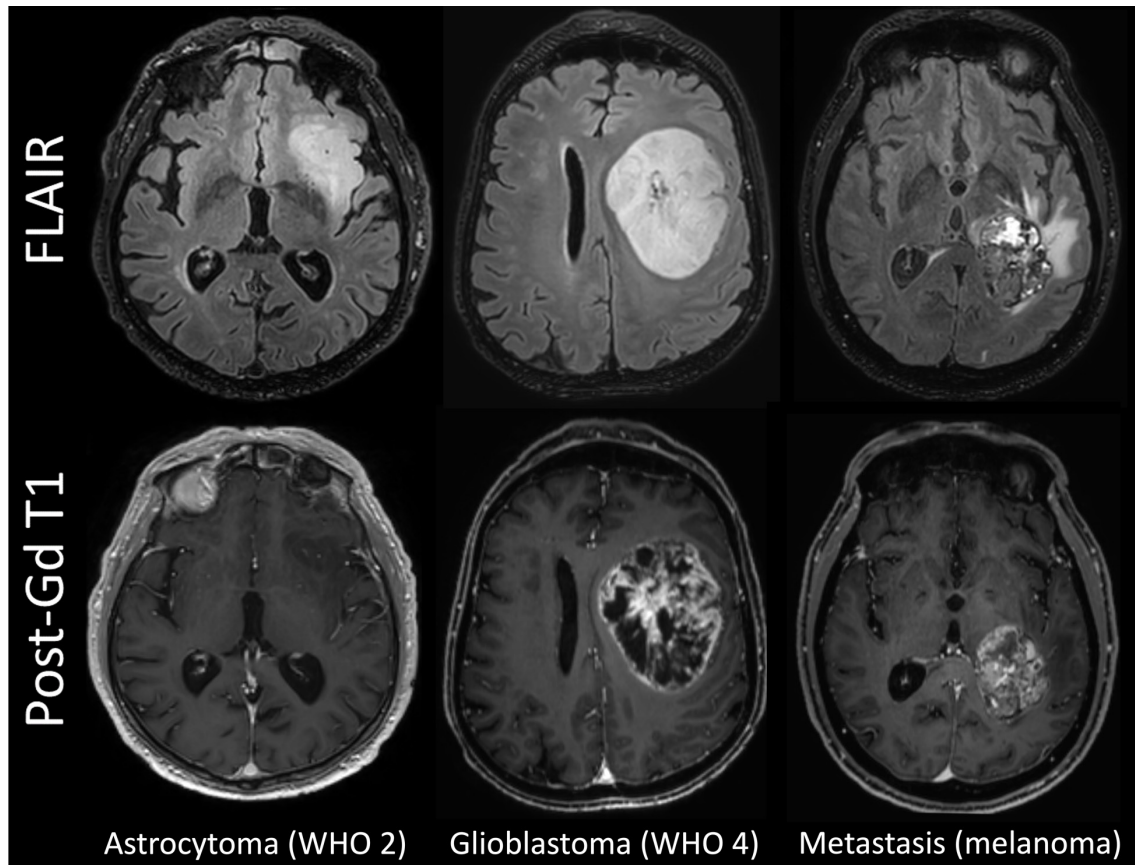


Figure 4.2 - FLAIR and T1w images in representative cases

For the purpose of quantitative analysis of the VERDICT parameters in the tumor core, lesions were classified according to different WHO grades and histologies.

4.4.2 Model selection

Following the stepwise model selection procedure described in the Materials and Methods, we found that:

- 1) In the comparison between two- and three-compartment models at high b , all the top-performing models included Tensor and/or Zeppelin, whereas models including

Stick, WatsonSticks, or Cylinder compartments performed worse on average. For this reason, only Tensor and Zeppelin were considered as candidates for the extracellular compartment in the following experiments. The considered models are ranked according to the average AIC across patients in **Table 4.4**.

| Model ranking in the tumor core | Model ranking in the peritumoral ROI |
|---------------------------------|--------------------------------------|
| Zeppelin-Tensor-Sphere | Zeppelin-Tensor-Sphere |
| Ball-Tensor-Sphere | Ball-Tensor-Sphere |
| Ball-Tensor | Tensor-Sphere |
| Tensor-Sphere | Zeppelin-Sphere |
| Ball-Zeppelin | Ball-WatsonSticks-Sphere |
| Ball-Zeppelin-Sphere | Zeppelin-Cylinder-Sphere |
| Ball-WatsonSticks-Sphere | Ball-Stick-Sphere |
| Ball-Cylinder | Ball-Zeppelin-Sphere |
| Zeppelin-Cylinder-Sphere | Ball-Cylinder-Sphere |
| Zeppelin-Sphere | Ball-Tensor |
| Ball-Stick-Sphere | Ball-Zeppelin |
| Zeppelin-Stick-Sphere | Ball-Stick |
| Ball-Stick | Ball-Cylinder |
| Ball-Cylinder-Sphere | Ball-Sphere |
| Zeppelin-WatsonSticks-Sphere | Zeppelin-WatsonSticks-Sphere |
| Ball-Sphere | Zeppelin-Stick-Sphere |
| Cylinder-Sphere | Ball |
| Ball | Cylinder-Sphere |
| Stick-Sphere | Stick-Sphere |

Table 4.4 - Ranking of two- and three-compartment models fitted on high-b signals, based on the average AIC across patients.

A single-Ball model is also included for comparison.

2) In all the cases, except for Tensor-Ball-Sphere in the tumor core and Tensor-AstroSticks-Sphere in the periphery, the AIC of the model with FWE is lower (better fitting) than that without FWE. The difference is higher and more significant in the peritumoral areas and when fixing the diffusivity in the vascular compartment. The average AIC of the considered models, fitted to the full signal, is reported in **Table 4.5**.

| Model | Core AIC | | Periphery AIC | |
|---|-------------|------|---------------|------|
| | no FWE | FWE | no FWE | FWE |
| Zeppelin-Ball-Sphere | 2726 | 2676 | 4389 | 2663 |
| Zeppelin-Ball-Sphere with fixed dv | 3211 | 2586 | 3295 | 2559 |
| Tensor-Ball-Sphere | 2774 | 2780 | 4611 | 4318 |
| Tensor-Ball-Sphere with fixed dv | 4591 | 2582 | 7673 | 2591 |
| Zeppelin-AstroSticks-Sphere | 2591 | 2585 | 2616 | 2568 |
| Zeppelin-AstroSticks-Sphere with fixed dv | 3719 | 2698 | 7265 | 2682 |
| Tensor-AstroSticks-Sphere | 2575 | 2575 | 2607 | 2661 |
| Tensor-AstroSticks-Sphere with fixed dv | 4246 | 3265 | 8940 | 4723 |

Table 4.5 - AIC of the considered models with and without FWE, averaged across patients.

The higher value of each pair is highlighted in bold if the difference is significant according to the Wilcoxon signed rank test

3) Comparing equivalent models where the only difference is the form of the extracellular compartment (Zeppelin or Tensor), models with Zeppelin showed stronger correlations with NODDI. The correlation coefficients between the ROI-averaged FA of the extracellular compartment from each model and the ROI-averaged ODI from NODDI are listed in **Table 4.6**.

| Model (excluding extracellular compartment) | Core | | Periphery | |
|---|--------------|--------|--------------|--------------|
| | Zeppelin | Tensor | Zeppelin | Tensor |
| Ball-Sphere | -0.54 | -0.42 | -0.10 | -0.13 |
| Ball-Sphere with fixed dv | -0.49 | -0.38 | -0.34 | -0.16 |
| Ball-Sphere with FWE | -0.50 | -0.33 | -0.48 | -0.18 |
| Ball-Sphere with FWE and fixed dv | -0.44 | -0.34 | -0.50 | -0.51 |
| AstroSticks-Sphere | -0.60 | -0.37 | -0.34 | -0.11 |
| AstroSticks-Sphere with fixed dv | -0.20 | -0.18 | 0.01 | 0.04 |
| AstroSticks-Sphere with FWE | -0.55 | -0.30 | -0.45 | -0.41 |
| AstroSticks-Sphere with FWE and fixed dv | -0.44 | -0.06 | -0.51 | -0.27 |

Table 4.6 - Pearson correlation coefficient between the mean FA of the extracellular compartment of each model and the mean ODI from NODDI in the same area (core or periphery).

For each pair of models (equivalent except for the extracellular compartment, which is Zeppelin on one side and Tensor on the other) the strongest correlation is highlighted in bold.

4) Very high values of fvasc were often estimated in areas of high free water content in models without FWE and when using Ball (as opposed to AstroSticks) to model the vascular compartment. An example is shown in **Figure 4.3A**. To assess this observation quantitatively, we measured the percentage of voxels with fvasc > 0.9 for each model out of those with fiso > 0.5 in NODDI. The highest values were found for models with fixed diffusivity of the vascular compartment without FWE; FWE reduces the extent of this issue, especially when dv is fixed and the AstroSticks models seem to be more robust (**Figure 4.3B**).

Based on all the results above, the selected model was Zeppelin-AstroSticks-Sphere with FWE.

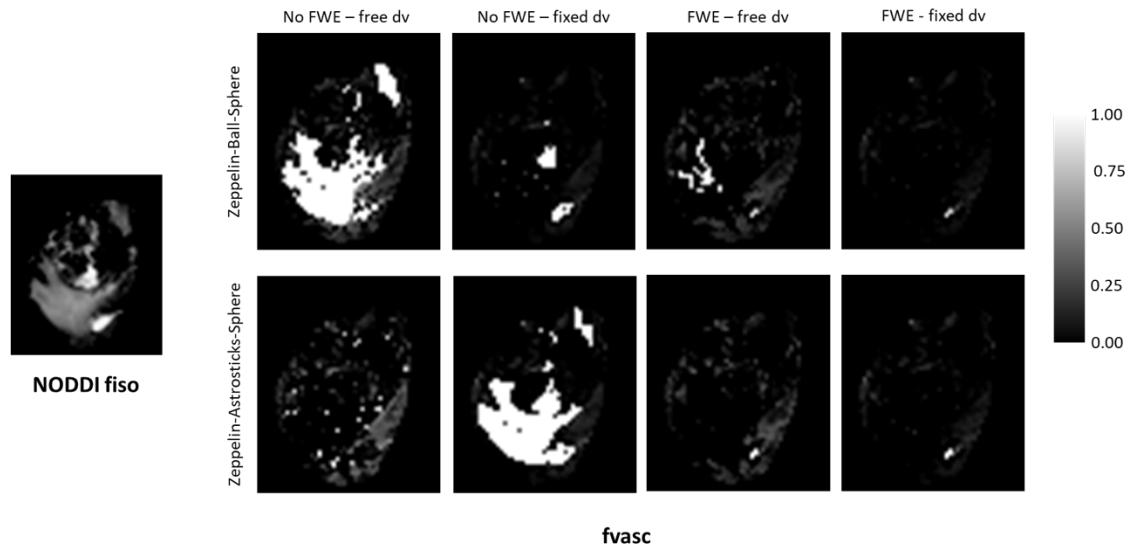


Figure 4.3 - Ambiguity between free water and pseudo-diffusion (vascularity).

Spurious high *fvasc* in areas with high water content and effect of FWE and fixing *dv*. In the top half, an example is shown where very high *fvasc* values were estimated by some of the considered models in an area of edema with high water content (see the free water fraction estimated by NODDI on the left). The bar graph in the bottom panel shows the percentage of voxels with *fvasc* > 0.9 out of those with *fiso* > 0.5, averaged among all patients, for the 4 considered VERDICT models.

4.4.3 Comparison between different histotypes

Boxplots of the VERDICT signal fractions in tumor cores for the different histotypes and grades are shown in **Figure 4.4** along with maps from representative cases. The median values of the intracellular fraction (*fic*) within the tumor core were significantly higher in metastases than in lower grade gliomas (WHO 2, $P = 0.0006$, and WHO 3, $P = 0.0013$) and glioblastomas ($P = 0.0027$), and there is a trend towards higher *fic* with

increasing grade. The extracellular fraction (fees) was significantly higher in WHO 2, WHO 3 and GBM than in metastases ($P = 0.0002$, 0.0007 and 0.0009 , respectively) and there is a trend towards higher fees in WHO2 than in WHO 3 and 4, although not significant ($P = 0.1142$, corrected for multiple comparisons). There is a trend towards decreasing free water fraction (ffw) going from GBM to WHO 3 and WHO 2. However, none of these differences is statistically significant. The radionecrosis case has a very high free water content and no vascular fraction, as expected.

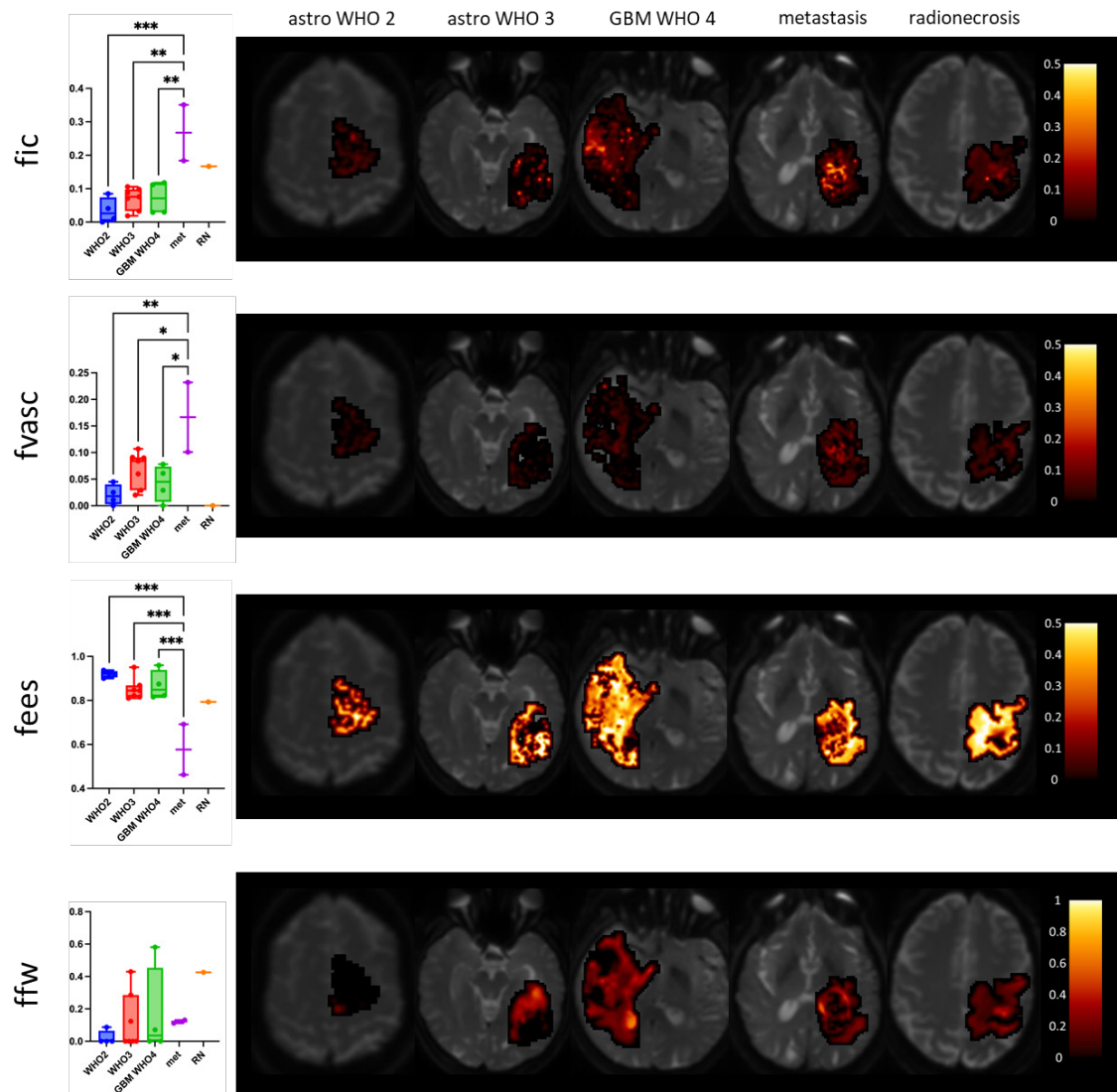


Figure 4.4 - VERDICT results in the tumor core in the whole patients' sample, according to histopathological classification

The boxplots on the left show the ROI median values in each patients group for the signal fraction of each compartment. Statistically significant differences are marked (* $p < 0.05$, ** $p < 0.01$, *** $p < 0.001$). Beside each plot, representative maps are shown for each group

Benign histotypes such as subependymoma WHO 1 and focal cortical dysplasia (**Figure 4.4**) have low fic values and high fees with low ffw and fvasc, as expected. Anaplastic ependymoma WHO 3 shows relatively high values of fic and low values of fees in the tumor core, consistent with the histological findings of high nuclear to cytoplasmic ratios and high mitotic activity with relatively low free water content and vascular fraction, consistent with the scarce microvascular proliferation and necrosis.

Boxplots of the free water fraction (ffw) and extracellular fraction (fees) in peritumoral areas for the different histotypes are shown in **Figure 4.5** along with maps from representative cases. Vasogenic oedemas around metastases had significantly higher ffw than the periphery of WHO 2 lesions ($P = 0.035$) and tended to have a larger ffw than infiltrative oedemas (around WHO 3 gliomas and GBM), and infiltrative oedemas tended to have a larger ffw than the periphery of WHO 2 lesions.

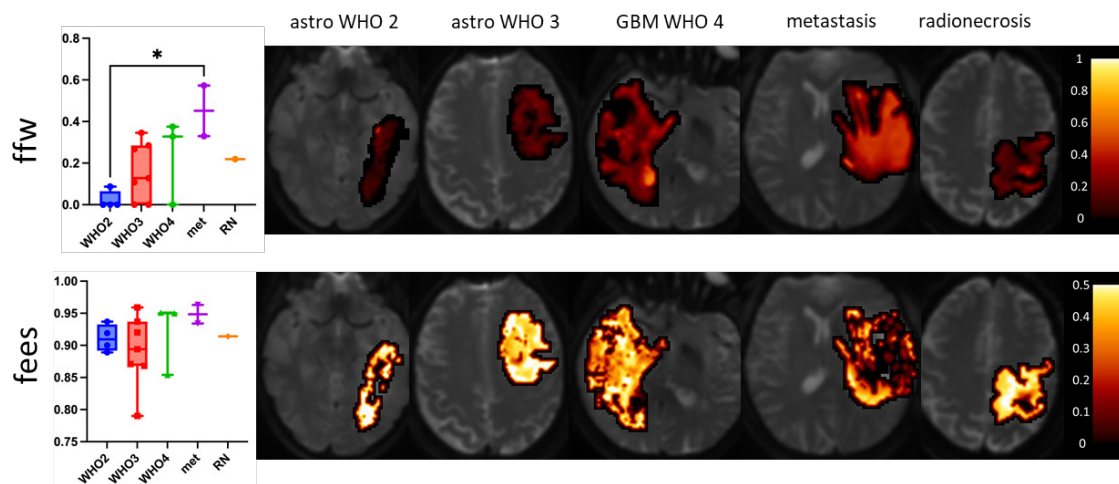


Figure 4.5 - VERDICT results in the peritumoral areas

The boxplots on the left show the ROI median values in each patients group for the signal fraction of each compartment. Statistically significant differences are marked ($* p < 0.05$). Beside each plot, representative maps are shown for each group

No significant differences in VERDICT-derived parameters were found between IDH-mutant and wild-type gliomas, although fic tends to be higher in the latter, as expected (**Figure 4.6**).

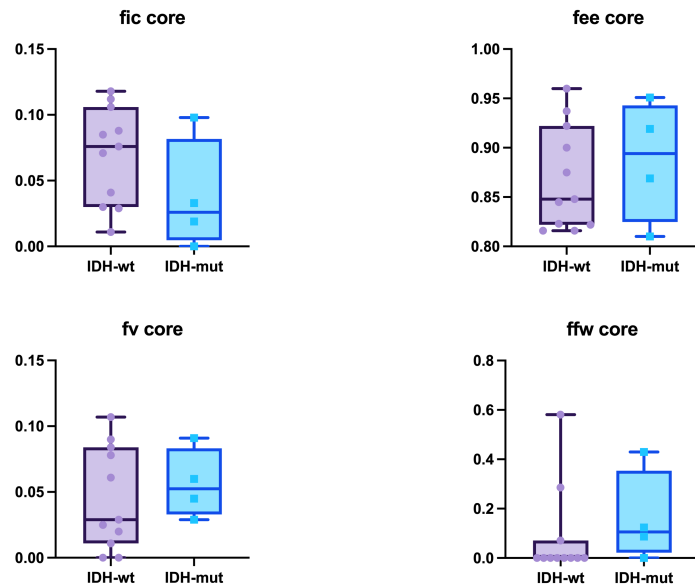


Figure 4.6 - VERDICT results in the tumor core in the whole patients' sample, according to IDH molecular status,

4.4.4 Correlation between VERDICT fv and PWI parameters

In Figure 4.7 the fvasc values from VERDICT are plotted against PWI-derived parameters rBV and vp in the core of each lesion. Pearson correlation test revealed statistically significant positive correlation between fvasc and Vp values ($r = 0.489$, $P = 0.046$), but not significant between fvasc and rBV values ($r = 0.313$, $P = 0.206$).

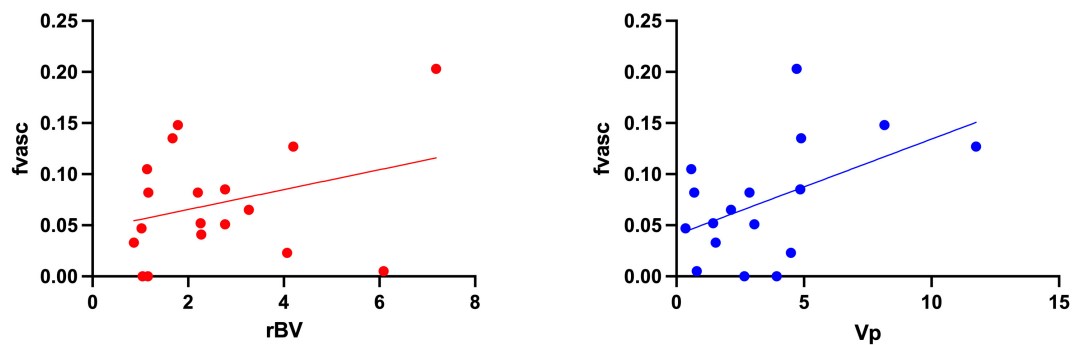


Figure 4.7 - Correlation between VERDICT fvasc and PWI metrics in the tumor core.

4.4.5 Comparison between histology and VERDICT maps

Figure 4.8 shows VERDICT maps and histology images from gross resection of a low-grade glioma and a metastasis. In the former case, VERDICT shows very low fic and fvasc, compatible with the low cellularity shown by histology. In the latter case,

VERDICT estimates areas of very high fic and fvasc in the core of the tumor, in agreement with the high cellularity typical of malignant tumors such as metastatic melanoma. The free water fraction is high in the peritumoral area (vasogenic edema) and in some intra-tumoral spots that may correspond to necrosis.

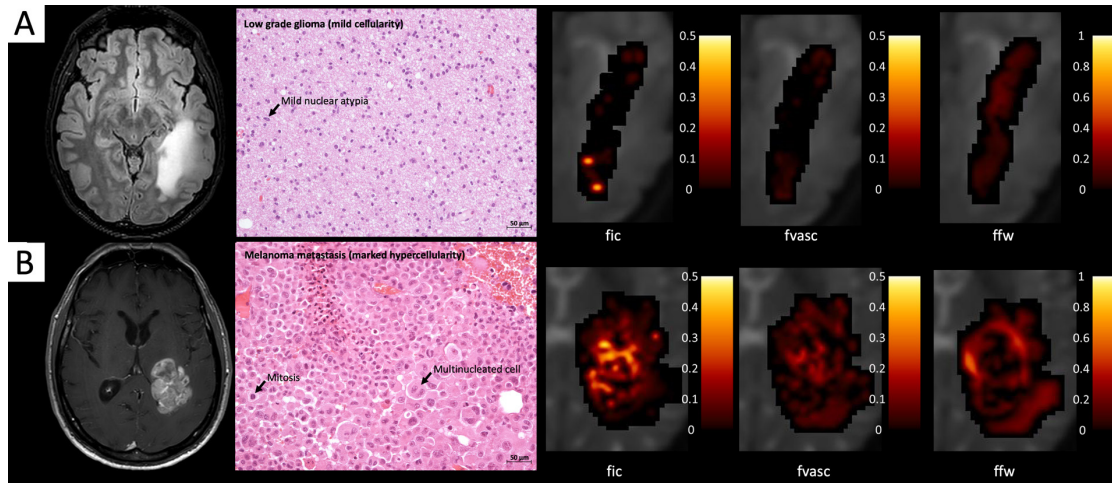


Figure 4.8 - Comparison between VERDICT maps and histology from gross resection.

(A) The first case (Patient 19) is a 19-year-old male patient who underwent surgical resection for a large left temporo-parietal low-grade astrocytoma (WHO II, IDH-1 mutated); the histopathology entails mild cellularity with the presence of fibrillary neoplastic astrocytes on a loose tumor matrix background; some mild nuclear atypias are identifiable. (B) The second case (Patient 4) underwent surgical removal for a large melanoma metastasis; histopathology shows marked hypercellularity with epithelioid cells with large nuclei, prominent nucleoli and abundant cytoplasm, interlaced by extravasated red blood cells.

Figure 4.9 shows VERDICT maps and histology images in multiple samples from stereotactic biopsy in two patients harboring high grade glioma. In the first case (patient 12), the fic values were higher in sample B, with histology features of high grade, than in A and C, with histology features of low grade and heterogeneous appearance respectively. The ffw values were highest in sample C, where histology showed some necrosis. In the second case (patient 3), fic was higher in sample A than in the other two, compatible with the higher grade shown by histology; fvasc was also slightly higher in sample A. ffw was low in sample A, intermediate in sample B and highest in sample C, compatible with the presence of edema as shown by anatomical MRI sequences.

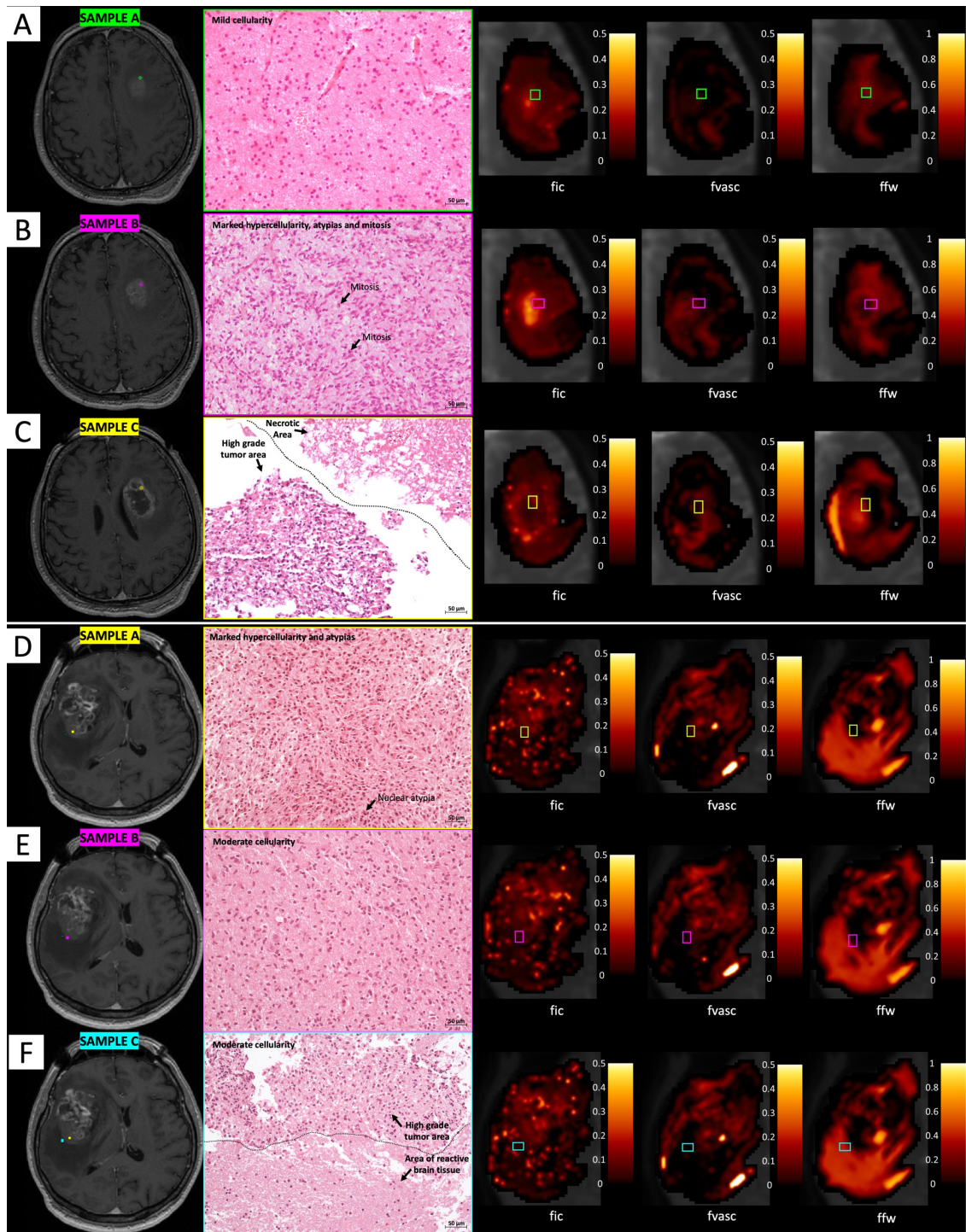


Figure 4.9 - Comparison between VERDICT maps and histology from stereotactic biopsies.

(A, B, C) The first case (patient 12) depicts a 58 year-old male patient who underwent stereotactic biopsy for a left frontal WHO IV glioblastoma (IDH-1 wild-type); from a histopathological point of view, sample A (A) was characterized by mild cellularity; the second bioptic sample (B) was performed in a higher grade tumor area, characterized by marker hypercellularity, atypias and mitotic figures; in the third sample (C) both necrotic and high grade tumor areas were identified.

(D, E, F) In the second case (patient 3), a 65-year-old male patient undergoing stereotactic biopsy for a right frontal WHO III anaplastic astrocytoma (IDH-1 wild-type) is represented. Histopathologically, the first sample (D) is characterized by marker hypercellularity and atypias; the second sample (E) entails areas of moderate cellularity; the last sample (F) shows areas of high-grade tumor adjacent to areas of reactive brain tissue with possible infiltration.

4.5 Discussion

This study developed and validated a microstructural model for brain tumors within the VERDICT framework. We focused on deriving estimates characterizing clinically relevant features such as cell density, vascularity, infiltration, and oedemas. We validated the VERDICT non-invasive estimates against histopathology from stereotactic biopsies in different types of tumors and peritumoral areas, and independent measures, such as plasma volume or cerebral blood volume from perfusion MRI.

We examined numerous diffusion models for the three VERDICT components. Following model selection, the best-performing model was Zeppelin-AstroSticks-Sphere with Free Water Elimination. To model the extracellular space, Zeppelin performed best, and we showed that it could characterize anisotropy in and around the lesions similarly to NODDI. As in VERDICT for body tumors (Panagiotaki *et al.*, 2015), AstroSticks was preferred to Ball for the vascular compartment. In particular, the Ball model tended to estimate high values of the vascular fraction in areas of significant free water content such as oedemas, where we don't expect any vascularity, meaning that the candidate model for vasculature could not reliably distinguish true diffusion with high diffusivity from pseudo-diffusion in vessels. Using AstroSticks rather than Ball in the vascular compartment helped reduce this ambiguity. To further address this phenomenon, we included a free water compartment to give the models enough flexibility to capture all the different aspects of the complex microstructure of brain tissue. Without increasing model complexity, we achieved this by using a two-stage Free Water Elimination approach; we fitted NODDI to the signal at higher b values to estimate the free water fraction, which was then fixed in the subsequent fitting of the full VERDICT model. This way, we effectively obtained four-compartment models without extra free parameters, and we showed that this improved the fitting performance, especially in peritumoral areas.

VERDICT maps reflected the main features shown by histology in low-grade cases and in the most aggressive metastases, and even differences between multiple biopsy samples in the same patients. Unfortunately, the biopsies were not planned specifically for this study and were performed only in a few patients; furthermore, the uncertainty in the localization of biopsy samples on morphological images and in the registration to dMRI images limited the spatial accuracy of the comparisons. More systematic

correlation studies will be carried out in the future, with localized quantification of histopathology. However, the qualitative comparison shown here holds great promise for the non-invasive characterization of brain tumors, as VERDICT could provide microstructural information not only about the entirety of each lesion, but also about the different areas of heterogeneous lesions. This would allow the identification of the most aggressive components, which would be fundamental in the context of surgery or treatment planning.

Our preliminary results comparing different histotypes showed that melanoma metastases had the highest intracellular and vascular fraction and the lowest extracellular fraction in the core, which we expected as these lesions are known to have particularly dense cell packing and high vascularity. Higher grade tumors also tended to have higher intracellular and vascular fractions and lower extracellular fractions than lower grades, as expected. In the radionecrosis case, the free water fraction was very high, showing that our VERDICT model is robust enough not to provide spurious cellularity or vascularity where no residual tissue is present. However, no significant difference was found in the free water fraction between the groups; as we focused on the solid component of lesions, larger areas of necrosis and cysts were not considered in the analysis, so only minor differences can be expected between grades. In the peritumoral areas, we observed a trend towards higher free water fraction in purely vasogenic oedemas compared to infiltrative oedemas. The patient population of this study was quite diverse, including several types of tumors and different histological features even within the same group; this allowed us to test VERDICT in a wide spectrum of conditions, but limited the number of lesions of each type and hence statistical significance. Future studies focusing on a few classes, but with a larger population, would be needed to assess the ability of VERDICT to differentiate brain tumor histotypes. We must also highlight that in this preliminary evaluation, we only compared ROI-averaged values, neglecting within-lesion variability in the comparison between tumor types. However, notwithstanding the limited statistical significance, the observed trends reflected the expected underlying microstructure. Assessing these differences would be clinically relevant, as it would allow characterizing tumor heterogeneity and microstructure non-invasively, giving clinicians very valuable information to plan surgery or bioptic procedures or to monitor the effectiveness of therapies.

Comparing the vascular VERDICT estimates f_{vasc} with independent perfusion MRI showed some correlation between... We found a certain degree of correlation between VERDICT vascular fraction and PWI-derived measures r_{BV} and v_p , but the correlation coefficient is not as high as it could be expected. We can speculate that this discrepancy may be due to the different mechanisms underlying PWI models and IVIM (Dolgorsuren *et al*, 2019; Federau, 2017; Le Bihan, 2019). Also, PWI and dMRI images had a different spatial resolution, and we can expect some degree of misregistration between r_{BV}/v_p and f_{vasc} maps, which might have contributed to decreasing the correlation.

Besides the relatively small and heterogeneous population, as discussed above, the main limitation of the current study is the long time needed for both acquisition and image processing, which would not be acceptable in a clinical context. The rich acquisition protocol was designed to allow us to fit an extended range of multi-compartment models to identify the appropriate VERDICT model for brain tumor tissue. Having identified the optimal model, we can now optimize the acquisition protocol using the procedure in (Alexander *et al*, 2008). We can expect that the number of diffusion directions may be reduced, as we found that Zeppelin is sufficient to characterize the extracellular anisotropy and we don't need more complex models. The next step is, therefore, to design multiple clinically feasible protocols and compare the results to those obtained from the extensive acquisition. The long time required for fitting was mainly due to our conservative choice of using the traditional non-linear least square optimization. In the next future, we will adopt machine-learning approaches, which will dramatically reduce the computation time and may also help avoiding local minima and regularize the parameter maps (de Almeida Martins *et al*, 2021; Grussu *et al*, 2020; Palombo *et al*, 2020). Machine learning could also be used for Free Water Elimination (Molina-Romero *et al*, 2018).

In conclusion, we optimized the VERDICT framework for the application to brain tumors, aimed at simultaneously characterizing cellular and vascular features non-invasively, both in the core of the lesions and in the surrounding tissue. Our model proved to be flexible and robust and gave promising preliminary results in agreement with histology, showing the potential for improving the management of brain tumor patients. The next steps will focus on optimizing the method for clinical standards with a shorter protocol and applying it to larger patient cohorts.

5 CLINICAL VALIDATION OF ADVANCED FUNCTIONAL IMAGING IN A LARGE GLIOMA SERIES.

In the third experiment of this thesis, the adoption of advanced functional MR imaging, using the most up-to-date DTI and task-based BOLD fMRI acquisition and elaboration techniques, in the pre- and intra-operative setting of a large series of consecutive patients undergoing surgical resection for brain gliomas at our Institution was evaluated. Moreover, the student developed and introduced in clinical practice an innovative imaging processing technique for the generation of detailed 3D-rendered anatomic-functional-pathological models using multi-modality datasets for preplanning in virtual reality and surgical simulation. The potential clinical application of the latter was also investigated, together with the effect of other imaging modalities such as modern neuronavigation systems and neuronavigated ultrasound systems. The impact of these techniques in terms of tumor's extent of resection (EOR), patient's functional status preservation, particularly in tumors located close to motor and language eloquent areas, and patient's overall survival (OS) was investigated.

5.1 Introduction

In brain tumors management, surgery remains, when feasible, the primary option, having the advantage to provide both histopathological diagnosis and cytoreduction prior to following therapies. Neurosurgical removal of cerebral neoplasms relies on a strict balance between achievement of maximum tumor resection and maximum functional preservation, since they are both related to treatment success and patient's prognosis (Dubey *et al.*, 2018). Tumor gross total removal (GTR) lower the risk of recurrence and allows a higher efficacy for subsequent chemo-radiotherapy (Chaichana *et al.*, 2014b; de Leeuw & Vogelbaum, 2019; Duffau, 2016, 2019; Eyupoglu *et al.*, 2016; Fujii *et al.*, 2018; Incekara *et al.*, 2020a; Karschnia *et al.*, 2021; Keles *et al.*, 2006; Li *et al.*, 2016; Marko *et al.*, 2014; Molinaro *et al.*, 2020; Nuno *et al.*, 2013; Oppenlander *et al.*, 2014; Orringer *et al.*, 2012; Pessina *et al.*, 2017; Sales *et al.*, 2019; Sanai *et al.*, 2011; Smith *et al.*, 2008; Stummer *et al.*, 2008; Wijnenga *et al.*, 2018); moreover, it is able to reduce symptoms

related to mass effect and cortical irritation, directly ameliorating patient's quality of life. On the other hand, the concurrent preservation of eloquent areas, such as those related to motor, language, or visual functions, is an additional variable significantly affecting patient's performance status and well-being and are therefore correlated too with overall survival (OS) and treatment success (Dubey *et al.*, 2018; Hervey-Jumper & Berger, 2014; Mandonnet *et al.*, 2007; Shalan *et al.*, 2021; Talos *et al.*, 2006).

At present, the gold standard to distinguish between tumoral tissue and functional brain areas relies on invasive methods such as histological analysis (multiple bioptic sampling, intraprocedural frozen sections) and cortical and subcortical mapping via direct electrical stimulation (DES), respectively. Unfortunately, being available only during the surgical procedure, not only these techniques are quite invasive (with possible related risks for the patients, such as seizures or intraoperative bleedings and neurological deficits) and time-consuming (since they do not provide a simultaneous, all-encompassing approach, but they rather require a repeated interruption of the resective procedure to perform a data collection, centimeter per centimeter, along the surgical margins), but they are also unable to provide information at the time of decision making, when the surgical approach is about to be planned, and the indications for resection have to be balanced with the perioperative risks and resective outcomes (Conti Nibali *et al.*, 2019; Costabile *et al.*, 2019; Duffau, 2007; Szelenyi *et al.*, 2010). Additionally, the occurrence of hemodynamic changes across wide areas of cerebral tissue (from 77 to 350 mm²) while performing DES has been reported, with effects not easily predictable as it involves several local and remote morphological and physiological aspects. Other aspects, like those related to instrumental, anesthesiologic and patients' conditions, can also alter the repeatability of the results. It is therefore deceiving to assume that DES alone can provide indisputable, objective data regarding the function of the mapped cerebral regions, and evidence suggests that improvements to this technique would be beneficial (Borchers *et al.*, 2012; Costabile *et al.*, 2019; Duffau, 2007; Szelenyi *et al.*, 2010).

In the last few years, the development and clinical adoption of new, advanced magnetic resonance imaging (aMRI) techniques such as fMRI and DTI Tractography have enriched and broadened our understanding of the functional pathways concealed deep within the brain, representing, to date, the most valuable imaging techniques to be implemented in

presurgical planning and intraoperative neuronavigation (Dubey *et al.*, 2018; Romano *et al.*, 2007; Shalan *et al.*, 2021).

Advanced diffusion MRI (dMRI) methods assess the physiological water directionality and motion and, by means of MR Tractography, provide images of relevant white matter tracts in the proximity of brain tumors, allowing to define the displacement, interruption, or infiltration of these tracts by the tumor itself.

fMRI has been reported to accurately identify eloquent cortices for motor and language function in the preoperative setting by using different stimulation paradigms. This task-based approach is very promising but has some drawbacks in clinical practice. Indeed, patient's task performance is often impaired due to language or cognitive deficits, making task-based functional mapping often difficult or impossible.

The assessment of the structural integrity and location of eloquent cortical and subcortical areas with respect to an intracranial lesion is pivotal in the planning of the surgical entry point through the cortex and the trajectory to be adopted inside the underlying white matter while reaching and resecting the neoplasm; moreover, this knowledge improves the neurosurgeon anatomical orientation towards functional areas to be spared during his/her commitment toward maximum tumor resection (Dubey *et al.*, 2018). Additionally, DTI and fMRI, providing a holistic portrait of cerebral connectivity and eloquent areas, hold the advantage of guiding DES to the proper target sites, possibly reducing intraoperative errors, the time needed for brain mapping and risk of seizures (Costabile *et al.*, 2019; Ostrý *et al.*, 2013; Vassal *et al.*, 2013).

5.2 Aims

The main goal of this project is to evaluate the clinical applications of advanced MRI techniques such as cutting-edge MR tractography and task-based functional MRI in the perioperative setting of a large series of patients undergoing resective surgery for brain gliomas. The clinical application of innovative image processing techniques generating detailed anatomic-functional-pathological 3D models for virtual reality and surgical planning/simulation, together with the utilization of intraoperative neuroimaging devices such as neuronavigation and ultrasound systems, will also be assessed in the same cohort and compared to the current gold standard, represented by DES and intraoperative neuromonitoring (IONM).

The clinical value of these advanced neuroimaging techniques will be evaluated in terms of their effect on:

- tumor's extent of resection (EOR)
- patient's functional status preservation, particularly in tumors located close to motor and language eloquent areas.
- patient's overall survival (OS)

Due to the remarkable heterogeneity of the sample (e.g., patients' age and preoperative clinical status, but also tumors size, contrast-enhancement, location, histological subtype, WHO grade, and molecular status), to thoroughly understand the impact of these advanced imaging methods on surgical and clinical results among different subpopulations, it was deemed necessary to perform a preliminary analysis describing the composition of the whole studied cohort and the general outcomes associated and to verify the influence of EOR on OS in the present series.

5.3 Materials and Methods

5.3.1 Patients

A retrospective study of 234 surgical procedures was performed on 226 patients affected by histologically confirmed brain gliomas. Patients included were admitted to San Raffaele Hospital for surgical treatment between January 2016 and December 2019; patients operated after that period were excluded to allow sufficient follow-up for the outcome analysis and due to the significant alterations of the clinical workflow that the Covid-19 outbreak generated in our center during the years 2020. Eligible patients included those with a pathologically confirmed diagnosis of brain glioma after surgical resection. Since all the histopathological diagnoses were performed between 2016 and 2019, tumors were classified according to the WHO 2016 classification (**Louis *et al.*, 2016**).

Male patients were 137 (61%), while females were 89 (39%). At the time of surgery, the median age was 55 years old (mean 52.5, range 8-82); seven patients were underage. Of the patients, 78% harbored a newly-diagnosed brain glioma, while 22% were undergoing redo-surgery for a recurrent one.

5.3.2 Data Collection

The pertinent literature was reviewed on the Pubmed database to identify the most significant variables to be collected and analyzed in the present series.

Patients' clinical data were retrieved from medical records registered in the prospectively collected databases of San Raffaele Hospital Neurosurgical department. In some cases, a telephone interview was necessary to complete missing information.

Histological diagnosis and molecular characteristics of the tumors were retrieved from the histological report.

A single anonymized database (each patient and procedure were automatically assigned a unique ID number) was created using the software Filemaker Pro Advanced v16 (FileMaker Inc., USA). Data were then exported as “.xlsx” files and imported into the statistical analysis software adopted (SPSS and R)

5.3.2.1 Clinical assessment

The first symptoms which led to the diagnosis were collected from anamnestic information. The present study registered a neurological examination at admission in the hospital, early postoperatively (within 24 hours from surgery), and at hospital discharge (median nine days after surgery). All patients were evaluated for motor, sensorial, visual, language, cranial nerves, and cerebellar functions, together with an analysis of orientation/cognitive functions and mood/behavior. Symptoms/signs after surgery were classified as improved, worsened, or unchanged.

Performance status was calculated before the surgical procedure and postoperatively (at hospital discharge) using the Karnofsky Performance Status (KPS) and Eastern Cooperative Oncology Group (ECOG) performance status.

Life status at the time of data collection was available after 224/234 procedures.

5.3.2.2 Morphological Imaging studies

DICOM images and neuroradiological reports from the following exams were collected and analyzed for all patients: preoperative MRI with and without gadolinium (performed less than 15 days from surgery), postoperative plain CT scan (performed

immediately at the end of the surgical procedure), postoperative MRI with and without gadolinium (performed less than 30 days from surgery).

5.3.2.3 *Advanced preoperative Imaging studies*

Preoperative advanced functional MRI exams were acquired on a 3T Ingenia CX scanner (Philips Healthcare, Best, The Netherlands) at the IRCCS San Raffaele Hospital Neuroradiology and CERMAC Department. Seventy-one patients underwent advanced probabilistic MR tractography reconstructions of relevant white matter tracts, using dedicated software (as previously described (Altabella *et al.*, 2018; Pieri *et al.*, 2021; Sanvito *et al.*, 2020)) after High Angular Resolution Diffusion Imaging (HARDI) acquisitions; the latter was obtained using an axial Single-Shot Spin-Echo Planar Imaging (EPI) sequence with gradients of diffusion applied along 60 non-collinear directions (b-value, 3000 s/mm²; TR=12000 ms, TE=74 ms; SENSE reduction factor, R=2; in-plane resolution, 1.87 × 1.87 mm²; 50 slices; thickness, 2.5 without gap; FOV, 240 mm; matrix, 128 × 128; acquisition time, 13 min)(Sanvito *et al.*, 2020). The following tracts were elaborated according to tumor location: corticospinal (89%), arcuate (62%), visual (44%), uncinate (25%), cingulate (21%), inferior fronto-occipital (35%), sensory (14%), superior longitudinal (14%), fornix (7%) and aslant (4%). Task-based fMRI was acquired in 41 patients; data were based on blood oxygenation level-dependent (BOLD) contrast obtained using T2*-weighted Gradient-Echo EPI (GE-EPI) sequences (TR=3700 ms, TE=30 ms; flip angle, 85°; FOV, 240 mm; matrix, 128 × 128; in-plane resolution 1.87 × 1.87 mm²; 32 slices; thickness, 4 mm; SENSE factor R = 2 (Sanvito *et al.*, 2020). Tasks were selected depending on the location of the lesion and patients' preoperative neurological status (Black *et al.*, 2017; Castellano *et al.*, 2017). Naming consisted in the denomination of a sequence of common objects those pictures were shown to the patient; auditory verb generation consisted in the formulation of the proper verb related to a given noun; verbal fluency consisted in the listing of all the possible names starting with a given letter of the alphabet; hand activation was generally based on the finger-tapping task, the mouth was assessed on lip movements. Fluency was analyzed in 62% of cases, hand activation in 48%, verb generation in 50%, mouth activation in 31%, naming in 33%, and foot activation in 26%.

A concomitant axial volumetric FLAIR (TR = 9000, TE = 285, IT = 2500, flip angle 90°, matrix, 204 × 204, slices; thickness 1.2 without gap, SENSE reduction factor R = 2, acquisition duration 5 min and 25 seconds) and a sagittal 3D T1-weighted sequence after gadolinium injection (TR = 11.2 ms, TE = 5.4 ms, flip angle, 8°; 236 slices; thickness, 0.9 without gap; matrix, 284 × 190; SENSE reduction factor R = 2; acquisition time 5 min 36 seconds) were also acquired in the same session.

5.3.2.4 Import of advanced imaging in the neuronavigation system

Due to the unfeasibility of direct import of the models generated with advanced DTI and fMRI software into the neuronavigation and neurosurgical planning systems, a dedicated pipeline was developed. Each elaborated fiber tract and task-related fMRI activation was exported as high-intensity blobs in separated DICOM series, using the 3D Flair concurrently acquired as the reference sequence. Then a 3D model of the object was created into the 3D preplanning software and the Neuronavigation system using the “threshold” function to select all the high-intensity voxels of the blobs (**Figure 5.1**). All the different acquired images were coregistered in the neuronavigation and preplanning system through rigid co-registration algorithms using the 3D-T1 contrast-enhanced sequence (or a preoperative volumetric CT scan when available) as reference. Intraoperative patients’ coordinates were acquired for neuronavigation using an optical tracking technology (Medtronic StealthStation® S7®). Neuronavigation accuracy was assessed using known anatomical landmarks before sterile draping, prior to craniotomy, after dural opening, and throughout repetitive checks, until the final resection state was achieved.

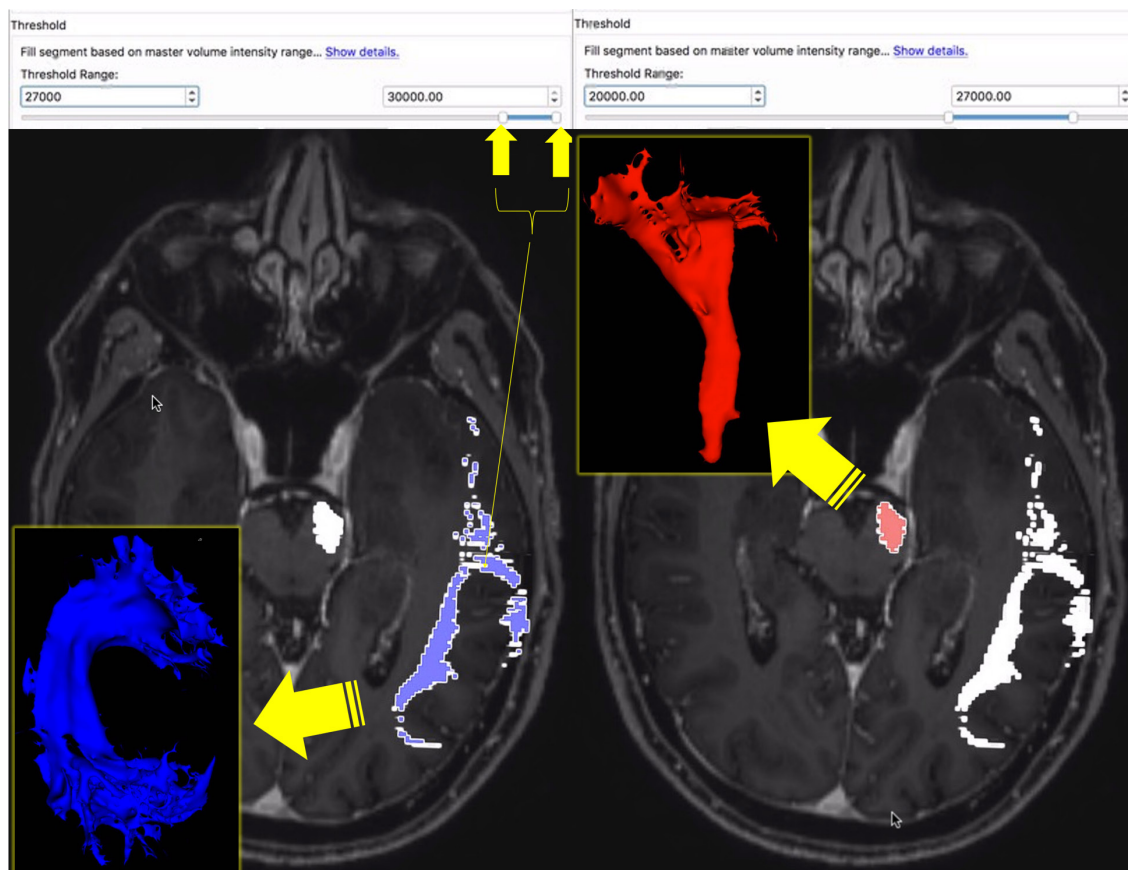


Figure 5.1 - Workaround utilized to extrapolate volumes-of-interest from DTI and fMRI outputs to be integrated into neurosurgical 3D preplanning and neuronavigation systems.

Elaborated fiber tract and task-related BOLD fMRI activation were exported as high-intensity blobs, each one in a separate DICOM series, using the concurrently acquired, 3D Flair as the reference sequence. Then a 3D model of the object was generated into the 3D preplanning software and the Neuronavigation system using the “threshold” function to select all the high-intensity voxels of the blobs.

5.3.2.5 Surgical procedure

All patients evaluated underwent craniotomy (craniectomy in the event of posterior fossa tumors) with resection under microscopic magnification (Zeiss OPMI Pentero 900 microscope). The following data were collected: date of hospital admission, duration of hospital stay, type of anesthesia (general anesthesia or awake procedure), duration of the preoperative phase (minutes from the patient entrance in the operating room to first skin incision), duration of the surgical procedure (minutes from first skin incision to the apposition of the last suture stitch), preoperative acquisition of advanced functional neuroimaging (DTI, fMRI), advanced preplanning of the surgical procedure with 3D reconstruction, use of intraoperative imaging and monitoring tools (neuronavigation, ultrasound, intraoperative neurophysiological monitoring).

The neuronavigation system (Medtronic StealthStation® S7®) was adopted in 150 patients, a neuronavigated intraoperative ultrasound (Esaote MyLab™Twice) was utilized in 152 patients, while 49 patients received intraoperative neurophysiological monitoring (IONM). Advanced preplanning of the surgical procedure with the 3D reconstruction of a detailed anatomic-functional-pathological model was performed in 63 patients using the open-source and multi-platform software 3D Slicer.

Eighteen patients (median age 48 years old, range 27-70) harboring tumors close to eloquent areas (left hemisphere was involved in 89% of the cases) and without contraindications (unwilling/non-cooperative patient, very large tumors, obesity, psychiatric disorders, claustrophobia, uncontrolled seizures, severely impaired motor/speech function or neurocognitive issues as dementia or mental retardation), were considered for awake craniotomies. A specific protocol for the intraoperative setting of awake surgery was developed: a particular effort was dedicated to achieving optimal anesthesia planning and the best positioning of the patient, involving different specialists and various instrumentations.

Direct electric stimulation (DES) to map the brain functions was performed with the intraoperative assistance of the Neurophysiology team, through a bipolar or monopolar (for subcortical and cortical assessment, respectively) electrode with typical use of a biphasic current (50-60 Hz): 1-6mA in an awake patient, higher amplitude under general anesthesia (<12-15mA). Muscle action potentials (cMAPs) from multiple muscles were recorded during DES (Ferguson & McCutcheon, 2018). Language mapping was obtained with an awake patient performing tests identified in preoperative neuropsychological evaluation (Saito *et al*, 2018). Stimulation was alternated with tumor removal until a response was clearly detected and maximum safe resection was achieved.

5.3.2.6 *Assessment of Tumor volume and Extent of resection (EOR).*

The extent of resection (EOR) was calculated after coregistering all the available imaging in the neurosurgical planning software Brainlab® Elements (BrainLAB AG, Munich, Germany). The preoperative and postoperative tumor volumes (expressed in cm³) were segmented semi-automatically with the “smartbrush” tool in the following way: the tumor is first manually segmented on one MRI slice, then, a second manual segmentation is performed on a different plane; then the software automatically generates

the full 3D volume-of-interest. Subsequently, the volume of interest was carefully checked slice by slice and, where necessary, manually adjusted using the “paintbrush” tool, which allows drawing the lesion using multiple reconstruction planes (axial, coronal, and sagittal) and multiple imaging sequences/modalities at once. 3D-T1 contrast-enhanced MR exams were utilized to segment the contrast-enhanced component of the tumor (when present), defined as “*CE-tumor*”. “*FLAIR-tumor*” was defined as the segmented volume based on T2/Flair-weighted signal hyperintensity, and it also included the *CE-tumor* component previously segmented.

Postoperative *CE-* and *FLAIR-tumor* were then segmented, after importing postoperative radiological studies in the same dataset, with the aid of the first available MRI post-surgery (acquired < 30 days from the intervention), and the CT took immediately after the surgical procedure; coregistered preoperative tumor volumes were also used as a helpful reference in the definition of the postoperative remnants. The extent of resection (EOR) was then calculated mathematically (for both *CE-* and *FLAIR-tumor* components) as a rate of postoperative tumor volume over the preoperative one.

5.3.2.7 *Advanced preplanning of the surgical procedure with 3D reconstruction*

After an accurate analysis of image-processing platforms available, 3D Slicer (Fedorov *et al.*, 2012; Kikinis & Pieper, 2011) was identified as the most suited for the purpose of this project due to its free license, high flexibility, large validation in literature, and the great number of features and sub-applications available. All different MR and CT sequences acquired were imported into a single dataset for each patient and coregistered via rigid algorithms (6 degrees of freedoms, linear interpolation mode, percentage of samples = 0.01) using the most recent preoperative 3D T1 contrast-enhanced MR sequence as coordinates reference. Skull segmentation was extrapolated from preoperative plain CT images using the threshold algorithm; brain masked sequences (including only the signal from the intracranial content) were subsequently generated from both 3D-T1 contrast-enhanced and 3D Flair sequences. Tumor, brain, and ventricles were segmented using semi-automated algorithms with subsequent manual verification and possible correction; they were then displayed (with different key colors and different grades of transparency) in the 3D view using the geometric surface rendering technique. BOLD fMRI areas of activation and eloquent fibers generated from MR tractography

were imported as high-intensity blobs “burned” in a 3D Flair reference sequence and extrapolated using the “threshold” algorithm to generate corresponding 3D models.

A direct volume rendering of the brain-masked 3D T1 contrast-enhanced sequence was plotted, using the appropriate windowing, in order to display only the cortical and subcortical vascular anatomy. The final relationship between tumor, critical anatomical structures (as vessels), and functional areas (as identified on advanced functional MR studies) was then carefully inspected via multiplanar and three-dimensional reconstruction of the anatomic-functional-pathologic model generated in order to understand their relations and simulate in advance the best surgical approach and strategy (see **Figure 5.2**).

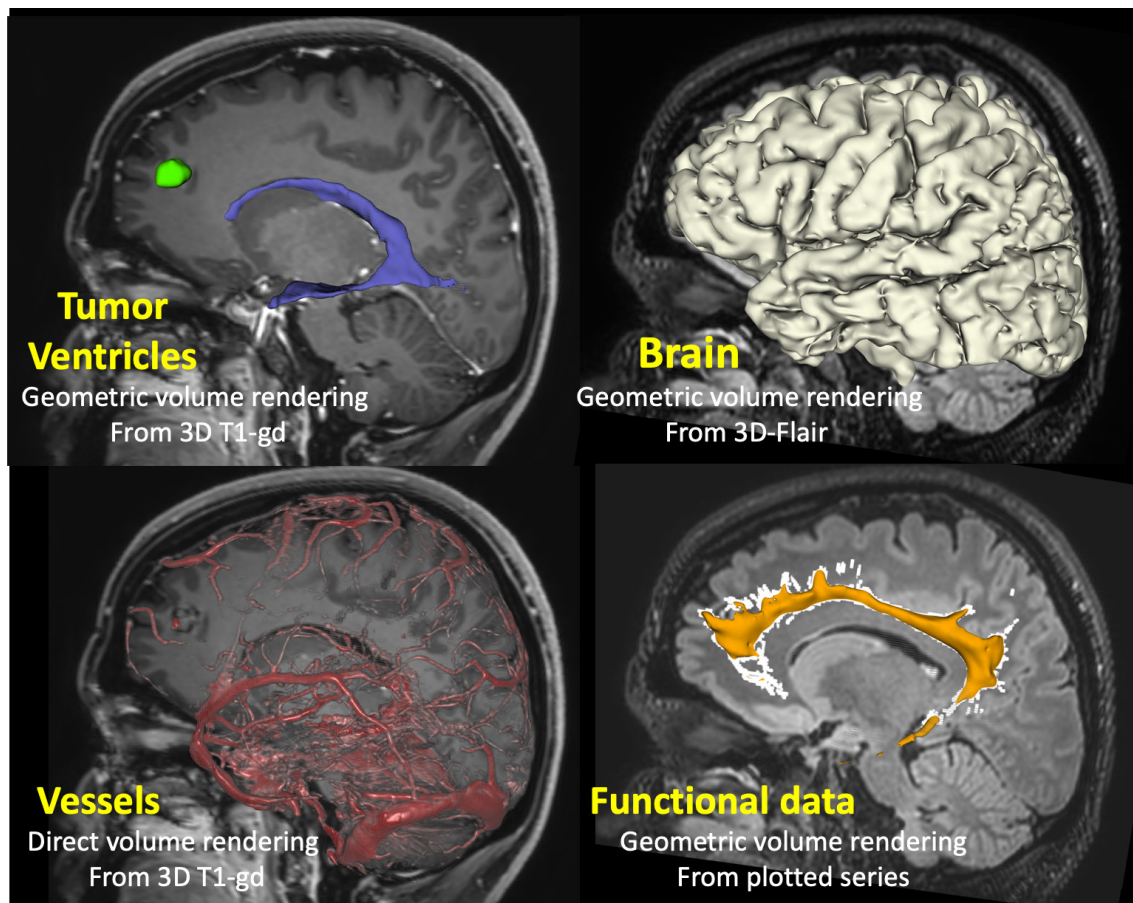


Figure 5.2 - Generation of the different volumes-of-interest for 3D representation in virtual reality
Diverse imaging datasets and rendering techniques (direct and geometric volume rendering) are utilized according to the structure to be represented.

5.3.3 Statistical Analysis

Statistical analysis and graphs were performed using SPSS Version 24.0 (IBM Corp, Armonk, NY, USA) and R (R Core Team, 2020), package ggplot2 (H. Wickham, 2016), survival (v3.2-7; Therneau, 2020), caret (M. Kuhn, 2021). A p-value ≤ 0.05 (95% confidence interval) was considered statistically significant unless otherwise specified.

Normality of the continuous variable was estimated through visual inspection of density and QQ-plots and formally assessed through Shapiro-Wilk's test.

The relationship between categorical variables was determined using Pearson's Chi-squared test or Fisher exact test (if expected cell frequencies were lower than five). The distributions of continuous variables between two groups determined by an independent variable were assessed with either the Student t-test or the Mann-Whitney U test according to whether the distribution was normal or not. Wilcoxon signed-rank was also used for paired or matched observations. The distribution of continuous variables between three or more groups determined by an independent variable was evaluated through ANOVA or Kruskal-Wallis rank-sum test, depending on the distribution of the continuous variable analyzed. Post-hoc analyses were undergone using Tukey HSD or Dunn's procedure and Bonferroni p-values adjustment.

We conducted Kaplan-Meier survival analyses to evaluate the impact of different variables (acquisition of preoperative DTI or fMRI, advanced 3D imaging preplanning, achievement of different cut-offs of EOR and residual postoperative tumor volume, use of intraoperative neuronavigation, intraoperative ultrasound, intraoperative neurophysiological monitoring) on overall survival (defined as the time from surgical procedure to patient's death or censorship). Log-rank, Breslow, and Tarone-Ware tests were undertaken to evaluate differences, at different time points, in the survival distributions between groups of patients stratified according to preoperative and postoperative features. The log-rank method was performed to detect differences between the curves late in the time period of the study, the Breslow method was performed to look for early differences, and the Tarone-Ware method was used as an intermediate strategy.

Multivariate analyses, applying the ENTER method, were eventually performed: linear regression was used to assess continuous dependent variables (*CE-tumor* EOR, *FLAIR-tumor* EOR), logistic regression to assess dichotomous dependent variables (achievement of *CE-tumor* gross total resection, achievement of *CE-tumor* postoperative

residual volume $<2 \text{ cm}^2$, achievement of 75% *FLAIR*-tumor EOR rate, achievement of *FLAIR*-tumor postoperative residual volume $<5 \text{ cm}^2$, occurrence of postoperative clinical improvement in any function, occurrence of postoperative clinical deterioration in any function, occurrence of postoperative KPS deterioration, occurrence of postoperative persistent language function deterioration, occurrence of postoperative persistent motor function deterioration), and Cox regression to assess overall survival (OS). Input variables were chosen beforehand to avoid overfitting, regardless of their possible significance in the present series at univariate analysis, since they have been proved as significant prognostic factors for clinical and radiological outcome at multivariate analysis in previous studies with large cohorts; the covariates put in the model were the following: patient's age at the time the surgical procedure, patient's sex, tumor's WHO 2016 grade, surgical status (first surgery in a newly diagnosed glioma or redo surgery for a recurrent one), IDH-1 status, number of brain lobes/regions involved by the tumor, presence of a midline (or deep located) tumor, tumor location close to language functional area (maximum distance $< 2 \text{ cm}$ from estimated location of Broca's area, Wernicke's areas and/or left arcuate fasciculus), tumor location close to motor functional area (maximum distance $< 2 \text{ cm}$ from estimated location of primary motor cortex and/or corticospinal tract), preoperative *FLAIR*-tumor volume, preoperative *CE-tumor* volume, use of intraoperative neuro-monitoring and cortical/subcortical stimulation, preoperative Karnofsky Performance Status, presence of a preoperative language deficit, presence of a preoperative motor deficit. The following covariates were also added to the model since they represented the main variables of interest to be assessed according to the aims of the present study: use of intraoperative neuronavigation, use of intraoperative ultrasound, preoperative Diffusion Tensor Imaging acquisition with fiber tracking, preoperative task-based BOLD functional MR acquisition, preoperative advanced 3D imaging preplanning.

A second Cox regression analysis was also performed to additionally assess the impact of variables related to the clinical and radiological postoperative outcome on OS using the following covariates: postoperative residual *CE-tumor*, achievement of *CE-tumor* gross total resection, achievement of *CE-tumor* postoperative residual volume $<2 \text{ cm}^2$, postoperative *FLAIR*-tumor residual, achievement of 75% *FLAIR*-tumor EOR rate, achievement of *FLAIR*-tumor postoperative residual volume $<5 \text{ cm}^2$, achievement of *FLAIR*-tumor postoperative residual volume $<25 \text{ cm}^2$, occurrence of postoperative

clinical deterioration in any function, postoperative Karnofsky Performance Status, the occurrence of postoperative language function deterioration, the occurrence of postoperative motor function deterioration.

Regarding the multiple regression models, linearity was assessed by visual inspection of partial regression plots and of scatterplots of the studentized residuals against the predicted values. Continuous Independent variables were log-transformed where necessary. The independence of residuals was confirmed by Durbin-Watson statistics. Homoscedasticity was estimated by visual inspection of plots of studentized residuals versus unstandardized predicted values. The presence of multicollinearity was evaluated via the inspection of the variance inflation factors. Unusual points were defined through studentized residuals ($SD \pm 3$), their influence in the model was further evaluated via leverage values (> 0.2) and Cook's distance (> 1). The assumption of normality of the residuals was tested via Q-Q plot; if not met, a new model was built after transforming the dependent variable via a squared or log transformation, as appropriate.

In the binomial logistic regression models, the assumption of linearity of the logit (linear relationship between continuous independent variables and the logit of the dependent variable) was assessed via the Box-Tidwell procedure, if not met, power transformation of the specific independent variables were done, according to lambda value calculated via the same procedure. Unusual points and multicollinearity were evaluated as described above.

To assess whether the Cox regression models were adequate, three assumptions were tested. The proportional hazard assumption was confirmed through visual inspection of plots of the Schoenfeld residuals against time. Linearity of the continuous covariates was evaluated via visual inspection of plots of the Martingale residuals against continuous covariates. Unusual points were detected as described above.

The models which did not meet the assumption after appropriate transformations of the variables were reported but not further described.

5.4 Results

5.4.1 Patients

A total of 234 surgical procedures among 226 patients affected from histologically confirmed brain glioma were analyzed in the present study.

Since all the histopathological diagnoses were performed between the beginning of 2016 and the end of 2019, tumors were classified according to the WHO 2016 classification. Tumor gradings and subtypes are reported in **Table 5.1** and **Table 5.2**, respectively.

| WHO 2016 Grade | Cases included in the series | |
|----------------|------------------------------|-------|
| | n | % |
| I | 21 | 9.0% |
| II | 49 | 20.9% |
| III | 43 | 18.4% |
| IV | 121 | 51.7% |

Table 5.1 - Tumors' grade according to WHO 2016 classification.

Glioblastoma (GBL, WHO IV) was the most common subtype (representing about a half of the considered cohort), being IDH-1 wild type in 86% of the cases. Other relatively common histologies were Anaplastic Astrocytoma (WHO III), Diffuse Astrocytoma (WHO II), and Oligodendroglioma (WHO II), each representing about 10% of the population. Tumors classified as WHO grade II or III represented, each, around 20% of the cohort. Ten percent of the cases were classified as WHO grade I tumors, with Pilocytic Astrocytoma being the most common histology (3.8%).

| WHO 2016 Classification | | Cases included in the series | | IDH-1 status | | |
|------------------------------|---------|------------------------------|-------|--------------|-----|-------|
| Histopathological Subtypes | Grading | n | % | status | n | % |
| Glioblastoma | IV | 119 | 50.9% | WT | 102 | 43.6% |
| | | | | Mut | 10 | 4.3% |
| | | | | N/A | 7 | 3.0% |
| Diffuse Astrocytoma | II | 22 | 9.4% | WT | 11 | 4.7% |
| | | | | Mut | 11 | 4.7% |
| | | | | N/A | 0 | 0.0% |
| Anaplastic Astrocytoma | III | 21 | 9.0% | WT | 13 | 5.6% |
| | | | | Mut | 7 | 3.0% |
| | | | | N/A | 1 | 0.4% |
| Oligodendroglioma | II | 17 | 7.3% | WT | 3 | 1.3% |
| | | | | Mut | 14 | 6.0% |
| | | | | N/A | 0 | 0.0% |
| Anaplastic Oligodendroglioma | III | 13 | 5.6% | WT | 4 | 1.7% |
| | | | | Mut | 9 | 3.8% |
| | | | | N/A | 0 | 0.0% |
| Pilocytic Astrocytoma | I | 9 | 3.8% | WT | 3 | 1.3% |
| | | | | Mut | 0 | 0.0% |
| | | | | N/A | 6 | 2.6% |
| Oligoastrocytoma | II | 8 | 3.4% | WT | 2 | 0.9% |

| | | | | | | |
|---|------------|-----|------|-----|-----|-------|
| | | | | Mut | 6 | 2.6% |
| | | | | N/A | 0 | 0.0% |
| Dysembryoplastic Neuroepithelial tumor | I | 6 | 2.6% | WT | 5 | 2.1% |
| | | | | Mut | 1 | 0.4% |
| | | | | N/A | 0 | 0.0% |
| Anaplastic Oligoastrocytoma | III | 6 | 2.6% | WT | 3 | 1.3% |
| | | | | Mut | 3 | 1.3% |
| | | | | N/A | 0 | 0.0% |
| Subependymoma | I | 2 | 0.9% | WT | 0 | 0.0% |
| | | | | Mut | 0 | 0.0% |
| | | | | N/A | 2 | 0.9% |
| Ganglioglioma | I | 2 | 0.9% | WT | 2 | 0.9% |
| | | | | Mut | 0 | 0.0% |
| | | | | N/A | 0 | 0.0% |
| Anaplastic Ganglioglioma | III | 2 | 0.9% | WT | 2 | 0.9% |
| | | | | Mut | 0 | 0.0% |
| | | | | N/A | 0 | 0.0% |
| Subependymal giant cell Astrocytoma | I | 1 | 0.4% | WT | 1 | 0.4% |
| | | | | Mut | 0 | 0.0% |
| | | | | N/A | 0 | 0.0% |
| Pleomorphic Xanthoastrocytoma | II | 1 | 0.4% | WT | 1 | 0.4% |
| | | | | Mut | 0 | 0.0% |
| | | | | N/A | 0 | 0.0% |
| Gliosarcoma | IV | 1 | 0.4% | WT | 1 | 0.4% |
| | | | | Mut | 0 | 0.0% |
| | | | | N/A | 0 | 0.0% |
| Ependymoma | II | 1 | 0.4% | WT | 0 | 0.0% |
| | | | | Mut | 0 | 0.0% |
| | | | | N/A | 1 | 0.4% |
| Diffuse midline glioma H3 K27M-mutant | IV | 1 | 0.4% | WT | 1 | 0.4% |
| | | | | Mut | 0 | 0.0% |
| | | | | N/A | 0 | 0.0% |
| Desmoplastic infantile Astrocytoma | I | 1 | 0.4% | WT | 0 | 0.0% |
| | | | | Mut | 0 | 0.0% |
| | | | | N/A | 1 | 0.4% |
| Anaplastic Ependymoma | III | 1 | 0.4% | WT | 0 | 0.0% |
| | | | | Mut | 0 | 0.0% |
| | | | | N/A | 1 | 0.4% |
| TOTAL | | 234 | 100% | WT | 154 | 65.8% |
| | | | | Mut | 61 | 26.1% |
| | | | | N/A | 19 | 8.1% |

Table 5.2 - Distribution of different tumor subtypes.

Since all the histopathological diagnoses were performed between 2016 and 2019, tumors were classified according to the WHO 2016 classification

In the present cohort, 183 patients (78% overall) harbored a newly diagnosed glioma undergoing the first surgical attempt. Among the 51 recurrent cases recruited in the series: 42 (82%) maintained their previous WHO grade, while 9 (18%) embodied a malignant degeneration to secondary Glioblastoma.

5.4.1.1 Clinical evaluation

Neurological signs/symptoms registered at hospital admission are reported in **Table 5.3**. **Table 5.4** reports the rate of patients improved or worsened in each functional field, compared to the preoperative status, at two different time points (early postoperatively

and at hospital discharge). The most common postoperative morbidity still present at hospital discharge was related to motor function (7.3%).

| Preoperative impairment at hospital admission | WHO 2016 Grade | | | | | | | | | | Difference among grades (Chi-square) |
|---|----------------|-------|----------------|-------|-----------------|-------|-----------------|-------|----------------------|-------|--------------------------------------|
| | I (n = 22) | | II (n = 47) | | III (n = 43) | | IV (n = 120) | | Overall (n = 234) | | |
| | n | % | n | % | n | % | n | % | n | % | |
| Motor | 4 | 18.2% | 10 | 20.8% | 13 | 29.5% | 55 | 45.8% | 82 | 35.0% | p = 0.003 |
| Cranial nerves ^{vii} | 3 | 13.6% | 7 | 14.6% | 10 | 22.7% | 32 | 26.7% | 52 | 22.2% | p = 0.268 |
| Language | 0 | 0.0% | 4 | 8.3% | 6 | 13.6% | 35 | 29.2% | 45 | 19.2% | p = 0.001 |
| Sensory | 1 | 4.5% | 4 | 8.3% | 7 | 15.9% | 25 | 20.8% | 37 | 15.8% | p = 0.094 |
| Visual | 1 | 4.5% | 3 | 6.3% | 4 | 9.1% | 26 | 21.7% | 34 | 14.5% | p = 0.016 |
| Orientation / Cognitive | 1 | 4.5% | 2 | 4.2% | 5 | 11.4% | 21 | 17.5% | 29 | 12.4% | p = 0.067 |
| Behavior / Mood | 1 | 4.5% | 3 | 6.3% | 5 | 11.4% | 13 | 10.8% | 22 | 9.4% | p = 0.647 |
| Cerebellar | 6 | 27.3% | 2 | 4.2% | 0 | 0.0% | 3 | 2.5% | 11 | 4.7% | p < 0.001 |

Table 5.3 - Symptoms/signs assessed at hospital admission according to WHO grade.

^{vii} Most cranial nerve impairments, particularly among high grade gliomas, were central facial nerve deficit.

| Function assessed | Preoperative impairment prevalence | | Early postoperative (<24h) (compared to admission) | | | | | | At Hospital discharge (compared to admission) | | | | | |
|-----------------------|------------------------------------|-------|--|-------|----------|------|----------|-------|---|-------|----------|-------|----------|------|
| | | | Unchanged | | Improved | | Worsened | | Unchanged | | Improved | | Worsened | |
| | n | % | n | % | n | % | n | % | n | % | n | % | n | % |
| Motor | 82 | 35.0% | 187 | 79.9% | 10 | 4.3% | 37 | 15.8% | 174 | 74.4% | 43 | 18.4% | 17 | 7.3% |
| Cranial nerves | 52 | 22.2% | 222 | 94.9% | 2 | 0.9% | 10 | 4.3% | 221 | 94.4% | 8 | 3.4% | 5 | 2.1% |
| Language | 45 | 19.2% | 208 | 88.9% | 3 | 1.3% | 23 | 9.8% | 210 | 89.7% | 18 | 7.7% | 6 | 2.6% |
| Sensitive | 37 | 15.8% | 218 | 93.2% | 4 | 1.7% | 12 | 5.1% | 217 | 92.7% | 12 | 5.1% | 5 | 2.1% |
| Visual | 34 | 14.5% | 219 | 93.6% | 0 | 0.0% | 15 | 6.4% | 221 | 94.4% | 0 | 0.0% | 13 | 5.6% |
| Orientation/Cognitive | 29 | 12.4% | 223 | 95.3% | 0 | 0.0% | 11 | 4.7% | 224 | 95.7% | 8 | 3.4% | 2 | 0.9% |
| Behavior/Mood | 22 | 9.4% | 220 | 94.0% | 0 | 0.0% | 14 | 6.0% | 221 | 94.4% | 5 | 2.1% | 8 | 3.4% |
| Cerebellar | 11 | 4.7% | 229 | 97.9% | 0 | 0.0% | 5 | 2.1% | 228 | 97.4% | 5 | 2.1% | 1 | 0.4% |

Table 5.4 - Signs/symptoms assessed at hospital admission, early postoperatively (within 24 hours from surgery), and at hospital discharge.

5.4.2 Preoperative tumor characteristics.

FLAIR-tumor and CE-tumor according to WHO grade are reported in Table 5.5. No significant correlations were found between FLAIR- and CE-tumor volumes and OS among different tumor grades. Data on tumor location and corresponding extent of resection (EOR) rates are provided in the Supplementary material (SM).

| WHO 2016 grade | FLAIR-tumor (cc) | | | CE-tumor (cc) | | | CE/FLAIR tumor ratio |
|----------------|------------------|--------|------------|---------------|--------|---------|----------------------|
| | Mean | Median | Range | Mean | Median | Range | Median |
| I | 31.7 | 22.8 | 2.1-107 | 17.7 | 12.8 | 0-78.3 | 0.6 |
| II | 44.3 | 24.6 | 4-349 | - | - | - | - |
| III | 56.6 | 36 | 3.3-221 | 17.4 | 6.0 | 0-105.7 | 0.14 |
| IV | 101.6 | 90.5 | 10.3-273.2 | 37.7 | 32.5 | 0-152 | 0.36 |
| Overall | 58.5 | 31.7 | 2.7-273.2 | 19.2 | 5.6 | 0-152 | 0.25 |

Table 5.5 - Preoperative tumor volume according to WHO grade.

The tumor is subdivided into contrast-enhancing components (CE-tumor) and areas of FLAIR/T2 hyperintensity (FLAIR-tumor).

5.4.3 Surgery

5.4.3.1 Extent of resection (EOR)

The median EOR rate in the present series was: 98.8% (mean 93.1%, range 29-100%) of contrast-enhancing components (CE-tumor) and 79.6% (mean 74.4%, range 8-100) for areas of FLAIR/T2 hyperintensity (FLAIR-tumor). Resection rates according to tumor grade are reported in **Table 5.6**.

| WHO Grade | CE-tumor extent of resection | | | | FLAIR-tumor extent of resection | | | |
|-----------|------------------------------|--------|---------|---------|---------------------------------|--------|---------|---------|
| | Mean | Median | Minimum | Maximum | Mean | Median | Minimum | Maximum |
| I | 93.3 | 98.6 | 34.4 | 100.0 | 83.9 | 95.8 | 27.3 | 100.0 |
| II | - | - | - | - | 77.2 | 84.1 | 26.7 | 100.0 |
| III | 96% | 100.0 | 53.8 | 100.0 | 74.8 | 75.5 | 19.4 | 100.0 |
| IV | 92.2 | 98.1 | 28.6 | 100.0 | 71.2 | 73.1 | 7.8 | 100.0 |

Table 5.6 - Extent of resection rate according to WHO grade.

CE-tumor = Gadolinium enhancing components; FLAIR-tumor = areas of FLAIR/T2 hyperintensity

Tumors located critically close to cortical or subcortical eloquent areas (related to motor or language function) showed a drop in median FLAIR-tumor EOR rate of about 10%, while a lower impact was observed in the case of CE-tumor EOR among HGGs (see **Table 5.7**)

| de | FLAIR-tumor extent of resection | | | | | CE-tumor extent of resection | | | | | |
|----------------|---------------------------------------|--------|-------|--------|------|---------------------------------------|--------|-------|--------|-------|--------------|
| | Tumor close to motor or language area | | | | Sig. | Tumor close to motor or language area | | | | Sig. | |
| | No | | Yes | | | No | | Yes | | | |
| | Mean | Median | Mean | Median | p | Mean | Median | Mean | Median | p | |
| WHO 2016 Grade | I | 86.8 | 100.0 | 81.8 | 90.8 | 0.331 | 98.4 | 100.0 | 88.2 | 95.8 | 0.050 |
| | II | 84.5 | 91.4 | 73.2 | 75.6 | 0.048 | - | - | - | - | - |
| | III | 81.7 | 81.8 | 71.3 | 73.2 | 0.050 | 95.9 | 100.0 | 96.3 | 100.0 | 0.814 |
| | IV | 72.3 | 79.6 | 70.7 | 72.4 | 0.774 | 93.6 | 98.4 | 91.4 | 97.9 | 0.483 |

Table 5.7 - Extent of resection according to tumor proximity to eloquent areas and WHO grade.
CE-tumor = Gadolinium enhancing components; FLAIR-tumor = areas of FLAIR/T2 hyperintensity.

5.4.4 Overall survival (OS) analysis

At the end of the present study, 41% of patients were alive, 53.8% were deceased, and for 5.1% (12 cases) patient's life status could not be traced.

5.4.4.1 Variables influencing Overall survival.

The following variables were confirmed correlated with a shorted OS in a statistically significant way (Log-Rank analysis, $p < 0.05$): *wild-type IDH-1 status, male sex, age > 65 years old, recurrent tumor, occipital lobe involvement* (while the frontal location was correlated with a better survival), *having two or more brain lobes or regions invaded by the tumor*. No significant correlation with OS was found for preoperative *CE-tumor* and *FLAIR-tumor* volume.

5.4.4.2 Overall survival according to extent of resection and residual tumor volumes.

5.4.4.2.1 Impact of postoperative FLAIR-tumor on OS in all infiltrating gliomas (WHO II-IV)

Statistical analysis was conducted to assess possible associations of different extent of resection (EOR) rates and postoperative residual volumes with OS.

Patients affected from WHO II-IV gliomas were grouped according to different EORs achieved (GTR, ≥ 90 and $< 100\%$, ≥ 75 and $< 90\%$, ≥ 40 and $< 75\%$, and $< 40\%$) and their estimated OS were calculated. Results confirmed that higher *FLAIR-tumor* resection rates were progressively related to longer survival in the present series ($p=0.001$ at Log-Rank).

When analyzing with Log-Rank analysis the achievement of different EOR cutoffs separately, statistical significance was stronger with lower values, as $\geq 75\%$ ($p < 0.001$) and $\geq 40\%$ ($p=0.002$), than higher values, as $\geq 90\%$ ($p=0.022$). The achievement of GTR, although showing better results, did not reach statistical significance (**Figure A1 in SM**).

5.4.4.2.2 Impact of postoperative FLAIR-tumor on OS among WHO II gliomas

Different cutoffs of *FLAIR-tumor* EOR in WHO grade II gliomas (**Figure A.2 in SM**) were analyzed in relation to the OS. Higher EOR values were associated with longer

estimated survival, although differences were statistically significant only for EOR \geq 90% ($p=0.034$), EOR \geq 75% ($p=0.013$), EOR \geq 40% ($p<0.001$), and not for GTR.

A cutoff of 5 cc was previously proposed by other authors (Smith *et al.*, 2008; Wijnenga *et al.*, 2018) as significantly affecting OS in WHO grade II gliomas and confirmed in our series ($p=0.018$, **Figure A.3 in SM**).

5.4.4.2.3 *Impact of postoperative FLAIR-tumor on OS among HGG (WHO III-IV)*

As displayed in **Figure A.4 in SM**, different cutoffs of EOR were analyzed in relation to the OS among HGGs. A significant difference ($p=0.002$) was identified only for EOR \geq 75%.

A cutoff of 25 cc was previously proposed by Fujii *et al.* (Fujii *et al.*, 2018) as significantly affecting OS in HGGs and also confirmed in our series ($p=0.008$, **Figure A.5 in SM**).

5.4.4.2.4 *Impact of postoperative CE-tumor on OS among higher grade gliomas (WHO III-IV)*

Overall survival was significantly higher ($p=0.050$) when CE-tumor GTR was obtained (**Figure A.6 in SM**). No significant differences were found for the 98%, 95%, and 90% EOR cutoffs.

A cut-off of 2 cc in the residual tumor was previously described in pertinent literature (Chaichana *et al.*, 2014a; Matthew M Grabowski 1, 2014) as possibly affecting outcomes in HGGs and corroborated by our series ($p=0.017$, **Figure A.7 in SM**).

5.4.5 *The impact of preoperative Advanced functional imaging (DTI and fMRI) on glioma surgery*

5.4.5.1 *Impact of preoperative advanced functional imaging on the extent of resection (EOR)*

Since MR tractography and BOLD task-based functional MR were predominantly performed in cases of tumors close to motor and language-related cortical and subcortical areas, the analysis of their impact on EOR was focused on lesions in proximity to those eloquent areas.

5.4.5.1.1 *Impact of preoperative DTI and fMRI on EOR in tumors close to motor functional areas*

When considering *FLAIR-tumor* in WHO grade II gliomas, an increase of median EOR was observed in cases with acquired preoperative DTI or fMRI (82.4 vs. 62.7% for both techniques). Median *FLAIR-tumor* EOR was slightly higher among WHO III neoplasms with preoperative DTI (72.3 vs. 69.0%), whereas slightly lower in cases with fMRI acquisition (65.8 vs. 71.3%). Amid WHO IV gliomas, a lower *FLAIR-tumor* EOR was noticed for both DTI (70.9 vs. 76.0%) and fMRI (66.2 vs. 74.8%) preoperative acquisition.

In the assessment of *CE-tumor*, no substantial differences emerged in median EOR for both advanced imaging techniques, while a slightly higher mean EOR rate was observed in either case.

None of the aforementioned associations between advanced imaging techniques and *FLAIR-* and *CE-tumor* EOR reached a significant p-value (Mann Whitney U test).

| Preoperative study type | WHO 2016 Grade | Preoperative acquisition | <i>FLAIR-tumor</i> extent of resection | | <i>CE-tumor</i> extent of resection | |
|-------------------------|----------------|--------------------------|--|-------------|-------------------------------------|--------------|
| | | | Mean | Median | Mean | Median |
| DTI | II | No | 67.1 | 62.7 | - | - |
| | | Yes | 74.5 | 82.4 | - | - |
| | III | No | 63.8 | 69.0 | 91.0 | 100.0 |
| | | Yes | 67.9 | 72.3 | 98.3 | 99.3 |
| | IV | No | 70.6 | 76.0 | 91.3 | 98.5 |
| | | Yes | 73.3 | 70.9 | 93.9 | 98.4 |
| | Overall | No | 69.3 | 71.3 | 90.5 | 99.0 |
| | | Yes | 72.5 | 73.6 | 95.1 | 98.4 |
| fMRI | II | No | 68.6 | 62.7 | - | - |
| | | Yes | 74.2 | 82.4 | - | - |
| | III | No | 66.7 | 71.3 | 89.7 | 100.0 |
| | | Yes | 65.4 | 65.8 | 98.6 | 100.0 |
| | IV | No | 73.2 | 74.8 | 92.4 | 98.4 |
| | | Yes | 65.5 | 66.2 | 92.5 | 98.3 |
| | Overall | No | 71.4 | 73.2 | 91.6 | 98.5 |
| | | Yes | 69.7 | 72.3 | 95.1 | 99.1 |

Table 5.8 - Extent of resection (EOR) in tumors close to motor functional areas according to preoperative DTI and fMRI acquisition.

5.4.5.1.2 *Impact of preoperative DTI and fMRI on EOR in tumors close to language functional areas*

When analyzing WHO grade II tumors close to language functional areas, a higher median *FLAIR-tumor* EOR was observed with the utilization of DTI (80.1 vs. 66.6%), while an opposite finding was noted when fMRI was acquired preoperatively (72.1 vs.

89.4%). Mean and median *FLAIR-tumor* EOR were generally slightly lower in HGGs where preoperative DTI and fMRI were obtained.

In the assessment of *CE-tumor* EOR, no substantial differences were noted in the case of WHO grade III gliomas, while results appeared to be slightly higher for WHO grade IV neoplasm studied preoperatively with DTI and/or fMRI.

No significant differences were found (Mann Whitney U test) for all the aforementioned associations.

| Preoperative study type | WHO grade | Preoperative acquisition | <i>FLAIR-tumor</i> extent of resection | | <i>CE-tumor</i> extent of resection | |
|-------------------------|-----------|--------------------------|--|-------------|-------------------------------------|--------------|
| | | | Mean | Median | Mean | Median |
| Preoperative DTI | II | No | 69.0 | 66.6 | - | - |
| | | Yes | 75.0 | 80.1 | - | - |
| | III | No | 75.2 | 85.1 | 99.1 | 100.0 |
| | | Yes | 74.4 | 75.1 | 98.4 | 100.0 |
| | IV | No | 65.7 | 70.6 | 88.1 | 94.5 |
| | | Yes | 66.7 | 61.9 | 94.8 | 98.5 |
| | Overall | No | 70.3 | 76.3 | 91.1 | 97.7 |
| | | Yes | 72.1 | 75.5 | 95.4 | 99.6 |
| Preoperative fMRI | II | No | 77.9 | 89.4 | - | - |
| | | Yes | 67.8 | 72.1 | - | - |
| | III | No | 76.9 | 85.1 | 99.1 | 100.0 |
| | | Yes | 72.5 | 73.3 | 98.4 | 100.0 |
| | IV | No | 66.7 | 69.2 | 90.2 | 97.4 |
| | | Yes | 62.6 | 70.1 | 92.2 | 98.3 |
| | Overall | No | 71.9 | 80.2 | 92.2 | 97.9 |
| | | Yes | 69.4 | 73.4 | 94.6 | 99.9 |

Table 5.9 - Extent of resection in tumors close to language functional areas

5.4.5.2 Impact of preoperative advanced functional imaging on clinical outcome

5.4.5.2.1 Impact of preoperative DTI and fMRI on motor functional outcome

The rate of symptoms worsened at hospital discharge was lower among patients studied preoperatively with DTI (6.5% vs. 20%), the difference was close to, although not reaching, statistical significance ($p = 0.054$, Pearson Chi-Square; $p = 0.074$, Fisher's Exact Test). A lower rate of motor function deterioration was also observed amid patients studied preoperatively with fMRI (10.3% vs. 14.9%), but it was not statistically significant.

The rate of clinical improvement at hospital discharge, compared to the preoperative status, was higher (but not statistically significant) among patients studied preoperatively with DTI (30.4% vs. 18.0%). Conversely, the same rate was slightly lower among patients studied preoperatively with fMRI (20.7% vs. 25.4%).

The associations of DTI and fMRI with motor clinical outcome, stratified according to the presence of a preoperative deficit, are reported in **Table 5.10**.

| Presence of preoperative motor deficit | Availability of the preoperative advanced imaging | Motor function (immediate postoperative assessment) | | | | | | Motor function (assessment at hospital discharge) | | | | | |
|--|---|---|-------|----------|-------|----------|-------|---|-------|----------|-------|----------|-------|
| | | Unchanged | | Improved | | Worsened | | Unchanged | | Improved | | Worsened | |
| | | n | % | n | % | n | % | n | % | n | % | n | % |
| No | no DTI | 12 | 57.1% | 0 | 0.0% | 9 | 42.9% | 14 | 66.7% | 0 | 0.0% | 7 | 33.3% |
| | DTI available | 18 | 75.0% | 0 | 0.0% | 6 | 25.0% | 21 | 87.5% | 0 | 0.0% | 3 | 12.5% |
| Yes | no DTI | 22 | 75.9% | 3 | 10.3% | 4 | 13.8% | 18 | 62.1% | 8 | 27.6% | 3 | 10.3% |
| | DTI available | 15 | 68.2% | 3 | 13.6% | 4 | 18.2% | 9 | 40.9% | 13 | 59.1% | 0 | 0.0% |
| No | no fMRI | 15 | 55.6% | 0 | 0.0% | 12 | 44.4% | 20 | 74.1% | 0 | 0.0% | 7 | 25.9% |
| | fMRI available | 15 | 83.3% | 0 | 0.0% | 3 | 16.7% | 15 | 83.3% | 0 | 0.0% | 3 | 16.7% |
| Yes | no fMRI | 31 | 77.5% | 4 | 10.0% | 5 | 12.5% | 22 | 55.0% | 15 | 37.5% | 3 | 7.5% |
| | fMRI available | 6 | 54.5% | 2 | 18.2% | 3 | 27.3% | 5 | 45.5% | 6 | 54.5% | 0 | 0.0% |

Table 5.10 - DTI and fMRI impact on motor clinical outcome, stratified by the presence of a preoperative deficit.

5.4.5.2.2 Impact of preoperative DTI and fMRI on language functional outcome

The rate of language function worsening at hospital discharge was lower among patients studied preoperatively with DTI (3% vs. 12.2%, but not statistically significant), whereas the rate of symptom improvement was higher in the same group (24.2% vs. 14.6%, not statistically significant).

The preoperative acquisition of fMRI was associated with a lower rate of deterioration of the language function (4.5% vs. 9.6 %) and a higher rate of its improvement (22.7% vs 17.3%. No statistical significance was identified in either case.

Table 5.11 reports the associations of DTI and fMRI with language clinical outcome, stratified according to the presence of a preoperative deficit.

| Presence of preoperative language deficit | Availability of the preoperative advanced imaging | Language function (immediate postoperative assessment) | | | | | | Language function (assessment at hospital discharge) | | | | | |
|---|---|--|-------|----------|-------|----------|-------|--|-------|----------|-------|----------|-------|
| | | Unchanged | | Improved | | Worsened | | Unchanged | | Improved | | Worsened | |
| | | n | % | n | % | n | % | n | % | n | % | n | % |
| No | no DTI | 15 | 78.9% | 0 | 0.0% | 4 | 21.1% | 17 | 89.5% | 0 | 0.0% | 2 | 10.5% |
| | DTI available | 17 | 81.0% | 0 | 0.0% | 4 | 19.0% | 20 | 95.2% | 0 | 0.0% | 1 | 4.8% |
| Yes | no DTI | 14 | 63.6% | 0 | 0.0% | 8 | 36.4% | 13 | 59.1% | 6 | 27.3% | 3 | 13.6% |
| | DTI available | 8 | 66.7% | 2 | 16.7% | 2 | 16.7% | 4 | 33.3% | 8 | 66.7% | 0 | 0.0% |
| No | no fMRI | 20 | 80.0% | 0 | 0.0% | 5 | 20.0% | 23 | 92.0% | 0 | 0.0% | 2 | 8.0% |
| | fMRI available | 12 | 80.0% | 0 | 0.0% | 3 | 20.0% | 14 | 93.3% | 0 | 0.0% | 1 | 6.7% |

| | | | | | | | | | | | | | |
|-----|----------------|----|-------|---|-------|---|-------|----|-------|---|-------|---|-------|
| Yes | no fMRI | 18 | 66.7% | 1 | 3.7% | 8 | 29.6% | 15 | 55.6% | 9 | 33.3% | 3 | 11.1% |
| | fMRI available | 4 | 57.1% | 1 | 14.3% | 2 | 28.6% | 2 | 28.6% | 5 | 71.4% | 0 | 0.0% |

Table 5.11 - DTI and fMRI impact on language clinical outcome, stratified according to the presence of a preoperative deficit.

5.4.5.3 Impact of preoperative advanced functional imaging (DTI and fMRI) on OS

5.4.5.3.1 Impact of preoperative DTI and fMRI on OS in tumor close to motor functional areas

Estimated OS (**Figure 5.3**, left panel) was higher among patients with acquired preoperative DTI (mean 25.6, median 20 months, actuarial OS at 36 months 25.5%) than patients with no DTI available (mean 17.3, median 9.7 months, actuarial OS at 36 months was 13.9%). The difference was statistically significant ($p = 0.038$, Log Rank; $p = 0.007$, Breslow; $p = 0.011$, Tarone-Ware).

A significantly higher ($p = 0.023$, Log-Rank; $p = 0.006$, Breslow; $p = 0.008$, Tarone-Ware) estimated OS (**Figure 5.3**, right panel) was also found among patients with acquired preoperative fMRI (mean 30.8, median 20.2 months) than patients with no preoperative fMRI available (mean 18.2, median 10.9 months), with an actuarial OS at 36 months was 35.7% for the first group and 14.0% for the second one

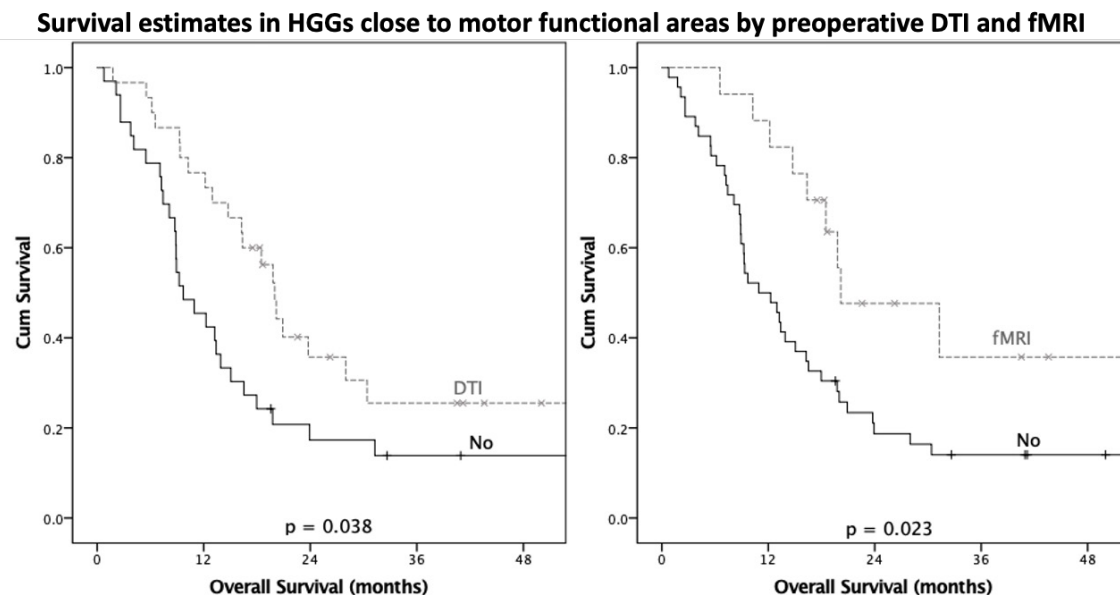


Figure 5.3 - Survival estimates according to preoperative DTI and fMRI acquisition among higher grade gliomas close to motor functional areas.

5.4.5.3.2 Impact of preoperative DTI and fMRI on OS in tumor *close to language functional areas*

Actuarial OS (**Figure 5.4**, left panel) was higher among patients with acquired preoperative DTI (mean 23.3, median 18.5 months, 21.8% actuarial OS at 36 months) than those with no DTI available (mean 20.7, median 11.4 months, 13.9% actuarial OS at 36 months), although the difference was not statistically significant.

When assessing the use of preoperative fMRI (**Figure 5.4**, right panel), estimated OS was slightly higher among those preoperatively assessed (mean 26.6, median 18.5 months, 25.7% actuarial OS at 36 months) than in those not subjected to fMRI (mean 20.4, median 9.6 months, 14.0% actuarial OS at 36 months). The difference didn't reach statistical significance.

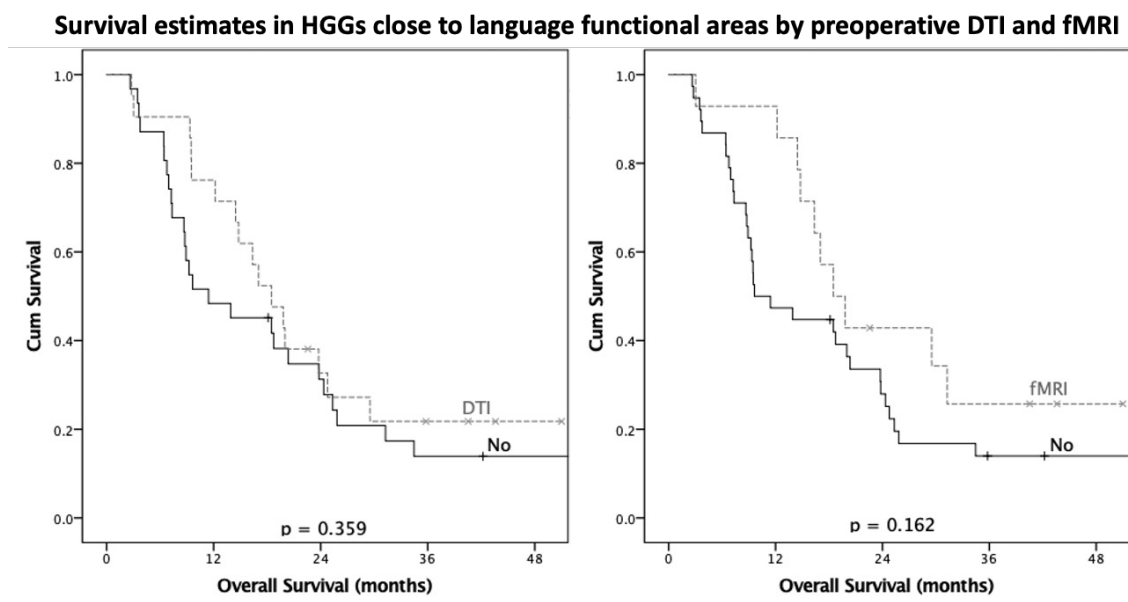


Figure 5.4 - Survival estimates according to preoperative DTI and fMRI acquisition among higher grade gliomas close to language functional areas.

5.4.6 The impact of Advanced 3D imaging preplanning in glioma surgery

Sixty-four cases over 234 underwent preoperative advanced 3D reconstruction, combining direct and surface volume rendering techniques with the image computing software 3D-Slicer, resulting in the generation of detailed anatomic-functional-pathological 3D models for virtual reality and surgical planning/simulation. Tumor and procedure characteristics of patients studied with and without advanced 3D imaging preplanning are reported in **Table 5.12**.

| Values | No preplanning | Advanced 3D imaging Preplanning |
|--|----------------|---------------------------------|
| Number of cases (n) | 170 | 64 |
| WHO grade I | 13 | 8 |
| WHO grade II | 34 | 15 |
| WHO grade III | 29 | 14 |
| WHO grade IV | 94 | 27 |
| Tumor location (% over total) * | 163 | 63 |
| Left | 70 | 35 |
| Frontal | 26 | 11 |
| Temporal | 33 | 8 |
| Insular | 16 | 7 |
| Parietal | 16 | 11 |
| Occipital | 8 | 2 |
| Right | 89 | 21 |
| Frontal | 35 | 13 |
| Temporal | 46 | 5 |
| Insular | 14 | 2 |
| Parietal | 22 | 10 |
| Occipital | 12 | 4 |
| Midline | 4 | 7 |
| Tumor located in any critical area (n) | 95 | 50 |
| Tumor located in motor critical area (n) | 62 | 34 |
| Tumor located in language critical area (n) | 48 | 26 |
| Hospitalization (days) | | |
| mean | 15 | 14 |
| median | 11 | 11 |
| Surgical time (min) | | |
| mean | 211 | 222 |
| median | 207 | 213 |
| range | 90-392 | 129-145 |

Table 5.12 - Tumor and procedure characteristics of patients to advanced 3D imaging preplanning availability.

5.4.6.1 Impact of Advanced 3D imaging preplanning on EOR

5.4.6.1.1 FLAIR-tumor EOR among LGGs (WHO II)

The FLAIR-tumor EOR reached was higher (median 93.1%, mean 85.1%) in WHO grade II gliomas undergoing advanced 3D imaging pre-planning compared to cases where it was not available (median 79.5%, mean 74.5%), although the difference did not reach statistical significance. **Table A.4 in SM** reports the impact of advanced 3D imaging preplanning in the resection of WHO grade II gliomas according to different tumor locations.

The use of advanced 3D imaging preplanning was correlated with a higher rate of LGG cases achieving $\geq 90\%$ EOR (58.3% vs. 31.4%) and $\geq 75\%$ EOR (75% vs. 54.3%) in. In the case of 90% cutoff, the difference was statistically significant ($p = 0.025$, Mann-Whitney U).

| Advanced 3D imaging preplanning | FLAIR-tumor EOR \geq 90% in LGG | | Sig (p) | FLAIR-tumor EOR \geq 75% in LGG | | Sig (p) |
|---------------------------------|-----------------------------------|-------|-------------|-----------------------------------|-------|---------|
| | n/row-tot | % | | n/row-tot | % | |
| No | 10/34 | 29.4% | .025 | 18/34 | 52.9% | .099 |
| Yes | 9/14 | 64.3% | | 11/14 | 78.6% | |

Table 5.13 - Achievement of 90% and 75% FLAIR-tumor EOR cutoffs according to advanced 3D imaging preplanning availability in low grade gliomas.

5.4.6.1.2 CE-tumor Extent of resection among HGG (WHO III-IV)

The CE-tumor EOR in HGG (WHO III and IV) was higher when advanced 3D imaging preplanning was performed (median 99.5%, mean 97%) compared to the remaining cases (median 98%, mean 92%). The difference did not reach statistical significance on non-parametric tests (Mann-Whitney U). Data according to tumor location and side are reported in **Table A.5 in SM**.

As reported in **Table 5.14**, advanced 3D imaging preplanning was correlated with a higher rate of cases achieving \geq 90% EOR (77.5% vs. 73.2%) and GTR (40% vs. 38.2%) in HGGs. Nevertheless, no statistical significance was identified for the aforementioned variables.

| Advanced 3D imaging preplanning | CE-tumor EOR \geq 90% in HGG | | Sig | CE-tumor GTR obtained in HGG | | Sig |
|---------------------------------|--------------------------------|-------|-----|------------------------------|-------|-----|
| | n/row-tot | % | | n/row-tot | % | |
| No | 90/123 | 73.2% | . | 47/123 | 38.2% | . |
| Yes | 31/40 | 77.5% | | 16/40 | 40% | |

Table 5.14 - Achievement of 90% and gross total resection of CE-tumor EOR cutoffs according to advanced 3D imaging preplanning availability in WHO grade III-IV tumors.

Only P values <0.150 are reported in the last column. GTR = gross total resection. HGG = high grade glioma

5.4.6.2 Impact of Advanced 3D imaging preplanning on OS in HGGs

When considering HGGs alone, median OS was higher (18.1 vs. 13 months) in cases where advanced 3D imaging preplanning was performed, although no statistical significance was obtained.

Considering that Advanced 3D imaging preplanning was introduced after 2018, allowing patients operated before that date for a longer FU and, therefore, a potential longer OS at the time of the survey, we decided to focus the following analysis only on the large WHO IV grade cohort (n = 120), opting out lower WHO grades that possibly entailed longer survivals. Among WHO grade IV tumors, median OS was higher (14.5 vs. 11.1 months) in patients who underwent advanced 3D imaging preplanning, although

not reaching the threshold of significance. Data according to tumor location and side are reported in **Table A.6 in SM**.

5.4.6.2.1 Impact of Advanced 3D imaging preplanning on OS in WHO grade IV gliomas located close to motor and language functional areas.

Mean estimated survival for tumors close to *motor* functional areas was 22.1 months (median 12.2 months, actuarial OS at 36 months was 25.7%) when advanced 3D imaging preplanning was available, while 15.9 (median 10.9 months, actuarial OS at 36 months was 9.7%) in the remaining cases. Differences were not statistically significant.

When analyzing tumors close to *language* eloquent areas, mean actuarial survival was 18 months (median 14.5 months, actuarial OS at 36 months was 12.5%) in patients with advanced 3D imaging preplanning, while 15.5 (median 8.9 months, actuarial OS at 36 months was 8.7%) in the other cases. The difference was not statistically significant.

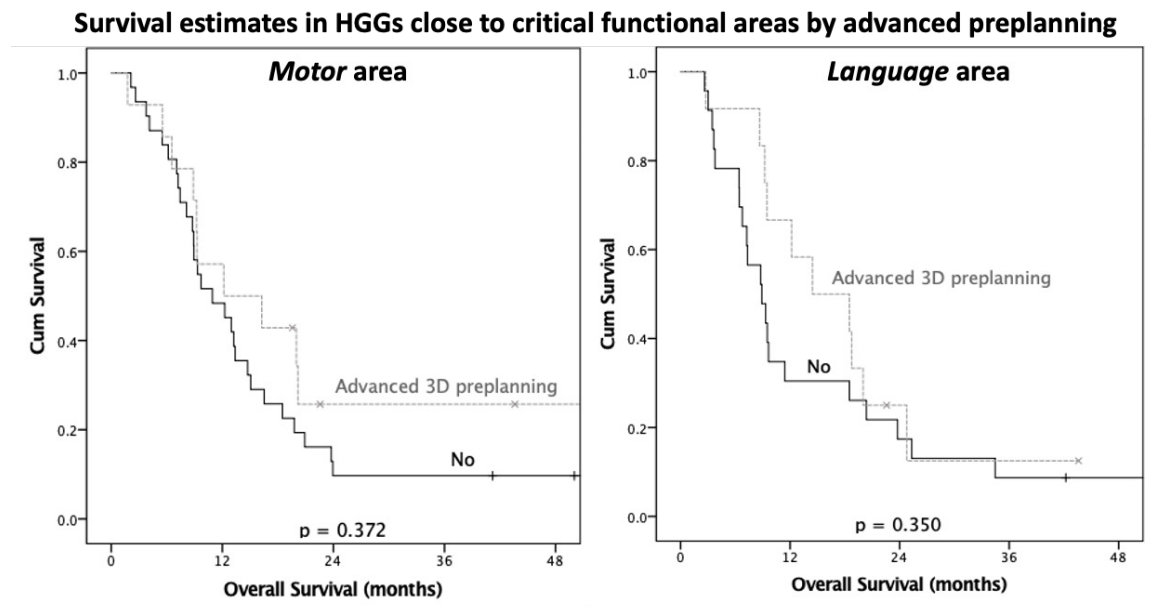


Figure 5.5 - Survival estimates according to advanced 3D imaging preplanning adoption in WHO grade IV gliomas close to motor (left) language (right) functional areas.

5.4.6.3 The impact of Advanced 3D imaging preplanning on neurological outcome

5.4.6.3.1 Impact of Advanced 3D imaging preplanning on motor function

Patients studied preoperatively with the advanced 3D imaging preplanning showed, at hospital discharge, a lower rate of motor function deterioration (8.8% vs. 16.1%, not

statistically significant) and a slightly lower rate of clinical improvement (20.6% vs. 22.6%, not statistically significant).

| Presence of preoperative motor deficit | Availability of the preoperative Advanced 3D imaging preplanning | Motor function (immediate postoperative assessment) | | | | | | Motor function (assessment at hospital discharge) | | | | | |
|--|--|---|-------|----------|-------|----------|-------|---|-------|----------|-------|----------|-------|
| | | Unchanged | | Improved | | Worsened | | Unchanged | | Improved | | Worsened | |
| | | n | % | n | % | n | % | n | % | n | % | n | % |
| No | no | 15 | 60.0% | 0 | 0.0% | 10 | 40.0% | 18 | 72.0% | 0 | 0.0% | 7 | 28.0% |
| | yes | 15 | 75.0% | 0 | 0.0% | 5 | 25.0% | 17 | 85.0% | 0 | 0.0% | 3 | 15.0% |
| Yes | no | 27 | 73.0% | 4 | 10.8% | 6 | 16.2% | 20 | 54.1% | 14 | 37.8% | 3 | 8.1% |
| | yes | 10 | 71.4% | 2 | 14.3% | 2 | 14.3% | 7 | 50.0% | 7 | 50.0% | 0 | 0.0% |
| Overall | no | 42 | 67.7% | 4 | 6.5% | 16 | 25.8% | 38 | 61.3% | 14 | 22.6% | 10 | 16.1% |
| | yes | 25 | 73.5% | 2 | 5.9% | 7 | 20.6% | 24 | 70.6% | 7 | 20.6% | 3 | 8.8% |

Table 5.15 - Advanced 3D preplanning impact on motor clinical outcome, stratified according to the presence of a preoperative deficit.

5.4.6.3.2 Impact of Advanced 3D imaging preplanning on language function

The rate of language function worsening at hospital discharge was lower among patients studied preoperatively with advanced 3D imaging preplanning (7.7% vs. 8.3%, not statistically significant), while a higher rate of clinical improvement in the language was registered in the same group (30.8% vs. 12.5%). The difference in clinical improvement was close to, although not reaching, statistical significance ($p = 0.055$, Pearson Chi-Square; $p = 0.068$, Fisher's Exact Test).

| Presence of preoperative language deficit | Availability of the preoperative advanced 3D preplanning | Language function (immediate postoperative assessment) | | | | | | Language function (assessment at hospital discharge) | | | | | |
|---|--|--|-------|----------|-------|----------|-------|--|-------|----------|-------|----------|-------|
| | | Unchanged | | Improved | | Worsened | | Unchanged | | Improved | | Worsened | |
| | | n | % | n | % | n | % | n | % | n | % | n | % |
| No | no | 19 | 82.6% | 0 | 0.0% | 4 | 17.4% | 22 | 95.7% | 0 | 0.0% | 1 | 4.3% |
| | yes | 13 | 76.5% | 0 | 0.0% | 4 | 23.5% | 15 | 88.2% | 0 | 0.0% | 2 | 11.8% |
| Yes | no | 17 | 68.0% | 0 | 0.0% | 8 | 32.0% | 16 | 64.0% | 6 | 24.0% | 3 | 12.0% |
| | yes | 5 | 55.6% | 2 | 22.2% | 2 | 22.2% | 1 | 11.1% | 8 | 88.9% | 0 | 0.0% |
| Overall | no | 36 | 75.0% | 0 | 0.0% | 12 | 25.0% | 38 | 79.2% | 6 | 12.5% | 4 | 8.3% |
| | yes | 18 | 69.2% | 2 | 7.7% | 6 | 23.1% | 16 | 61.5% | 8 | 30.8% | 2 | 7.7% |

Table 5.16 - Advanced 3D preplanning impact on language clinical outcome, stratified according to the presence of a preoperative deficit.

5.4.7 The impact of intraoperative neuroimaging and neuromonitoring tools in glioma surgery

Intraoperative *neuronavigation* and *ultrasound* were adopted in 150 and 156 cases, respectively, predominantly (67% and 64%, respectively) in tumors close to critical motor

or language areas (see **Table 5.17**). Of the 49 cases with intra-operative neuromonitoring (IONM), 96% were in proximity to critical motor or language areas; in the remaining two patients, IONM was adopted for the mapping of the optic radiations. The aforementioned differences according to tumor location were statistically significant in the case of neuronavigation ($p = 0.048$, Chi-square) and IONM ($p < 0.001$, Chi-square).

| | | Tumor location close to motor or language area | | | | | | Sig. |
|--------------------------------|-----|--|---------|-------|---------|-------|---------|----------------|
| | | No | | Yes | | Total | | |
| | | Count | Row N % | Count | Row N % | Count | Row N % | p |
| Neuronavigation | No | 39 | 46.4% | 45 | 53.6% | 84 | 100.0% | 0.048 |
| | Yes | 50 | 33.3% | 100 | 66.7% | 150 | 100.0% | |
| Ultrasound | No | 33 | 42.3% | 45 | 57.7% | 78 | 100.0% | 0.341 |
| | Yes | 56 | 35.9% | 100 | 64.1% | 156 | 100.0% | |
| Intraoperative neuromonitoring | No | 87 | 47.0% | 98 | 53.0% | 185 | 100.0% | ≤ 0.001 |
| | Yes | 2 | 4.1% | 47 | 95.9% | 49 | 100.0% | |

Table 5.17 - Number of cases where Neuronavigation, Ultrasound, and Intraoperative neuromonitoring were adopted according to tumor location proximity to critical eloquent (motor and/or language) areas.

5.4.7.1 Impact of intraoperative neuroimaging and neuromonitoring tools on EOR

Table 5.18 and **Table 5.19** analyze the impact of the use of intraoperative neuroimaging (*neuronavigation* and *ultrasound*) and *IONM* techniques on the EOR achieved.

EOR was higher when adopting *neuronavigation* for both *CE-tumor* (median: 99.4 vs 98.1%; mean 94.2 vs 91.1%) and *FLAIR-tumor* (median: 80.6 vs 75.4; mean: 75.8 vs 71.8%). Similar findings were observed with *intraoperative ultrasound*: median EOR 100 vs 96% (mean 94.2 vs 91%) for *CE-tumor*, whereas 80.1 vs 79.4% (mean 75.7 vs 71.9%) for *FLAIR-tumor*. On the contrary, the use of *IONM* was related to a lower median resection rate for *FLAIR-tumor* (76.8% vs 80.6%; mean: 75.4 vs 74.1%), while higher rates (100 vs 98.6%; mean 95.9 vs 92.4%) were still noted in *CE-tumor* removal.

A statistically significant difference in EOR was found for *CE-tumor* when using intraoperative *ultrasound* ($p = 0.009$, Mann-Whitney U) and for *FLAIR-tumor* when adopting intraoperative *neuronavigation* ($p = 0.03$, Mann-Whitney U).

| Intraoperative Technologies | | FLAIR-tumor extent of resection (%) (overall) | | | | Sig | CE-tumor extent of resection (%) (WHO III-IV) | | | | Sig |
|--------------------------------|-----|---|--------|------|-------|-------------|---|--------|------|-------|-------------|
| | | Mean | Median | Min | Max | p | Mean | Median | Min | Max | p |
| Neuronavigation | No | 71.8 | 75.4 | 16.3 | 100.0 | .030 | 91.1 | 98.1 | 34.4 | 100.0 | .079 |
| | Yes | 75.8 | 80.6 | 7.8 | 100.0 | | 94.2 | 99.4 | 28.6 | 100.0 | |
| Ultrasound | No | 71.9 | 79.4 | 7.8 | 100.0 | | 91.0 | 96.0 | 34.4 | 100.0 | .009 |
| | Yes | 75.7 | 80.1 | 19.2 | 100.0 | | 94.2 | 100.0 | 28.6 | 100.0 | |
| Intraoperative neuromonitoring | No | 74.1 | 80.6 | 7.8 | 100.0 | | 92.4 | 98.6 | 28.6 | 100.0 | .101 |
| | Yes | 75.4 | 76.8 | 30.1 | 100.0 | | 95.9 | 100.0 | 72.3 | 100.0 | |

Table 5.18 - Mean degree of FLAIR and CE-tumor extent of resection with and without neuroimaging and neuromonitoring tools.

Only p values lower than 0.15 were reported in the table.

| Intraoperative Technologies | | FLAIR-tumor EOR $\geq 90\%$ (overall) | | | FLAIR-tumor EOR $\geq 75\%$ (overall) | | | CE-tumor GTR obtained (in HGG) | | |
|--------------------------------|---|---------------------------------------|----------|------|---------------------------------------|----------|------|--------------------------------|----------|-------------|
| | | event (%) | over (n) | Sig. | event (%) | over (n) | Sig. | event (%) | over (n) | Sig. |
| Neuronavigation | N | 26.2% | 84 | | 51.2% | 84 | | 31.7% | 60 | |
| | Y | 37.3 | 150 | | 56.7% | 150 | | 43.3% | 104 | |
| Ultrasound | N | 29.5% | 78 | | 53.8% | 78 | | 27.8% | 54 | .042 |
| | Y | 35.3% | 156 | | 55.1% | 156 | | 44.5% | 110 | |
| Intraoperative neuromonitoring | N | 35.1% | 185 | | 53.5% | 185 | | 36.2% | 130 | |
| | Y | 26.5% | 49 | | 59.2% | 49 | | 50.0% | 34 | |

Table 5.19 - Number of cases achieving different cut-off values for extent of resection according to intraoperative neuroimaging and neuromonitoring tools usage.

Only p values lower than 0.15 were reported. Sig= Chi-square 2-sided.

5.4.7.2 Impact of intraoperative neuroimaging and neuromonitoring tools on OS in HGGs

The effect of intraoperative technologies on OS was analyzed among WHO III and IV gliomas. Mean and median estimated OS were higher when *neuronavigation* was adopted (26.7 and 17.0 months, respectively; actuarial OS at 36 months was 26.5%) compared to cases without its utilization (18.2 and 11.7 months respectively; actuarial OS at 36 months was 13.8%). The difference was statistically significant at Log-rank ($p = 0.012$), Breslow ($p = 0.008$) and Tarone-Ware ($p = 0.008$).

Similarly, mean and median estimated OS were higher when *ultrasound* was adopted (25.7 and 17.0 months, respectively; actuarial OS at 36 months was 23.0%) compared to cases without its utilization (19.0 and 11.0 months, respectively; actuarial OS at 36 months was 15.8%). The difference was statistically significant at Log-rank ($p = 0.048$), Breslow ($p = 0.031$) and Tarone-Ware ($p = 0.035$) analysis.

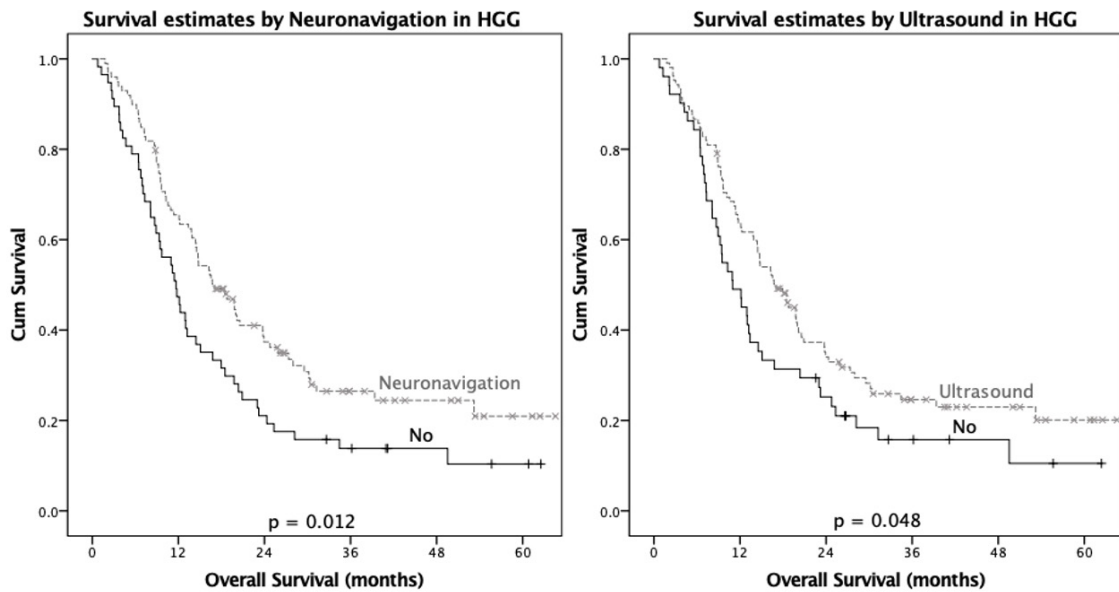


Figure 5.6 - Survival estimates in WHO grade III-IV tumors according to the adoption of intraoperative neuronavigation (left) and ultrasound (right)

When analyzing *IONM*, mean and median estimated OS were higher with its adoption (34.1 and 23.8 months, respectively; actuarial OS at 36 months was 41.7%) compared to cases without its utilization (20.9 and 13.0 months respectively; actuarial OS at 36 months was 17.0%). The difference was statistically significant at Log-rank ($p = 0.004$), Breslow ($p = 0.006$) and Tarone-Ware ($p = 0.005$) analysis.

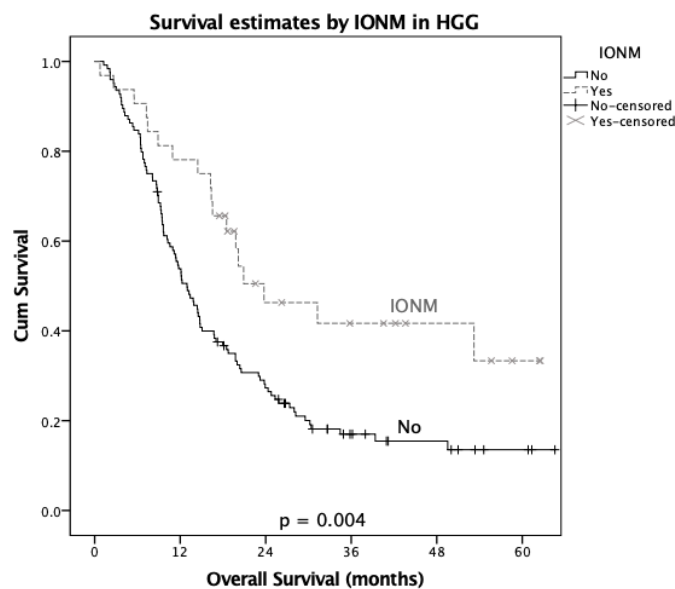


Figure 5.7 - Survival estimates in WHO grade III-IV tumors according to the adoption of intraoperative neuro-monitoring (*IONM*).

5.4.7.3 Impact of intraoperative neuroimaging and neuromonitoring tools on postoperative morbidity

When assessing the impact of intraoperative tools on postoperative clinical deterioration in any functional areas, *neuronavigation* and *ultrasound* were associated with a higher rate of morbidity (about 21 vs. 17% in either case), and similar results were noted for *IONM* (about 26.5 vs. 17.2%); however, none of these differences reached a significant p-value at statistical tests. Moreover, considering that these tools were more frequently adopted in challenging tumors (at risk of postoperative clinical deterioration), to avoid biased results, a further analysis was performed (reported in the following paragraphs), focusing only on cases close to eloquent areas.

| Evaluation of the number of clinical functions worsened postoperatively with the use of intraoperative tools | | | | | | | |
|--|---------------------|------------------------------|------------|-------------|-------------|-------------|-----------------------|
| Intraoperative technique | Intraop utilization | Patients WORSENERD in | | | | | |
| | | <i>NO</i> function | 1 function | 2 functions | 3 functions | 4 functions | Tot patients worsened |
| | | % | % | % | % | % | % |
| Neuronavigation | No | 83.3% | 11.9% | 2.4% | 1.2% | 1.2% | 16.7% |
| | Yes | 79.3% | 17.3% | 3.3% | 0.0% | 0.0% | 20.6% |
| Ultrasound | No | 83.3% | 14.1% | 0.0% | 1.3% | 1.3% | 16.7% |
| | Yes | 79.5% | 16.0% | 4.5% | 0.0% | 0.0% | 20.5% |
| Intraoperative neuromonitoring | No | 82.7% | 13.0% | 3.2% | 0.5% | 0.5% | 17.2% |
| | Yes | 73.5% | 24.5% | 2.0% | 0.0% | 0.0% | 26.5% |

Table 5.20 - Number of clinical functions worsened postoperatively according to intraoperative neuroimaging and neuromonitoring tools adoption.

5.4.7.3.1 Impact of intraoperative neuroimaging and neuromonitoring tools on motor function

An analysis of the impact of different intraoperative imaging and neurophysiological tools on the motor function was performed among the 96/234 cases harboring a tumor close to motor functional areas (primary motor cortex, corticospinal tract) and is reported in **Table 5.21**.

The rate of motor function deterioration at hospital discharge was higher with the adoption of *ultrasound* (15.2 vs. 10.0%) and slightly higher in cases where *neuronavigation* (13.8 vs. 12.9%) or *IONM* was involved (15.4 vs. 12.3%). These differences were not statistically significant.

| Intraoperative technology | Intraoperative adoption | Count on (n) | Motor function (assessment at hospital discharge) | | |
|--------------------------------|-------------------------|--------------|---|--------------|--------------|
| | | | Unchanged (%) | Improved (%) | Worsened (%) |
| Neuronavigation | No | 31 | 58.1% | 29.0% | 12.9% |
| | Yes | 65 | 64.6% | 21.5% | 13.8% |
| Ultrasound | No | 30 | 63.3% | 26.7% | 10.0% |
| | Yes | 66 | 62.1% | 22.7% | 15.2% |
| Intraoperative neuromonitoring | No | 57 | 59.6% | 28.1% | 12.3% |
| | Yes | 39 | 66.7% | 17.9% | 15.4% |

Table 5.21 - Impact of intraoperative neuroimaging and neuromonitoring tools on postoperative motor function as assessed at hospital discharge.

5.4.7.3.2 Impact of intraoperative neuroimaging and neuromonitoring tools on language function

The impact of different intraoperative tools on the language function was analyzed among the 74/234 cases of lesion close to language functional areas (Broca's area, Wernicke's areas, left arcuate fasciculus) and reported in **Table 5.22**. The rate of language function deterioration was registered higher when *neuronavigated* (10.7 vs. 0%) and *IONM* were involved (10.5 vs. 7.3%), while slightly lower (7.4 vs. 10.0%) in cases with *ultrasound* utilization; no statistical significance was highlighted for the aforementioned associations.

| Intraoperative technology | Intraoperative adoption | Count on (n) | Language function (assessment at hospital discharge) | | |
|--------------------------------|-------------------------|--------------|--|--------------|--------------|
| | | | Unchanged (%) | Improved (%) | Worsened (%) |
| Neuronavigation | No | 18 | 72.2% | 27.8% | 0.0% |
| | Yes | 56 | 73.2% | 16.1% | 10.7% |
| Ultrasound | No | 20 | 75.0% | 15.0% | 10.0% |
| | Yes | 54 | 72.2% | 20.4% | 7.4% |
| Intraoperative neuromonitoring | No | 55 | 74.5% | 18.2% | 7.3% |
| | Yes | 19 | 68.4% | 21.1% | 10.5% |

Table 5.22 - Impact of intraoperative neuroimaging and neuromonitoring tools on postoperative language function as assessed at hospital discharge

5.4.7.4 Impact of intraoperative neuroimaging and neuromonitoring tools on procedure duration

Since the adoption of *Neuronavigation* and *IONM* requires a preoperative setting, their impact on the duration of the preparatory phase (from patient entering the operating room to skin incision) was assessed (**Table 5.23**). Mean and median values were significantly augmented (of about 15 minutes) both in the case of *Neuronavigation* ($p < 0.001$, Mann-Whitney U) and *IONM* ($p < 0.001$, Mann-Whitney U).

| Intraoperative technology | Adoption | Preoperative phase duration (from patient entrance in O.R. to skin incision) | | | Surgical time (from skin incision to last stitch) | | |
|--------------------------------|----------|--|----------------|------------------|---|----------------|--------------|
| | | Median (minutes) | Mean (minutes) | Sig. | Median (minutes) | Mean (minutes) | Sig. |
| Neuronavigation | No | 73.5 | 77.0 | <0.001 | 208.6 | 202.5 | 0.277 |
| | Yes | 91.5 | 93.7 | | 217.0 | 210.5 | |
| Ultrasound | No | 86.7 | 84.0 | 0.261 | 201.6 | 199.0 | 0.034 |
| | Yes | 88.3 | 89.0 | | 220.1 | 212.5 | |
| Intraoperative neuromonitoring | No | 83.0 | 84.6 | <0.001 | 207.4 | 209.0 | 0.048 |
| | Yes | 97.0 | 99.6 | | 228.4 | 230.2 | |

Table 5.23 - Duration of surgical procedures according to intraoperative neuroimaging and neuromonitoring tools usage.

The impact of intraoperative imaging and monitoring tools on surgical time (defined as the time from skin incision to the placement of the last suture stitch) was also assessed. The use of intraoperative *neuronavigation* was associated with a procedure duration about 10 minutes higher, although not statistically significant. Conversely, intraoperative *ultrasound* appeared to significantly ($p = 0.034$, Mann-Whitney U) increase the procedure by about 15 minutes, while *IONM* significantly ($p = 0.048$, Mann-Whitney U) prolonged the surgical time of about 20-25 minutes.

5.4.8 Multivariate analysis

Additional information regarding multi-variate models and analysis are presented in the corresponding **Supplementary data** section

5.4.8.1 FLAIR-tumor EOR and residual postoperative volume

The following covariates were found to be statistically predictive for **higher chances** of FLAIR-tumor EOR: *dealing with a newly diagnosed tumor* and a *lower preoperative FLAIR-tumor*.

The following predictor variables were significantly associated with a **decrease in the likelihood** of reaching FLAIR-tumor 75% EOR cutoff: *higher WHO 2016 grade* OR 0.617, $p = 0.033$), *recurrent tumor* (Odd Ratio (OR) 0.370, $p = 0.012$), *tumor close to motor area* (OR 0.352, $p = 0.009$), *preoperative FLAIR-tumor volume* (OR 0.992, $p = 0.018$). Conversely, the following variables were significantly associated with an **increase in the likelihood** of reaching FLAIR-tumor 75% EOR threshold: *use of IONM* (OR 2.967, $p = 0.018$) and a higher *preoperative CE-tumor volume* ($p = 0.008$); however, in the latter case the OR was close to one (1.022).

Higher WHO 2016 grade (OR 0.486, $p = 0.006$), recurrent tumor (OR 0.280, $p = 0.012$), a higher number of lobes involved by the tumor (OR 0.333, $p = 0.007$), preoperative FLAIR-tumor volume (OR 0.984, $p = 0.001$), and preoperative KPS (OR 0.961, $p = 0.027$) were significantly associated with a **decrease in the likelihood** of reaching a FLAIR-tumor residual ≤ 5 cc. On the contrary, the use of intraoperative neuronavigation (OR 3.107, $p = 0.014$) entailed a significant **increase in the likelihood** of reaching a FLAIR-tumor residual ≤ 5 cc; preoperative DTI (OR 2.671, $p = 0.100$) showed a weak trend toward statistical significance despite not reaching it.

5.4.8.2 CE-tumor EOR and residual postoperative volume

Higher WHO 2016 grade (OR = 0.526, $p = 0.036$) and tumor close to language area (OR = 0.375, $p = 0.049$) were significantly associated with a **lower probability** of reaching a GTR of CE-tumor volume, whereas *more than one lobe involved* (OR = 0.477, $p = 0.068$) showed a trend toward statistical significance although not reaching it: Conversely, the use of *intra-operative ultrasound* (OR = 2.402, $p = 0.036$) was significantly associated with a **higher probability** of reaching a CE-tumor GTR, while IONM demonstrated a positive trend but not enough for significance threshold (OR = 2.712, $p = 0.086$).

The following predictor variables were significantly associated with a **lower likelihood** of reaching CE-tumor residual volume ≤ 2 cc: *higher WHO 2016 grade* (OR 0.109, $p = 0.005$). Conversely, *preoperative CE-tumor volume* (OR 0.984, $p = 0.075$) and the presence of *IDH-mutation* (OR = 0.229, $p = 0.063$) showed a trend toward statistical significance although not reaching it.

5.4.8.3 Postoperative deterioration/improvement in at least one neurological function.

Tumors close to motor area ($p = 0.003$, OR 4.524) showed a **higher likelihood** of deterioration in at least one clinical function, while *tumor midline/deep location* exhibited a trend toward statistical significance although not reaching it. Conversely, the following predictor variables were significantly associated with a **lower likelihood** of reaching deterioration in at least one clinical function: *higher preoperative CE-tumor volume* ($p =$

0.037, OR 0.970), *preoperative DTI acquisition* ($p = 0.028$, OR 0.109), and *presence of a preoperative motor deficit* ($p = 0.001$, OR 0.127).

The following covariates were significantly associated with a **higher likelihood** of postoperative improvement in at least one clinical function: *preoperative DTI acquisition* ($p = 0.004$, OR 6.018), *higher preoperative KPS score* ($p = 0.001$, OR 1.069), *preoperative language deficit* ($p = 0.009$, OR 4.393), *preoperative motor deficit* ($p < 0.001$, OR 20.201). On the other hand, *recurrent tumor* ($p = 0.037$, OR 0.280) was significantly associated with a **lower likelihood** of postoperative clinical improvement. The *midline/deep location of the tumor* ($p = 0.068$, OR 0.057) and *IDH-1 mutation* ($p = 0.065$, OR 0.330) showed a trend toward statistical significance although not reaching it.

5.4.8.4 Postoperative motor and language functional outcome

The following predictor variables were significantly associated with a **lower probability** of postoperative deterioration in motor function: *DTI acquisition* (OR = 0.029, $p = 0.014$) and *preoperative motor deficit* (OR = 0.108, $p = 0.025$); *tumor close to language area* (OR = 0.116, $p = 0.073$) showed a trend toward statistical significance despite not reaching it. Contrarily, *tumor close to motor area* (OR = 25.204, $p = 0.001$) was significantly associated with a **higher probability** of postoperative deterioration in motor function.

No preoperative independent variable was found to be significantly associated with postoperative deterioration in language function.

5.4.8.5 Postoperative Karnofsky Performance Status

Older age ($p = 0.005$, OR 1.061) and *female sex* ($p = 0.007$, OR 4.174) were significantly associated with a **higher likelihood** of reaching deterioration in KPS, whereas patients with a *higher preoperative KPS score* entailed a **lower likelihood** of further deterioration ($p = 0.014$, OR 0.954).

5.4.8.6 Overall survival

5.4.8.6.1 Impact of preoperative variables on Overall survival

When assessing impact of preoperative covariates on OS, the following were found to have an **increased hazard ratio** (HR): *older age* ($p = 0.003$, HR = 1.030), *higher WHO 2016 grade* ($p < 0.001$, HR = 3.889), *recurrent tumor* ($p < 0.001$, HR = 4.082), *multiple of lobes invaded by the tumor* ($p = 0.022$, HR = 1.630), *midline/deep tumor location* ($p = 0.005$, HR = 8.412), *tumor close to language area* ($p = 0.020$, HR = 1.917). Conversely the undermentioned variables were found to have a **reduced HR**: *female sex* ($p = 0.011$, HR = 0.565), *IDH-1 mutation* ($p = 0.007$, HR = 0.372), *use of intraoperative IONM* ($p = 0.002$, HR = 0.368), *preoperative DTI acquisition* ($p = 0.004$, HR = 0.406), *preoperative fMRI acquisition* ($p = 0.007$, HR = 0.368), *preoperative language deficit* ($p = 0.036$, HR = 0.553).

5.4.8.6.2 Impact of postoperative variables on Overall survival

When assessing impact of postoperative covariates on OS, the following were found were found to have an **increased HR**: *postoperative CE-tumor volume* ($p = 0.002$, HR = 1.057) and *postoperative language deterioration* ($p < 0.001$, HR = 9.194). Conversely, *achievement of FLAIR-tumor 75% EOR* ($p = 0.013$, HR = 0.404), *higher CE-tumor EOR* ($p = 0.035$, HR = 0.990), *achievement of CE-tumor GTR* ($p = 0.024$, HR = 0.558) entailed a **reduced HR**.

5.5 Discussion

The main aim of the present research was to evaluate the clinical applications of advanced MRI techniques as cutting-edge MR tractography and task-based functional MRI in the perioperative setting of a large series of patients (234 surgical procedures among 226 patients) undergoing resective surgery for brain gliomas.

Concurrently, the clinical application of innovative image processing techniques as advanced 3D rendering for virtual reality and surgical planning/simulation, together with the utilization of modern intraoperative neuroimaging devices such as neuronavigation and ultrasound systems were assessed in the same cohort and compared to the current gold standard, represented by DES and intraoperative neuromonitoring (IONM).

5.5.1 Advanced functional imaging (DTI and fMRI) in glioma surgery

Diffusion tensor imaging (DTI) is a noninvasive advanced MR technique which represents, *in vivo*, the probable location and orientation of white matter tracts and their relationships with the neoplasm (Chanraud *et al.*, 2010; Dubey *et al.*, 2018). This has the potential to provide the neurosurgeon precious information, both prior to surgery, when deciding indications to resection and selecting the optimal approach in case of proximity with highly eloquent cortical and subcortical areas, and during the procedure when correct identification of the latter regions is pivotal (Arfanakis *et al.*, 2006; Basser *et al.*, 2000; Berman, 2009; Chanraud *et al.*, 2010; Dubey *et al.*, 2018; Karimi *et al.*, 2006; Provenzale *et al.*, 2006; Yu *et al.*, 2005). A published survey reported that only about 64% of European neurosurgical centers have access to tractography studies preoperatively (Thust *et al.*, 2018b). When available, the main reason DTI tractography is requested remains presurgical planning for about 90% of cases, while only 20-60% of neurosurgeons eventually import DTI into the intraoperative neuronavigation system, using this data as guidance during surgical resection (Conti Nibali *et al.*, 2019; Thust *et al.*, 2018a; Thust *et al.*, 2018b). In most reported cases (94%), the technique was used to identify the corticospinal tract (CST), followed by the fascicles involved in language abilities and optic radiations (OR) (Conti Nibali *et al.*, 2019; Thust *et al.*, 2018a; Thust *et al.*, 2018b). In the present study, 30.8% of cases overall were preoperatively studied with DTI (it raised to 45% when dealing with tumors in proximity to motor or language functional areas), with CST (89%), arcuate fasciculus (AF; 62%) and OR (44%) being the most represented outputs. DTI was integrated into the neuronavigation system in all of our cases.

BOLD fMRI has three principal functions in the neurosurgical setting: preoperative noninvasive assessment of the relationship between tumors and eloquent cortical areas, intraoperative guidance of DES mapping and tumor resection, and postoperative evaluation of the surgical effects on functional areas (Rigolo *et al.*, 2011; Sang *et al.*, 2018). A survey conducted showed that only about 30-50% of the neurosurgical centers have access to preoperative fMRI investigation, which is requested, when available, mostly for surgical planning, being imported in the intraoperative neuronavigation systems in only about 60% of cases (Conti Nibali *et al.*, 2019; Freyschlag *et al.*, 2018; Thust *et al.*, 2018b).

5.5.1.1 DTI/fMRI in preplanning

Integrating DTI information in the presurgical planning is advantageous for both the patient and the surgeon as it enhances the understanding of the interactions between the tumor and eloquent areas, aiding in the formulation of a tailored, patient- and disease-specific approach, possibly decreasing the danger of neurological morbidity after surgery (Costabile *et al.*, 2019; Dubey *et al.*, 2018). Previous studies found that functional information from fMRI and DTI tractography were more accurate than those derived merely from anatomical landmarks (Kleiser *et al.*, 2010) (**Figure 5.8**) in the localization of functional areas and that the disclosure of white matter and cortical eloquent regions from DTI/fMRI led the surgeon to choose a different site of corticectomy and surgical approach in about 16%-21% of cases (Dimou *et al.*, 2013; Romano *et al.*, 2009; Romano *et al.*, 2007; Van Heerden *et al.*, 2014; Wengenroth *et al.*, 2011; Zakaria *et al.*, 2017). More recent studies also revealed that DTI/fMRI allows a preoperative estimation of surgery-related damage (Fernandez-Miranda *et al.*, 2010) and EOR (Castellano *et al.*, 2012), increasing the achievement of the latter in about 64-80% (Khan *et al.*, 2019; Romano *et al.*, 2009; Romano *et al.*, 2007; Shalan *et al.*, 2021) cases, while significantly improving the neurologic outcome (Cao *et al.*, 2010).

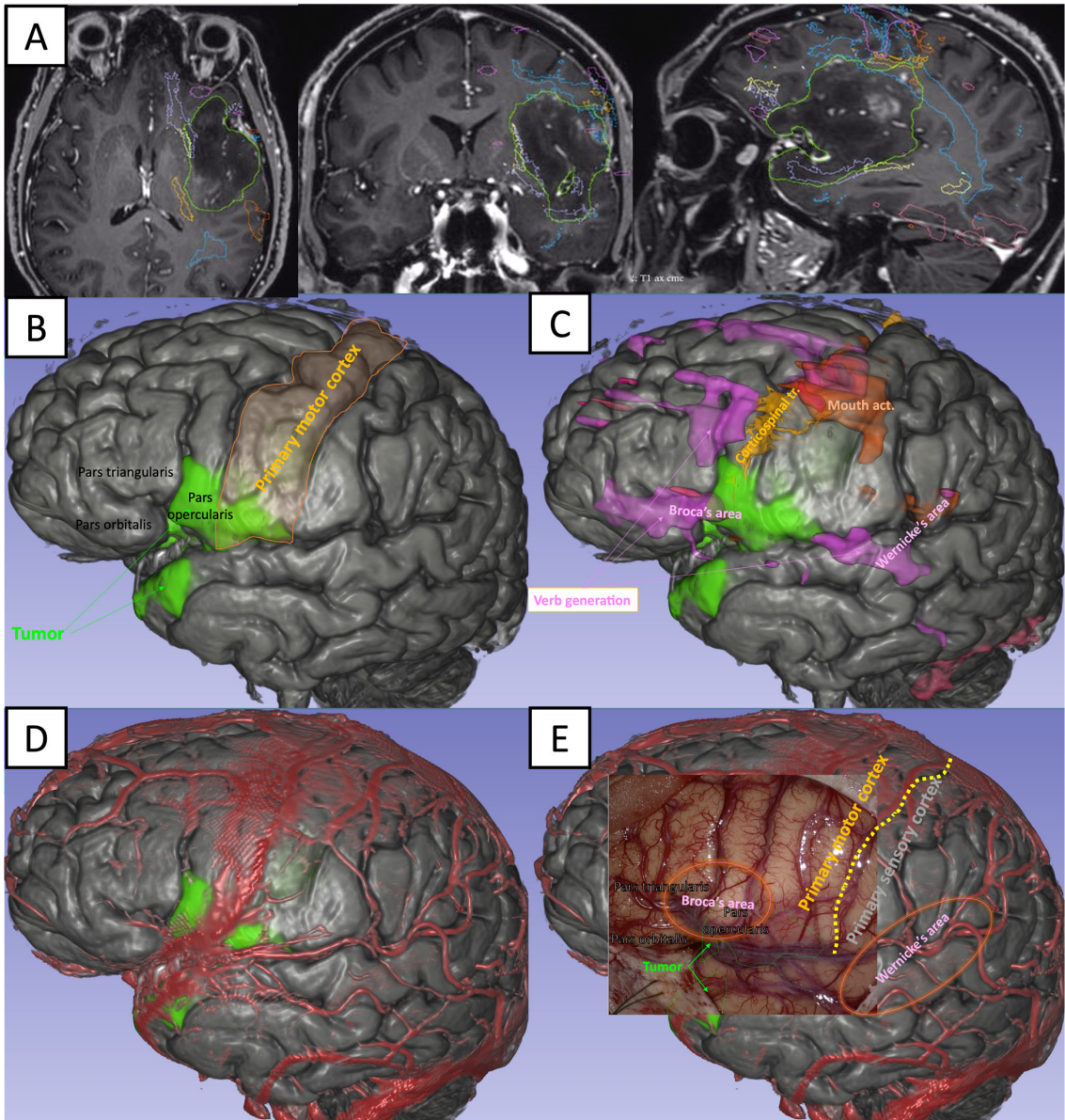


Figure 5.8 - Illustrative case showing the aid provided by morphological and advanced imaging (fMRI and DTI) in identifying the critical functional areas.

(A) Axial, coronal, and sagittal contrast-enhanced T1-weighted imaging of a left fronto-temporal-insular WHO grade III anaplastic astrocytoma are displayed; tumor and functional data from DTI and fMRI elaborations are delineated with different colors. (B) Anatomical landmarks are initially used to identify the prefrontal gyrus, pars opercularis, triangularis, and orbitalis. (C) Fiber tracts (corticospinal, arcuate, inferior fronto-occipital fasciculus, and uncinate fasciculus) and areas of activation (verb generation, fluency, naming, and mouth activation) were elaborated from DTI and task-based BOLD fMRI in the present case; their information integrated into the anatomical landmarks proved extremely helpful in the identification of primary motor cortex, Broca's area, and Wernicke's area, subsequently guiding the intraoperative cortical and subcortical mapping. (D) Vascular anatomy is carefully assessed during the preplanning since it represents a crucial feature for both surgical approach and anatomical orientation in the intraoperative setting (E). The exact locations and limits of the motor and language functional areas are eventually confirmed intraoperatively by direct electrical stimulation (DES).

5.5.1.1.1 Preoperative use of DTI for candidate selection, preplanning, and outcome prognostication

Brain tumors and surrounding edema are well known to alter white matter tracts by displacing, infiltrating, or disrupting them (Dubey *et al.*, 2018; Jellison *et al.*, 2004; Sinha *et al.*, 2002). Incorporation of white matter fibers within the tumor boundaries can be present in LGGs, while fiber tracts displacement and destruction are generally seen in the case of HGGs (Bello *et al.*, 2008; Dubey *et al.*, 2018; Jellison *et al.*, 2004; Khan *et al.*, 2019; Shalan *et al.*, 2021; Witwer *et al.*, 2002; Zhukov *et al.*, 2016). These features have profound implications for the surgical planning and the EOR amenable in the specific case (Dubey *et al.*, 2018; Shalan *et al.*, 2021). If preoperative imaging demonstrated displaced (but intact) fiber tracts, the surgical approach should be customized in order to preserve those fibers during tumor removal (Shalan *et al.*, 2021). Conversely, if specific white matter tracts appeared disrupted by the tumor, GTR could probably be attempted without concerns about further functional damage, although limitations in DTI sensibility (with possible false negatives due to edema and tumor infiltration, or other intrinsic limitation of the technique) have always to be taken into account (Jellison *et al.*, 2004; Salama *et al.*, 2017; Shalan *et al.*, 2021).

As viewable in **Table 5.24**, the preoperative status of white matter fibers can vary significantly according to the tumor type, grade, location, the studied white matter tract and DTI acquisition and elaboration technique (Shalan *et al.*, 2021).

| Authors | Year | Cases | Preoperative status of white matter fibers | | | |
|---|------|-------|--|--------------|--------------|------------|
| | | | Intact | Displacement | Infiltration | Disruption |
| Shalan et al. (Shalan <i>et al.</i> , 2021) | 2021 | 20 | 10% | 75% | 60% | 20% |
| Zhukov et al. (Zhukov <i>et al.</i> , 2016) | 2016 | 29 | 41.1% | 24.1% | 34.5% | N/A |
| Dubey et al. (Dubey <i>et al.</i> , 2018) | 2018 | 34 | N/A | 52.9% | 32.3% | 11.7% |
| Khan et al. (Khan <i>et al.</i> , 2019) | 2019 | 128 | N/A | 32.8% | 25% | 42.2% |

Table 5.24 - Preoperative status of white matter fibers among different published series.

N/A = not available/applicable

A study by Castellano *et al.* showed that data from DTI is able to predict the EOR, and therefore prognosis, since tumors showing white matter tracts infiltration were less likely

to be completely resected compared to those cases with intact fiber tracts (Castellano *et al.*, 2012). This was also confirmed in another clinical series from Dubey *et al.* (Dubey *et al.*, 2018), where 34 patients underwent a preoperative design of the surgical corridor and planning of the highest EOR achievable without affecting the eloquent tracts: GTR was obtained in 61% of cases with dislocated (but intact) fibers, while in 31% of cases with tracts infiltration/disruption (Dubey *et al.*, 2018).

DTI analysis is able to predict also functional outcome, as a reorganization of tracts after resection (with consequent functional improvement) is more likely to happen in neoplasms generating displaced or edematous patterns than infiltrated and disruptive patterns (Shalan *et al.*, 2021). This hypothesis was confirmed both clinically and radiologically, with disruptive patterns showing higher rates of functional deterioration, lower rates of functional improvement, and lower case without fiber tracts normalization and FA improvement when comparing pre- and postoperative DTI (Alexander *et al.*, 2003; Khan *et al.*, 2019; Laundre *et al.*, 2005; Lazar *et al.*, 2006; Li *et al.*, 2019b; Nimsky *et al.*, 2005a; Shalan *et al.*, 2021).

MR tractography and fMRI have also demonstrated usefulness in candidate-selection for resective surgery, for instance, excluding cases harboring neoplasms in close relation to critical eloquent areas (Berntsen *et al.*, 2010; Costabile *et al.*, 2019). However, the identification of an infiltrated tract by DTI studies or the activation of a cortical area involved by the tumor at fMRI does not necessarily indicate that those regions are preserving their normal function. It is a common experience that considerable large portions of DTI-reconstructed fiber tracts within the tumor are eventually found as non-functional during IONM and can be safely removed if that allows the achievement of a higher tumor EOR rate (Conti Nibali *et al.*, 2019). This concept also applies to activated cortical areas at fMRI.

Furthermore, as acquisition techniques and analyses keep improving, DTI and fMRI could prove valuable in those individuals with contraindication to awake surgery, therefore not amenable to surgical mapping for language and cognitive functions, possibly allowing safe procedures under general anesthesia (Costabile *et al.*, 2019; D'Andrea *et al.*, 2016; Soni *et al.*, 2017).

5.5.1.2 Intraoperative use of DTI/fMRI

5.5.1.2.1 Intraoperative use of DTI/fMRI and EOR

Intraoperative use of DTI has been indicated as significantly contributing to obtaining maximal safe resection (Bello *et al.*, 2008). A large amount of literature has been published on applying this tool in the neurosurgical routine, with nearly all authors reporting a favorable experience. However, it is extremely problematic to objectively quantify the degree of surgical improvement and the effects on patient outcome since most of these cohorts are extremely heterogeneous and many biases from lack of randomization are present (Conti Nibali *et al.*, 2019; Potgieser *et al.*, 2014).

Wu *et al.* (Wu *et al.*, 2007) conducted a prospective study of 328 cerebral gliomas, randomizing patients to either “functional” navigation (including DTI; n = 118) or conventional neuronavigation (with only volumetric conventional MR sequences; n = 120). In the group with DTI, they noticed a significantly greater rate of GTR (74.4% vs. 33.3%, p < 0.001) among HHGs. Another series of 375 cases from Sang *et al.* (Sang *et al.*, 2018) confirmed a significant increase in GTR rate (94.8 vs. 84.1%, p = 0.001), among both LGG and HGG, in patients operated under functional neuronavigation (DTI ± fMRI).

In the present series, when considering lesions close to **motor** functional areas, preoperative DTI was associated with an increased rate of *FLAIR-tumor* EOR (median 82.4 vs. 62.7%) among WHO grade II and a slightly higher *FLAIR-tumor* EOR in WHO III neoplasms (72.3 vs. 69.0%). On the contrary, DTI seemed to be correlated with a (non-significant) reduction of *FLAIR-tumor* EOR in WHO grade IV (70.9 vs. 76.0%). This could perhaps be explained by the fact that in case of no or poorly enhancing tumor (most of WHO II-III lesions) the preoperative and intraoperative knowledge of the actual position of eloquent fiber tracts could induce the surgeon in seeking the highest degree of safe resection of T2/FLAIR hyperintense white matter, with relatively low apprehension for neurological morbidity. On the contrary, in the case of a tumor with wide areas of necrosis and contrast enhancement (as in most WHO grade IV tumors), the awareness of multiple eloquent tracts embracing the tumor enhancing/necrotic core might lead the neurosurgeon to a more cautious resection of the surrounding T2/FLAIR hyperintense white matter, “sticking” to the tumor mass that appears macroscopically altered at gross inspection and tactile sensation. Similar findings were observed in the case of

preoperative fMRI acquisition, with a consistent increase in median *FLAIR-tumor* EOR among LGGs (82.4 vs. 62.7%) and lower impact when dealing with contrast-enhancing neoplasms (WHO III-IV).

When considering *CE-tumor* among HGGs (WHO III and IV), both DTI and fMRI appeared to provide a similar median (close to 99% independently from the preoperative acquisition of advanced imaging) but higher mean (from about 91% to 95% when DTI and/or fMRI were available) EOR values.

When evaluating tumors close to **language** functional areas, preoperative DTI still proved capable of increasing *FLAIR-tumor* resection among WHO grade II tumors (80.1 vs. 66.6%), while no aid seemed to be derived, in the present series, from the preoperative fMRI acquisition: median value appeared lower in the case of fMRI: 72.1 vs. 89.4% (although this latter analysis was based on only 15 patients). Again, no benefit was noticeable from DTI and fMRI in *FLAIR-tumor* resection among higher grade gliomas, while an increase in *CE-tumor* median (from about 98 to 100%) and mean EOR (from about 91 to 95%) were noted in the same group (WHO III and IV tumors).

At multivariate analysis, DTI showed an extremely weak tendency towards statistical significance (p values between 0.1 and 0.15, with odd ratios higher than 2.5), although never reaching it, in the prediction of higher *FLAIR* and *CE-tumor* EOR and lower *residual postoperative volume*; fMRI, on the contrary, showed an opposite trend.

5.5.1.2.2 *Intraoperative use of DTI/fMRI and neurological outcome*

The incorporation of DTI tractography in the intraoperative setting has also been correlated with a general improvement of neurological outcome (Shalan *et al.*, 2021). Bello *et al* confirmed the advantages of DTI integration in the surgical workflow in a large series (Bello *et al.*, 2010; Bello *et al.*, 2008), obtaining a high rate of functional preservation, particularly in LGGs. During a study of 35 glioma patients (Caverzasi *et al.*, 2016a), Caverzasi *et al.* reported that patients with postoperative evidence of preserved left superior-longitudinal and arcuate fasciculus did not show persistent deficits in the language function; conversely, an apparent deflection of the same tracts exhibited a higher association with persistent language disturbances. The results from this group seem to support the importance of the intraoperative utilization of these tracts to prevent language morbidity (Caverzasi *et al.*, 2016a). Sang *et al.* reported a significantly lower

rate of postoperative complications (6.3 vs. 16.7%, $p = 0.003$) and higher KPS scores among cases operated under functional navigation (Sang *et al.*, 2018). In the study from Wu *et al.*, higher Karnofsky Performance Scale scores were noted in HGGs (median 77 vs. 52 points, $p = 0.001$) and LGGs (median 93 versus 86 points, $p < 0.001$) when integrating DTI in the neuronavigation system; additionally, a lower postoperative motor deterioration (15.3 vs. 32.8%, $p < 0.001$) was documented with the same technique (Wu *et al.*, 2007).

Results in accordance with the previous literature were identified in our research, where the rate of **motor** function deterioration appeared lower in patients preoperatively studied with DTI (6.5 vs. 20%) and fMRI (10.3 vs. 14.9%). The rate of motor clinical improvement was higher in the case of DTI acquisition (30.4% vs. 18% for DTI) while slightly lower, but not statistically significant, among cases studied with fMRI (20.7 vs. 25.4%). Similarly, when assessing the **language** function, a lower rate of patients experienced clinical worsening at hospital discharge when studied with DTI (3% vs. 12.2%) or fMRI (4.5 vs. 9.6%) prior to surgery. Once more, the rate of postoperative language function improvement was higher whenever DTI (24.2% vs. 14.6%) and fMRI (22.7% vs. 17.3%) were available. In multivariate analysis, DTI was able to significantly predict a lower rate of *postoperative motor function deterioration* ($p = 0.014$, OR 0.029) and *any postoperative complication* ($p = 0.028$, OR 0.109) and a higher rate of *postoperative clinical improvement* ($p = 0.004$, OR 6.018); conversely, no significant advantage was identified with fMRI adoption.

5.5.1.2.3 Intraoperative use of DTI/fMRI and overall survival

A significant rise in OS was previously reported in the literature when functional data was integrated into the neuronavigation system (Sang *et al.*, 2018). Sang. *et al.* reported a significant gain in OS among both the whole cohort of 375 cases (from 30 to 39 months, $p < 0.001$) and the subgroup of tumors close to eloquent areas (from 25 to 39 months, $p = 0.012$), with an estimated reduction of the risk of death, calculated from Cox regression analysis, of 47% (Sang *et al.*, 2018). Wu *et al.* reported a significant median increment in OS (from 14 to 21.2 months) among HHGs operated with intraoperative DTI availability ($p = 0.048$), with an estimated reduction in death risk of 43% (Wu *et al.*, 2007).

The benefit in EOR rate and postoperative clinical outcome gathered by preoperative acquisition of advanced functional imaging (DTI and fMRI) was presumably reflected on the better related OS observed in our cohort too. A significant increase in OS was noted with either DTI (median estimated OS 20.2 vs. 9.7 months; $p = 0.038$) and fMRI (median estimated OS 20.2 vs. 10.9 months; $p = 0.023$) preoperative acquisition among tumors close to **motor** functional areas. A higher, but not statistically significant, OS was also noted among lesions close to **language** functional areas for DTI (median estimated OS 18.5 vs. 11.4 months) and fMRI (median estimated OS 18.5 vs. 9.6 months). At multivariate Cox regression analysis, DTI was related to increased survival ($p = 0.004$, HR 0.406), while fMRI did not reach the threshold of statistical significance.

These data, altogether, seem to point out a general benefit of DTI and fMRI on clinical and surgical outcome; nevertheless, it is important to highlight that these analyses suffered from a not negligible bias: lesion more critically located and closer to motor and language functional areas were more prone to be preoperatively studied with advanced functional imaging, meaning that surgery for most of these tumors harbored, at least in origin, fewer chances of achieving a GTR without postoperative neurological deficits and, therefore, a worse prognosis. Conclusively, we might state that the advantage that emerged in the present series from DTI and fMRI acquisition is probably an underestimation of the real benefit that these two advanced techniques might entail.

5.5.1.2.4 Combination of DTI and DES techniques

Numerous researches have established a direct association between DES current amplitude and the space separating the probe from the corticospinal tracts elaborated with DTI: the closer is the probe from the tracts, the lower stimulation current is needed to elicit a clinical response (Costabile *et al.*, 2019; Kamada *et al.*, 2009; Ohue *et al.*, 2012; Ostrý *et al.*, 2013; Shiban *et al.*, 2015; Zhuang *et al.*, 2016; Zolal *et al.*, 2012). This appears even more consistent when the potential brain-shift is corrected with intraoperative imaging acquisition as (MR or ultrasound) (Javadi *et al.*, 2017; Maesawa *et al.*, 2010; Nossek *et al.*, 2011; Ostrý *et al.*, 2013; Prabhu *et al.*, 2011; Shahar *et al.*, 2018).

Many studies have also validated DTI clinically in the noninvasive tracking of language tracts, such as the arcuate fasciculus, showing a high sensitivity (97%) when correlated with the results elicited by intraoperative DES (Bello *et al.*, 2008; Kuhnt *et al.*,

2012; Sang *et al.*, 2018; Stieglitz *et al.*, 2012). It has been reported that the occurrence of a temporary language impairment when performing high-frequency DES at the bottom of the resection cavity correlates with a distance from the stimulus site and the arcuate fasciculus less than 5 mm (Costabile *et al.*, 2019; Yamao *et al.*, 2017).

Since an exact relationship between current amplitude and space interval from the elicited tract has never been thoroughly assessed using verified models, we might assume that a DTI-DES combination, as opposed to DES only, might represent the current gold standard for mapping functionality. In particular, conjoining these two techniques has been proved to offer a higher efficacy in the intraoperative delineation of the CST, consenting mean EOR values over 97% when dealing with gliomas in critical functional regions (Costabile *et al.*, 2019; Javadi *et al.*, 2017; Zhu *et al.*, 2012).

5.5.1.2.5 DTI drawbacks

Unfortunately, DTI entails some limitations. First, it is a user-defined process; therefore, the results can diverge according to the parameters selected such as FA and angular thresholds, step length, numbers of sampling in a voxel length, site and dimension of the seed regions of interest drawn, the software utilized and user experience (Shalan *et al.*, 2021). The elaboration and evaluation of tractography data in the preoperative situation also imply some additional problems, predominantly associated with distinguishing among the anisotropy value reduction due to either actual neoplastic infiltration or peritumoral edema (Bello *et al.*, 2008; Dubey *et al.*, 2018). Consequently, a variable percentage of false-negative (due to white matter alteration) and false-positive (i.e., tracts with no clinical function) tracts can be elaborated (Conti Nibali *et al.*, 2019).

A particular limit of DTI tractography is its susceptibility to partial volume effects, inability to resolve white matter compositions when the same voxel is occupied by more than one fiber population (which affects the trustworthiness of tracking in areas containing many crossing routes) and relatively poor performance in portraying lateral projections compared to medial ones (Azad & Duffau, 2020).

Advances towards the resolution of these problems have been accomplished with the adoption of *alternative models* of calculation of the diffusion properties, *more complex imaging sequences* acquired from higher field MR scanners, and the use of *additional gradients* directions and magnitudes (Costabile *et al.*, 2019).

Alternative models implicate an expansion of the diffusion model to include diffusion features of a higher-order [e.g., diffusion kurtosis imaging (DKI)], the replacement of the tensor with a different shape [e.g., constrained spherical deconvolution (CSD)], or by modeling the Fourier transform relationship among diffusion MR signals and the underlying diffusion displacement [e.g., generalized Q-ball imaging] (Castellano *et al.*, 2017; Costabile *et al.*, 2019). While models like CSD and DKI necessitate more extensive imaging sets, enhancements of tractographic techniques can be achieved applying models different from standard DTI (Costabile *et al.*, 2019; Zhang *et al.*, 2013). For instance, it has been reported the possibility to visualize a motor pathway passing through regions of edema (not identifiable with DTI) using the Q-ball model (Castellano *et al.*, 2017; Costabile *et al.*, 2019; Zhang *et al.*, 2013).

Advanced diffusion imaging sequences comprise high angular resolution diffusion imaging (HARDI), diffusion spectrum imaging (DSI), Crossing Fiber Angular Resolution Intra-voxel structure (CFARI), and DKI (Wedeen *et al.*, 2008). DSI tractography has the advantage of detecting crossing fibers utilizing functions of probability density that specify microscopic displacements of MR-visible spins using 3D Fourier encoding of displacements (Costabile *et al.*, 2019). In contrast to regular DTI, DSI has the capability to identify crossing fibers and truthfully depict the convergence of different routes; conversely, HARDI creates maps that estimate the functions of diffusion orientation density (Costabile *et al.*, 2019; Wedeen *et al.*, 2008). Caverzasi *et al.* (Caverzasi *et al.*, 2016a) and Berman *et al.* (Berman, 2009) demonstrated that conjoining Q-ball and HARDI techniques perfected tractography resolution in areas characterized by a high density of crossing fibers, providing more detailed structures (and possibly more accurate presurgical information) compared to DTI tractography (Castellano *et al.*, 2017; Costabile *et al.*, 2019).

Moreover, to date, sophisticated acquisition sequences that compute *diffusion magnitudes and directions* involving complex distributions of intravoxel fiber orientation have been implemented; these methods rely on the enhancement of resolution by acquiring more sequences from a higher number of magnetic field gradient directions (Costabile *et al.*, 2019).

Apart from the intrinsic limitations of the DTI technique, other issues might come from its intraoperative utilization: a considerable brain shifting compromising DTI reliability

was reported in more than a third of cases (Azad & Duffau, 2020; Ostrý *et al.*, 2013). Considering the potential underestimation of the fiber bundles by DTI fiber tracking and the issues related to image-to-patient registration and intraoperative brain-shifting, a safety margin of about 5 mm during resection was recommended by some authors (Conti Nibali *et al.*, 2019; Nimsky *et al.*, 2006; Nimsky *et al.*, 2005a; Nimsky *et al.*, 2005b).

In conclusion, notwithstanding the multiple clinical applications for DTI within oncological and functional neurosurgery, this technique remains so far underutilized, lacking the support of level I evidence (Costabile *et al.*, 2019).

5.5.1.2.6 Functional MRI drawbacks

When compared to the gold standard (DES), fMRI's reported sensitivity and specificity vary widely among the literature, probably due to a profound lack of standardization, with different task selection, patients' compliance, protocols of acquisition, and different post-processing and thresholding choice. Giussani *et al.* (Giussani *et al.*, 2010) reported a fMRI sensitivity ranging from 59% to 100% and specificity ranging from 0% to 97%, whereas Kuchcinski *et al.* (Kuchcinski *et al.*, 2015) described a sensitivity and specificity of 37.1% and 83.4%, respectively (Azad & Duffau, 2020).

Multiple studies have confirmed a fair accuracy of fMRI in predicting *motor* cortical areas location, despite sensibility and specificity might fall under 35% in cases of recurrent tumors (Conti Nibali *et al.*, 2019), while reliability in *language* function localization is more uncertain and debated (Krings *et al.*, 2002; Sang *et al.*, 2018). In a recent metanalysis, mean fMRI sensitivity and specificity for the detection of *motor* functional areas were 92% (range 88-100%) and 76% (range 68%-87%), respectively (Metwali *et al.*, 2019); conversely, the mean sensitivity and specificity of fMRI lowered to 80% (range 64%-100%) and 72% (range 50%-89%), respectively (Metwali *et al.*, 2019), when aiming to identify *language* functional areas (Azad & Duffau, 2020). Different studies with smaller samples also confirmed higher sensitivity and specificity for the *motor* mapping (85%-88% and 81%-87%) compared to the *language* one (40%-80% and 74%-84%) (Azad & Duffau, 2020; Bizzi *et al.*, 2008; Ille *et al.*, 2015; Morrison *et al.*, 2016).

Some authors state that the manifestation of activated areas in fMRI imaging does not necessarily preclude their resection during surgery and, therefore, should not be considered for treatment decision per se (Conti Nibali *et al.*, 2019). Furthermore, fMRI alone does not provide information regarding the subcortical connectivity, that usually represents the main and most challenging functional boundary during glioma surgery (Azad & Duffau, 2020).

Due to the aforementioned flaws, some authors concluded that language fMRI cannot replace DES, particularly when dealing with tumors close to language functional areas (Azad & Duffau, 2020; Giussani *et al.*, 2010; Sang *et al.*, 2018). In the latter case, apart from the relatively low specificity and sensitivity, a key limitation of fMRI is also its inability to discern between compensable regions that can be safely removed, and critical regions to be well-preserved (Azad & Duffau, 2020).

Nevertheless, it must be considered that language mapping with DES requires an awake procedure on an extremely collaborative patient, which increases the time and risks of surgery and that could require the sudden need for deep sedation in case of emerging complications (surgical, anesthesiologic, or DES-related) or the inability of the patient to cooperate. Additionally, it has to be considered that most uncertainties and errors found in fMRI outputs are caused by patient's insufficient cooperation and trustworthiness during MR acquisition, and there are no guarantees that the same patient will prove to be more fit and reliable in performing tasks in an even more challenging setting such as an awake surgery. DES also entails other potential weaknesses; particularly regarding the generation of after-discharge activity (Wyler & Ward, 1981), the specificity of the language task (Roux *et al.*, 2007; Sang *et al.*, 2018), and local hemodynamic changes (Borchers *et al.*, 2012; Costabile *et al.*, 2019).

5.5.2 Impact of advanced 3D imaging preplanning on surgical outcome.

5.5.2.1.1 Advantages

The possibility of 3D imaging fusion, in which many sequences, each one carrying its unique information, can be meshed in a single dataset, has enhanced the expansion of 3D rendering and virtual reality in neurosurgery, consenting to an interactive appraisal of surgical procedures simulating expected surgical field, along with an easy acquisition of detailed anatomical data (Kin *et al.*, 2017). This represents a revolution since, historically,

when studying the preoperative neuroimaging of a novel case, the neurosurgeon needed to build in his/her mind a virtual, tridimensional representation of all the structures involved in the intervention starting from the observation of sequential 2D slice images; this requires a complicated mental process that mainly relies on the surgeon's preexisting knowledge and practice. Virtual reality is able to overcome these difficulties: 3D models generated can be easily displayed on any personal computer and explored by everyone (independently from the neurosurgical experience); moreover, they can be shared, in a straightforward manner, with other, less expert, individuals (Kin *et al.*, 2017; Ruparelia *et al.*, 2020). Virtual simulation of the procedure is noninvasive and repeatable countless times; for these reasons, it is specifically ideal in the education and training of neurosurgeons inexperienced in that particular procedure (Kin *et al.*, 2017).

A questionnaire survey conducted by Oishi *et al.* reported that the 3D preplanning approach was way more beneficial and practical compared to the 2D approach in 44% of cases for strategy evaluation, facilitating intraoperative dissection and removal of brain lesions and proceeding according to what planned in most cases (Oishi *et al.*, 2012). The authors also noticed that 2D images were not sufficient to formulate a feasible surgical plan in about 20% of the cases, as opposed to 3D images which invariably succeeded (Oishi *et al.*, 2011b).

Since the relative position between anatomical landmarks remains unchanged even after brain-shifting phenomena caused by dural opening and surgical manipulation, visual navigation of the cortical anatomy assimilated with this technique does not suffer the same limitations of neuronavigation systems (those strictly rely on the absolute position of intracranial structures as registered preoperatively) (de Oliveira Santos *et al.*, 2018; Gosal *et al.*, 2021; Harput *et al.*, 2014).

Another great advantage of this image-guided surgery, compared with other intraoperative tools, is that it can be inexpensive and readily available in practically any setting (Gosal *et al.*, 2021; Malilay *et al.*, 2021), and, for this reason, it might possibly become a precious asset for neurosurgeons in charge of the over 5 billion people living nowadays in resource-constrained countries (Servadei *et al.*, 2018), where other expensive image-guided surgery tools have poor availability (Malilay *et al.*, 2021).

5.5.2.1.2 Integration of DTI/fMRI

A further step for virtual reality is the integration of morphological data from conventional volumetric MR/CT images with functional data from advanced neuroimaging modalities as DTI and fMRI. The latter could produce a comprehensive patient- and disease-specific functional model for better surgical planning, with the aim to avoid critical regions (vessels, eloquent cortical or subcortical areas), identify safe entry sites, lower surgical time, and reduce invasiveness (i.e., the size of the craniotomy) (an illustrative case depicted in **Figure 5.9**). In particular, with this technique, the relation between the tumor burden and surrounding (or incorporated) fiber tracts and eloquent cortical areas can be gathered much easily and faster, compared to their representation as lines plotted on 2D slicing images (Qiu *et al*, 2010a). However, to date, this integration of advanced functional MR to conventional imaging techniques in virtual reality has been reported by only a few authors (Goha, 2006; Lo *et al*, 2007; Qiu *et al*, 2010a; Spicer *et al*, 2004; Tronnier *et al*, 2000).

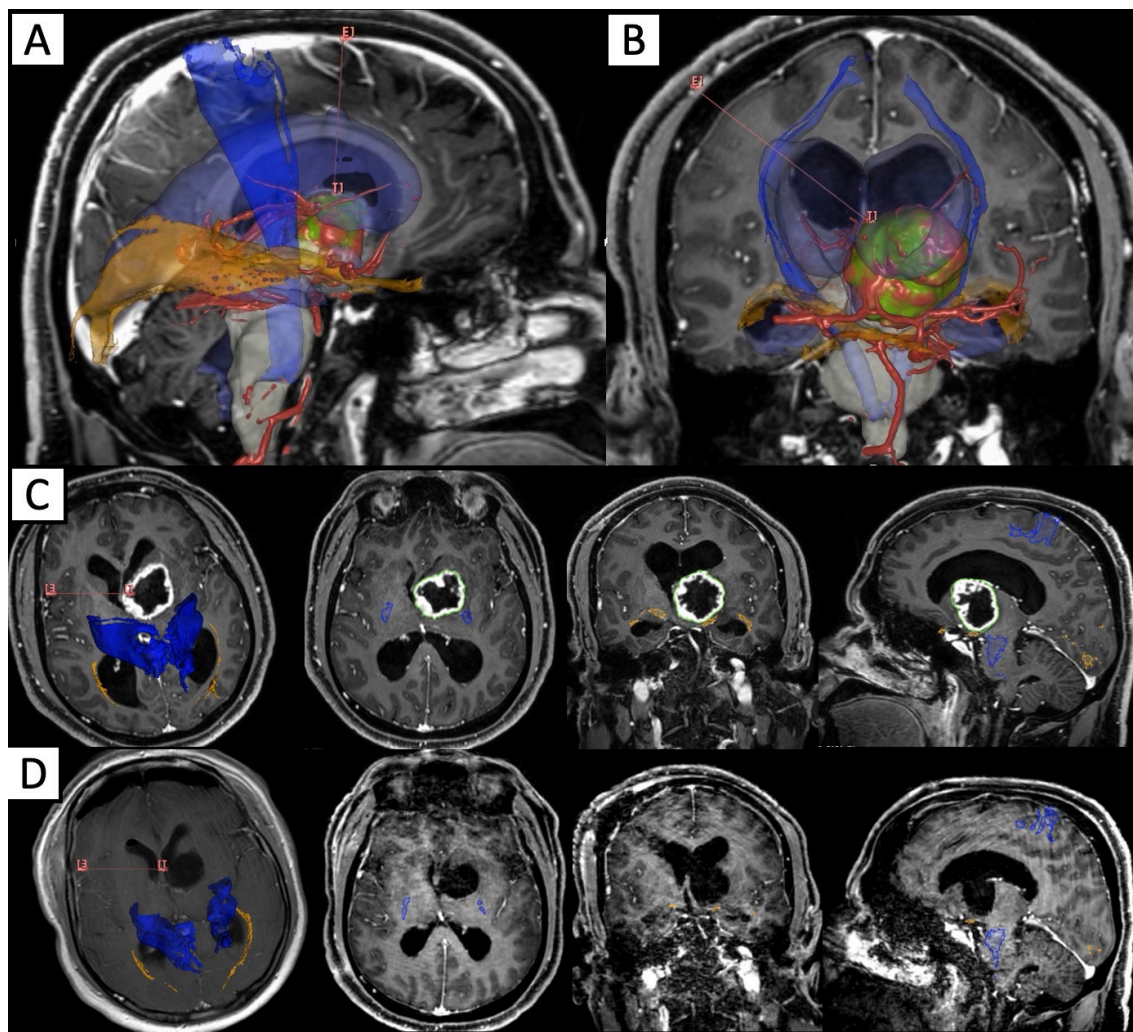


Figure 5.9 - Illustrative case of an advanced 3D preoperative planning of a thalamic lesion integrating direct and geometric rendering techniques.

The deep venous system surrounding the tumor was represented via direct volume rendering of a masked contrast-enhanced 3D T1 weighted imaging; corticospinal tracts and optic radiations from DTI tractography were integrated into the planning and rendered, together with lateral ventricles, using geometric techniques. The tumor was previously hypothesized to be a high-grade glioma and judged inoperable by a different center and referred to radiotherapy; considering the patient's young age (33 years old), after careful functional preplanning and risks assessment, surgical resection was attempted. All the structures above were pivotal in the decision of the final trajectory; the tumor was removed entirely via contralateral ventricular access using a portal system (Vycor, Vycor Medical Inc. USA); the patient did not suffer from any neurological deficit. The final histological diagnosis was Pilocytic astrocytoma

5.5.2.1.3 Clinical results from virtual reality

Clinical evaluations of virtual reality in surgical planning/simulation reported in previous literature were predominantly qualitative, with quantitative assessments only performed using surveys or founded on pre-defined research interrogations/hypotheses concerning diagnosis and technical accuracy: no articles analyzed 3D simulation in relation to surgical outcomes in a quantitative manner (Kin *et al.*, 2017). Moreover, the

description about image processing phase and volume rendering techniques was largely unsatisfactory among most published studies, denoting that the precision, risk of bias, reproducibility and level of evidence, has to be engaged in the next future to achieve more advances and eventually a definite clinical application (Kin *et al.*, 2017).

Authors usually reported a subjective clinical advantage from the virtual simulation of the surgical procedure. The main documented advantages were the following. It permits concurrent depiction of several sequences from distinct imaging morphological modalities (i.e., MR, CT) (Kin *et al.*, 2017). It provides patient-specific anatomy along with the specific disease-related modifications (as neoplastic invasion and displacement of surrounding brain structures) (Kin *et al.*, 2017; Stadie *et al.*, 2008). The detailed tridimensional information about the complicated spatial relationships between the tumor and surrounding structures can be easily and directly acquired (while it is difficult to mentally process them starting from 2D image sections) (Kin *et al.*, 2017). Data from advanced functional and physiologic neuroimaging techniques can also be integrated into the virtual model (i.e., DTI, fMRI, PWI, DWI, MRS, as long as PET with different tracers) in order to display the tumor volume (and its different metabolic regions) together with the morphological and functional anatomy to be preserved (Qiu *et al.*, 2010b; Takahashi *et al.*, 2014; Zhao *et al.*, 2012). It can provide spatial depiction through the same visual field expected during microsurgery, which is particularly helpful in the selection of the most suited surgical approach) (Kin *et al.*, 2012; Oishi *et al.*, 2012; Stadie *et al.*, 2008; Yoshino *et al.*, 2013) and allows the surgeon to familiarize with the positioning of all the structures, memorizing them in advance and subsequently providing him/her a “*déjà-vu*” experience during actual surgery (possibly reducing the risk of disorientation and the time needed to reorient) (Oishi *et al.*, 2011a). Lastly, contrarily to intraoperative neuronavigation, it does not suffer from the issue of brain-shift and the displayed anatomy can be carefully evaluated in advance for as long as needed without impacting on the duration of surgery.

Qiu *et al.* investigated the advantages of DTI integration in the preoperative virtual reality simulation using a tool denominated Dextroscope; the study included 45 patients with cerebral gliomas, the majority being WHO grade II astrocytomas. Integration of the pyramidal tracts into the 3D planning was reported to influence the surgical approach selection and patient positioning, but also the final EOR. Although no association

between the tumor EOR hypothesized preoperatively and the final one reached was reported, they suggested that preoperative rehearsal could facilitate a more aggressive resection of the infiltrating tumor by enhancing neurosurgeon's confidence in the ability to safely preserve critical structures. A GTR was obtained in 73.3%, with a 13.3% rate of motor function deterioration and 20% improvement (Qiu *et al.*, 2010b).

Since a quantitative assessment of this technique's impact on surgical and clinical outcomes is lacking in the current literature, the present represents the first study analyzing, in terms of EOR, functional preservation and OS, the possible benefits of advanced 3D preplanning using combined direct and surface volume rendering techniques and integrating both morphological and advanced functional imaging (DTI, fMRI) datasets in a large neurosurgical series (64 cases over a cohort of 234 patient). Although we believe that these represent only preliminary data from an initial experience, advanced 3D imaging preplanning resulted, for what concerns *FLAIR-tumor*, in a higher median EOR rate in LGGs (93.1 vs 79.5%; $p = 0.126$), a higher rate of postoperative tumor remnant $\leq 5 \text{ cm}^3$ (73.3% vs. 52.9%; $p = 0.181$), a higher rate of LGGs achieving at least 90% (60% vs. 29.4%; $p = 0.043$) and 75% (75% vs. 54.3%; $p = 0.073$) of EOR rate. When considering *CE-tumor* in HGGs, EOR was higher (median 99.5 vs 98%; mean 97 vs 92%; $p = 0.080$) when 3D preplanning was performed; the latter was also correlated with a higher rate of cases achieving GTR (47.2 vs 39.5%), $\geq 98\%$ EOR (72.2% vs. 52.1%, $p = 0.033$), $\geq 90\%$ EOR (77.5% vs. 73.2%; $p = 0.089$) and postoperative residual $\leq 2 \text{ cc}$ (80.5% vs 71.5%). A lower motor (8.8 vs. 16.1%) and language (7.4 vs. 8.5%) function deterioration was identified in those cases with 3D preplanning. OS in all WHO grade IV was higher among patients studied with preplanning (median 14.5 vs. 11.1 months) and, when analyzing specifically tumors located close to eloquent areas, median OS increased from 10.9 to 12.2 for motor functional areas, and 8.9 to 14.5 months for language functional areas, when 3D preplanning was available. However, it was not possible to identify significant associations at multi-variate analysis between advanced 3D imaging preplanning and surgical/clinical outcomes.

5.5.2.1.4 Drawbacks

One main limitation of 3D virtual representation is related to the time needed for image processing, which has been reported to vary from approximately 10 min to over six hours

(Kin *et al.*, 2017), mostly depending on the operator's acquaintance with the technique, software used, and the quality of output sought. However, the time needed to process a single model can be reduced to an average of 1-2 hours when experience from a large number (>100) of cases is gathered, demonstrating that building 3D representations can be reasonably integrated into the clinical routine (Kin *et al.*, 2017). Similar findings were noted in our experience with processing time around 4-6 hours for the first cases approached with this technique, while it generally took less than 2 hours in the last elaborated cases (notwithstanding the dramatic improvement in the output quality).

Despite the clear clinical value and easy availability, the adoption of these image processing software is still unpopular among most neurosurgeons, mostly because of the complex user interface and the long learning curve (Gosal *et al.*, 2021; Harput *et al.*, 2014). Hence, these platforms continue to be used mainly by diverse professional figures, largely in a research setting (Gosal *et al.*, 2021).

The lack of evidence (especially from series reporting quantitative assessments) and standardization of the image processing techniques still represent a major issue in the validation of this tool. Additionally, it has to be noticed that a surgical simulation from 3D rendering is not able to provide information regarding all the possible surgical issues, such as the tumor's bleeding attitude, hard consistency and attachment to the surrounding critical structure without an easy cleavage plane (Oishi *et al.*, 2011b); those problems can lead to procedure abortion regardless of the EOR planned preoperatively. Moreover, virtual models have some limits in the visual resolution of the fine anatomy, mainly depending on the quality and resolution of the processed volumetric imaging sequence; for instance, Giordano *et al.* when analyzing 3D-rendered surrounding venous anatomy in 33 pineal tumors, concluded that the VR models resolution was adequate to represent only medium-sized veins but not smaller ones (Giordano *et al.*, 2011).

5.5.2.1.5 *Future directions*

No statistically significant association was found in our series between advanced 3D imaging preplanning and surgical or clinical outcomes, despite essentially observing better values. However, these represent preliminary results of an initial experience in a technique requiring a not negligible learning curve and, that, due to the relatively long time necessary for image processing (especially when approaching the first elaborations),

was utilized predominantly in those considered the most challenging cases. We believe that the higher experience gathered in our center over the last few years, that brought to a dramatical boost in the quality and fidelity of the 3D representation achieved in the latest elaborated cases, together with a higher number of cases studied (possibly from an unbiased candidate selection), will provide much better and significant results in the next future.

Other interesting, ongoing expansions of virtual reality's clinical applications in the intraoperative setting are represented by its integration with the real world using operating microscopes, exoscopes and glasses equipped with augmented-reality and mixed-reality technologies (Kin *et al.*, 2017). Likewise, also the rapid development, availability, and application of 3D printing technology in neurosurgery will probably revolutionize its teaching and planning (Randazzo *et al.*, 2016), since it becomes straightforward to convert 3D rendered volumes into 3D printed models that can be assessed preoperatively but also taken to the operating room for surgical reference and guidance.

5.5.3 Other considerations regarding the present series

In order to pursue the aims of the study and validate advanced neuroimaging techniques in this markedly heterogeneous cohort, a general analysis (and comparison with other published series in literature) of the preoperative characteristics and clinical and radiological outcomes of the whole population was deemed necessary as a preliminary step. Discussion on the results of this preparatory part of the experiment is reported in the relative paragraphs (A.5) of the **Appendix**.

5.5.4 Study limitations

Despite its innovativeness, this study entails some limitations. First, although most data were prospectively collected, the analyses are inherently limited by the retrospective design, which might have generated some degree of selection bias and makes it problematic the determination of direct causal relationships. Generally, randomized control studies would be ideal, but such studies are poorly ethical and practical in this setting. We tried to constraint selection bias by including all consecutive glioma patients operated from 2016 to 2019 in a single institution.

We were not able to analyze functional clinical data following hospital discharge: it is reasonable to believe that a consistent part of patients might have shown a resolution or at least a significant improvement of the symptoms they suffered in the early postoperative period. No analysis was performed on the effect of advanced neuroimaging and intraoperative tools on the long-term radiological outcome (i.e., progression-free survival). Additionally, some patients were lost at FU and complete data were missing in a few cases.

Despite being quite large, this cohort was extremely heterogeneous regarding patients' characteristics and tumor histology, grade, and location: the need for stratifying analysis among different subpopulations might have generated false-negative results due to the reduced sample size; this was especially true in the smaller subcohort of lower-grade gliomas. Histopathological and molecular data such as IDH-1 status, MGMT status, 1p/19q codeletion, and Ki-67 expression were not available in all cases and since all the histopathological diagnoses were performed between 2016 and 2019, some data were missing to allow a proper reclassification of all tumors according to the recently introduced WHO 2021 classification.

As previously described by many authors, some degree of uncertainty always exists when segmenting tumor burdens, especially in the postoperative setting, in case of redo-surgery and for what concern *FLAIR-tumor* (preoperative edema, ischemia, and contusions may have been part of the calculation to some degree). Moreover, segmentation was seldom performed on 3D-FLAIR and contrast-enhanced 3D-T1 sequences acquired with slightly different parameters on diverse MR scanners, sometimes at slightly different timings. We tried to overcome these issues and increase reproducibility by having the evaluation validated by two different experienced observers and repeating the assessment at a second time-point, though some degree of subjectivity might still persist (Grabowski *et al.*, 2014; Incekara *et al.*, 2020a; Incekara *et al.*, 2020b).

Despite the fact that all patients were operated in the same center by the same team, the operating surgeon was not always the same individual, adding possible variations in surgical aggressiveness and technical abilities in functional preservation.

In some procedures, especially the most challenging ones, multiple aids were adopted simultaneously (advanced 3D planning, DTI/fMRI integration in the neuronavigation system, ultrasound, IONM), we might therefore speculate that, at least in some cases, the

better outcome could be provided by the combinations of these techniques rather than the unique advantage of a single one. On the other hand, all these techniques were predominantly used in the most challenging cases, therefore with an original higher risk for a negative outcome, generating a possible underestimation of their real benefits.

In some cases, the neuronavigation system was adopted merely to identify the ideal place of skin incision and bone craniotomy and not for continuous surgical guidance during tumor resection, this might have reduced the possible advantage observed for this intraoperative tool alone; however, neuronavigation was always adopted for intraoperative guidance when DTI/fMRI were integrated into the planning.

Lastly, advanced 3D planning with virtual reality was performed only after the year 2018, and this might have generated a bias when analyzing its impact on OS since patients operated before that date had a higher chance for longer survival.

5.6 Conclusions

In this study, we investigated the clinical application of advanced imaging techniques as DTI tractography and fMRI obtained with cutting-edge acquisition and processing procedures, as well as detailed 3D-rendered anatomic-functional-pathological models for virtual reality, in the preoperative and intraoperative management of 234 brain gliomas undergoing surgical resection. The complementary role of modern modalities of image-guided surgery, such as intraoperative neuronavigation and ultrasound, was also investigated.

Overall, DTI tractography and fMRI have confirmed that preoperative non-invasive mapping of critical functional area and eloquent white matter tracts and their combined use with other preoperative (as 3D virtual reality) and intraoperative tools (as neuronavigation, ultrasound, and DES) help to maximize the EOR while reducing postoperative neurological morbidity, eventually ameliorating OS and quality of life in patients affected from cerebral glioma.

We believe that, in the next future, with the continued enlargement of our study population with prospectively-collected data, we'll be able to further validate the efficacy on clinical outcome of these techniques, particularly for what concerns the innovative advanced 3D planning. At the same time, more sophisticated imaging acquisition and

processing techniques will continue to improve the current limitations, possibly opening up new frontiers in the surgical management of this disease.

6 FINAL REMARKS

In the present thesis, we validated the application of advanced neuroimaging in terms of:

- *characterization of tumor biological heterogeneity* and ability to *guide the neurosurgeon in a more accurate target definition* for bioptic sampling and surgical resection, allowing a more comprehensive diagnosis of tumor biological and molecular characteristics and a more appropriate treatment.
- *increase of the rate of maximum safe resection*, patient's *quality of life*, and *eventual survival*.

In the **first experiment**, we presented an innovative PET and MRI approach, defined *HYPERDirect*, for the evaluation of *HYpoxia*, *PERfusion*, and *Diffusion* in high-grade gliomas to derive combined *habitats* representing intra-tumor biologic heterogeneity. Our preliminary analyses in 17 patients confirmed that quantitative imaging features from metabolic maps of PWI, dMRI, and 18F-FAZA-PET, expressing vascularization, cellularity, and hypoxia, respectively, may reflect this heterogeneity non-invasively and can consistently divide malignant gliomas into some small number of clusters. We were able to identify the unique corresponding morphological and physiological MR characteristics and histopathologic correlate (in the ten patients subjected to stereotactic sampling) of each cluster, observing an outstanding reproducibility in pattern distribution among different cases and allowing us to even speculate about the possible evolution over the time of one habitat into each other.

In the **second experiment**, we investigated “*VERDICT*” MR imaging, a pioneering computational multi-compartment modeling framework originally developed for the extraction of quantitative maps from advanced dMRI acquisitions in body tumors, representing their vascular, extracellular and restricted component. We optimized this model for the assessment of brain neoplasms, which entail a variable surrounding infiltration and therefore a higher complexity, eventually obtaining a four-compartment model without extra free parameters, showing its improved fitting performance, especially for peritumoral areas. The results from our *VERDICT* model were validated

against PWI parameters (rCBV and Vp) and histopathology from corresponding stereotactic sampling, noting a good correlation. In particular, we observed higher intracellular and vascular fractions and lower extracellular fractions in more malignant histologies and tumor areas, an extremely high free water fraction in radionecrosis, and a trend towards higher free water fraction and extracellular diffusivity in purely vasogenic edemas (compared to infiltrative ones).

In the **third experiment**, we investigated the clinical application of advanced *Diffusion Tensor Imaging (DTI)* tractography and *BOLD functional MRI (fMRI)*, as well as the generation of detailed *3D-rendered anatomic-functional-pathological models* for virtual reality, in the preoperative and intraoperative management of 234 brain gliomas undergoing surgical resection. The role of modern modalities of image-guided surgery, such as intraoperative *neuronavigation* and *ultrasound*, was also investigated. All these imaging techniques generally proved advantageous in terms of extent of resection and functional outcome. In particular, the availability of DTI and fMRI was found significantly correlated with a longer survival at multivariate analysis; the former was also significantly associated with a lower chance of postoperative morbidity and a higher chance of recovering preexisting deficits.

Conclusively, we presented, for the *first time*, innovative approaches for enhanced brain tumor characterization (*HYPERDirect* approach and optimized *VERDICT* model) and evaluated *DTI* and *fMRI* techniques, together with pioneering *anatomic-functional-pathological 3D models*, for virtual reality in a large surgical series. We demonstrated that advanced neuroimaging techniques could represent a formidable tool to increase maximum safe resection and patient survival and to assess tumor heterogeneity, histopathologic/molecular characteristics, and expected behavior, possibly guiding the surgical sampling to the most aggressive cluster and perhaps, in the next future, even representing a valid alternative to invasive diagnostic procedures.

7 REFERENCES

- Abdalla G, Dixon L, Sanverdi E, Machado PM, Kwong JSW, Panovska-Griffiths J, Rojas-Garcia A, Yoneoka D, Veraart J, Van Cauter S et al (2020) The diagnostic role of diffusional kurtosis imaging in glioma grading and differentiation of gliomas from other intra-axial brain tumours: a systematic review with critical appraisal and meta-analysis. *Neuroradiology* 62: 791-802
- Abdo RA, Lamare F, Fernandez P, Bentourkia M (2019) Analysis of hypoxia in human glioblastoma tumors with dynamic 18F-FMISO PET imaging. *Australas Phys Eng Sci Med* 42: 981-993
- Ahn SS, Shin NY, Chang JH, Kim SH, Kim EH, Kim DW, Lee SK (2014) Prediction of methylguanine methyltransferase promoter methylation in glioblastoma using dynamic contrast-enhanced magnetic resonance and diffusion tensor imaging. *J Neurosurg* 121: 367-373
- Aki T, Nakayama N, Yonezawa S, Takenaka S, Miwa K, Asano Y, Shinoda J, Yano H, Iwama T (2012) Evaluation of brain tumors using dynamic 11 C-methionine-PET. *Journal of neuro-oncology* 109: 115-122
- Albert NL, Weller M, Suchorska B, Galldiks N, Soffietti R, Kim MM, la Fougere C, Pope W, Law I, Arbizu J et al (2016) Response Assessment in Neuro-Oncology working group and European Association for Neuro-Oncology recommendations for the clinical use of PET imaging in gliomas. *Neuro Oncol* 18: 1199-1208
- Alcaide-Leon P, Pareto D, Martinez-Saez E, Auger C, Bharatha A, Rovira A (2015) Pixel-by-pixel comparison of volume transfer constant and estimates of cerebral blood volume from dynamic contrast-enhanced and dynamic susceptibility contrast-enhanced MR imaging in high-grade gliomas. *American Journal of Neuroradiology* 36: 871-876
- Alexander A, Badie B, Field A, 2003. Diffusion tensor MRI depicts white matter reorganization after surgery, *Proceedings of the ISMRM 11th Scientific Meeting International Society of Magnetic Resonance in Medicine, Berkeley*. p. 399.
- Alexander DC (2008) A general framework for experiment design in diffusion MRI and its application in measuring direct tissue-microstructure features. *Magnetic Resonance in Medicine* 60: 439-448
- Aliotta E, Batchala PP, Schiff D, Lopes BM, Druzgal JT, Mukherjee S, Patel SH (2019a) Increased intratumoral infiltration in IDH wild-type lower-grade gliomas observed with diffusion tensor imaging. *J Neurooncol* 145: 257-263
- Aliotta E, Nourzadeh H, Batchala PP, Schiff D, Lopes MB, Druzgal JT, Mukherjee S, Patel SH (2019b) Molecular Subtype Classification in Lower-Grade Glioma with Accelerated DTI. *AJNR Am J Neuroradiol* 40: 1458-1463
- Altabella L, Broggi S, Mangili P, Conte GM, Pieri V, Iadanza A, Del Vecchio A, Anzalone N, di Muzio N, Calandrino R et al (2018) Integration of Diffusion Magnetic Resonance Tractography into tomotherapy radiation treatment planning for high-grade gliomas. *Phys Med* 55: 127-134
- Anderson DR, Trobe JD, Hood TW, Gebarski SS (1989) Optic tract injury after anterior temporal lobectomy. *Ophthalmology* 96: 1065-1070
- Andronesi OC, Kim GS, Gerstner E, Batchelor T, Tzika AA, Fantin VR, Vander Heiden MG, Sorensen AG (2012) Detection of 2-hydroxyglutarate in IDH-mutated glioma patients by in vivo spectral-editing and 2D correlation magnetic resonance spectroscopy. *Sci Transl Med* 4: 116ra114

- Anzalone N, Castellano A, Cadioli M, Conte GM, Cuccarini V, Bizzi A, Grimaldi M, Costa A, Grillea G, Vitali P (2018a) Brain gliomas: multicenter standardized assessment of dynamic contrast-enhanced and dynamic susceptibility contrast MR images. *Radiology* 287: 933-943
- Anzalone N, Castellano A, Cadioli M, Conte GM, Cuccarini V, Bizzi A, Grimaldi M, Costa A, Grillea G, Vitali P et al (2018b) Brain Gliomas: Multicenter Standardized Assessment of Dynamic Contrast-enhanced and Dynamic Susceptibility Contrast MR Images. *Radiology* 287: 933-943
- Arfanakis K, Gui M, Lazar M (2006) Optimization of white matter tractography for pre-surgical planning and image-guided surgery. *Oncology reports* 15: 1061-1064
- Awad AW, Karsy M, Sanai N, Spetzler R, Zhang Y, Xu Y, Mahan MA (2017) Impact of removed tumor volume and location on patient outcome in glioblastoma. *J Neurooncol* 135: 161-171
- Aydin K, Cokluk C, Kuruoglu E, Gelmez S, Diren B, Rakunt C, Celik F (2006) Using the magnetic resonance three-dimensional volume rendering for tissues technique in the planning of craniotomy flaps with linear scalp incision. *min-Minimally Invasive Neurosurgery* 49: 189-193
- Azad TD, Duffau H (2020) Limitations of functional neuroimaging for patient selection and surgical planning in glioma surgery. *Neurosurgical focus* 48: E12
- Babu R, Komisarow JM, Agarwal VJ, Rahimpour S, Iyer A, Britt D, Karikari IO, Grossi PM, Thomas S, Friedman AH et al (2016) Glioblastoma in the elderly: the effect of aggressive and modern therapies on survival. *J Neurosurg* 124: 998-1007
- Bai J, Varghese J, Jain R (2020) Adult Glioma WHO Classification Update, Genomics, and Imaging: What the Radiologists Need to Know. *Top Magn Reson Imaging* 29: 71-82
- Bai Y, Lin Y, Tian J, Shi D, Cheng J, Haacke EM, Hong X, Ma B, Zhou J, Wang M (2016) Grading of Gliomas by Using Monoexponential, Biexponential, and Stretched Exponential Diffusion-weighted MR Imaging and Diffusion Kurtosis MR Imaging. *Radiology* 278: 496-504
- Bailey C, Collins DJ, Tunariu N, Orton MR, Morgan VA, Feiweier T, Hawkes DJ, Leach MO, Alexander DC, Panagiotaki E (2018) Microstructure Characterization of Bone Metastases from Prostate Cancer with Diffusion MRI: Preliminary Findings. *Front Oncol* 8: 26
- Barajas RF, Jr., Phillips JJ, Parvataneni R, Molinaro A, Essock-Burns E, Bourne G, Parsa AT, Aghi MK, McDermott MW, Berger MS et al (2012) Regional variation in histopathologic features of tumor specimens from treatment-naïve glioblastoma correlates with anatomic and physiologic MR Imaging. *Neuro Oncol* 14: 942-954
- Barnett GH, Kormos DW, Steiner CP, Weisenberger J (1993) Intraoperative localization using an armless, frameless stereotactic wand. *Journal of neurosurgery* 78: 510-514
- Basser PJ, Pajevic S, Pierpaoli C, Duda J, Aldroubi A (2000) In vivo fiber tractography using DT-MRI data. *Magn Reson Med* 44: 625-632
- Bastiani M, Roebroeck A (2015) Unraveling the multiscale structural organization and connectivity of the human brain: the role of diffusion MRI. *Frontiers in neuroanatomy* 9: 77
- Beig N, Bera K, Prasanna P, Antunes J, Correa R, Singh S, Saeed Bamashmos A, Ismail M, Braman N, Verma R et al (2020) Radiogenomic-Based Survival Risk Stratification of Tumor Habitat on Gd-T1w MRI Is Associated with Biological Processes in Glioblastoma. *Clin Cancer Res* 26: 1866-1876
- Bello L, Castellano A, Fava E, Casaceli G, Riva M, Scotti G, Gaini SM, Falini A (2010a) Intraoperative use of diffusion tensor imaging fiber tractography and subcortical mapping for resection of gliomas: Technical considerations. *Neurosurgical focus* 28: E6.1-E6.14

- Bello L, Castellano A, Fava E, Casaceli G, Riva M, Scotti G, Gaini SM, Falini A (2010b) Intraoperative use of diffusion tensor imaging fiber tractography and subcortical mapping for resection of gliomas: technical considerations. *Neurosurgical focus* 28: E6
- Bello L, Gambini A, Castellano A, Carrabba G, Acerbi F, Fava E, Giussani C, Cadioli M, Blasi V, Casarotti A et al (2008) Motor and language DTI Fiber Tracking combined with intraoperative subcortical mapping for surgical removal of gliomas. *Neuroimage* 39: 369-382
- Bello L, Riva M, Fava E, Ferpozzi V, Castellano A, Raneri F, Pessina F, Bizzi A, Falini A, Cerri G (2014) Tailoring neurophysiological strategies with clinical context enhances resection and safety and expands indications in gliomas involving motor pathways. *Neuro Oncol* 16: 1110-1128
- Berman J (2009) Diffusion MR tractography as a tool for surgical planning. *Magn Reson Imaging Clin N Am* 17: 205-214
- Berntsen EM, Gulati S, Solheim O, Kvistad KA, Torp SH, Selbekk T, Unsgård G, Håberg AK (2010) Functional magnetic resonance imaging and diffusion tensor tractography incorporated into an intraoperative 3-dimensional ultrasound-based neuronavigation system: impact on therapeutic strategies, extent of resection, and clinical outcome. *Neurosurgery* 67: 251-264
- Bette S, Barz M, Wiestler B, Huber T, Gerhardt J, Buchmann N, Combs SE, Schmidt-Graf F, Delbridge C, Zimmer C et al (2018) Prognostic Value of Tumor Volume in Glioblastoma Patients: Size Also Matters for Patients with Incomplete Resection. *Ann Surg Oncol* 25: 558-564
- Beyer J, Hadwiger M, Wolfsberger S, Buhler K (2007) High-quality multimodal volume rendering for preoperative planning of neurosurgical interventions. *IEEE Trans Vis Comput Graph* 13: 1696-1703
- Bizzi A, Blasi V, Falini A, Ferroli P, Cadioli M, Danesi U, Aquino D, Marras C, Caldiroli D, Broggi G (2008) Presurgical functional MR imaging of language and motor functions: validation with intraoperative electrocortical mapping. *Radiology* 248: 579-589
- Black DF, Vachha B, Mian A, Faro SH, Maheshwari M, Sair HI, Petrella JR, Pillai JJ, Welker K (2017) American Society of Functional Neuroradiology-Recommended fMRI Paradigm Algorithms for Presurgical Language Assessment. *AJNR Am J Neuroradiol* 38: E65-E73
- Bonn AV, Ritterbusch R, Throckmorton P, Graber JJ (2020) Clinical Imaging for Diagnostic Challenges in the Management of Gliomas: A Review. *J Neuroimaging* 30: 139-145
- Borchers S, Himmelbach M, Logothetis N, Karnath H-O (2012) Direct electrical stimulation of human cortex—the gold standard for mapping brain functions? *Nature Reviews Neuroscience* 13: 63-70
- Branzoli F, Di Stefano AL, Capelle L, Ottolenghi C, Valabregue R, Deelchand DK, Bielle F, Villa C, Baussart B, Lehericy S et al (2018) Highly specific determination of IDH status using edited in vivo magnetic resonance spectroscopy. *Neuro Oncol* 20: 907-916
- Brat D, Verhaak R, Aldape K, Yung W, Salama S, Cooper L, Rheinbay E, Miller C, Vitucci M, Morozova O (2015) Comprehensive, integrative genomic analysis of diffuse lower-grade gliomas. *N. Engl. J. Med.* 2015 2481: 10
- Brat DJ, Castellano-Sanchez A, Kaur B, Van Meir EG (2002) Genetic and biologic progression in astrocytomas and their relation to angiogenic dysregulation. *Adv Anat Pathol* 9: 24-36
- Brown TJ, Brennan MC, Li M, Church EW, Brandmeir NJ, Rakszawski KL, Patel AS, Rizk EB, Suki D, Sawaya R et al (2016) Association of the Extent of Resection With Survival in Glioblastoma: A Systematic Review and Meta-analysis. *JAMA Oncol* 2: 1460-1469

- Bucci M, Mandelli ML, Berman JI, Amirbekian B, Nguyen C, Berger MS, Henry RG (2013) Quantifying diffusion MRI tractography of the corticospinal tract in brain tumors with deterministic and probabilistic methods. *Neuroimage Clin* 3: 361-368
- Bulakbasi N, Paksoy Y (2019) Advanced imaging in adult diffusely infiltrating low-grade gliomas. *Insights Imaging* 10: 122
- Callewaert B, Jones EAV, Himmelreich U, Gsell W (2021) Non-Invasive Evaluation of Cerebral Microvasculature Using Pre-Clinical MRI: Principles, Advantages and Limitations. *Diagnostics (Basel)* 11
- Cao Z, Lv J, Wei X, Quan W (2010) Appliance of preoperative diffusion tensor imaging and fiber tractography in patients with brainstem lesions. *Neurology India* 58: 886
- Capitano U, Pepe G, Incerti E, Larcher A, Trevisani F, Luciano R, Mapelli P, Bettinardi V, Monterisi C, Necchi A et al (2020) The role of 18F-FAZA PET/CT in detecting lymph node metastases in renal cell carcinoma patients: a prospective pilot trial. *Eur J Nucl Med Mol Imaging*
- Carrano A, Juarez JJ, Incontri D, Ibarra A, Guerrero Cazares H (2021) Sex-Specific Differences in Glioblastoma. *Cells* 10
- Castellano A, Bailo M, Cicone F, Carideo L, Quartuccio N, Mortini P, Falini A, Cascini GL, Minniti G (2021) Advanced Imaging Techniques for Radiotherapy Planning of Gliomas. *Cancers (Basel)* 13
- Castellano A, Bello L, Michelozzi C, Gallucci M, Fava E, Iadanza A, Riva M, Casaceli G, Falini A (2012) Role of diffusion tensor magnetic resonance tractography in predicting the extent of resection in glioma surgery. *Neuro Oncol* 14: 192-202
- Castellano A, Cirillo S, Bello L, Riva M, Falini A (2017) Functional MRI for Surgery of Gliomas. *Curr Treat Options Neurol* 19: 34
- Castellano A, Donativi M, Rudà R, De Nunzio G, Riva M, Iadanza A, Bertero L, Rucco M, Bello L, Soffietti R (2016) Evaluation of low-grade glioma structural changes after chemotherapy using DTI-based histogram analysis and functional diffusion maps. *European radiology* 26: 1263-1273
- Castellano A, Falini A (2016) Progress in neuro-imaging of brain tumors. *Curr Opin Oncol* 28: 484-493
- Caverzasi E, Hervey-Jumper SL, Jordan KM, Lobach IV, Li J, Panara V, Racine CA, Sankaranarayanan V, Amirbekian B, Papinutto N et al (2016a) Identifying preoperative language tracts and predicting postoperative functional recovery using HARDI q-ball fiber tractography in patients with gliomas. *J Neurosurg* 125: 33-45
- Caverzasi E, Papinutto N, Castellano A, Zhu AH, Scifo P, Riva M, Bello L, Falini A, Bharatha A, Henry RG (2016b) Neurite Orientation Dispersion and Density Imaging Color Maps to Characterize Brain Diffusion in Neurologic Disorders. *J Neuroimaging* 26: 494-498
- Chabrierie A, Ozlen F, Nakajima S, Leventon ME, Atsumi H, Grimson E, Jolesz F, Kikinis R, Black PM (1998) Three-dimensional image reconstruction for low-grade glioma surgery. *Neurosurgical focus* 4: e7
- Chaichana KL, Cabrera-Aldana EE, Jusue-Torres I, Wijesekera O, Olivi A, Rahman M, Quinones-Hinojosa A (2014a) When gross total resection of a glioblastoma is possible, how much resection should be achieved? *World neurosurgery* 82: e257-e265
- Chaichana KL, Jusue-Torres I, Navarro-Ramirez R, Raza SM, Pascual-Gallego M, Ibrahim A, Hernandez-Hermann M, Gomez L, Ye X, Weingart JD et al (2014b) Establishing percent resection and residual volume thresholds affecting survival and recurrence for patients with newly diagnosed intracranial glioblastoma. *Neuro Oncol* 16: 113-122

- Chaichana KL, Parker SL, Olivi A, Quinones-Hinojosa A (2009) Long-term seizure outcomes in adult patients undergoing primary resection of malignant brain astrocytomas. *Clinical article. J Neurosurg* 111: 282-292
- Chang SM, Parney IF, Huang W, Anderson FA, Jr., Asher AL, Bernstein M, Lillehei KO, Brem H, Berger MS, Laws ER et al (2005) Patterns of care for adults with newly diagnosed malignant glioma. *JAMA* 293: 557-564
- Chang SM, Parney IF, McDermott M, Barker FG, 2nd, Schmidt MH, Huang W, Laws ER, Jr., Lillehei KO, Bernstein M, Brem H et al (2003) Perioperative complications and neurological outcomes of first and second craniotomies among patients enrolled in the Glioma Outcome Project. *J Neurosurg* 98: 1175-1181
- Chanraud S, Zahr N, Sullivan EV, Pfefferbaum A (2010) MR diffusion tensor imaging: a window into white matter integrity of the working brain. *Neuropsychology review* 20: 209-225
- Chaumeil MM, Lupo JM, Ronen SM (2015) Magnetic Resonance (MR) Metabolic Imaging in Glioma. *Brain Pathol* 25: 769-780
- Chen J-R, Yao Y, Xu H-Z, Qin Z-Y (2016) Isocitrate dehydrogenase (IDH) 1/2 mutations as prognostic markers in patients with glioblastomas. *Medicine* 95
- Chen L, Liu M, Bao J, Xia Y, Zhang J, Zhang L, Huang X, Wang J (2013) The correlation between apparent diffusion coefficient and tumor cellularity in patients: a meta-analysis. *PLoS One* 8: e79008
- Chen L-P, Jiang X-Q, Zhao Z, Wang X-H (2018) Apparent diffusion coefficient value for prediction of hemorrhagic transformation in acute ischemic infarction. *Int J Clin Exp Med* 11: 109-117
- Chen X, Weigel D, Ganslandt O, Buchfelder M, Nimsky C (2009) Prediction of visual field deficits by diffusion tensor imaging in temporal lobe epilepsy surgery. *Neuroimage* 45: 286-297
- Choi C, Ganji SK, DeBerardinis RJ, Hatanpaa KJ, Rakheja D, Kovacs Z, Yang XL, Mashimo T, Raisanen JM, Marin-Valencia I et al (2012) 2-Hydroxyglutarate detection by magnetic resonance spectroscopy in IDH-mutated patients with gliomas. *Nat Med* 18: 624-629
- Choi C, Raisanen JM, Ganji SK, Zhang S, McNeil SS, An Z, Madan A, Hatanpaa KJ, Vemireddy V, Sheppard CA et al (2016a) Prospective Longitudinal Analysis of 2-Hydroxyglutarate Magnetic Resonance Spectroscopy Identifies Broad Clinical Utility for the Management of Patients With IDH-Mutant Glioma. *J Clin Oncol* 34: 4030-4039
- Choi C, Raisanen JM, Ganji SK, Zhang S, McNeil SS, An Z, Madan A, Hatanpaa KJ, Vemireddy V, Sheppard CA et al (2016b) Prospective longitudinal analysis of 2-hydroxyglutarate magnetic resonance spectroscopy identifies broad clinical utility for the management of patients with IDH-mutant glioma. *Journal of Clinical Oncology* 34: 4030-4039
- Chu JP, Song YK, Tian YS, Qiu HS, Huang XH, Wang YL, Huang YQ, Zhao J (2021) Diffusion kurtosis imaging in evaluating gliomas: different region of interest selection methods on time efficiency, measurement repeatability, and diagnostic ability. *Eur Radiol* 31: 729-739
- Conti Nibali M, Rossi M, Sciortino T, Riva M, Gay LG, Pessina F, Bello L (2019) Preoperative surgical planning of glioma: limitations and reliability of fMRI and DTI tractography. *Journal of neurosurgical sciences* 63: 127-134
- Costabile JD, Alaswad E, D'Souza S, Thompson JA, Ormond DR (2019) Current Applications of Diffusion Tensor Imaging and Tractography in Intracranial Tumor Resection. *Front Oncol* 9: 426
- Cui Y, Tha KK, Terasaka S, Yamaguchi S, Wang J, Kudo K, Xing L, Shirato H, Li R (2016) Prognostic Imaging Biomarkers in Glioblastoma: Development and Independent Validation on the Basis of Multiregion and Quantitative Analysis of MR Images. *Radiology* 278: 546-553

- D'Andrea G, Familiari P, Di Lauro A, Angelini A, Sessa G (2016) Safe resection of gliomas of the dominant angular gyrus availing of preoperative FMRI and intraoperative DTI: preliminary series and surgical technique. *World neurosurgery* 87: 627-639
- Darefsky AS, King JT, Jr., Dubrow R (2012) Adult glioblastoma multiforme survival in the temozolomide era: a population-based analysis of Surveillance, Epidemiology, and End Results registries. *Cancer* 118: 2163-2172
- de Almeida Martins JP, Nilsson M, Lampinen B, Palombo M, While PT, Westin C-F, Szczepankiewicz F (2021) Neural Networks for parameter estimation in microstructural MRI: a study with a high-dimensional diffusion-relaxation model of white matter microstructure. *bioRxiv*: 2021.2003.2012.435163
- de la Fuente MI, Young RJ, Rubel J, Rosenblum M, Tisnado J, Briggs S, Arevalo-Perez J, Cross JR, Campos C, Straley K (2015) Integration of 2-hydroxyglutarate-proton magnetic resonance spectroscopy into clinical practice for disease monitoring in isocitrate dehydrogenase-mutant glioma. *Neuro-oncology* 18: 283-290
- de Leeuw CN, Vogelbaum MA (2019) Supratotal resection in glioma: a systematic review. *Neuro Oncol* 21: 179-188
- de Notaris M, Palma K, Serra L, Ensenat J, Alobid I, Poblete J, Gonzalez JB, Solari D, Ferrer E, Prats-Galino A (2014) A three-dimensional computer-based perspective of the skull base. *World Neurosurg* 82: S41-48
- de Oliveira Santos BF, da Costa MDS, Centeno RS, Cavalheiro S, de Paiva Neto MA, Lawton MT, Chaddad-Neto F (2018) Clinical application of an open-source 3D volume rendering software to neurosurgical approaches. *World neurosurgery* 110: e864-e872
- De Witt Hamer PC, De Witt Hamer PC, Klein M, Hervey-Jumper SL, Wefel JS, Berger MS (2021) Functional Outcomes and Health-Related Quality of Life Following Glioma Surgery. *Neurosurgery* 88: 720-732
- De Witt Hamer PC, Robles SG, Zwinderman AH, Duffau H, Berger MS (2012) Impact of intraoperative stimulation brain mapping on glioma surgery outcome: a meta-analysis. *J Clin Oncol* 30: 2559-2565
- Del Mar Alvarez-Torres M, Juan-Albarracin J, Fuster-Garcia E, Bellvis-Bataller F, Lorente D, Reynes G, Font de Mora J, Aparici-Robles F, Botella C, Munoz-Langa J et al (2020) Robust association between vascular habitats and patient prognosis in glioblastoma: An international multicenter study. *J Magn Reson Imaging* 51: 1478-1486
- Dextraze K, Saha A, Kim D, Narang S, Lehrer M, Rao A, Narang S, Rao D, Ahmed S, Madhugiri V et al (2017) Spatial habitats from multiparametric MR imaging are associated with signaling pathway activities and survival in glioblastoma. *Oncotarget* 8: 112992-113001
- Dhermain FG, Hau P, Lanfermann H, Jacobs AH, van den Bent MJ (2010) Advanced MRI and PET imaging for assessment of treatment response in patients with gliomas. *Lancet Neurol* 9: 906-920
- Dimou S, Battisti R, Hermens D, Lagopoulos J (2013) A systematic review of functional magnetic resonance imaging and diffusion tensor imaging modalities used in presurgical planning of brain tumour resection. *Neurosurgical review* 36: 205-214
- Dolgorsuren EA, Harada M, Kanazawa Y, Abe T, Otomo M, Matsumoto Y, Mizobuchi Y, Nakajima K (2019) Correlation and Characteristics of Intravoxel Incoherent Motion and Arterial Spin Labeling Techniques Versus Multiple Parameters Obtained on Dynamic Susceptibility Contrast Perfusion MRI for Brain Tumors. *J Med Invest* 66: 308-313
- Doskaliyev A, Yamasaki F, Ohtaki M, Kajiwara Y, Takeshima Y, Watanabe Y, Takayasu T, Amatya VJ, Akiyama Y, Sugiyama K et al (2012) Lymphomas and glioblastomas:

- differences in the apparent diffusion coefficient evaluated with high b-value diffusion-weighted magnetic resonance imaging at 3T. *Eur J Radiol* 81: 339-344
- Dowling C, Bollen AW, Noworolski SM, McDermott MW, Barbaro NM, Day MR, Henry RG, Chang SM, Dillon WP, Nelson SJ et al (2001) Preoperative proton MR spectroscopic imaging of brain tumors: correlation with histopathologic analysis of resection specimens. *AJNR Am J Neuroradiol* 22: 604-612
- Dubbink H, Taal W, van Marion R, Kros J, van Heuvel I, Bromberg J, Zonnenberg B, Zonnenberg C, Postma T, Gijtenbeek J (2009) IDH1 mutations in low-grade astrocytomas predict survival but not response to temozolomide. *Neurology* 73: 1792-1795
- Dubey A, Kataria R, Sinha VD (2018) Role of Diffusion Tensor Imaging in Brain Tumor Surgery. *Asian J Neurosurg* 13: 302-306
- Dubinski D, Won SY, Rauch M, Behmanesh B, Ngassam LDC, Baumgarten P, Senft C, Harter PN, Bernstock JD, Freiman TM et al (2021) Association of Isocitrate Dehydrogenase (IDH) Status With Edema to Tumor Ratio and Its Correlation With Immune Infiltration in Glioblastoma. *Front Immunol* 12: 627650
- Duffau H (2007) Contribution of cortical and subcortical electrostimulation in brain glioma surgery: methodological and functional considerations. *Neurophysiol Clin* 37: 373-382
- Duffau H (2016) Long-term outcomes after supratotal resection of diffuse low-grade gliomas: a consecutive series with 11-year follow-up. *Acta Neurochir (Wien)* 158: 51-58
- Duffau H (2019) Higher-Order Surgical Questions for Diffuse Low-Grade Gliomas: Supramaximal Resection, Neuroplasticity, and Screening. *Neurosurg Clin N Am* 30: 119-128
- Duffau H, Lopes M, Arthuis F, Bitar A, Sichez JP, Van Effenterre R, Capelle L (2005) Contribution of intraoperative electrical stimulations in surgery of low grade gliomas: a comparative study between two series without (1985-96) and with (1996-2003) functional mapping in the same institution. *J Neurol Neurosurg Psychiatry* 76: 845-851
- Easaw JC, Mason WP, Perry J, Laperriere N, Eisenstat DD, Del Maestro R, Belanger K, Fulton D, Macdonald D, Canadian Glioblastoma Recommendations C (2011) Canadian recommendations for the treatment of recurrent or progressive glioblastoma multiforme. *Curr Oncol* 18: e126-136
- Eder K, Kalman B (2014) Molecular heterogeneity of glioblastoma and its clinical relevance. *Pathology & Oncology Research* 20: 777-787
- Ellingson BM, Wen PY, van den Bent MJ, Cloughesy TF (2014) Pros and cons of current brain tumor imaging. *Neuro Oncol* 16 Suppl 7: vii2-11
- Englander ZK, Horenstein CI, Bowden SG, Chow DS, Otten ML, Lignelli A, Bruce JN, Canoll P, Grinband J (2018) Extent of BOLD Vascular Dysregulation Is Greater in Diffuse Gliomas without Isocitrate Dehydrogenase 1 R132H Mutation. *Radiology* 287: 965-972
- Esposito V, Paolini S, Morace R (2006) Resection of a left insular cavernoma aided by a simple navigational tool. Technical note. *Neurosurgical focus* 21: e16
- Eyupoglu IY, Hore N, Merkel A, Buslei R, Buchfelder M, Savaskan N (2016) Supra-complete surgery via dual intraoperative visualization approach (DiVA) prolongs patient survival in glioblastoma. *Oncotarget* 7: 25755-25768
- Fathi Kazerooni A, Nabil M, Zeinali Zadeh M, Firouznia K, Azmoudeh-Ardalan F, Frangi AF, Davatzikos C, Saligheh Rad H (2018) Characterization of active and infiltrative tumorous subregions from normal tissue in brain gliomas using multiparametric MRI. *J Magn Reson Imaging* 48: 938-950
- Federau C (2017) Intravoxel incoherent motion MRI as a means to measure in vivo perfusion: A review of the evidence. *NMR in Biomedicine* 30: e3780

- Federau C, O'Brien K, Meuli R, Hagmann P, Maeder P (2014) Measuring brain perfusion with intravoxel incoherent motion (IVIM): initial clinical experience. *J Magn Reson Imaging* 39: 624-632
- Fedorov A, Beichel R, Kalpathy-Cramer J, Finet J, Fillion-Robin JC, Pujol S, Bauer C, Jennings D, Fennessy F, Sonka M et al (2012) 3D Slicer as an image computing platform for the Quantitative Imaging Network. *Magn Reson Imaging* 30: 1323-1341
- Ferda J, Ferdová E, Hes O, Mraček J, Kreuzberg B, Baxa J (2017) PET/MRI: Multiparametric imaging of brain tumors. *European journal of radiology* 94: A14-A25
- Ferguson SD, McCutcheon IE (2018) Surgical Management of Gliomas in Eloquent Cortex. *Prog Neurol Surg* 30: 159-172
- Fernandez-Miranda JC, Engh JA, Pathak SK, Madhok R, Boada FE, Schneider W, Kassam AB (2010) High-definition fiber tracking guidance for intraparenchymal endoscopic port surgery. *J Neurosurg* 113: 990-999
- Figini M, Riva M, Graham M, Castelli GM, Fernandes B, Grimaldi M, Baselli G, Pessina F, Bello L, Zhang H et al (2018) Prediction of Isocitrate Dehydrogenase Genotype in Brain Gliomas with MRI: Single-Shell versus Multishell Diffusion Models. *Radiology* 289: 788-796
- Frey D, Schilt S, Strack V, Zdunczyk A, Rosler J, Niraula B, Vajkoczy P, Picht T (2014) Navigated transcranial magnetic stimulation improves the treatment outcome in patients with brain tumors in motor eloquent locations. *Neuro Oncol* 16: 1365-1372
- Freyschlag CF, Krieg SM, Kerschbaumer J, Pinggera D, Forster MT, Cordier D, Rossi M, Miceli G, Roux A, Reyes A et al (2018) Imaging practice in low-grade gliomas among European specialized centers and proposal for a minimum core of imaging. *Journal of Neuro-Oncology* 139: 699-711
- Fujii Y, Muragaki Y, Maruyama T, Nitta M, Saito T, Ikuta S, Iseki H, Hongo K, Kawamata T (2018) Threshold of the extent of resection for WHO Grade III gliomas: retrospective volumetric analysis of 122 cases using intraoperative MRI. *J Neurosurg* 129: 1-9
- Fuster-Garcia E, Juan-Albarracin J, Garcia-Ferrando GA, Marti-Bonmati L, Aparici-Robles F, Garcia-Gomez JM (2018) Improving the estimation of prognosis for glioblastoma patients by MR based hemodynamic tissue signatures. *NMR Biomed* 31: e4006
- Galldiks N, Lohmann P, Albert NL, Tonn JC, Langen K-J (2019) Current status of PET imaging in neuro-oncology. *Neuro-Oncology Advances* 1: vdz010
- Ganslandt O, Behari S, Gralla J, Fahlbusch R, Nimsky C (2002) Neuronavigation: concept, techniques and applications. *Neurol India* 50: 244-255
- Gatenby RA, Grove O, Gillies RJ (2013) Quantitative imaging in cancer evolution and ecology. *Radiology* 269: 8-15
- Gates EDH, Lin JS, Weinberg JS, Hamilton J, Prabhu SS, Hazle JD, Fuller GN, Baladandayuthapani V, Fuentes D, Schellingerhout D (2019) Guiding the first biopsy in glioma patients using estimated Ki-67 maps derived from MRI: conventional versus advanced imaging. *Neuro Oncol* 21: 527-536
- Gatidis S, Schmidt H, Martirosian P, Nikolaou K, Schwenzer NF (2016) Apparent diffusion coefficient-dependent voxelwise computed diffusion-weighted imaging: An approach for improving SNR and reducing T2 shine-through effects. *J Magn Reson Imaging* 43: 824-832
- Gerganov VM, Samii A, Akbarian A, Stieglitz L, Samii M, Fahlbusch R (2009) Reliability of intraoperative high-resolution 2D ultrasound as an alternative to high-field strength MR imaging for tumor resection control: a prospective comparative study. *Journal of neurosurgery* 111: 512-519
- Giordano M, Lüdemann WO, Stieglitz L, Gerganov VM, Columbano L, Samii A, Samii M (2011) Identification of venous variants in the pineal region with three-dimensional preoperative

magnetic resonance imaging navigation in patients harbouring tumors in this area: significance for surgical approach to the lesion. *Clinical neurology and neurosurgery* 113: 387-392

- Gittleman H, Ostrom QT, Stetson LC, Waite K, Hodges TR, Wright CH, Wright J, Rubin JB, Berens ME, Lathia J et al (2019) Sex is an important prognostic factor for glioblastoma but not for nonglioblastoma. *Neurooncol Pract* 6: 451-462
- Giussani C, Roux F-E, Ojemann J, Sganzerla EP, Pirillo D, Papagno C (2010) Is preoperative functional magnetic resonance imaging reliable for language areas mapping in brain tumor surgery? Review of language functional magnetic resonance imaging and direct cortical stimulation correlation studies. *Neurosurgery* 66: 113-120
- Goha KY, 2006. Virtual reality applications in neurosurgery, 2005 IEEE Engineering in Medicine and Biology 27th Annual Conference. IEEE, pp. 4171-4173.
- Gong XY, Higano S, Mugikura S, Umetsu A, Murata T, Kumabe T, Takahashi S (2008) Virtually peeling off the skull and scalp: a simple way of mapping the superficial cerebral veins on the brain surface. *Stereotact Funct Neurosurg* 86: 345-350
- Gordon Y, Partovi S, Muller-Eschner M, Amarteifio E, Bauerle T, Weber MA, Kauczor HU, Rengier F (2014) Dynamic contrast-enhanced magnetic resonance imaging: fundamentals and application to the evaluation of the peripheral perfusion. *Cardiovasc Diagn Ther* 4: 147-164
- Gosal JS, Tiwari S, Sharma T, Agrawal M, Garg M, Mahal S, Bhaskar S, Sharma RK, Janu V, Jha DK (2021) Simulation of surgery for supratentorial gliomas in virtual reality using a 3D volume rendering technique: a poor man's neuronavigation. *Neurosurgical focus* 51: E23
- Grabowski MM, Recinos PF, Nowacki AS, Schroeder JL, Angelov L, Barnett GH, Vogelbaum MA (2014) Residual tumor volume versus extent of resection: predictors of survival after surgery for glioblastoma. *J Neurosurg* 121: 1115-1123
- Griffith B, Jain R (2015) Perfusion imaging in neuro-oncology: basic techniques and clinical applications. *Radiol Clin North Am* 53: 497-511
- Grussu F, Battiston M, Palombo M, Schneider T, Gandini Wheeler-Kingshott CAM, Alexander DC (2020) Deep learning model fitting for diffusion-relaxometry: a comparative study. [bioRxiv: 2020.2010.2020.347625](https://doi.org/10.20932/biorxiv.2020.2010.2020.347625)
- Guo J, Yao C, Chen H, Zhuang D, Tang W, Ren G, Wang Y, Wu J, Huang F, Zhou L (2012) The relationship between Cho/NAA and glioma metabolism: implementation for margin delineation of cerebral gliomas. *Acta Neurochir (Wien)* 154: 1361-1370; discussion 1370
- Halefoglu AM, Yousem DM (2018) Susceptibility weighted imaging: Clinical applications and future directions. *World J Radiol* 10: 30-45
- Halmos GB, Bruine de Bruin L, Langendijk JA, van der Laan BF, Pruim J, Steenbakkens RJ (2014) Head and neck tumor hypoxia imaging by 18F-fluoroazomycin-arabinoiside (18F-FAZA)-PET: a review. *Clin Nucl Med* 39: 44-48
- Hardee ME, Zagzag D (2012) Mechanisms of glioma-associated neovascularization. *Am J Pathol* 181: 1126-1141
- Harpur MV, Gonzalez-Lopez P, Ture U (2014) Three-dimensional reconstruction of the topographical cerebral surface anatomy for presurgical planning with free OsiriX Software. *Neurosurgery* 10 Suppl 3: 426-435; discussion 435
- Hatzoglou V, Yang TJ, Omuro A, Gavrilovic I, Ulaner G, Rubel J, Schneider T, Woo KM, Zhang Z, Peck KK (2016) A prospective trial of dynamic contrast-enhanced MRI perfusion and fluorine-18 FDG PET-CT in differentiating brain tumor progression from radiation injury after cranial irradiation. *Neuro-oncology* 18: 873-880

- Hempel JM, Bisdas S, Schittenhelm J, Brendle C, Bender B, Wassmann H, Skardelly M, Tabatabai G, Vega SC, Ernemann U et al (2017) In vivo molecular profiling of human glioma using diffusion kurtosis imaging. *J Neurooncol* 131: 93-101
- Herholz K, Coope D, Jackson A (2007) Metabolic and molecular imaging in neuro-oncology. *Lancet Neurol* 6: 711-724
- Hervey-Jumper SL, Berger MS (2014) Role of surgical resection in low-and high-grade gliomas. *Curr Treat Options Neurol* 16: 284
- Heye AK, Culling RD, Hernández MdCV, Thrippleton MJ, Wardlaw JM (2014) Assessment of blood-brain barrier disruption using dynamic contrast-enhanced MRI. A systematic review. *NeuroImage: Clinical* 6: 262-274
- Holash J, Maisonpierre PC, Compton D, Boland P, Alexander CR, Zagzag D, Yancopoulos GD, Wiegand SJ (1999) Vessel cooption, regression, and growth in tumors mediated by angiopoietins and VEGF. *Science* 284: 1994-1998
- Hollingsworth W, Medina LS, Lenkinski RE, Shibata DK, Bernal B, Zurakowski D, Comstock B, Jarvik JG (2006) A Systematic Literature Review of Magnetic Resonance Spectroscopy for the Characterization of Brain Tumors. *American Journal of Neuroradiology* 27: 1404-1411
- Houillier C, Wang X, Kaloshi G, Mokhtari K, Guillemin R, Laffaire J, Paris S, Boisselier B, Idhahbi A, Laigle-Donadey F et al (2010) IDH1 or IDH2 mutations predict longer survival and response to temozolomide in low-grade gliomas. *Neurology* 75: 1560-1566
- Howe F, Barton S, Cudlip S, Stubbs M, Saunders D, Murphy M, Wilkins P, Opstad K, Doyle V, McLean M (2003) Metabolic profiles of human brain tumors using quantitative in vivo ¹H magnetic resonance spectroscopy. *Magnetic Resonance in Medicine: An Official Journal of the International Society for Magnetic Resonance in Medicine* 49: 223-232
- Hsu CC, Watkins TW, Kwan GN, Haacke EM (2016) Susceptibility-Weighted Imaging of Glioma: Update on Current Imaging Status and Future Directions. *J Neuroimaging* 26: 383-390
- Hu LS, Ning S, Eschbacher JM, Gaw N, Dueck AC, Smith KA, Nakaji P, Plasencia J, Ranjbar S, Price SJ et al (2015) Multi-Parametric MRI and Texture Analysis to Visualize Spatial Histologic Heterogeneity and Tumor Extent in Glioblastoma. *PLoS One* 10: e0141506
- Huang WJ, Chen WW, Zhang X (2016) Glioblastoma multiforme: Effect of hypoxia and hypoxia inducible factors on therapeutic approaches. *Oncol Lett* 12: 2283-2288
- Hutterer M, Hattingen E, Palm C, Proescholdt MA, Hau P (2015) Current standards and new concepts in MRI and PET response assessment of antiangiogenic therapies in high-grade glioma patients. *Neuro Oncol* 17: 784-800
- Ille S, Sollmann N, Hauck T, Maurer S, Tanigawa N, Obermueller T, Negwer C, Droese D, Zimmer C, Meyer B (2015) Combined noninvasive language mapping by navigated transcranial magnetic stimulation and functional MRI and its comparison with direct cortical stimulation. *Journal of neurosurgery* 123: 212-225
- Incekara F, Smits M, van der Voort SR, Dubbink HJ, Atmodimedjo PN, Kros JM, Vincent A, van den Bent M (2020a) The Association Between the Extent of Glioblastoma Resection and Survival in Light of MGMT Promoter Methylation in 326 Patients With Newly Diagnosed IDH-Wildtype Glioblastoma. *Front Oncol* 10: 1087
- Incekara F, van der Voort SR, Dubbink HJ, Atmodimedjo PN, Nandoe Tewarie R, Lycklama G, Vincent A, Kros JM, Klein S, van den Bent M et al (2020b) Topographical Mapping of 436 Newly Diagnosed IDH Wildtype Glioblastoma With vs. Without MGMT Promoter Methylation. *Front Oncol* 10: 596
- Iseki H, Nakamura R, Muragaki Y, Suzuki T, Chernov M, Hori T, Takakura K (2008) Advanced computer-aided intraoperative technologies for information-guided surgical management of

- gliomas: Tokyo Women's Medical University experience. *Minim Invasive Neurosurg* 51: 285-291
- Ishikawa T, MURaGaki Y, MaRUYaMa T, Abe K, Kawamata T (2017) Roles of the Wada test and functional magnetic resonance imaging in identifying the language-dominant hemisphere among patients with gliomas located near speech areas. *Neurologia medico-chirurgica* 57: 28-34
- Ismail M, Hill V, Statsevych V, Huang R, Prasanna P, Correa R, Singh G, Bera K, Beig N, Thawani R et al (2018) Shape Features of the Lesion Habitat to Differentiate Brain Tumor Progression from Pseudoprogression on Routine Multiparametric MRI: A Multisite Study. *AJNR Am J Neuroradiol* 39: 2187-2193
- Jabehdar Maralani P, Myrehaug S, Mehrabian H, Chan AKM, Wintermark M, Heyn C, Conklin J, Ellingson BM, Rahimi S, Lau AZ et al (2021) Intravoxel incoherent motion (IVIM) modeling of diffusion MRI during chemoradiation predicts therapeutic response in IDH wildtype glioblastoma. *Radiother Oncol* 156: 258-265
- Jackson RJ, Fuller GN, Abi-Said D, Lang FF, Gokaslan ZL, Shi WM, Wildrick DM, Sawaya R (2001) Limitations of stereotactic biopsy in the initial management of gliomas. *Neuro Oncol* 3: 193-200
- Jaimovich SG, Guevara M, Pampin S, Jaimovich R, Gardella JL (2014) [Neurosurgical planning using osirix software]. *Surgical neurology international* 5: S267-271
- Jain R, Narang J, Schultz L, Scarpace L, Saksena S, Brown S, Rock J, Rosenblum M, Gutierrez J, Mikkelsen T (2011) Permeability estimates in histopathology-proved treatment-induced necrosis using perfusion CT: can these add to other perfusion parameters in differentiating from recurrent/progressive tumors? *American Journal of neuroradiology* 32: 658-663
- Jain R, Narang J, Sundgren PM, Hearshen D, Saksena S, Rock JP, Gutierrez J, Mikkelsen T (2010) Treatment induced necrosis versus recurrent/progressing brain tumor: going beyond the boundaries of conventional morphologic imaging. *J Neurooncol* 100: 17-29
- Jain R, Scarpace L, Ellika S, Schultz LR, Rock JP, Rosenblum ML, Patel SC, Lee TY, Mikkelsen T (2007) First-pass perfusion computed tomography: initial experience in differentiating recurrent brain tumors from radiation effects and radiation necrosis. *Neurosurgery* 61: 778-786; discussion 786-777
- James JS, Radhakrishnan A, Thomas B, Madhusoodanan M, Kesavadas C, Abraham M, Menon R, Rathore C, Vilanilam G (2015) Diffusion tensor imaging tractography of Meyer's loop in planning resective surgery for drug-resistant temporal lobe epilepsy. *Epilepsy research* 110: 95-104
- Javadi SA, Nabavi A, Giordano M, Faghihzadeh E, Samii A (2017) Evaluation of Diffusion Tensor Imaging-Based Tractography of the Corticospinal Tract: A Correlative Study With Intraoperative Magnetic Resonance Imaging and Direct Electrical Subcortical Stimulation. *Neurosurgery* 80: 287-299
- Jelescu IO, Palombo M, Bagnato F, Schilling KG (2020) Challenges for biophysical modeling of microstructure. *Journal of neuroscience methods* 344: 108861
- Jelescu IO, Veraart J, Fieremans E, Novikov DS (2016) Degeneracy in model parameter estimation for multi-compartmental diffusion in neuronal tissue. *NMR Biomed* 29: 33-47
- Jellison BJ, Field AS, Medow J, Lazar M, Salamat MS, Alexander AL (2004) Diffusion tensor imaging of cerebral white matter: a pictorial review of physics, fiber tract anatomy, and tumor imaging patterns. *AJNR Am J Neuroradiol* 25: 356-369
- Jenkinson M, Bannister P, Brady M, Smith S (2002) Improved optimization for the robust and accurate linear registration and motion correction of brain images. *Neuroimage* 17: 825-841

- Jenkinson MD, du Plessis DG, Smith TS, Brodbelt AR, Joyce KA, Walker C (2010) Cellularity and apparent diffusion coefficient in oligodendroglial tumours characterized by genotype. *J Neurooncol* 96: 385-392
- Jha DK, Khera P, Bhaskar S, Garg M (2019) Three-Dimensional Volume Rendering: An Underutilized Tool in Neurosurgery. *World Neurosurg* 130: 485-492
- Jiang X, Li H, Xie J, McKinley ET, Zhao P, Gore JC, Xu J (2017) In vivo imaging of cancer cell size and cellularity using temporal diffusion spectroscopy. *Magn Reson Med* 78: 156-164
- John F, Bosnyak E, Robinette NL, Amit-Yousif AJ, Barger GR, Shah KD, Michelhaugh SK, Klinger NV, Mittal S, Juhasz C (2019) Multimodal imaging-defined subregions in newly diagnosed glioblastoma: impact on overall survival. *Neuro Oncol* 21: 264-273
- Johnson GB, Harms HJ, Johnson DR, Jacobson MS, 2020. PET Imaging of Tumor Perfusion-A Potential Cancer Biomarker?, *Semin Nucl Med*. Elsevier.
- Johnston EW, Bonet-Carne E, Ferizi U, Yvernault B, Pye H, Patel D, Clemente J, Piga W, Heavey S, Sidhu HS et al (2019) VERDICT MRI for Prostate Cancer: Intracellular Volume Fraction versus Apparent Diffusion Coefficient. *Radiology* 291: 391-397
- Juan-Albarracin J, Fuster-Garcia E, Garcia-Ferrando GA, Garcia-Gomez JM (2019) ONCOhabitats: A system for glioblastoma heterogeneity assessment through MRI. *Int J Med Inform* 128: 53-61
- Juan-Albarracin J, Fuster-Garcia E, Perez-Girbes A, Aparici-Robles F, Alberich-Bayarri A, Revert-Ventura A, Marti-Bonmati L, Garcia-Gomez JM (2018) Glioblastoma: Vascular Habitats Detected at Preoperative Dynamic Susceptibility-weighted Contrast-enhanced Perfusion MR Imaging Predict Survival. *Radiology* 287: 944-954
- Juhasz C, Bosnyak E (2016) PET and SPECT studies in children with hemispheric low-grade gliomas. *Childs Nerv Syst* 32: 1823-1832
- Jun P, Garcia J, Tihan T, McDermott MW, Cha S (2006) Perfusion MR imaging of an intracranial collision tumor confirmed by image-guided biopsy. *AJNR Am J Neuroradiol* 27: 94-97
- Kadota Y, Hirai T, Azuma M, Hattori Y, Khant ZA, Hori M, Saito K, Yokogami K, Takeshima H (2020) Differentiation between glioblastoma and solitary brain metastasis using neurite orientation dispersion and density imaging. *J Neuroradiol* 47: 197-202
- Kamada K, Todo T, Masutani Y, Aoki S, Ino K, Takano T, Kirino T, Kawahara N, Morita A (2005) Combined use of tractography-integrated functional neuronavigation and direct fiber stimulation. *Journal of neurosurgery* 102: 664-672
- Kamada K, Todo T, Ota T, Ino K, Masutani Y, Aoki S, Takeuchi F, Kawai K, Saito N (2009) The motor-evoked potential threshold evaluated by tractography and electrical stimulation. *J Neurosurg* 111: 785-795
- Kang BK, Na DG, Ryoo JW, Byun HS, Roh HG, Pyeun YS (2001) Diffusion-weighted MR imaging of intracerebral hemorrhage. *Korean J Radiol* 2: 183-191
- Karimi S, Petrovich NM, Peck KK, Hou BL, Holodny AI (2006) Advanced MR techniques in brain tumor imaging. *Applied Radiology* 35: 9
- Karschnia P, Vogelbaum MA, van den Bent M, Cahill DP, Bello L, Narita Y, Berger MS, Weller M, Tonn JC (2021) Evidence-based recommendations on categories for extent of resection in diffuse glioma. *Eur J Cancer* 149: 23-33
- Keles GE, Chang EF, Lamborn KR, Tihan T, Chang CJ, Chang SM, Berger MS (2006) Volumetric extent of resection and residual contrast enhancement on initial surgery as predictors of outcome in adult patients with hemispheric anaplastic astrocytoma. *J Neurosurg* 105: 34-40
- Keles GE, Lundin DA, Lamborn KR, Chang EF, Ojemann G, Berger MS (2004) Intraoperative subcortical stimulation mapping for hemispheric perirolandic gliomas located within or

- adjacent to the descending motor pathways: evaluation of morbidity and assessment of functional outcome in 294 patients. *Journal of neurosurgery* 100: 369-375
- Kelly P, Dumas-Duport C, Kispert D, Kall B, Scheithauer B, Illig J (1987) Imaging-based stereotaxic serial biopsies in untreated intracranial glial neoplasms. *J Neurosurg* 66: 865-874
- Khan I, Waqas M, Shamim MS (2017) Prognostic significance of IDH 1 mutation in patients with glioblastoma multiforme. *J Pak Med Assoc* 67: 816-817
- Khan KA, Jain SK, Sinha VD, Sinha J (2019) Preoperative Diffusion Tensor Imaging: A Landmark Modality for Predicting the Outcome and Characterization of Supratentorial Intra-Axial Brain Tumors. *World Neurosurg*
- Kikinis R, Pieper S (2011) 3D Slicer as a tool for interactive brain tumor segmentation. *Annu Int Conf IEEE Eng Med Biol Soc* 2011: 6982-6984
- Kim G, Jung H-J, Lee H-J, Lee J-S, Koo S, Chang S-H (2012) Accuracy and reliability of length measurements on three-dimensional computed tomography using open-source OsiriX software. *Journal of digital imaging* 25: 486-491
- Kim JY, Gatenby RA (2017) Quantitative Clinical Imaging Methods for Monitoring Intratumoral Evolution. *Methods Mol Biol* 1513: 61-81
- Kim M, Park JE, Kim HS, Kim N, Park SY, Kim YH, Kim JH (2021a) Spatiotemporal habitats from multiparametric physiologic MRI distinguish tumor progression from treatment-related change in post-treatment glioblastoma. *Eur Radiol*
- Kim M, Park JE, Kim HS, Kim N, Park SY, Kim YH, Kim JH (2021b) Spatiotemporal habitats from multiparametric physiologic MRI distinguish tumor progression from treatment-related change in post-treatment glioblastoma. *Eur Radiol* 31: 6374-6383
- Kim SS, McCutcheon IE, Suki D, Weinberg JS, Sawaya R, Lang FF, Ferson D, Heimberger AB, DeMonte F, Prabhu SS (2009) Awake craniotomy for brain tumors near eloquent cortex: correlation of intraoperative cortical mapping with neurological outcomes in 309 consecutive patients. *Neurosurgery* 64: 836-845; discussion 345-836
- Kin T, Nakatomi H, Shojima M, Tanaka M, Ino K, Mori H, Kunimatsu A, Oyama H, Saito N (2012) A new strategic neurosurgical planning tool for brainstem cavernous malformations using interactive computer graphics with multimodal fusion images. *J Neurosurg* 117: 78-88
- Kin T, Nakatomi H, Shono N, Nomura S, Saito T, Oyama H, Saito N (2017) Neurosurgical Virtual Reality Simulation for Brain Tumor Using High-definition Computer Graphics: A Review of the Literature. *Neurol Med Chir (Tokyo)* 57: 513-520
- Kin T, Shin M, Oyama H, Kamada K, Kunimatsu A, Momose T, Saito N (2011) Impact of multiorgan fusion imaging and interactive 3-dimensional visualization for intraventricular neuroendoscopic surgery. *Neurosurgery* 69: ons40-48; discussion ons48
- Kleiser R, Staempfli P, Valavanis A, Boesiger P, Kollias S (2010) Impact of fMRI-guided advanced DTI fiber tracking techniques on their clinical applications in patients with brain tumors. *Neuroradiology* 52: 37
- Koivukangas J, Louhisalmi Y, Alakuijala J, Oikarinen J (1993) Ultrasound-controlled neuronavigator-guided brain surgery. *J Neurosurg* 79: 36-42
- Komori T, Muragaki Y, Chernov MF (2018) Pathology and Genetics of Gliomas. *Prog Neurol Surg* 31: 1-37
- Kotrotsou A, Zinn PO, Colen RR (2016) Radiomics in brain tumors: an emerging technique for characterization of tumor environment. *Magnetic Resonance Imaging Clinics* 24: 719-729
- Krings T, Schreckenberger M, Rohde V, Spetzger U, Sabri O, Reinges MH, Hans FJ, Meyer PT, Moller-Hartmann W, Gilsbach JM et al (2002) Functional MRI and 18F FDG-positron

- emission tomography for presurgical planning: comparison with electrical cortical stimulation. *Acta Neurochir (Wien)* 144: 889-899; discussion 899
- Kristensen BW, Priesterbach-Ackley LP, Petersen JK, Wesseling P (2019) Molecular pathology of tumors of the central nervous system. *Ann Oncol* 30: 1265-1278
- Krivosheya D, Prabhu SS, Weinberg JS, Sawaya R (2016) Technical principles in glioma surgery and preoperative considerations. *J Neurooncol* 130: 243-252
- Krolak-Salmon P, Guenot M, Tiliket C, Isnard J, Sindou M, Manguiere F, Vighetto A (2000) Anatomy of optic nerve radiations as assessed by static perimetry and MRI after tailored temporal lobectomy. *British Journal of Ophthalmology* 84: 884-889
- Kuchcinski G, Mellerio C, Pallud J, Dezamis E, Turc G, Rigaux-Viodé O, Malherbe C, Roca P, Leclerc X, Varlet P (2015) Three-tesla functional MR language mapping: comparison with direct cortical stimulation in gliomas. *Neurology* 84: 560-568
- Kuhnt D, Bauer MH, Becker A, Merhof D, Zolal A, Richter M, Grummich P, Ganslandt O, Buchfelder M, Nimsy C (2012) Intraoperative visualization of fiber tracking based reconstruction of language pathways in glioma surgery. *Neurosurgery* 70: 911-919; discussion 919-920
- Kuhnt D, Bauer MH, Sommer J, Merhof D, Nimsy C (2013) Optic radiation fiber tractography in glioma patients based on high angular resolution diffusion imaging with compressed sensing compared with diffusion tensor imaging - initial experience. *PLoS One* 8: e70973
- Lacroix M, Abi-Said D, Fourney DR, Gokaslan ZL, Shi W, DeMonte F, Lang FF, McCutcheon IE, Hassenbusch SJ, Holland E et al (2001) A multivariate analysis of 416 patients with glioblastoma multiforme: prognosis, extent of resection, and survival. *J Neurosurg* 95: 190-198
- Lasocki A, Tsui A, Tacey MA, Drummond KJ, Field KM, Gaillard F (2015) MRI grading versus histology: predicting survival of World Health Organization grade II-IV astrocytomas. *AJNR Am J Neuroradiol* 36: 77-83
- Latysheva A, Emblem KE, Brandal P, Vik-Mo EO, Pahnke J, Roysland K, Hald JK, Server A (2019) Dynamic susceptibility contrast and diffusion MR imaging identify oligodendroglioma as defined by the 2016 WHO classification for brain tumors: histogram analysis approach. *Neuroradiology* 61: 545-555
- Laundre BJ, Jellison BJ, Badie B, Alexander AL, Field AS (2005) Diffusion tensor imaging of the corticospinal tract before and after mass resection as correlated with clinical motor findings: preliminary data. *American Journal of Neuroradiology* 26: 791-796
- Law I, Albert NL, Arbizu J, Boellaard R, Drzezga A, Galldiks N, La Fougère C, Langen K-J, Lopci E, Lowe V (2019) Joint EANM/EANO/RANO practice guidelines/SNMMI procedure standards for imaging of gliomas using PET with radiolabelled amino acids and [18 F] FDG: version 1.0. *European journal of nuclear medicine and molecular imaging* 46: 540-557
- Law M, Young RJ, Babb JS, Peccerelli N, Chheang S, Gruber ML, Miller DC, Golfinos JG, Zagzag D, Johnson G (2008) Gliomas: predicting time to progression or survival with cerebral blood volume measurements at dynamic susceptibility-weighted contrast-enhanced perfusion MR imaging. *Radiology* 247: 490-498
- Lazar M, Alexander A, Thottakara P, Badie B, Field A (2006) White matter reorganization after surgical resection of brain tumors and vascular malformations. *American journal of neuroradiology* 27: 1258-1271
- Le Bihan D (2019) What can we see with IVIM MRI? *Neuroimage* 187: 56-67
- Lee J, Narang S, Martinez J, Rao G, Rao A (2015a) Spatial Habitat Features Derived from Multiparametric Magnetic Resonance Imaging Data Are Associated with Molecular Subtype and 12-Month Survival Status in Glioblastoma Multiforme. *PLoS One* 10: e0136557

- Lee J, Narang S, Martinez JJ, Rao G, Rao A (2015b) Associating spatial diversity features of radiologically defined tumor habitats with epidermal growth factor receptor driver status and 12-month survival in glioblastoma: methods and preliminary investigation. *J Med Imaging (Bellingham)* 2: 041006
- LeRoux PD, Berger MS, Ojemann GA, Wang K, Mack LA (1989) Correlation of intraoperative ultrasound tumor volumes and margins with preoperative computerized tomography scans. An intraoperative method to enhance tumor resection. *J Neurosurg* 71: 691-698
- Leu K, Ott GA, Lai A, Nghiemphu PL, Pope WB, Yong WH, Liao LM, Cloughesy TF, Ellingson BM (2017) Perfusion and diffusion MRI signatures in histologic and genetic subtypes of WHO grade II-III diffuse gliomas. *J Neurooncol* 134: 177-188
- Li C, Yan JL, Torheim T, McLean MA, Boonzaier NR, Zou J, Huang Y, Yuan J, van Dijken BRJ, Matys T et al (2019a) Low perfusion compartments in glioblastoma quantified by advanced magnetic resonance imaging and correlated with patient survival. *Radiother Oncol* 134: 17-24
- Li W, An D, Tong X, Liu W, Xiao F, Ren J, Niu R, Tang Y, Zhou B, Lei D (2019b) Different patterns of white matter changes after successful surgery of mesial temporal lobe epilepsy. *NeuroImage: Clinical* 21: 101631
- Li X, Zhu Y, Kang H, Zhang Y, Liang H, Wang S, Zhang W (2015) Glioma grading by microvascular permeability parameters derived from dynamic contrast-enhanced MRI and intratumoral susceptibility signal on susceptibility weighted imaging. *Cancer Imaging* 15: 1-9
- Li YM, Suki D, Hess K, Sawaya R (2016) The influence of maximum safe resection of glioblastoma on survival in 1229 patients: Can we do better than gross-total resection? *J Neurosurg* 124: 977-988
- Li ZC, Bai H, Sun Q, Li Q, Liu L, Zou Y, Chen Y, Liang C, Zheng H (2018a) Multiregional radiomics features from multiparametric MRI for prediction of MGMT methylation status in glioblastoma multiforme: A multicentre study. *Eur Radiol* 28: 3640-3650
- Li ZC, Bai H, Sun Q, Zhao Y, Lv Y, Zhou J, Liang C, Chen Y, Liang D, Zheng H (2018b) Multiregional radiomics profiling from multiparametric MRI: Identifying an imaging predictor of IDH1 mutation status in glioblastoma. *Cancer Med* 7: 5999-6009
- Lo C-Y, Chao Y-P, Chou K-H, Guo W-Y, Su J-L, Lin C-P, 2007. DTI-based virtual reality system for neurosurgery, 2007 29th Annual International Conference of the IEEE Engineering in Medicine and Biology Society. IEEE, pp. 1326-1329.
- Lohmann P, Galldiks N, Kocher M, Heinzl A, Filss CP, Stegmayr C, Mottaghy FM, Fink GR, Shah NJ, Langen K-J (2021) Radiomics in neuro-oncology: Basics, workflow, and applications. *Methods* 188: 112-121
- Lombardi G, Barresi V, Castellano A, Tabouret E, Pasqualetti F, Salvalaggio A, Cerretti G, Caccese M, Padovan M, Zagonel V et al (2020) Clinical management of diffuse low-grade gliomas. *Cancers* 12: 1-25
- Lopci E, Riva M, Olivari L, Raneri F, Soffietti R, Piccardo A, Bizzi A, Navarra P, Ascolese AM, Ruda R et al (2017) Prognostic value of molecular and imaging biomarkers in patients with supratentorial glioma. *Eur J Nucl Med Mol Imaging* 44: 1155-1164
- Louis DN, Perry A, Reifenberger G, von Deimling A, Figarella-Branger D, Cavenee WK, Ohgaki H, Wiestler OD, Kleihues P, Ellison DW (2016) The 2016 World Health Organization Classification of Tumors of the Central Nervous System: a summary. *Acta Neuropathol* 131: 803-820

- Louis DN, Perry A, Wesseling P, Brat DJ, Cree IA, Figarella-Branger D, Hawkins C, Ng HK, Pfister SM, Reifenberger G et al (2021) The 2021 WHO Classification of Tumors of the Central Nervous System: a summary. *Neuro Oncol* 23: 1231-1251
- Lovato RM, Araujo JLV, Paiva ALC, Pesente FS, Yaltirik CK, Harput MV, Veiga JCE (2019) The use of osirix for surgical planning using cranial measures and region of interest tools. *Asian journal of neurosurgery* 14: 762
- Lu Y, Yeung C, Radmanesh A, Wiemann R, Black PM, Golby AJ (2015) Comparative effectiveness of frame-based, frameless, and intraoperative magnetic resonance imaging-guided brain biopsy techniques. *World Neurosurg* 83: 261-268
- Mabray MC, Barajas RF, Cha S (2015) Modern brain tumor imaging. *Brain tumor research and treatment* 3: 8-23
- Maesawa S, Fujii M, Nakahara N, Watanabe T, Wakabayashi T, Yoshida J (2010) Intraoperative tractography and motor evoked potential (MEP) monitoring in surgery for gliomas around the corticospinal tract. *World Neurosurg* 74: 153-161
- Maier SE, Sun Y, Mulkern RV (2010) Diffusion imaging of brain tumors. *NMR Biomed* 23: 849-864
- Majós C, Julià-Sapé M, Alonso J, Serrallonga M, Aguilera C, Acebes JJ, Arús C, Gili J (2004) Brain tumor classification by proton MR spectroscopy: comparison of diagnostic accuracy at short and long TE. *American Journal of Neuroradiology* 25: 1696-1704
- Malilay ORM, Ferraris KP, Navarro JEV (2021) Editorial. Neurosurgical planning in a low-resource setting using free open-source three-dimensional volume-rendering software. *Neurosurgical focus* 50: E2
- Mandonnet E, Jbabdi S, Taillandier L, Galanaud D, Benali H, Capelle L, Duffau H (2007) Preoperative estimation of residual volume for WHO grade II glioma resected with intraoperative functional mapping. *Neuro Oncol* 9: 63-69
- Mapelli P, Bettinardi V, Fallanca F, Incerti E, Compierchio A, Rossetti F, Coliva A, Savi A, Doglioni C, Negri G et al (2018) 18F-FAZA PET/CT in the Preoperative Evaluation of NSCLC: Comparison with 18F-FDG and Immunohistochemistry. *Curr Radiopharm* 11: 50-57
- Mapelli P, Callea M, Fallanca F, Castellano A, Bailo M, Scifo P, Bettinardi V, Conte GM, Monterisi C, Rancoita PMV et al (2021) 18F-FAZA PET/CT in pretreatment assessment of hypoxic status in high-grade glioma: correlation with hypoxia immunohistochemical biomarkers. *Nucl Med Commun* 42: 763-771
- Mapelli P, Fallanca F, Scifo P, Barbera M, Castellano A, Bettinardi V, Incerti E, Gianolli L, Anzalone N, Picchio M (2020) Hypoxia and Amino Acid Imaging of High-Grade Glioma: 18F-FAZA PET/CT and 11C-Methionine PET/MRI. *Clin Nucl Med* 45: e290-e293
- Mapelli P, Incerti E, Fallanca F, Bettinardi V, Compierchio A, Masiello V, Doglioni C, Rossetti F, Negri G, Gianolli L et al (2017a) Concomitant Lung Cancer and Gastrointestinal Stromal Tumor: First Report of Hypoxia Imaging With 18F-FAZA PET/CT. *Clin Nucl Med* 42: e349-e351
- Mapelli P, Picchio M (2020) 18F-FAZA PET imaging in tumor hypoxia: A focus on high-grade glioma. *Int J Biol Markers* 35: 42-46
- Mapelli P, Zerbetto F, Incerti E, Conte GM, Bettinardi V, Fallanca F, Anzalone N, Di Muzio N, Gianolli L, Picchio M (2017b) 18F-FAZA PET/CT Hypoxia Imaging of High-Grade Glioma Before and After Radiotherapy. *Clin Nucl Med* 42: e525-e526
- Marko NF, Weil RJ, Schroeder JL, Lang FF, Suki D, Sawaya RE (2014) Extent of resection of glioblastoma revisited: personalized survival modeling facilitates more accurate survival

- prediction and supports a maximum-safe-resection approach to surgery. *J Clin Oncol* 32: 774-782
- Marongiu A, D'Andrea G, Raco A (2017) 1.5-T Field Intraoperative Magnetic Resonance Imaging Improves Extent of Resection and Survival in Glioblastoma Removal. *World Neurosurgery* 98: 578-586
- Masui K, Mischel PS, Reifenberger G (2016) Chapter 6 - Molecular classification of gliomas. In: *Handbook of Clinical Neurology*, Berger M.S., Weller M. (eds.) pp. 97-120. Elsevier:
- Matthew M Grabowski 1 PFR, Amy S Nowacki, Jason L Schroeder, Lilyana Angelov, Gene H Barnett, Michael A Vogelbaum (2014) Residual tumor volume versus extent of resection: predictors of survival after surgery for glioblastoma. *J Neurosurg*
- McGirt MJ, Mukherjee D, Chaichana KL, Than KD, Weingart JD, Quinones-Hinojosa A (2009) Association of surgically acquired motor and language deficits on overall survival after resection of glioblastoma multiforme. *Neurosurgery* 65: 463-470
- McKnight TR, Mary H, Vigneron DB, Lu Y, Berger MS, McDermott MW, Dillon WP, Graves EE, Pirzkall A, Nelson SJ (2002) Histopathological validation of a three-dimensional magnetic resonance spectroscopy index as a predictor of tumor presence. *Journal of neurosurgery* 97: 794-802
- Metwali H, Raemaekers M, Kniese K, Kardavani B, Fahlbusch R, Samii A (2019) Reliability of functional magnetic resonance imaging in patients with brain tumors: a critical review and meta-analysis. *World neurosurgery* 125: 183-190
- Mikkelsen VE, Solheim O, Salvesen O, Torp SH (2021) The histological representativeness of glioblastoma tissue samples. *Acta Neurochir (Wien)* 163: 1911-1920
- Mikkelsen VE, Stensjoen AL, Berntsen EM, Nordrum IS, Salvesen O, Solheim O, Torp SH (2018) Histopathologic Features in Relation to Pretreatment Tumor Growth in Patients with Glioblastoma. *World Neurosurg* 109: e50-e58
- Mills S, Du Plessis D, Pal P, Thompson G, Buonacorsi G, Soh C, Parker G, Jackson A (2016) Mitotic activity in glioblastoma correlates with estimated extravascular extracellular space derived from dynamic contrast-enhanced MR imaging. *American Journal of Neuroradiology* 37: 811-817
- Millward CP, Brodbelt AR, Haylock B, Zakaria R, Baborie A, Crooks D, Husband D, Shenoy A, Wong H, Jenkinson MD (2016) The impact of MGMT methylation and IDH-1 mutation on long-term outcome for glioblastoma treated with chemoradiotherapy. *Acta Neurochir (Wien)* 158: 1943-1953
- Miloushev VZ, Chow DS, Filippi CG (2015) Meta-analysis of diffusion metrics for the prediction of tumor grade in gliomas. *AJNR Am J Neuroradiol* 36: 302-308
- Miner RC (2017) Image-Guided Neurosurgery. *J Med Imaging Radiat Sci* 48: 328-335
- Mishra SK, Singh P (2010) History of neuroimaging: the legacy of William Oldendorf. *Journal of child neurology* 25: 508-517
- Molina-Romero M, Wiestler B, Gómez PA, Menzel MI, Menze BH, 2018. Deep Learning with Synthetic Diffusion MRI Data for Free-Water Elimination in Glioblastoma Cases. Springer International Publishing, Cham, pp. 98-106.
- Molinaro AM, Hervey-Jumper S, Morshed RA, Young J, Han SJ, Chunduru P, Zhang Y, Phillips JJ, Shai A, Lafontaine M et al (2020) Association of Maximal Extent of Resection of Contrast-Enhanced and Non-Contrast-Enhanced Tumor With Survival Within Molecular Subgroups of Patients With Newly Diagnosed Glioblastoma. *JAMA Oncol* 6: 495-503
- Mormina E, Longo M, Arrigo A, Alafaci C, Tomasello F, Calamuneri A, Marino S, Gaeta M, Vinci SL, Granata F (2015) MRI Tractography of Corticospinal Tract and Arcuate

- Fasciculus in High-Grade Gliomas Performed by Constrained Spherical Deconvolution: Qualitative and Quantitative Analysis. *AJNR Am J Neuroradiol* 36: 1853-1858
- Morrison MA, Tam F, Garavaglia MM, Hare GM, Cusimano MD, Schweizer TA, Das S, Graham SJ (2016) Sources of variation influencing concordance between functional MRI and direct cortical stimulation in brain tumor surgery. *Frontiers in neuroscience* 10: 461
- Moussazadeh N, Tsiouris AJ, Ramakrishna R (2016) Advanced Imaging for Biopsy Guidance in Primary Brain Tumors. *Cureus* 8: e504
- Muragaki Y, Chernov M, Maruyama T, Ochiai T, Taira T, Kubo O, Nakamura R, Iseki H, Hori T, Takakura K (2008) Low-grade glioma on stereotactic biopsy: how often is the diagnosis accurate? *Minim Invasive Neurosurg* 51: 275-279
- Nagane M, Kobayashi K, Tanaka M, Tsuchiya K, Shishido-Hara Y, Shimizu S, Shiokawa Y (2014) Predictive significance of mean apparent diffusion coefficient value for responsiveness of temozolomide-refractory malignant glioma to bevacizumab: preliminary report. *Int J Clin Oncol* 19: 16-23
- Napolitano M, Vaz G, Lawson TM, Docquier M-A, van Maanen A, Duprez T, Raftopoulos C (2014) Glioblastoma surgery with and without intraoperative MRI at 3.0 T. *Neuro-Chirurgie* 60: 143-150
- Negwer C, Sollmann N, Ille S, Hauck T, Maurer S, Kirschke JS, Ringel F, Meyer B, Krieg SM (2017) Language pathway tracking: comparing nTMS-based DTI fiber tracking with a cubic ROIs-based protocol. *Journal of neurosurgery* 126: 1006-1014
- Nguyen T, Cron G, Bezzina K, Perdrizet K, Torres C, Chakraborty S, Woulfe J, Jansen G, Thornhill R, Zanette B (2016) Correlation of tumor immunohistochemistry with dynamic contrast-enhanced and DSC-MRI parameters in patients with gliomas. *American Journal of Neuroradiology* 37: 2217-2223
- Nguyen TB, Melkus G, Taccone M, Moldovan ID, Ghinda D, Gotfrit R, Torres CH, Zakhari N, Chakraborty S, Woulfe J et al (2021) Preoperative Determination of Isocitrate Dehydrogenase Mutation in Gliomas Using Spectral Editing MRS: A Prospective Study. *J Magn Reson Imaging* 53: 416-426
- Nilsson M, Englund E, Szczepankiewicz F, van Westen D, Sundgren PC (2018a) Imaging brain tumour microstructure. *Neuroimage* 182: 232-250
- Nilsson M, Szczepankiewicz F, Brabec J, Taylor M, Westin CF, Golby A, van Westen D, Sundgren PC (2020) Tensor-valued diffusion MRI in under 3 minutes: an initial survey of microscopic anisotropy and tissue heterogeneity in intracranial tumors. *Magn Reson Med* 83: 608-620
- Nilsson M, Szczepankiewicz F, Lampinen B, Ahlgren A, de Almeida Martins JP, Lasic S, Westin C-F, Topgaard D, 2018b. An open-source framework for analysis of multidimensional diffusion MRI data implemented in MATLAB, Joint Annual Meeting ISMRM-ESMRMB. Paris, France, p. 5355.
- Nimsky C, Carl B (2015) Intraoperative Imaging. In: *Image-Guided Neurosurgery*, Golby A.J. (ed.) pp. 163-190. Academic Press: Boston
- Nimsky C, Ganslandt O, Fahlbusch R (2006) Implementation of fiber tract navigation. *Neurosurgery* 58: ONS-292-ONS-303
- Nimsky C, Ganslandt O, Hastreiter P, Wang R, Benner T, Sorensen AG, Fahlbusch R (2005a) Intraoperative diffusion-tensor MR imaging: shifting of white matter tracts during neurosurgical procedures—initial experience. *Radiology* 234: 218-225
- Nimsky C, Ganslandt O, Hastreiter P, Wang R, Benner T, Sorensen AG, Fahlbusch R (2005b) Preoperative and intraoperative diffusion tensor imaging-based fiber tracking in glioma surgery. *Neurosurgery* 56: 130-137

- Nimsky C, Grummich P, Sorensen AG, Fahlbusch R, Ganslandt O (2005c) Visualization of the pyramidal tract in glioma surgery by integrating diffusion tensor imaging in functional neuronavigation. *Zentralbl Neurochir* 66: 133-141
- Nossek E, Korn A, Shahar T, Kanner AA, Yaffe H, Marcovici D, Ben-Harosh C, Ben Ami H, Weinstein M, Shapira-Lichter I et al (2011) Intraoperative mapping and monitoring of the corticospinal tracts with neurophysiological assessment and 3-dimensional ultrasonography-based navigation. Clinical article. *J Neurosurg* 114: 738-746
- Nuno M, Birch K, Mukherjee D, Sarmiento JM, Black KL, Patil CG (2013) Survival and prognostic factors of anaplastic gliomas. *Neurosurgery* 73: 458-465; quiz 465
- O'Connor JP, Rose CJ, Waterton JC, Carano RA, Parker GJ, Jackson A (2015) Imaging intratumor heterogeneity: role in therapy response, resistance, and clinical outcome. *Clin Cancer Res* 21: 249-257
- Ogawa S, Lee TM, Kay AR, Tank DW (1990) Brain magnetic resonance imaging with contrast dependent on blood oxygenation. *Proc Natl Acad Sci U S A* 87: 9868-9872
- Ohue S, Kohno S, Inoue A, Yamashita D, Harada H, Kumon Y, Kikuchi K, Miki H, Ohnishi T (2012) Accuracy of diffusion tensor magnetic resonance imaging-based tractography for surgery of gliomas near the pyramidal tract: a significant correlation between subcortical electrical stimulation and postoperative tractography. *Neurosurgery* 70: 283-293; discussion 294
- Oishi M, Fukuda M, Hiraishi T, Yajima N, Sato Y, Fujii Y (2012) Interactive virtual simulation using a 3D computer graphics model for microvascular decompression surgery. *J Neurosurg* 117: 555-565
- Oishi M, Fukuda M, Ishida G, Saito A, Hiraishi T, Fujii Y (2011a) Prediction of the microsurgical window for skull-base tumors by advanced three-dimensional multi-fusion volumetric imaging. *Neurol Med Chir (Tokyo)* 51: 201-207
- Oishi M, Fukuda M, Ishida G, Saito A, Hiraishi T, Fujii Y (2011b) Presurgical simulation with advanced 3-dimensional multifusion volumetric imaging in patients with skull base tumors. *Neurosurgery* 68: 188-199; discussion 199
- Okuchi S, Rojas-Garcia A, Ulyte A, Lopez I, Usinskiene J, Lewis M, Hassanein SM, Sanverdi E, Golay X, Thust S et al (2019) Diagnostic accuracy of dynamic contrast-enhanced perfusion MRI in stratifying gliomas: A systematic review and meta-analysis. *Cancer Med* 8: 5564-5573
- Ono Y, Chernov MF, Muragaki Y, Maruyama T, Abe K, Iseki H (2018) Imaging of Intracranial Gliomas. *Prog Neurol Surg* 30: 12-62
- Oppenlander ME, Wolf AB, Snyder LA, Bina R, Wilson JR, Coons SW, Ashby LS, Brachman D, Nakaji P, Porter RW et al (2014) An extent of resection threshold for recurrent glioblastoma and its risk for neurological morbidity. *J Neurosurg* 120: 846-853
- Orringer D, Lau D, Khatri S, Zamora-Berridi GJ, Zhang K, Wu C, Chaudhary N, Sagher O (2012) Extent of resection in patients with glioblastoma: limiting factors, perception of resectability, and effect on survival. *J Neurosurg* 117: 851-859
- Ostrom QT BL, Davis FG, Deltour I, Fisher 505., JL LC, Pekmezci M, Schwartzbaum JA, Turner MC, Walsh KM, Wrensch MR, Barnholtz- Sloan JS (2014) The epidemiology of glioma in adults: a "state of the science" review. *Neuro Oncol* 16: 896-913
- Ostrom QT, Cote DJ, Ascha M, Kruchko C, Barnholtz-Sloan JS (2018a) Adult Glioma Incidence and Survival by Race or Ethnicity in the United States From 2000 to 2014. *JAMA Oncology* 4: 1254-1262

- Ostrom QT, Gittleman H, Liao P, Rouse C, Chen Y, Dowling J, Wolinsky Y, Kruchko C, Barnholtz-Sloan J (2014) CBTRUS statistical report: primary brain and central nervous system tumors diagnosed in the United States in 2007-2011. *Neuro Oncol* 16
- Ostrom QT, Gittleman H, Stetson L, Virk S, Barnholtz-Sloan JS (2018b) Epidemiology of Intracranial Gliomas. *Prog Neurol Surg* 30: 1-11
- Ostrom QT, Rubin JB, Lathia JD, Berens ME, Barnholtz-Sloan JS (2018c) Females have the survival advantage in glioblastoma. *Neuro-oncology* 20: 576
- Ostrý S, Belšan T, Otáhal J, Beneš V, Netuka D (2013) Is intraoperative diffusion tensor imaging at 3.0 T comparable to subcortical corticospinal tract mapping? *Neurosurgery* 73: 797-807
- Ozhinsky E, Vigneron DB, Chang SM, Nelson SJ (2013) Automated prescription of oblique brain 3D magnetic resonance spectroscopic imaging. *Magn Reson Med* 69: 920-930
- Pak RW, Hadjiabadi DH, Senarathna J, Agarwal S, Thakor NV, Pillai JJ, Pathak AP (2017) Implications of neurovascular uncoupling in functional magnetic resonance imaging (fMRI) of brain tumors. *Journal of Cerebral Blood Flow & Metabolism* 37: 3475-3487
- Palombo M, Ianus A, Guerreri M, Nunes D, Alexander DC, Shemesh N, Zhang H (2020) SANDI: A compartment-based model for non-invasive apparent soma and neurite imaging by diffusion MRI. *NeuroImage* 215: 116835
- Panagiotaki E, Chan RW, Dikaos N, Ahmed HU, O'Callaghan J, Freeman A, Atkinson D, Punwani S, Hawkes DJ, Alexander DC (2015) Microstructural characterization of normal and malignant human prostate tissue with vascular, extracellular, and restricted diffusion for cytometry in tumours magnetic resonance imaging. *Invest Radiol* 50: 218-227
- Panagiotaki E, Schneider T, Siow B, Hall MG, Lythgoe MF, Alexander DC (2012) Compartment models of the diffusion MR signal in brain white matter: a taxonomy and comparison. *Neuroimage* 59: 2241-2254
- Panagiotaki E, Walker-Samuel S, Siow B, Johnson SP, Rajkumar V, Pedley RB, Lythgoe MF, Alexander DC (2014) Noninvasive quantification of solid tumor microstructure using VERDICT MRI. *Cancer Res* 74: 1902-1912
- Park JE, Kim HS, Kim N, Park SY, Kim YH, Kim JH (2021) Spatiotemporal Heterogeneity in Multiparametric Physiologic MRI Is Associated with Patient Outcomes in IDH-Wildtype Glioblastoma. *Clin Cancer Res* 27: 237-245
- Patankar TF, Haroon HA, Mills SJ, Balériaux D, Buckley DL, Parker GJ, Jackson A (2005) Is volume transfer coefficient (K_{trans}) related to histologic grade in human gliomas? *American Journal of Neuroradiology* 26: 2455-2465
- Pessina F, Navarria P, Cozzi L, Ascolese AM, Simonelli M, Santoro A, Clerici E, Rossi M, Scorsetti M, Bello L (2017) Maximize surgical resection beyond contrast-enhancing boundaries in newly diagnosed glioblastoma multiforme: is it useful and safe? A single institution retrospective experience. *J Neurooncol* 135: 129-139
- Pieri V, Sanvito F, Riva M, Petrini A, Rancoita PMV, Cirillo S, Iadanza A, Bello L, Castellano A, Falini A (2021) Along-tract statistics of neurite orientation dispersion and density imaging diffusion metrics to enhance MR tractography quantitative analysis in healthy controls and in patients with brain tumors. *Hum Brain Mapp* 42: 1268-1286
- Pierpaoli C, Jezzard P, Basser PJ, Barnett A, Di Chiro G (1996) Diffusion tensor MR imaging of the human brain. *Radiology* 201: 637-648
- Pillai JJ, Zaca D (2012) Comparison of BOLD cerebrovascular reactivity mapping and DSC MR perfusion imaging for prediction of neurovascular uncoupling potential in brain tumors. *Technol Cancer Res Treat* 11: 361-374
- Piovesana A, Senior G (2018) How Small Is Big: Sample Size and Skewness. *Assessment* 25: 793-800

- Ponte KF, Berro DH, Collet S, Constans JM, Emery E, Valable S, Guillamo JS (2017) In Vivo Relationship Between Hypoxia and Angiogenesis in Human Glioblastoma: A Multimodal Imaging Study. *J Nucl Med* 58: 1574-1579
- Potgieser ARE, Wagemakers M, Van Hulzen ALJ, De Jong BM, Hoving EW, Groen RJM (2014) The role of diffusion tensor imaging in brain tumor surgery: A review of the literature. *Clinical Neurology and Neurosurgery* 124: 51-58
- Prabhu SS, Gasco J, Tummala S, Weinberg JS, Rao G (2011) Intraoperative magnetic resonance imaging-guided tractography with integrated monopolar subcortical functional mapping for resection of brain tumors. *Clinical article. J Neurosurg* 114: 719-726
- Pramanik PP, Parmar HA, Mammoser AG, Junck LR, Kim MM, Tsien CI, Lawrence TS, Cao Y (2015) Hypercellularity components of glioblastoma identified by high b-value diffusion-weighted imaging. *International Journal of Radiation Oncology* Biology* Physics* 92: 811-819
- Preibisch C, Shi K, Kluge A, Lukas M, Wiestler B, Gottler J, Gempt J, Ringel F, Al Jaber M, Schlegel J et al (2017) Characterizing hypoxia in human glioma: A simultaneous multimodal MRI and PET study. *NMR Biomed* 30: e3775
- Provenzale JM, Mukundan S, Barboriak DP (2006) Diffusion-weighted and perfusion MR imaging for brain tumor characterization and assessment of treatment response. *Radiology* 239: 632-649
- Qiu T-m, Zhang Y, Wu J-S, Tang W-J, Zhao Y, Pan Z-G, Mao Y, Zhou L-F (2010a) Virtual reality presurgical planning for cerebral gliomas adjacent to motor pathways in an integrated 3-D stereoscopic visualization of structural MRI and DTI tractography. *Acta neurochirurgica* 152: 1847-1857
- Qiu TM, Zhang Y, Wu JS, Tang WJ, Zhao Y, Pan ZG, Mao Y, Zhou LF (2010b) Virtual reality presurgical planning for cerebral gliomas adjacent to motor pathways in an integrated 3-D stereoscopic visualization of structural MRI and DTI tractography. *Acta Neurochir (Wien)* 152: 1847-1857
- Qiuting W, Douglas ACK, Suchandrima B, Janine ML, Susan MC, Duan X, Christopher PH, Sarah JN (2015) Clinically feasible NODDI characterization of glioma using multiband EPI at 7 T. *NeuroImage: Clinical* 9: 291-299
- Raab P, Hattingen E, Franz K, Zanella FE, Lanfermann H (2010) Cerebral gliomas: diffusional kurtosis imaging analysis of microstructural differences. *Radiology* 254: 876-881
- Raja R, Sinha N, Saini J, Mahadevan A, Rao KN, Swaminathan A (2016) Assessment of tissue heterogeneity using diffusion tensor and diffusion kurtosis imaging for grading gliomas. *Neuroradiology* 58: 1217-1231
- Randazzo M, Pisapia JM, Singh N, Thawani JP (2016) 3D printing in neurosurgery: A systematic review. *Surgical neurology international* 7: S801-S809
- Reithmeier T, Lopez WO, Doostkam S, Machein MR, Pinsker MO, Trippel M, Nikkhah G (2013) Intraindividual comparison of histopathological diagnosis obtained by stereotactic serial biopsy to open surgical resection specimen in patients with intracranial tumours. *Clin Neurol Neurosurg* 115: 1955-1960
- Ribom D, Engler H, Blomquist E, Smits A (2002) Potential significance of 11 C-methionine PET as a marker for the radiosensitivity of low-grade gliomas. *European journal of nuclear medicine and molecular imaging* 29: 632-640
- Ricci PE, Dungan DH (2001) Imaging of low- and intermediate-grade gliomas. *Semin Radiat Oncol* 11: 103-112
- Rigolo L, Stern E, Deaver P, Golby AJ, Mukundan S, Jr. (2011) Development of a clinical functional magnetic resonance imaging service. *Neurosurg Clin N Am* 22: 307-314, x

- Riva M, Hiepe P, Frommert M, Divenuto I, Gay LG, Sciortino T, Nibali MC, Rossi M, Pessina F, Bello L (2020) Intraoperative Computed Tomography and Finite Element Modelling for Multimodal Image Fusion in Brain Surgery. *Operative neurosurgery (Hagerstown, Md)* 18: 531-541
- Roberts TA, Hyare H, Agliardi G, Hipwell B, d'Esposito A, Ianus A, Breen-Norris JO, Ramasawmy R, Taylor V, Atkinson D et al (2020) Noninvasive diffusion magnetic resonance imaging of brain tumour cell size for the early detection of therapeutic response. *Sci Rep* 10: 9223
- Roder C, Bisdas S, Ebner FH, Honegger J, Naegele T, Ernemann U, Tatagiba M (2014) Maximizing the extent of resection and survival benefit of patients in glioblastoma surgery: high-field iMRI versus conventional and 5-ALA-assisted surgery. *Eur J Surg Oncol* 40: 297-304
- Romano A, D'andrea G, Minniti G, Mastronardi L, Ferrante L, Fantozzi L, Bozzao A (2009) Pre-surgical planning and MR-tractography utility in brain tumour resection. *European radiology* 19: 2798-2808
- Romano A, Ferrante M, Cipriani V, Fasoli F, Ferrante L, D'Andrea G, Fantozzi LM, Bozzao A (2007) Role of magnetic resonance tractography in the preoperative planning and intraoperative assessment of patients with intra-axial brain tumours. *Radiol Med* 112: 906-920
- Rosenstock T, Giampiccolo D, Schneider H, Runge SJ, Bährend I, Vajkoczy P, Picht T (2017a) Specific DTI seeding and diffusivity-analysis improve the quality and prognostic value of TMS-based deterministic DTI of the pyramidal tract. *Neuroimage: Clinical* 16: 276-285
- Rosenstock T, Grittner U, Acker G, Schwarzer V, Kulchytska N, Vajkoczy P, Picht T (2017b) Risk stratification in motor area-related glioma surgery based on navigated transcranial magnetic stimulation data. *Journal of neurosurgery* 126: 1227-1237
- Rosinska S, Gavard J (2021) Tumor Vessels Fuel the Fire in Glioblastoma. *Int J Mol Sci* 22
- Rotariu DI, Ziyad F, Budu A, Poata I (2017) The Role of OsiriX Based Virtual Endoscopy in Planning Endoscopic Transsphenoidal Surgery for Pituitary Adenoma. *Turkish neurosurgery* 27: 339-345
- Roth A, Buttrick SS, Cajigas I, Jagid JR, Ivan ME (2018) Accuracy of frame-based and frameless systems for deep brain stimulation: A meta-analysis. *J Clin Neurosci* 57: 1-5
- Rotkopf LT, Wiestler B, Preibisch C, Liesche-Starnecker F, Pyka T, Norenberg D, Bette S, Gempt J, Thierfelder KM, Zimmer C et al (2020) The wavelet power spectrum of perfusion weighted MRI correlates with tumor vascularity in biopsy-proven glioblastoma samples. *PLoS One* 15: e0228030
- Roux F-E, Lubrano V, Lotterie J-A, Giussani C, Pierroux C, Demonet J-F (2007) When “abegg” is read and (“A, B, E, G, G”) is not: A cortical stimulation study of musical score reading. *Journal of neurosurgery* 106: 1017-1027
- Roux FE, Boulanouar K, Lotterie JA, Mejdoubi M, LeSage JP, Berry I (2003) Language functional magnetic resonance imaging in preoperative assessment of language areas: correlation with direct cortical stimulation. *Neurosurgery* 52: 1335-1345; discussion 1345-1337
- Roy B, Gupta RK, Maudsley AA, Awasthi R, Sherif S, Gu M, Husain N, Mohakud S, Behari S, Pandey CM et al (2013) Utility of multiparametric 3-T MRI for glioma characterization. *Neuroradiology* 55: 603-613
- Rundle-Thiele D, Day B, Stringer B, Fay M, Martin J, Jeffree RL, Thomas P, Bell C, Salvado O, Gal Y et al (2015) Using the apparent diffusion coefficient to identifying MGMT promoter methylation status early in glioblastoma: importance of analytical method. *J Med Radiat Sci* 62: 92-98

- Ruparelia J, Gosal JS, Garg M, Bhaskar S, Jha DK (2020) Letter to the Editor: Challenges to Neurosurgical Residency Training During COVID-19 Pandemic: An Indian Perspective. *World Neurosurg* 140: 464-466
- Ryken TC, Kalkanis SN, Buatti JM, Olson JJ, Committee ACJG (2014) The role of cytoreductive surgery in the management of progressive glioblastoma : a systematic review and evidence-based clinical practice guideline. *J Neurooncol* 118: 479-488
- Saito T, Maruyama T, Muragaki Y, Tanaka M, Nitta M, Shinoda J, Aki T, Iseki H, Kurisu K, Okada Y (2013) 11C-methionine uptake correlates with combined 1p and 19q loss of heterozygosity in oligodendroglial tumors. *AJNR Am J Neuroradiol* 34: 85-91
- Saito T, Tamura M, Chernov MF, Ikuta S, Muragaki Y, Maruyama T (2018) Neurophysiological Monitoring and Awake Craniotomy for Resection of Intracranial Gliomas. *Prog Neurol Surg* 30: 117-158
- Salama GR, Heier LA, Patel P, Ramakrishna R, Magge R, Tsiouris AJ (2017) Diffusion Weighted/Tensor Imaging, Functional MRI and Perfusion Weighted Imaging in Glioblastoma-Foundations and Future. *Front Neurol* 8: 660
- Sales AHA, Bette S, Barz M, Huber T, Wiestler B, Ryang YM, Schmidt-Graf F, Liesche F, Combs SE, Meyer B et al (2019) Role of postoperative tumor volume in patients with MGMT-unmethylated glioblastoma. *J Neurooncol* 142: 529-536
- Sanai N, Mirzadeh Z, Berger MS (2008) Functional outcome after language mapping for glioma resection. *N Engl J Med* 358: 18-27
- Sanai N, Polley MY, McDermott MW, Parsa AT, Berger MS (2011) An extent of resection threshold for newly diagnosed glioblastomas. *J Neurosurg* 115: 3-8
- Sang S, Wanggou S, Wang Z, Lin X, Jiang N, Ye N, Li X (2018) Clinical Long-Term Follow-Up Evaluation of Functional Neuronavigation in Adult Cerebral Gliomas. *World Neurosurg* 119: e262-e271
- Santarosa C, Castellano A, Conte GM, Cadioli M, Iadanza A, Terreni MR, Franzin A, Bello L, Caulo M, Falini A (2016) Dynamic contrast-enhanced and dynamic susceptibility contrast perfusion MR imaging for glioma grading: preliminary comparison of vessel compartment and permeability parameters using hotspot and histogram analysis. *European Journal of Radiology* 85: 1147-1156
- Sanvito F, Castellano A, Falini A (2021) Advancements in Neuroimaging to Unravel Biological and Molecular Features of Brain Tumors. *Cancers (Basel)* 13: 424
- Sanvito F, Caverzasi E, Riva M, Jordan KM, Blasi V, Scifo P, Iadanza A, Crespi SA, Cirillo S, Casarotti A et al (2020) fMRI-Targeted High-Angular Resolution Diffusion MR Tractography to Identify Functional Language Tracts in Healthy Controls and Glioma Patients. *Front Neurosci* 14: 225
- Sauwen N, Acou M, Van Cauter S, Sima DM, Veraart J, Maes F, Himmelreich U, Achten E, Van Huffel S (2016) Comparison of unsupervised classification methods for brain tumor segmentation using multi-parametric MRI. *Neuroimage Clin* 12: 753-764
- Savi A, Incerti E, Fallanca F, Bettinardi V, Rossetti F, Monterisi C, Compierchio A, Negri G, Zannini P, Gianolli L et al (2017a) First Evaluation of PET-Based Human Biodistribution and Dosimetry of (18)F-FAZA, a Tracer for Imaging Tumor Hypoxia. *J Nucl Med* 58: 1224-1229
- Savi A, Incerti E, Fallanca F, Bettinardi V, Rossetti F, Monterisi C, Compierchio A, Negri G, Zannini P, Gianolli L et al (2017b) First Evaluation of PET-Based Human Biodistribution and Dosimetry of (18)F-FAZA, a Tracer for Imaging Tumor Hypoxia. *J Nucl Med* 58: 1224-1229

- Sawaya R, Hammoud M, Schoppa D, Hess KR, Wu SZ, Shi WM, Wildrick DM (1998) Neurosurgical outcomes in a modern series of 400 craniotomies for treatment of parenchymal tumors. *Neurosurgery* 42: 1044-1055; discussion 1055-1046
- Sciortino T, Fernandes B, Conti Nibali M, Gay LG, Rossi M, Lopci E, Colombo AE, Elefante MG, Pessina F, Bello L et al (2019) Frameless stereotactic biopsy for precision neurosurgery: diagnostic value, safety, and accuracy. *Acta Neurochir (Wien)* 161: 967-974
- Senft C, Bink A, Franz K, Vatter H, Gasser T, Seifert V (2011a) Intraoperative MRI guidance and extent of resection in glioma surgery: a randomised, controlled trial. *Lancet Oncol* 12: 997-1003
- Senft C, Bink A, Heckelmann M, Gasser T, Seifert V (2011b) Glioma extent of resection and ultra-low-field iMRI: interim analysis of a prospective randomized trial. In: *Intraoperative Imaging*, pp. 49-53. Springer:
- Servadei F, Rossini Z, Nicolosi F, Morselli C, Park KB (2018) The Role of Neurosurgery in Countries with Limited Facilities: Facts and Challenges. *World Neurosurg* 112: 315-321
- Shah V, Kochar P (2018) Brain Cancer: Implication to Disease, Therapeutic Strategies and Tumor Targeted Drug Delivery Approaches. *Recent Pat Anticancer Drug Discov* 13: 70-85
- Shahar T, Korn A, Barkay G, Biron T, Hadanny A, Gazit T, Nossek E, Ekstein M, Kesler A, Ram Z (2018) Elaborate mapping of the posterior visual pathway in awake craniotomy. *J Neurosurg* 128: 1503-1511
- Shaikh F, Dupont-Roettger D, Dehmeshki J, Awan O, Kubassova O, Bisdas S (2020) The Role of Imaging Biomarkers Derived From Advanced Imaging and Radiomics in the Management of Brain Tumors. *Front Oncol* 10
- Shalan ME, Soliman AY, Nassar IA, Alarabawy RA (2021) Surgical planning in patients with brain glioma using diffusion tensor MR imaging and tractography. *Egyptian Journal of Radiology and Nuclear Medicine* 52: 110
- Shiban E, Krieg SM, Haller B, Buchmann N, Obermueller T, Boeckh-Behrens T, Wostrack M, Meyer B, Ringel F (2015) Intraoperative subcortical motor evoked potential stimulation: how close is the corticospinal tract? *Journal of neurosurgery* 123: 711-720
- Shinojima N, Kochi M, Hamada J, Nakamura H, Yano S, Makino K, Tsuiki H, Tada K, Kuratsu J, Ishimaru Y et al (2004) The influence of sex and the presence of giant cells on postoperative long-term survival in adult patients with supratentorial glioblastoma multiforme. *J Neurosurg* 101: 219-226
- Singh G, Manjila S, Sakla N, True A, Wardeh AH, Beig N, Vaysberg A, Matthews J, Prasanna P, Spektor V (2021) Radiomics and radiogenomics in gliomas: a contemporary update. *Br J Cancer* 125: 641-657
- Sinha S, Bastin ME, Whittle IR, Wardlaw JM (2002) Diffusion tensor MR imaging of high-grade cerebral gliomas. *AJNR Am J Neuroradiol* 23: 520-527
- Smith JS, Chang EF, Lamborn KR, Chang SM, Prados MD, Cha S, Tihan T, Vandenberg S, McDermott MW, Berger MS (2008) Role of extent of resection in the long-term outcome of low-grade hemispheric gliomas. *J Clin Oncol* 26: 1338-1345
- Smits A, Jakola AS (2019) Clinical Presentation, Natural History, and Prognosis of Diffuse Low-Grade Gliomas. *Neurosurg Clin N Am* 30: 35-42
- Sollmann N, Kelm A, Ille S, Schroder A, Zimmer C, Ringel F, Meyer B, Krieg SM (2018) Setup presentation and clinical outcome analysis of treating highly language-eloquent gliomas via preoperative navigated transcranial magnetic stimulation and tractography. *Neurosurgical focus* 44: E2
- Sollmann N, Negwer C, Tussis L, Hauck T, Ille S, Maurer S, Giglhuber K, Bauer JS, Ringel F, Meyer B (2017) Interhemispheric connectivity revealed by diffusion tensor imaging fiber

- tracking derived from navigated transcranial magnetic stimulation maps as a sign of language function at risk in patients with brain tumors. *Journal of neurosurgery* 126: 222-233
- Soni N, Mehrotra A, Behari S, Kumar S, Gupta N (2017) Diffusion-tensor imaging and tractography application in pre-operative planning of intra-axial brain lesions. *Cureus* 9
- Sottoriva A, Spiteri I, Piccirillo SG, Touloumis A, Collins VP, Marioni JC, Curtis C, Watts C, Tavare S (2013) Intratumor heterogeneity in human glioblastoma reflects cancer evolutionary dynamics. *Proc Natl Acad Sci U S A* 110: 4009-4014
- Spicer MA, van Velsen M, Caffrey JP, Apuzzo ML (2004) Virtual reality neurosurgery: a simulator blueprint. *Neurosurgery* 54: 783-798
- Spiegel EA, Wycis HT, Marks M, Lee AJ (1947) Stereotaxic Apparatus for Operations on the Human Brain. *Science* 106: 349-350
- Spiriev T, Nakov V, Laleva L, Tzekov C (2017) OsiriX software as a preoperative planning tool in cranial neurosurgery: A step-by-step guide for neurosurgical residents. *Surgical neurology international* 8: 241
- Stabellini N, Krebs H, Patil N, Waite K, Barnholtz-Sloan JS (2021) Sex Differences in Time to Treat and Outcomes for Gliomas. *Front Oncol* 11: 630597
- Stadie AT, Kockro RA, Reisch R, Tropine A, Boor S, Stoeter P, Perneczky A (2008) Virtual reality system for planning minimally invasive neurosurgery. Technical note. *J Neurosurg* 108: 382-394
- Stadlbauer A, Buchfelder M, Doelken MT, Hammen T, Ganslandt O (2011) Magnetic resonance spectroscopic imaging for visualization of the infiltration zone of glioma. *Cent Eur Neurosurg* 72: 63-69
- Stadlbauer A, Mouridsen K, Doerfler A, Bo Hansen M, Oberndorfer S, Zimmermann M, Buchfelder M, Heinz G, Roessler K (2018a) Recurrence of glioblastoma is associated with elevated microvascular transit time heterogeneity and increased hypoxia. *J Cereb Blood Flow Metab* 38: 422-432
- Stadlbauer A, Zimmermann M, Doerfler A, Oberndorfer S, Buchfelder M, Coras R, Kitzwogerer M, Roessler K (2018b) Intratumoral heterogeneity of oxygen metabolism and neovascularization uncovers 2 survival-relevant subgroups of IDH1 wild-type glioblastoma. *Neuro Oncol* 20: 1536-1546
- Stadlbauer A, Zimmermann M, Kitzwogerer M, Oberndorfer S, Rossler K, Dorfler A, Buchfelder M, Heinz G (2017) MR Imaging-derived Oxygen Metabolism and Neovascularization Characterization for Grading and IDH Gene Mutation Detection of Gliomas. *Radiology* 283: 799-809
- Sternberg EJ, Lipton ML, Burns J (2014) Utility of diffusion tensor imaging in evaluation of the peritumoral region in patients with primary and metastatic brain tumors. *AJNR Am J Neuroradiol* 35: 439-444
- Steven AJ, Zhuo J, Melhem ER (2014) Diffusion kurtosis imaging: an emerging technique for evaluating the microstructural environment of the brain. *American journal of roentgenology* 202: W26-W33
- Stieglitz LH, Seidel K, Wiest R, Beck J, Raabe A (2012) Localization of primary language areas by arcuate fascicle fiber tracking. *Neurosurgery* 70: 56-65
- Stringfield O, Arrington JA, Johnston SK, Rognin NG, Peeri NC, Balagurunathan Y, Jackson PR, Clark-Swanson KR, Swanson KR, Egan KM et al (2019) Multiparameter MRI Predictors of Long-Term Survival in Glioblastoma Multiforme. *Tomography* 5: 135-144
- Stummer W, Reulen HJ, Meinel T, Pichlmeier U, Schumacher W, Tonn JC, Rohde V, Opperl F, Turowski B, Woiciechowsky C et al (2008) Extent of resection and survival in glioblastoma

- multiforme: identification of and adjustment for bias. *Neurosurgery* 62: 564-576; discussion 564-576
- Sugahara T, Korogi Y, Kochi M, Ikushima I, Shigematu Y, Hirai T, Okuda T, Liang L, Ge Y, Komohara Y et al (1999) Usefulness of diffusion-weighted MRI with echo-planar technique in the evaluation of cellularity in gliomas. *J Magn Reson Imaging* 9: 53-60
- Sugahara T, Korogi Y, Kochi M, Ushio Y, Takahashi M (2001) Perfusion-sensitive MR imaging of gliomas: comparison between gradient-echo and spin-echo echo-planar imaging techniques. *American Journal of Neuroradiology* 22: 1306-1315
- Suh CH, Kim HS, Jung SC, Choi CG, Kim SJ (2018) 2-Hydroxyglutarate MR spectroscopy for prediction of isocitrate dehydrogenase mutant glioma: a systemic review and meta-analysis using individual patient data. *Neuro Oncol* 20: 1573-1583
- Suh CH, Kim HS, Jung SC, Choi CG, Kim SJ (2019) Imaging prediction of isocitrate dehydrogenase (IDH) mutation in patients with glioma: a systemic review and meta-analysis. *Eur Radiol* 29: 745-758
- Svolos P, Kousi E, Kapsalaki E, Theodorou K, Fezoulidis I, Kappas C, Tsougos I (2014) The role of diffusion and perfusion weighted imaging in the differential diagnosis of cerebral tumors: a review and future perspectives. *Cancer Imaging* 14: 20
- Szczepankiewicz F, van Westen D, Englund E, Westin CF, Stahlberg F, Latt J, Sundgren PC, Nilsson M (2016) The link between diffusion MRI and tumor heterogeneity: Mapping cell eccentricity and density by diffusional variance decomposition (DIVIDE). *Neuroimage* 142: 522-532
- Szelenyi A, Bello L, Duffau H, Fava E, Feigl GC, Galanda M, Neuloh G, Signorelli F, Sala F, Workgroup for Intraoperative Management in Low-Grade Glioma Surgery within the European Low-Grade Glioma N (2010) Intraoperative electrical stimulation in awake craniotomy: methodological aspects of current practice. *Neurosurgical focus* 28: E7
- Takahashi S, Tanizaki Y, Akaji K, Kano T, Hiraga K, Mihara B (2014) Usefulness of Preoperative Surgical Simulation with Three-Dimensional Fusion Images for Resection of Cerebral Cavernous Malformations Near Broca's Area. *Case Rep Neurol Med* 2014: 853425
- Talos IF, Zou KH, Ohno-Machado L, Bhagwat JG, Kikinis R, Black PM, Jolesz FA (2006) Supratentorial low-grade glioma resectability: statistical predictive analysis based on anatomic MR features and tumor characteristics. *Radiology* 239: 506-513
- Tan WL, Huang WY, Yin B, Xiong J, Wu JS, Geng DY (2014) Can diffusion tensor imaging noninvasively detect IDH1 gene mutations in astroglomas? A retrospective study of 112 cases. *AJNR Am J Neuroradiol* 35: 920-927
- Taoka T, Sakamoto M, Nakagawa H, Nakase H, Iwasaki S, Takayama K, Taoka K, Hoshida T, Sakaki T, Kichikawa K (2008) Diffusion tensor tractography of the Meyer loop in cases of temporal lobe resection for temporal lobe epilepsy: correlation between postsurgical visual field defect and anterior limit of Meyer loop on tractography. *American Journal of Neuroradiology* 29: 1329-1334
- Tariq M, Schneider T, Alexander DC, Gandini Wheeler-Kingshott CA, Zhang H (2016) Bingham-NODDI: Mapping anisotropic orientation dispersion of neurites using diffusion MRI. *Neuroimage* 133: 207-223
- Thomas NWD, Sinclair J (2015) Image-Guided Neurosurgery: History and Current Clinical Applications. *J Med Imaging Radiat Sci* 46: 331-342
- Thust SC, Heiland S, Falini A, Jager HR, Waldman AD, Sundgren PC, Godi C, Katsaros VK, Ramos A, Bargallo N et al (2018a) Glioma imaging in Europe: A survey of 220 centres and recommendations for best clinical practice. *Eur Radiol* 28: 3306-3317

- Thust SC, Heiland S, Falini A, Jäger HR, Waldman AD, Sundgren PC, Godi C, Katsaros VK, Ramos A, Bargallo N et al (2018b) Glioma imaging in Europe: A survey of 220 centres and recommendations for best clinical practice. *European Radiology* 28: 3306-3317
- Thust SC, van den Bent MJ, Smits M (2018c) Pseudoprogression of brain tumors. *J Magn Reson Imaging*
- Tietze A, Hansen MB, Ostergaard L, Jespersen SN, Sangill R, Lund TE, Geneser M, Hjelm M, Hansen B (2015) Mean Diffusional Kurtosis in Patients with Glioma: Initial Results with a Fast Imaging Method in a Clinical Setting. *AJNR Am J Neuroradiol* 36: 1472-1478
- Tournier JD, Smith R, Raffelt D, Tabbara R, Dhollander T, Pietsch M, Christiaens D, Jeurissen B, Yeh CH, Connelly A (2019) MRtrix3: A fast, flexible and open software framework for medical image processing and visualisation. *Neuroimage* 202: 116137
- Treglia G, Muoio B, Trevisi G, Mattoli MV, Albano D, Bertagna F, Giovanella L (2019) Diagnostic performance and prognostic value of PET/CT with different tracers for brain tumors: a systematic review of published meta-analyses. *International journal of molecular sciences* 20: 4669
- Tronnier V, Staubert A, Bonsanto M, Wirtz C, Kunze S (2000) Virtual reality in neurosurgery. *Der Radiologe* 40: 211-217
- Upadhyay N, Waldman AD (2011) Conventional MRI evaluation of gliomas. *Br J Radiol* 84 Spec No 2: S107-111
- Van Heerden J, Desmond PM, Phal PM (2014) Functional MRI in clinical practice: A pictorial essay. *Journal of medical imaging and radiation oncology* 58: 320-326
- Vassal F, Schneider F, Nuti C (2013) Intraoperative use of diffusion tensor imaging-based tractography for resection of gliomas located near the pyramidal tract: comparison with subcortical stimulation mapping and contribution to surgical outcomes. *British journal of neurosurgery* 27: 668-675
- Verma A, Kumar I, Verma N, Aggarwal P, Ojha R (2016) Magnetic resonance spectroscopy - Revisiting the biochemical and molecular milieu of brain tumors. *BBA Clin* 5: 170-178
- Verma R, Correa R, Hill VB, Statsevych V, Bera K, Beig N, Mahammedi A, Madabhushi A, Ahluwalia M, Tiwari P (2020) Tumor Habitat-derived Radiomic Features at Pretreatment MRI That Are Prognostic for Progression-free Survival in Glioblastoma Are Associated with Key Morphologic Attributes at Histopathologic Examination: A Feasibility Study. *Radiol Artif Intell* 2: e190168
- Villanueva-Meyer JE, Mabray MC, Cha S (2017) Current Clinical Brain Tumor Imaging. *Neurosurgery* 81: 397-415
- Vogelbaum MA, Jost S, Aghi MK, Heimberger AB, Sampson JH, Wen PY, Macdonald DR, Van den Bent MJ, Chang SM (2012) Application of novel response/progression measures for surgically delivered therapies for gliomas: Response Assessment in Neuro-Oncology (RANO) Working Group. *Neurosurgery* 70: 234-243; discussion 243-234
- Vorster SJ, Barnett GH (1998) A proposed preoperative grading scheme to assess risk for surgical resection of primary and secondary intraaxial supratentorial brain tumors. *Neurosurgical focus* 4: e2
- Wang L, Wei L, Wang J, Li N, Gao Y, Ma H, Qu X, Zhang M (2020) Evaluation of perfusion MRI value for tumor progression assessment after glioma radiotherapy: A systematic review and meta-analysis. *Medicine* 99: e23766
- Wang Q, Li Q, Mi R, Ye H, Zhang H, Chen B, Li Y, Huang G, Xia J (2019) Radiomics Nomogram Building From Multiparametric MRI to Predict Grade in Patients With Glioma: A Cohort Study. *J Magn Reson Imaging* 49: 825-833

- Wang YC, Liu YC, Hsieh TC, Lee ST, Li ML (2010) Aneurysmal subarachnoid hemorrhage diagnosis with computed tomographic angiography and OsiriX. *Acta Neurochir (Wien)* 152: 263-269; discussion 269
- Watanabe E, Mayanagi Y, Kosugi Y, Manaka S, Takakura K (1991) Open surgery assisted by the neuronavigator, a stereotactic, articulated, sensitive arm. *Neurosurgery* 28: 792-799; discussion 799-800
- Watanabe E, Watanabe T, Manaka S, Mayanagi Y, Takakura K (1987) Three-dimensional digitizer (neuronavigator): new equipment for computed tomography-guided stereotaxic surgery. *Surg Neurol* 27: 543-547
- Weber MA, Henze M, Tutenberg J, Stieltjes B, Meissner M, Zimmer F, Burkholder I, Kroll A, Combs SE, Vogt-Schaden M et al (2010) Biopsy targeting gliomas: do functional imaging techniques identify similar target areas? *Invest Radiol* 45: 755-768
- Wedeen VJ, Wang RP, Schmahmann JD, Benner T, Tseng WY, Dai G, Pandya DN, Hagmann P, D'Arceuil H, de Crespigny AJ (2008) Diffusion spectrum magnetic resonance imaging (DSI) tractography of crossing fibers. *Neuroimage* 41: 1267-1277
- Wei J, Yang G, Hao X, Gu D, Tan Y, Wang X, Dong D, Zhang S, Wang L, Zhang H et al (2019) A multi-sequence and habitat-based MRI radiomics signature for preoperative prediction of MGMT promoter methylation in astrocytomas with prognostic implication. *Eur Radiol* 29: 877-888
- Wen PY, Macdonald DR, Reardon DA, Cloughesy TF, Sorensen AG, Galanis E, Degroot J, Wick W, Gilbert MR, Lassman AB et al (2010) Updated response assessment criteria for high-grade gliomas: response assessment in neuro-oncology working group. *J Clin Oncol* 28: 1963-1972
- Wen Q, Kelley DA, Banerjee S, Lupo JM, Chang SM, Xu D, Hess CP, Nelson SJ (2015) Clinically feasible NODDI characterization of glioma using multiband EPI at 7 T. *Neuroimage Clin* 9: 291-299
- Weng H-H, Noll KR, Johnson JM, Prabhu SS, Tsai Y-H, Chang S-W, Huang Y-C, Lee J-D, Yang J-T, Yang C-T (2018) Accuracy of presurgical functional MR imaging for language mapping of brain tumors: a systematic review and meta-analysis. *Radiology* 286: 512-523
- Wengenroth M, Blatow M, Guenther J, Akbar M, Tronnier VM, Stippich C (2011) Diagnostic benefits of presurgical fMRI in patients with brain tumours in the primary sensorimotor cortex. *Eur Radiol* 21: 1517-1525
- Whitmire P, Rickertsen CR, Hawkins-Daarud A, Carrasco E, Jr., Lorence J, De Leon G, Curtin L, Bayless S, Clark-Swanson K, Peeri NC et al (2020) Sex-specific impact of patterns of imageable tumor growth on survival of primary glioblastoma patients. *BMC Cancer* 20: 447
- Whitmore RG, Krejza J, Kapoor GS, Huse J, Woo JH, Bloom S, Lopinto J, Wolf RL, Judy K, Rosenfeld MR et al (2007) Prediction of oligodendroglial tumor subtype and grade using perfusion weighted magnetic resonance imaging. *J Neurosurg* 107: 600-609
- Wijnenga MMJ, French PJ, Dubbink HJ, Dinjens WNM, Atmodimedjo PN, Kros JM, Smits M, Gahrman R, Rutten GJ, Verheul JB et al (2018) The impact of surgery in molecularly defined low-grade glioma: an integrated clinical, radiological, and molecular analysis. *Neuro Oncol* 20: 103-112
- Willems PW, Taphoorn MJ, Burger H, Berkelbach van der Sprenkel JW, Tulleken CA (2006) Effectiveness of neuronavigation in resecting solitary intracerebral contrast-enhancing tumors: a randomized controlled trial. *J Neurosurg* 104: 360-368
- Wilson M, Andronesi O, Barker PB, Bartha R, Bizzi A, Bolan PJ, Brindle KM, Choi IY, Cudalbu C, Dydak U et al (2019) Methodological consensus on clinical proton MRS of the brain: Review and recommendations. *Magn Reson Med* 82: 527-550

- Witwer BP, Moftakhar R, Hasan KM, Deshmukh P, Haughton V, Field A, Arfanakis K, Noyes J, Moritz CH, Meyerand ME et al (2002) Diffusion-tensor imaging of white matter tracts in patients with cerebral neoplasm. *J Neurosurg* 97: 568-575
- Wu EX, Cheung MM (2010) MR diffusion kurtosis imaging for neural tissue characterization. *NMR Biomed* 23: 836-848
- Wu H, Tong H, Du X, Guo H, Ma Q, Zhang Y, Zhou X, Liu H, Wang S, Fang J et al (2020) Vascular habitat analysis based on dynamic susceptibility contrast perfusion MRI predicts IDH mutation status and prognosis in high-grade gliomas. *Eur Radiol* 30: 3254-3265
- Wu JS, Zhou LF, Tang WJ, Mao Y, Hu J, Song YY, Hong XN, Du GH (2007) Clinical evaluation and follow-up outcome of diffusion tensor imaging-based functional neuronavigation: a prospective, controlled study in patients with gliomas involving pyramidal tracts. *Neurosurgery* 61: 935-948; discussion 948-939
- Wyler AR, Ward AA, Jr. (1981) Neurons in human epileptic cortex. Response to direct cortical stimulation. *J Neurosurg* 55: 904-908
- Xiong J, Tan WL, Pan JW, Wang Y, Yin B, Zhang J, Geng DY (2016) Detecting isocitrate dehydrogenase gene mutations in oligodendroglial tumors using diffusion tensor imaging metrics and their correlations with proliferation and microvascular density. *J Magn Reson Imaging* 43: 45-54
- Xu XH, Gao T, Zhang WJ, Tong LS, Gao F (2017) Remote Diffusion-Weighted Imaging Lesions in Intracerebral Hemorrhage: Characteristics, Mechanisms, Outcomes, and Therapeutic Implications. *Front Neurol* 8: 678
- Yamao Y, Suzuki K, Kunieda T, Matsumoto R, Arakawa Y, Nakae T, Nishida S, Inano R, Shibata S, Shimotake A et al (2017) Clinical impact of intraoperative CCEP monitoring in evaluating the dorsal language white matter pathway. *Hum Brain Mapp* 38: 1977-1991
- Yan J-L, van der Hoorn A, Larkin TJ, Boonzaier NR, Matys T, Price SJ (2017) Extent of resection of peritumoral diffusion tensor imaging-detected abnormality as a predictor of survival in adult glioblastoma patients. *Journal of neurosurgery* 126: 234-241
- Yoshino M, Kin T, Nakatomi H, Oyama H, Saito N (2013) Presurgical planning of feeder resection with realistic three-dimensional virtual operation field in patient with cerebellopontine angle meningioma. *Acta Neurochir (Wien)* 155: 1391-1399
- Young GS (2007) Advanced MRI of adult brain tumors. *Neurol Clin* 25: 947-973, viii
- Young RJ, Gupta A, Shah AD, Graber JJ, Schweitzer AD, Prager A, Shi W, Zhang Z, Huse J, Omuro AM (2013) Potential role of preoperative conventional MRI including diffusion measurements in assessing epidermal growth factor receptor gene amplification status in patients with glioblastoma. *AJNR Am J Neuroradiol* 34: 2271-2277
- Young RM, Jamshidi A, Davis G, Sherman JH (2015) Current trends in the surgical management and treatment of adult glioblastoma. *Ann Transl Med* 3: 121
- Yrjana SK, Tuominen J, Koivukangas J (2007) Intraoperative magnetic resonance imaging in neurosurgery. *Acta Radiol* 48: 540-549
- Yu CS, Li KC, Xuan Y, Ji XM, Qin W (2005) Diffusion tensor tractography in patients with cerebral tumors: a helpful technique for neurosurgical planning and postoperative assessment. *Eur J Radiol* 56: 197-204
- Yu W, Zhang L, Wei Q, Shao A (2019) O(6)-Methylguanine-DNA Methyltransferase (MGMT): Challenges and New Opportunities in Glioma Chemotherapy. *Front Oncol* 9: 1547
- Zaccagna F, Riemer F, Priest AN, McLean MA, Allinson K, Grist JT, Dragos C, Matys T, Gillard JH, Watts C et al (2019) Non-invasive assessment of glioma microstructure using VERDICT MRI: correlation with histology. *Eur Radiol* 29: 5559-5566

- Zach L, Guez D, Last D, Daniels D, Grober Y, Nissim O, Hoffmann C, Nass D, Talianski A, Spiegelmann R et al (2015) Delayed contrast extravasation MRI: a new paradigm in neuro-oncology. *Neuro Oncol* 17: 457-465
- Zakaria H, Haider S, Lee I (2017) Automated whole brain tractography affects preoperative surgical decision making. *Cureus* 9
- Zhang H, Schneider T, Wheeler-Kingshott CA, Alexander DC (2012) NODDI: practical in vivo neurite orientation dispersion and density imaging of the human brain. *Neuroimage* 61: 1000-1016
- Zhang H, Wang Y, Lu T, Qiu B, Tang Y, Ou S, Tie X, Sun C, Xu K, Wang Y (2013) Differences between generalized q-sampling imaging and diffusion tensor imaging in the preoperative visualization of the nerve fiber tracts within peritumoral edema in brain. *Neurosurgery* 73: 1044-1053
- Zhang J, Chen X, Zhao Y, Wang F, Li F, Xu B (2015) Impact of intraoperative magnetic resonance imaging and functional neuronavigation on surgical outcome in patients with gliomas involving language areas. *Neurosurg Rev* 38: 319-330; discussion 330
- Zhang J, Liu H, Tong H, Wang S, Yang Y, Liu G, Zhang W (2017) Clinical Applications of Contrast-Enhanced Perfusion MRI Techniques in Gliomas: Recent Advances and Current Challenges. *Contrast media & molecular imaging* 2017: 7064120
- Zhang JS, Qu L, Wang Q, Jin W, Hou YZ, Sun GC, Li FY, Yu XG, Xu BN, Chen XL (2018) Intraoperative visualisation of functional structures facilitates safe frameless stereotactic biopsy in the motor eloquent regions of the brain. *British journal of neurosurgery* 32: 372-380
- Zhang X, Lu H, Tian Q, Feng N, Yin L, Xu X, Du P, Liu Y (2019) A radiomics nomogram based on multiparametric MRI might stratify glioblastoma patients according to survival. *Eur Radiol* 29: 5528-5538
- Zhao J, Wang YL, Li XB, Hu MS, Li ZH, Song YK, Wang JY, Tian YS, Liu DW, Yan X et al (2019) Comparative analysis of the diffusion kurtosis imaging and diffusion tensor imaging in grading gliomas, predicting tumour cell proliferation and IDH-1 gene mutation status. *J Neurooncol* 141: 195-203
- Zhao Y, Chen X, Wang F, Sun G, Wang Y, Song Z, Xu B (2012) Integration of diffusion tensor-based arcuate fasciculus fibre navigation and intraoperative MRI into glioma surgery. *Journal of Clinical Neuroscience* 19: 255-261
- Zhou M, Chaudhury B, Hall LO, Goldgof DB, Gillies RJ, Gatenby RA (2017) Identifying spatial imaging biomarkers of glioblastoma multiforme for survival group prediction. *J Magn Reson Imaging* 46: 115-123
- Zhou M, Hall L, Goldgof D, Russo R, Balagurunathan Y, Gillies R, Gatenby R (2014) Radiologically defined ecological dynamics and clinical outcomes in glioblastoma multiforme: preliminary results. *Transl Oncol* 7: 5-13
- Zhou M, Scott J, Chaudhury B, Hall L, Goldgof D, Yeom KW, Iv M, Ou Y, Kalpathy-Cramer J, Napel S (2018) Radiomics in brain tumor: image assessment, quantitative feature descriptors, and machine-learning approaches. *American Journal of Neuroradiology* 39: 208-216
- Zhu F-P, Wu J-S, Song Y-Y, Yao C-J, Zhuang D-X, Xu G, Tang W-j, Qin Z-Y, Mao Y, Zhou L-F (2012) Clinical application of motor pathway mapping using diffusion tensor imaging tractography and intraoperative direct subcortical stimulation in cerebral glioma surgery: a prospective cohort study. *Neurosurgery* 71: 1170-1184
- Zhuang DX, Wu JS, Yao CJ, Qiu TM, Lu JF, Zhu FP, Xu G, Zhu W, Zhou LF (2016) Intraoperative Multi-Information-Guided Resection of Dominant-Sided Insular Gliomas in

a 3-T Intraoperative Magnetic Resonance Imaging Integrated Neurosurgical Suite. World Neurosurg 89: 84-92

Zhukov VY, Goryaynov S, Ogurtsova A, Ageev I, Protskiy S, Pronin I, Tonoyan A, Kobayakov G, Nenashev E, Smirnov A (2016) Diffusion tensor imaging tractography and intraoperative neurophysiological monitoring in surgery of intracranial tumors located near the pyramidal tract. Zh Vopr Neurokhir Im NN Burdenko 80: 5-18

Zinreich SJ, Tebo SA, Long DM, Brem H, Mattox DE, Loury ME, vander Kolk CA, Koch WM, Kennedy DW, Bryan RN (1993) Frameless stereotaxic integration of CT imaging data: accuracy and initial applications. Radiology 188: 735-742

Zolal A, Hejčl A, Vachata P, Bartoš R, Humhej I, Malucelli A, Nováková M, Hrach K, Derner M, Sameš M (2012) The use of diffusion tensor images of the corticospinal tract in intrinsic brain tumor surgery: a comparison with direct subcortical stimulation. Neurosurgery 71: 331-340

Michal Balš

Appendix: Supplementary material to *Experiment III*

A.1 *Extent of resection according to tumor location.*

| WHO 2016 Grade | Tumor Side | | | | | |
|----------------|------------|---------|-------|---------|---------|---------|
| | Right | | Left | | Midline | |
| | Count | Row N % | Count | Row N % | Count | Row N % |
| I | 6 | 28.6% | 9 | 42.9% | 6 | 28.6% |
| II | 24 | 49.0% | 23 | 46.9% | 2 | 4.1% |
| III | 17 | 39.5% | 25 | 58.1% | 1 | 2.3% |
| IV | 70 | 57.9% | 49 | 40.5% | 2 | 1.7% |

Table A.1 - Side location of gliomas according to their WHO grade.

| WHO 2016 grade | Frontal | | Temporal | | Parietal | | Occipital | | Insula | | Posterior fossa | | Midline | | Tot lesions |
|----------------|---------|-------|----------|-------|----------|-------|-----------|-------|--------|-------|-----------------|-------|---------|-------|-------------|
| | n | % | n | % | n | % | n | % | n | % | n | % | n | % | n |
| I | 4 | 19.0% | 5 | 23.8% | 2 | 9.5% | 0 | 0.0% | 1 | 4.8% | 6 | 28.6% | 6 | 28.6% | 21 |
| II | 26 | 53.1% | 15 | 30.6% | 11 | 22.4% | 3 | 6.1% | 7 | 14.3% | 1 | 2.0% | 2 | 4.1% | 49 |
| III | 20 | 46.5% | 17 | 39.5% | 11 | 25.6% | 4 | 9.3% | 7 | 16.3% | 0 | 0.0% | 1 | 2.3% | 43 |
| IV | 37 | 30.6% | 70 | 57.9% | 37 | 30.6% | 19 | 15.7% | 26 | 21.5% | 0 | 0.0% | 2 | 1.7% | 121 |

Table A.2 - Cerebral lobes/regions invaded by tumors according to different WHO grades.

Some tumors showed concurrent invasion of multiple lobes/regions. In 71% of cases the lesion affected one lobe, while in 23% it involved 2 lobes and in 3% of cases 3 lobes. Overall, 3.4% of lesions were affecting the midline area of the brain (that included the diencephalon, third ventricle, and brainstem).

| Lobe/area involved | Extent of resection among all gliomas (WHO I-IV) | | | |
|--------------------------------|--|-------------|--------------|-------------|
| | FLAIR-tumor EOR | | CE-tumor EOR | |
| | Mean | Median | Mean | Median |
| Frontal | 74.7 | 80.1 | 93.6 | 99.1 |
| Temporal | 71.9 | 75.4 | 92.4 | 98.3 |
| Insular | 68.5 | 72.2 | 91.5 | 96.3 |
| Parietal | 72.2 | 75.4 | 92.7 | 98.6 |
| Occipital | 70.3 | 75.4 | 96.3 | 97.9 |
| Cerebellar | 92.4 | 100.0 | 98.9 | 100.0 |
| Midline / Deep location | 75.6 | 84.0 | 89.4 | 95.7 |
| All lesions | 81.5 | 90.6 | 93.2 | 98.6 |

Table A.3 - Extent of resection according to the cerebral region involved.

The analysis included all gliomas (WHO I-IV)

A.2 Overall survival according to extent of resection and residual tumor volumes.

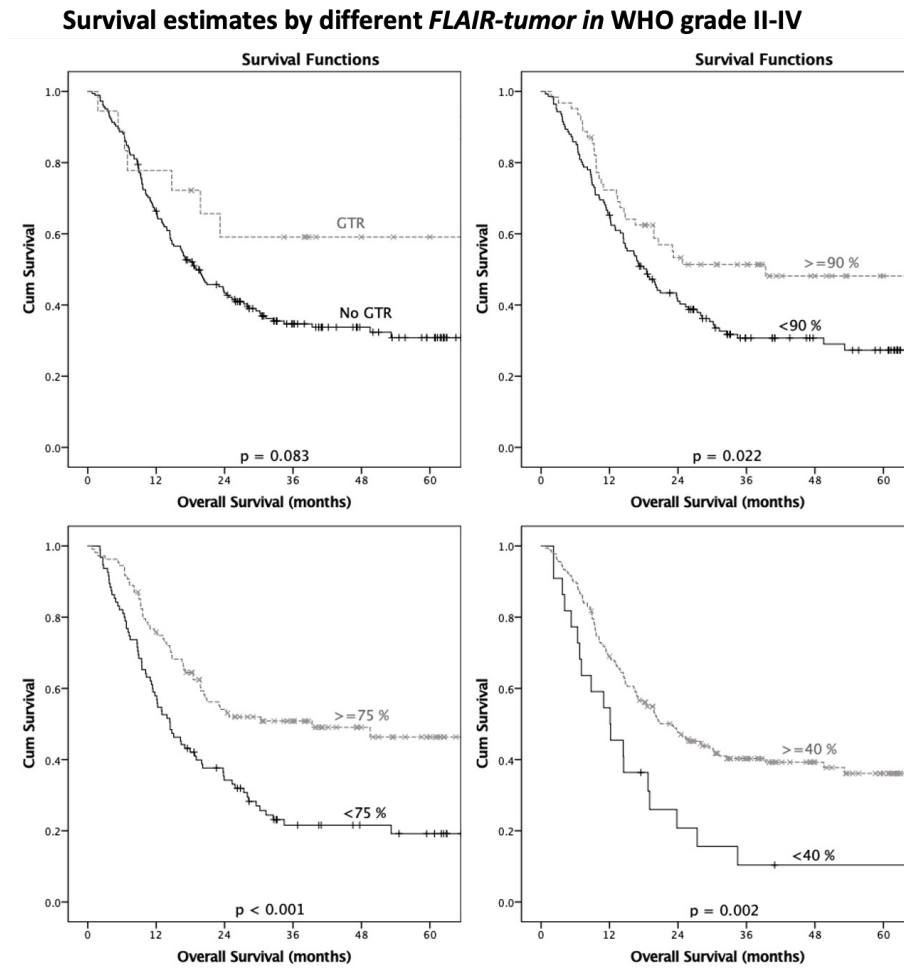


Figure A.1 - Survival estimates according to different cutoffs of FLAIR-tumor extent of resections (Gross Total Resection, $\geq 90\%$, $\geq 75\%$ and $\geq 40\%$ cutoffs in WHO grade II-IV)

Survival estimates by different FLAIR-tumor EOR in WHO grade II

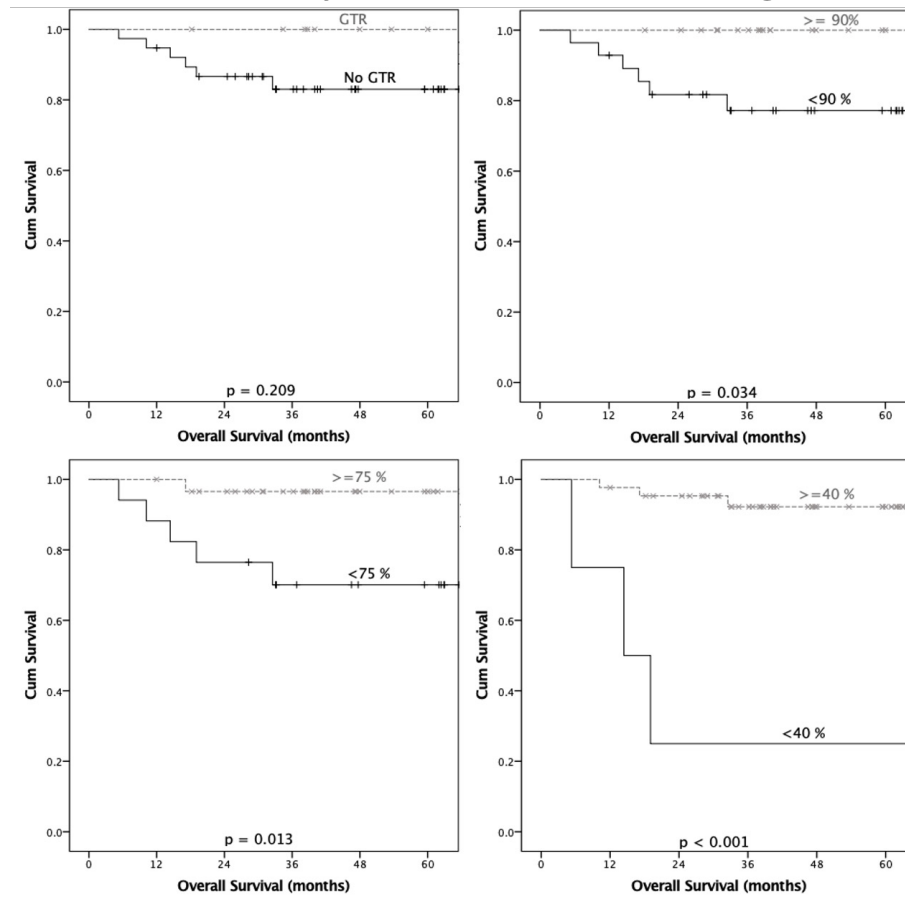


Figure A.2 - Survival estimates according to different FLAIR-tumor EOR cutoffs (Gross Total Resection, $\geq 90\%$, $\geq 75\%$, $\geq 40\%$ cutoffs for WHO grade II tumors)

Survival estimates by postoperative FLAIR-tumor volume in WHO grade II

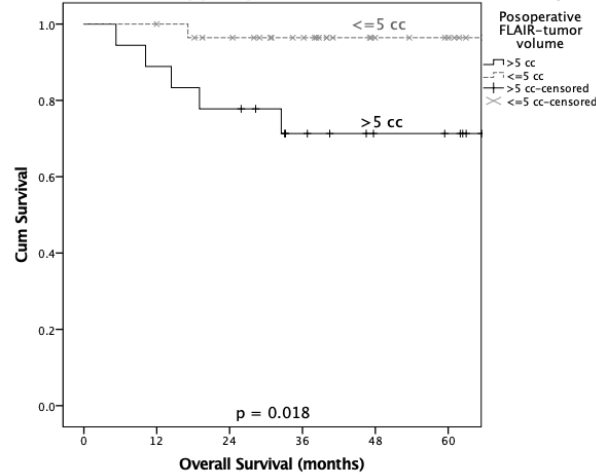


Figure A.3 - Survival estimates according to postoperative residual FLAIR-tumor volume (5 cc cutoff in WHO grade II tumors).

Survival estimates by different FLAIR-tumor in WHO grade III-IV

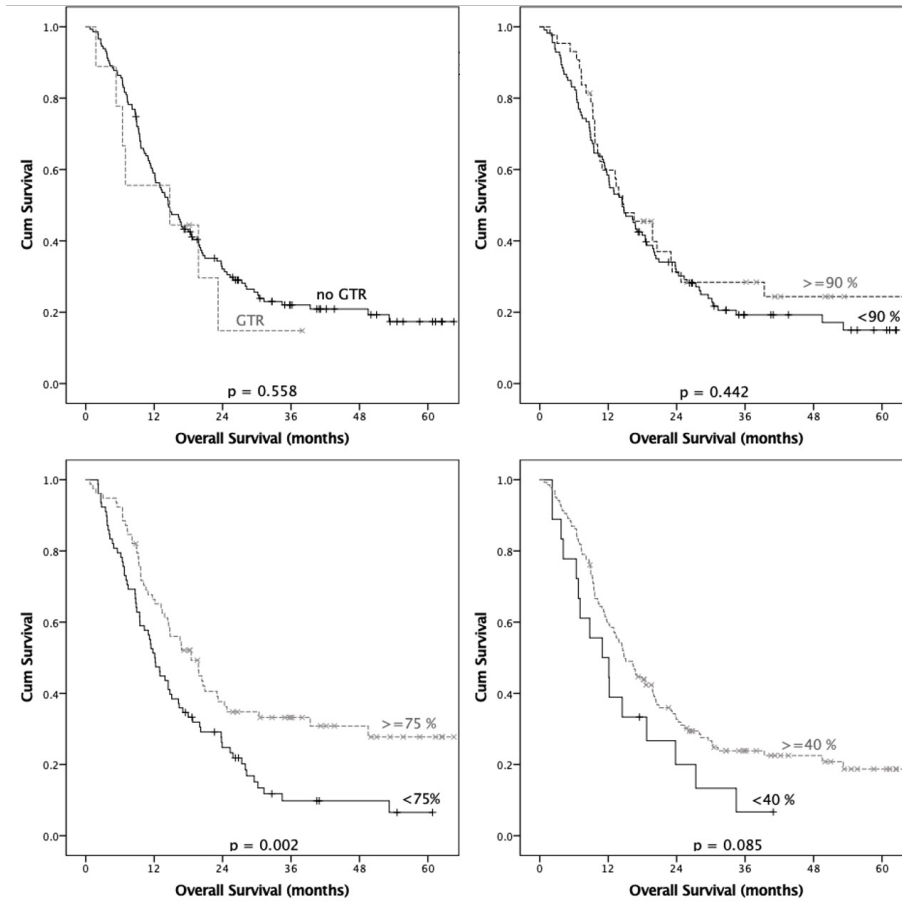


Figure A.4 - Survival estimates according to different FLAIR-tumor EOR cutoffs (Gross Total Resection, $\geq 90\%$, $\geq 75\%$ and $\geq 40\%$ cutoffs in WHO grade III-IV tumors)

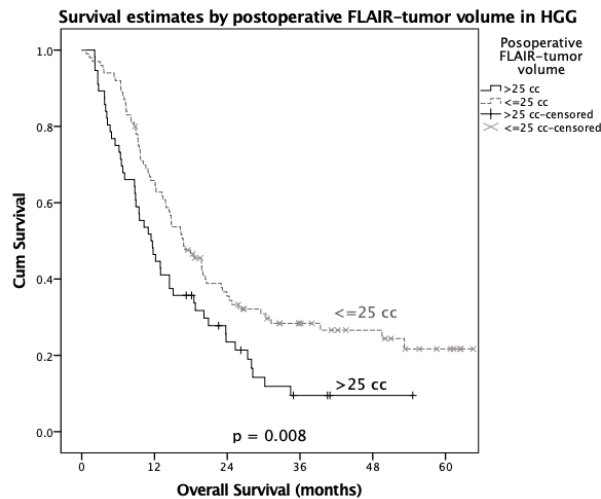


Figure A.5 - Survival estimates according to postoperative residual FLAIR-tumor volume (25 cc cutoff in WHO grade III-IV tumors).

Survival estimates by different CE-tumor in WHO grade III-IV

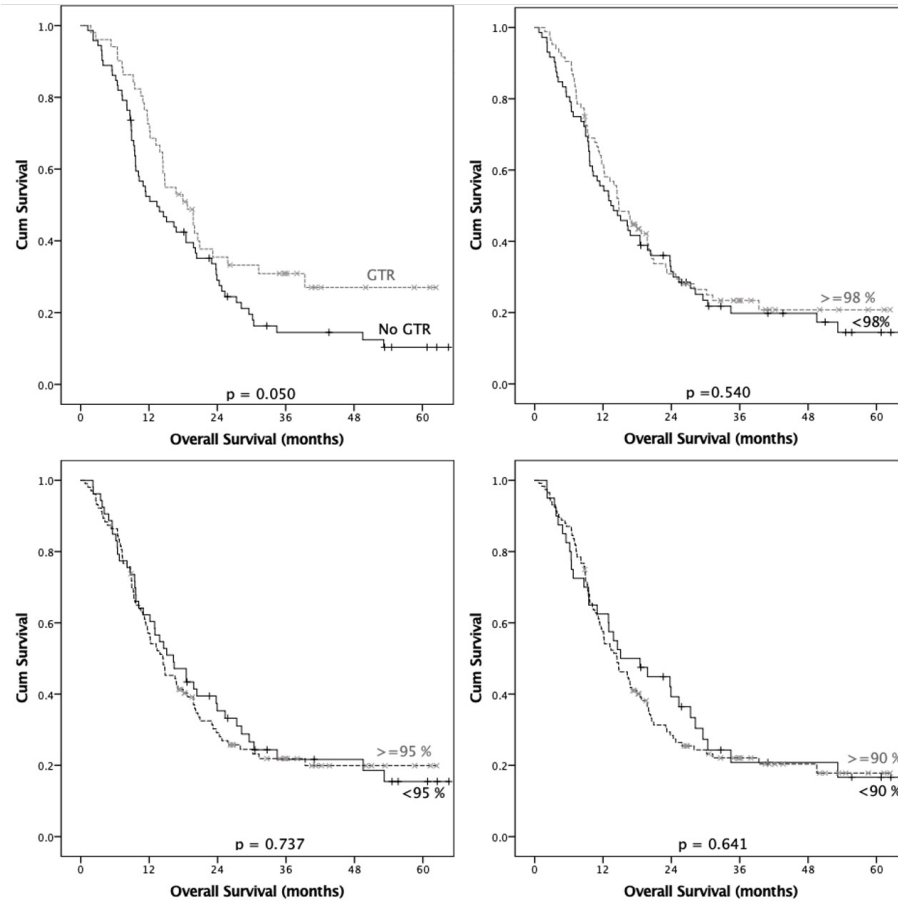


Figure A.6 - Survival estimates according to different CE-tumor EOR cutoffs (Gross Total Resection, ≥98%, ≥95% and ≥90% cutoffs in WHO grade III-IV tumors)

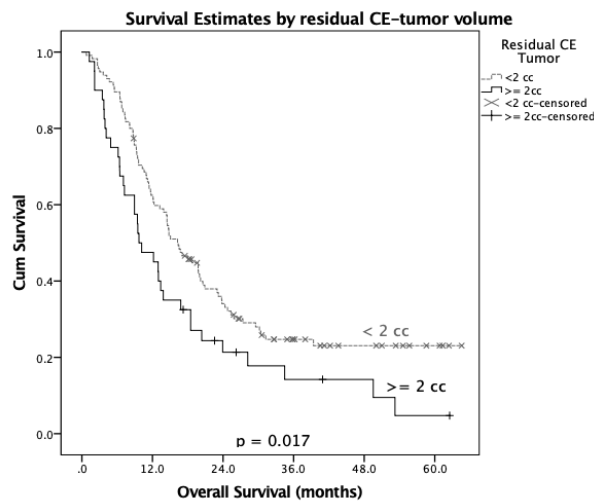


Figure A.7 - Survival estimates according to postoperative residual CE-tumor volume (2 cc cutoff in WHO grade III-IV tumors).

A.3 Impact of advanced 3D imaging preplanning on EOR and OS according to tumor location

| FLAIR-tumor EOR (%) WITH ADVANCED 3D IMAGING PREPLANNING IN LGG (WHO II GRADE) | | | | | | | | | | | | | | | | | |
|--|------|---------------------|------|-------|------|-------|---------------------------------|-------------|-------------|------|-------|---------------------|-------------|-------------|------|-------|----------|
| Lobe involved | Side | Total | | | | | Advanced 3D imaging preplanning | | | | | | | | | | Sig. (p) |
| | | | | | | | No | | | | | Yes | | | | | |
| | | FLAIR-tumor EOR (%) | | | | | FLAIR-tumor EOR (%) | | | | | FLAIR-tumor EOR (%) | | | | | |
| n | MN | MD | Min | Max | n | MN | MD | Min | Max | n | MN | MD | Min | Max | | | |
| Frontal | R | 17 | 77.9 | 86.3 | 26.7 | 100.0 | 14 | 73.7 | 76.9 | 26.7 | 100.0 | 3 | 97.7 | 97.2 | 96.4 | 99.4 | . |
| | L | 9 | 64.9 | 58.8 | 34.8 | 100.0 | 5 | 54.9 | 51.9 | 36.0 | 89.3 | 4 | 77.3 | 87.2 | 34.8 | 100.0 | . |
| | Tot | 26 | 73.4 | 79.8 | 26.7 | 100.0 | 19 | 68.7 | 63.0 | 26.7 | 100.0 | 7 | 86.0 | 96.4 | 34.8 | 100.0 | .176 |
| Temporal | R | 6 | 72.7 | 69.2 | 48.8 | 100.0 | 6 | 72.7 | 69.2 | 48.8 | 100.0 | 0 | . | . | . | . | . |
| | L | 8 | 61.7 | 56.0 | 34.8 | 100.0 | 5 | 65.6 | 53.1 | 36.0 | 100.0 | 3 | 55.3 | 58.8 | 34.8 | 72.1 | . |
| | Tot | 14 | 66.4 | 61.0 | 34.8 | 100.0 | 11 | 69.4 | 63.0 | 36.0 | 100.0 | 3 | 55.3 | 58.8 | 34.8 | 72.1 | . |
| Insular | R | 3 | 56.9 | 59.0 | 48.8 | 63.0 | 3 | 56.9 | 59.0 | 48.8 | 63.0 | 0 | . | . | . | . | . |
| | L | 3 | 49.3 | 53.1 | 36.0 | 58.8 | 2 | 44.6 | 44.6 | 36.0 | 53.1 | 1 | 58.8 | 58.8 | 58.8 | 58.8 | . |
| | Tot | 6 | 53.1 | 56.0 | 36.0 | 63.0 | 5 | 52.0 | 53.1 | 36.0 | 63.0 | 1 | 58.8 | 58.8 | 58.8 | 58.8 | . |
| Parietal | R | 4 | 83.6 | 89.2 | 56.0 | 100.0 | 2 | 69.0 | 69.0 | 56.0 | 82.0 | 2 | 98.2 | 98.2 | 96.4 | 100.0 | . |
| | L | 7 | 76.1 | 83.0 | 36.0 | 96.2 | 4 | 66.2 | 66.6 | 36.0 | 96.2 | 3 | 85.9 | 90.4 | 75.6 | 91.7 | . |
| | Tot | 11 | 79.1 | 86.2 | 36.0 | 100.0 | 6 | 67.3 | 66.6 | 36.0 | 96.2 | 5 | 90.8 | 91.7 | 75.6 | 100.0 | .082 |
| Occipital | R | 2 | 90.3 | 90.3 | 82.0 | 98.7 | 2 | 90.3 | 90.3 | 82.0 | 98.7 | 0 | . | . | . | . | . |
| | L | 1 | 36.0 | 36.0 | 36.0 | 36.0 | 1 | 36.0 | 36.0 | 36.0 | 36.0 | 0 | . | . | . | . | . |
| | Tot | 3 | 72.2 | 82.0 | 36.0 | 98.7 | 3 | 72.2 | 82.0 | 36.0 | 98.7 | 0 | . | . | . | . | . |
| Midline | | 3 | 97.1 | 100.0 | 91.4 | 100.0 | 2 | 95.7 | 95.7 | 91.4 | 100.0 | 1 | 100.0 | 100.0 | 100. | 100.0 | . |
| Total | | 48 | 77.6 | 86.3 | 26.7 | 100.0 | 34 | <u>74.5</u> | <u>79.5</u> | 26.7 | 100.0 | 14 | <u>85.1</u> | <u>93.1</u> | 34.8 | 100.0 | .112 |

Table A.4 - Impact of advanced 3D imaging preplanning in the resection of WHO grade II gliomas according to different tumor locations.

Only P values <0.150 are reported in the last column

| CE-TUMOR EOR (%) WITH ADVANCED 3D IMAGING PREPLANNING IN HGG (WHO III-IV GRADE) | | | | | | | | | | | | | | | | | |
|---|------|------------------|------|------|------|-------|---------------------------------|------|------|------|-------|------------------|-------|-------|-------|-------|----------|
| Lobe involved | Side | Total | | | | | Advanced 3D imaging preplanning | | | | | | | | | | Sig. (p) |
| | | | | | | | No | | | | | Yes | | | | | |
| | | CE-tumor EOR (%) | | | | | CE-tumor EOR (%) | | | | | CE-tumor EOR (%) | | | | | |
| n | MN | MD | Min | Max | n | MN | MD | Min | Max | n | MN | MD | Min | Max | | | |
| Frontal | R | 30 | 94.3 | 99.5 | 53.8 | 100.0 | 21 | 92.9 | 99.0 | 53.8 | 100.0 | 9 | 97.5 | 100.0 | 80.6 | 100.0 | . |
| | L | 26 | 93.4 | 98.0 | 63.6 | 100.0 | 21 | 92.9 | 97.8 | 63.6 | 100.0 | 5 | 95.2 | 100.0 | 84.5 | 100.0 | . |
| | Tot | 56 | 93.9 | 98.9 | 53.8 | 100.0 | 42 | 92.9 | 98.1 | 53.8 | 100.0 | 14 | 96.7 | 100.0 | 80.6 | 100.0 | . |
| Temporal | R | 46 | 92.4 | 99.9 | 28.6 | 100.0 | 41 | 92.0 | 99.9 | 28.6 | 100.0 | 5 | 96.3 | 97.7 | 89.7 | 100.0 | . |
| | L | 41 | 92.2 | 97.7 | 35.1 | 100.0 | 28 | 90.0 | 96.4 | 35.1 | 100.0 | 13 | 97.8 | 100.0 | 86.7 | 100.0 | .057 |
| | Tot | 87 | 92.3 | 98.1 | 28.6 | 100.0 | 69 | 91.2 | 97.9 | 28.6 | 100.0 | 18 | 97.4 | 100.0 | 86.7 | 100.0 | . |
| Insular | R | 14 | 87.5 | 95.3 | 28.6 | 100.0 | 12 | 85.3 | 94.7 | 28.6 | 100.0 | 2 | 100.0 | 100.0 | 100.0 | 100.0 | .051 |
| | L | 19 | 93.8 | 96.8 | 72.3 | 100.0 | 15 | 93.1 | 96.4 | 72.3 | 100.0 | 4 | 97.4 | 98.5 | 93.6 | 100.0 | . |
| | Tot | 33 | 91.2 | 96.1 | 28.6 | 100.0 | 27 | 89.8 | 95.9 | 28.6 | 100.0 | 6 | 98.4 | 100.0 | 93.6 | 100.0 | . |
| Parietal | R | 30 | 91.2 | 98.4 | 28.6 | 100.0 | 22 | 90.3 | 98.3 | 28.6 | 100.0 | 8 | 94.5 | 98.4 | 80.6 | 100.0 | . |
| | L | 18 | 94.7 | 99.1 | 72.3 | 100.0 | 11 | 92.0 | 96.2 | 72.3 | 100.0 | 7 | 99.1 | 99.3 | 96.9 | 100.0 | . |

| | | | | | | | | | | | | | | | | | |
|------------------|------------|-----|------|------|------|-------|-----|-------------|-------------|------|-------|----|-------------|-------------|------|-------|------|
| | Tot | 48 | 92.6 | 98.6 | 28.6 | 100.0 | 33 | 90.8 | 98.0 | 28.6 | 100.0 | 15 | 97.0 | 99.2 | 80.6 | 100.0 | . |
| Occipital | R | 15 | 95.5 | 97.4 | 80.2 | 100.0 | 11 | 94.8 | 96.9 | 80.2 | 100.0 | 4 | 97.9 | 98.3 | 95.4 | 100.0 | . |
| | L | 9 | 96.0 | 97.7 | 81.0 | 100.0 | 7 | 95.0 | 96.2 | 81.0 | 100.0 | 2 | 99.5 | 99.5 | 99.3 | 99.6 | . |
| | Tot | 24 | 95.7 | 97.7 | 80.2 | 100.0 | 18 | 94.9 | 96.5 | 80.2 | 100.0 | 6 | 98.5 | 99.3 | 95.4 | 100.0 | . |
| Midline | | 3 | 93.5 | 93.5 | 93.3 | 93.7 | 0 | . | . | . | . | 3 | 93.5 | 93.5 | 93.3 | 93.7 | . |
| Total | | 163 | 93.1 | 98.6 | 28.6 | 100.0 | 123 | <u>92.0</u> | <u>98.0</u> | 28.6 | 100.0 | 40 | <u>97.0</u> | <u>99.5</u> | 80.6 | 100.0 | .106 |

Table A.5 - Extent of resection according to advanced 3D imaging preplanning availability in WHO III-IV tumors. Only P values <0.150 are reported in the last column

| OVERALL SURVIVAL (MONTHS) USING ADVANCED 3D IMAGING PREPLANNING AMONG GBL (WHO IV GRADE) | | | | | | | | | | | | | | | | | | |
|--|------------|---------------------------|------|------|-----|------|---------------------------------|-------------|-------------|-----|------|---------------------------|-------------|-------------|------|------|------|----------|
| Lobe involved | Side | Total | | | | | Advanced 3D imaging preplanning | | | | | | | | | | | Sig. (p) |
| | | Overall Survival (months) | | | | | No | | | | | Yes | | | | | | |
| | | Overall Survival (months) | | | | | Overall Survival (months) | | | | | Overall Survival (months) | | | | | | |
| | | n | MN | MD | Min | Max | n | MN | MD | Min | Max | n | MN | MD | Min | Max | | |
| Frontal | R | 19 | 19.5 | 14.4 | 3.7 | 53.2 | 14 | 17.3 | 12.6 | 3.7 | 49.5 | 5 | 23.9 | 19.6 | 9.3 | 53.2 | .165 | |
| | L | 18 | 21.4 | 15.3 | 2.6 | 62.5 | 16 | 21.9 | 13.9 | 2.6 | 62.5 | 2 | 17.4 | 17.4 | 12.2 | 22.6 | . | |
| | Tot | 37 | 20.5 | 14.4 | 2.6 | 62.5 | 30 | 20.1 | 12.6 | 2.6 | 62.5 | 7 | 22.0 | 19.6 | 9.3 | 53.2 | . | |
| Temporal | R | 41 | 15.0 | 11.8 | 1.3 | 58.6 | 36 | 15.3 | 11.7 | 1.3 | 58.6 | 5 | 13.3 | 13.8 | 1.8 | 27.4 | . | |
| | L | 28 | 15.5 | 9.5 | 2.8 | 62.5 | 18 | 14.5 | 9.1 | 3.0 | 62.5 | 10 | 17.0 | 16.5 | 2.8 | 43.6 | . | |
| | Tot | 69 | 15.2 | 11.2 | 1.3 | 62.5 | 54 | 15.0 | 10.4 | 1.3 | 62.5 | 15 | 15.8 | 14.5 | 1.8 | 43.6 | . | |
| Insular | R | 12 | 9.0 | 7.9 | 2.1 | 19.6 | 10 | 7.0 | 5.4 | 2.1 | 16.8 | 2 | 17.2 | 17.2 | 14.8 | 19.6 | .089 | |
| | L | 13 | 16.2 | 11.0 | 2.6 | 62.5 | 10 | 17.7 | 10.2 | 2.6 | 62.5 | 3 | 11.1 | 12.2 | 2.8 | 18.5 | . | |
| | Tot | 25 | 13.1 | 9.6 | 2.1 | 62.5 | 20 | 12.9 | 9.1 | 2.1 | 62.5 | 5 | 13.6 | 14.8 | 2.8 | 19.6 | .199 | |
| Parietal | R | 25 | 17.1 | 12.3 | 1.8 | 58.6 | 20 | 16.3 | 11.6 | 2.1 | 58.6 | 5 | 20.5 | 13.8 | 1.8 | 53.2 | . | |
| | L | 12 | 15.1 | 12.4 | 6.8 | 43.6 | 6 | 10.7 | 9.1 | 6.8 | 18.5 | 6 | 19.5 | 16.6 | 8.9 | 43.6 | .065 | |
| | Tot | 37 | 16.5 | 12.3 | 1.8 | 58.6 | 26 | 15.0 | 10.6 | 2.1 | 58.6 | 11 | 20.0 | 14.5 | 1.8 | 53.2 | . | |
| Occipital | R | 14 | 10.6 | 8.0 | 1.3 | 28.2 | 10 | 10.4 | 8.0 | 1.3 | 28.2 | 4 | 11.2 | 7.7 | 1.8 | 27.4 | . | |
| | L | 5 | 12.7 | 12.1 | 3.6 | 24.8 | 4 | 9.7 | 10.9 | 3.6 | 13.4 | 1 | 24.8 | 24.8 | 24.8 | 24.8 | . | |
| | Tot | 19 | 11.1 | 8.9 | 1.3 | 28.2 | 14 | 10.2 | 9.3 | 1.3 | 28.2 | 5 | 13.9 | 8.9 | 1.8 | 27.4 | . | |
| Midline | | 2 | 10.9 | 10.9 | 5.5 | 16.3 | 0 | . | . | . | . | 2 | 10.9 | 10.9 | 5.5 | 16.3 | . | |
| Total | | 121 | 15.8 | 11.7 | 1.3 | 62.5 | 93 | <u>15.7</u> | <u>11.1</u> | 1.3 | 62.5 | 27 | <u>16.3</u> | <u>14.5</u> | 1.8 | 53.2 | . | |

Table A.6 - Overall survival (months) according to advanced 3D imaging preplanning among WHO IV grade tumors.

Independent-Samples Mann-Whitney U test significance is displayed when <0.20.

A.4 Multivariate analysis models.

A.4.1 FLAIR-tumor EOR

A multiple regression analysis was run to predict FLAIR-tumor EOR (see **Table A.7**); After removing the influential values, according to Cook's distance, the dependent variable (FLAIR-tumor EOR) and the continuous independent variables (*age*, *preoperative FLAIR-tumor volume* and *preoperative CE-tumor volume*) were transformed as appropriate to meet the assumptions of linearity and normality of the

residuals. The model proved statistically significantly [$F(20, 199) = 2.237, p = 0.003, \text{adj. } R^2 = 0.0994$].

| Model | Unstandardized Coefficients | | Standardized Coefficients | Sig. | 95.0% Confidence Interval for B | |
|--|-----------------------------|------------|---------------------------|--------------|---------------------------------|-------------|
| | B | Std. Error | Beta | | Lower Bound | Upper Bound |
| (Constant) | 105.73880 | 17.2633 | | .000 | 71.696 | 139.781 |
| Age (yrs) | -0.0544 | 0.1206 | -0.037 | .652 | -0.292 | 0.183 |
| Sex | 3.235 | 3.072 | 0.070 | 0.293 | -2.822 | 9.293 |
| WHO 2016 Grade | -2.808 | 2.379 | -0.118 | 0.239 | -7.5 | 1.883 |
| Primary or recurrent tumor | -11.686 | 3.758 | -0.213 | 0.002 | -19.098 | -4.274 |
| IDH-1 status | -0.279 | 3.943 | -0.005 | 0.943 | -8.055 | 7.497 |
| Number of brain lobes/regions involved | -3.011 | 11.637 | -0.065 | 0.372 | -9.648 | 3.626 |
| Midline / Deep location | -6.262 | 3.366 | -0.041 | 0.591 | -29.209 | 16.685 |
| Tumor close to language area | -3.560 | 3.847 | -0.074 | 0.356 | -11.147 | 4.026 |
| Tumor close to motor area | -5.831 | 3.807 | -0.127 | 0.127 | -13.339 | 1.676 |
| Preop. FLAIR-volume (cc) | -4.817 | 2.182 | -0.222 | 0.028 | -9.121 | -0.513 |
| Preop. CE-volume (cc) | 2.519 | 1.564 | 0.182 | 0.108 | -0.564 | 5.604 |
| Intraop. Neuronavigation | 2.607 | 3.563 | 0.055 | 0.465 | -4.42 | 9.633 |
| Intraop. Ultrasound | 2.831 | 3.3 | 0.058 | 0.391 | -3.675 | 9.339 |
| Intraop. IONM | 5.799 | 4.32 | 0.106 | 0.180 | -2.719 | 14.317 |
| Preop. DTI acquisition | 7.597 | 4.837 | 0.156 | 0.117 | -1.942 | 17.136 |
| Preop. fMRI acquisition | -10.507 | 5.918 | -0.181 | 0.077 | -22.178 | 1.164 |
| Preop. 3D Slicer preplanning | -0.7 | 4.19 | -0.013 | 0.867 | -8.96 | 7.565 |
| Preop. KPS | -0.049 | 0.145 | -0.024 | 0.732 | -0.335 | 0.236 |
| Preop. language deficit | -6.797 | 4.48 | -0.121 | 0.13 | -15.633 | 2.038 |
| Preop. motor deficit | 1.173 | 3.738 | 0.024 | 0.754 | -6.199 | 8.545 |

Table A.7 - Multiple regression analysis of relevant preoperative covariates on “FLAIR-tumor extent of resection” as dependent variable

A.4.2 FLAIR-tumor 75% EOR achievement

A binomial logistic regression was performed to ascertain the effects of preoperative independent variables on the likelihood of achieving *FLAIR-tumor 75% EOR* cutoff (as shown in **Table A.8**). The logistic regression model was statistically significant, $\chi^2(20) = 41.429, p = 0.003$. The model explained 22.8% (Nagelkerke R^2) of the variance in *CE-tumor GTR* and correctly classified 65.6% of cases. Sensitivity was 73.9%, specificity was 55.9%.

| Variables in the Equation | B | S.E. | Wald | df | Sig. | Exp(B) | 95% C.I. for EXP(B) | |
|-----------------------------------|-------|------|-------|----|-------------|--------|---------------------|-------|
| | | | | | | | Lower | Upper |
| Age (yrs) | .001 | .012 | .008 | 1 | .927 | 1.001 | .977 | 1.026 |
| Sex | .253 | .316 | .643 | 1 | .423 | 1.288 | .693 | 2.394 |
| WHO 2016 Grade | -.484 | .227 | 4.531 | 1 | .033 | .617 | .395 | .962 |
| Primary or recurrent tumor | -.993 | .396 | 6.276 | 1 | .012 | .370 | .170 | .806 |
| IDH-1 status | -.248 | .404 | .376 | 1 | .540 | .781 | .354 | 1.723 |

| | | | | | | | | |
|--|--------|-------|-------|---|-------------|--------|-------|-------|
| Number of brain lobes/regions involved | -.166 | .334 | .245 | 1 | .620 | .847 | .440 | 1.632 |
| Midline / Deep location | -.574 | 1.174 | .239 | 1 | .625 | .563 | .056 | 5.628 |
| Tumor close to language area | -.181 | .392 | .212 | 1 | .645 | .835 | .387 | 1.801 |
| Tumor close to motor area | -1.044 | .400 | 6.825 | 1 | .009 | .352 | .161 | .771 |
| Preop. FLAIR-volume (cc) | -.008 | .004 | 5.577 | 1 | .018 | .992 | .985 | .999 |
| Preop. CE-volume (cc) | .022 | .008 | 7.100 | 1 | .008 | 1.022 | 1.006 | 1.038 |
| Intraop. Neuronavigation | .256 | .362 | .500 | 1 | .480 | 1.291 | .636 | 2.623 |
| Intraop. Ultrasound | .188 | .349 | .290 | 1 | .590 | 1.206 | .609 | 2.390 |
| Intraop. IONM | 1.088 | .458 | 5.636 | 1 | .018 | 2.967 | 1.209 | 7.282 |
| Preop. DTI acquisition | .779 | .520 | 2.245 | 1 | .134 | 2.180 | .787 | 6.041 |
| Preop. fMRI acquisition | -1.075 | .619 | 3.013 | 1 | .083 | .341 | .101 | 1.149 |
| Preop. 3D Slicer preplanning | -.340 | .419 | .657 | 1 | .418 | .712 | .313 | 1.619 |
| Preop. KPS | -.005 | .014 | .107 | 1 | .744 | .995 | .967 | 1.024 |
| Preop. language deficit | -.647 | .465 | 1.936 | 1 | .164 | .524 | .211 | 1.303 |
| Preop. motor deficit | .170 | .383 | .197 | 1 | .657 | 1.185 | .559 | 2.514 |
| Constant | 2.566 | 1.724 | 2.216 | 1 | .137 | 13.020 | | |

Table A.8 - Binomial logistic regression analysis of relevant preoperative covariates on “FLAIR-tumor 75% extent of resection achievement” as dependent variable

A.4.3 FLAIR-tumor residual ≤ 5 cc achievement

A binomial logistic regression was performed to ascertain the effects of preoperative independent variables on the likelihood of achieving a *FLAIR-tumor* residual ≤ 5 cc (as shown in **Table A.9**). The logistic regression model was statistically significant, $\chi^2(20) = 83.152$, $p < 0.0001$. The model explained 43% (Nagelkerke R²) of the variance in *CE-tumor* GTR and correctly classified 79.2% of cases. Sensitivity was 59.5%, specificity was 90.1%.

| Variables in the Equation | B | S.E. | Wald | df | Sig. | Exp(B) | 95% C.I. for EXP(B) | |
|---|--------|-------|--------|----|-------------|--------|---------------------|--------|
| | | | | | | | Lower | Upper |
| Age (yrs) | -.011 | .014 | .591 | 1 | .442 | .989 | .961 | 1.017 |
| Sex | .044 | .365 | .015 | 1 | .903 | 1.045 | .511 | 2.137 |
| WHO 2016 Grade | -.722 | .263 | 7.524 | 1 | .006 | .486 | .290 | .814 |
| Primary or recurrent tumor | -1.275 | .505 | 6.376 | 1 | .012 | .280 | .104 | .752 |
| IDH-1 status | -.460 | .467 | .971 | 1 | .325 | .631 | .253 | 1.577 |
| Number of brain lobes/regions involved | -1.100 | .407 | 7.304 | 1 | .007 | .333 | .150 | .739 |
| Midline / Deep location | -.314 | 1.506 | .044 | 1 | .835 | .730 | .038 | 13.973 |
| Tumor close to language area | -.695 | .451 | 2.376 | 1 | .123 | .499 | .206 | 1.207 |
| Tumor close to motor area | -.386 | .463 | .695 | 1 | .405 | .680 | .274 | 1.685 |
| Preop. FLAIR-volume (cc) | -.016 | .005 | 11.040 | 1 | .001 | .984 | .974 | .993 |
| Preop. CE-volume (cc) | .010 | .010 | .962 | 1 | .327 | 1.010 | .990 | 1.030 |
| Intraop. Neuronavigation | 1.134 | .462 | 6.018 | 1 | .014 | 3.107 | 1.256 | 7.687 |
| Intraop. Ultrasound | -.467 | .408 | 1.307 | 1 | .253 | .627 | .282 | 1.396 |
| Intraop. IONM | .232 | .511 | .206 | 1 | .650 | 1.261 | .463 | 3.433 |
| Preop. DTI acquisition | .982 | .600 | 2.683 | 1 | .100 | 2.671 | .824 | 8.651 |
| Preop. fMRI acquisition | -1.201 | .728 | 2.720 | 1 | .099 | .301 | .072 | 1.254 |
| Preop. 3D Slicer preplanning | -.198 | .493 | .161 | 1 | .689 | .821 | .312 | 2.157 |
| Preop. KPS | -.040 | .018 | 4.910 | 1 | .027 | .961 | .928 | .995 |
| Preop. language deficit | -.054 | .558 | .009 | 1 | .923 | .948 | .317 | 2.830 |

| | | | | | | | | |
|----------------------|-------|-------|--------|---|------|----------|------|-------|
| Preop. motor deficit | .162 | .463 | .123 | 1 | .726 | 1.176 | .475 | 2.911 |
| Constant | 7.479 | 2.194 | 11.617 | 1 | .001 | 1770.545 | | |

Table A.9 - Binomial logistic regression analysis of preoperative covariates on “FLAIR-tumor residual \leq cc achievement” as dependent variable

A.4.4 CE-tumor EOR

A multiple regression analysis was run to predict CE-tumor EOR, but the model didn’t meet the assumptions of homoscedasticity and linearity of the relationship between dependent and each continuous independent variable, probably due to the extremely high number of 100% EOR rate achieved for CE-tumor (median 98.6% among HGGs).

A.4.5 CE-tumor GTR

A binomial logistic regression was performed to ascertain the effects of preoperative independent variables on the likelihood of achieving a CE-volume gross total resection (GTR) (as shown in **Table A.10**). Leverage and influential value were detected according to Cook’s distance. The assumption of linearity of the logit was tested with the Box-Tidwell procedure and a power transformation was done on the independent variable preoperative CE-tumor volume.

The logistic regression model was statistically significant, $\chi^2(20) = 45,068$, $p < 0.006$. The model explained 34.2% (Nagelkerke R²) of the variance in CE-tumor GTR and correctly classified 72.1% of cases. Sensitivity was 55%, specificity was 83.5%.

| Variables in the Equation | B | S.E. | Wald | df | Sig. | Exp(B) | 95% C.I. for EXP(B) | |
|---|---------|-----------|-------|----|-------------|--------|---------------------|-------|
| | | | | | | | Lower | Upper |
| Age (yrs) | .016 | .015 | 1.056 | 1 | .304 | 1.016 | .986 | 1.047 |
| Sex | -.119 | .377 | .100 | 1 | .751 | .887 | .424 | 1.857 |
| WHO 2016 Grade | -.642 | .306 | 4.392 | 1 | .036 | .526 | .289 | .959 |
| Primary or recurrent tumor | -.516 | .476 | 1.178 | 1 | .278 | .597 | .235 | 1.516 |
| IDH-1 status | -.417 | .539 | .599 | 1 | .439 | .659 | .229 | 1.895 |
| Number of brain lobes/regions involved | -.741 | .406 | 3.331 | 1 | .068 | .477 | .215 | 1.056 |
| Midline / Deep location | -23.767 | 22067.535 | .000 | 1 | .999 | .000 | .000 | . |
| Tumor close to language area | -.982 | .499 | 3.865 | 1 | .049 | .375 | .141 | .997 |
| Tumor close to motor area | -.028 | .490 | .003 | 1 | .955 | .973 | .372 | 2.542 |
| Preop. FLAIR-volume (cc) | -.003 | .003 | 1.128 | 1 | .288 | .997 | .990 | 1.003 |
| Preop. CE-volume (cc) | .000 | .000 | .967 | 1 | .326 | 1.000 | 1.000 | 1.000 |
| Intraop. Neuronavigation | .293 | .424 | .478 | 1 | .489 | 1.340 | .584 | 3.076 |
| Intraop. Ultrasound | .876 | .419 | 4.377 | 1 | .036 | 2.402 | 1.057 | 5.457 |
| Intraop. IONM | .998 | .581 | 2.948 | 1 | .086 | 2.712 | .868 | 8.467 |
| Preop. DTI acquisition | .923 | .592 | 2.430 | 1 | .119 | 2.518 | .789 | 8.040 |
| Preop. fMRI acquisition | -.953 | .737 | 1.670 | 1 | .196 | .386 | .091 | 1.636 |
| Preop. 3D Slicer preplanning | .191 | .490 | .152 | 1 | .697 | 1.211 | .463 | 3.165 |
| Preop. KPS | .005 | .016 | .110 | 1 | .740 | 1.005 | .974 | 1.037 |

| | | | | | | | | |
|-------------------------|-------|-------|------|---|------|-------|------|-------|
| Preop. language deficit | .112 | .516 | .047 | 1 | .828 | 1.119 | .407 | 3.074 |
| Preop. motor deficit | -.002 | .450 | .000 | 1 | .996 | .998 | .413 | 2.413 |
| Constant | .749 | 1.927 | .151 | 1 | .698 | 2.114 | | |

Table A.10 - Binomial logistic regression analysis of preoperative covariates on “CE-tumor postoperative residual volume ≤ 2 cc” as dependent variable.

A.4.6 CE-tumor postoperative residual volume ≤ 2 cc

A binomial logistic regression was performed to ascertain the effects of pre-operative independent variables on the likelihood of achieving CE-tumor residual volume ≤ 2 cc (as shown in **Table A.11**). The logistic regression model was statistically significant, $\chi^2(20) = 40.774$, $p < 0.018$. The model explained 32.3% (Nagelkerke R²) of the variance in CE-tumor residual volume ≤ 2 cc and correctly classified 76.1% of cases. Sensitivity was 93.3%, specificity was 27.9%.

| Variables in the Equation | B | S.E. | Wald | df | Sig. | Exp(B) | 95% C.I. for EXP(B) | |
|--|---------------|-------------|--------------|----------|-------------|--------------|---------------------|-------------|
| | | | | | | | Lower | Upper |
| Age (yrs) | -.008 | .020 | .150 | 1 | .699 | .992 | .954 | 1.032 |
| Sex | .452 | .461 | .961 | 1 | .327 | 1.571 | .637 | 3.879 |
| WHO 2016 Grade | -2.217 | .782 | 8.039 | 1 | .005 | .109 | .024 | .504 |
| Primary or recurrent tumor | -.582 | .558 | 1.087 | 1 | .297 | .559 | .187 | 1.668 |
| IDH-1 status | -1.473 | .734 | 4.025 | 1 | .063 | .229 | .054 | .967 |
| Number of brain lobes/regions involved | -.682 | .455 | 2.253 | 1 | .133 | .505 | .207 | 1.232 |
| Midline / Deep location | 17.671 | 22606.022 | .000 | 1 | .999 | 47251887.272 | .000 | . |
| Tumor close to language area | .046 | .593 | .006 | 1 | .938 | 1.047 | .327 | 3.348 |
| Tumor close to motor area | -.012 | .547 | .000 | 1 | .983 | .988 | .338 | 2.887 |
| Preop. FLAIR-volume (cc) | .001 | .005 | .016 | 1 | .899 | 1.001 | .991 | 1.010 |
| Preop. CE-volume (cc) | -.016 | .009 | 3.165 | 1 | .075 | .984 | .966 | 1.002 |
| Intraop. Neuronavigation | .066 | .480 | .019 | 1 | .890 | 1.069 | .417 | 2.741 |
| Intraop. Ultrasound | .439 | .445 | .972 | 1 | .324 | 1.551 | .648 | 3.712 |
| Intraop. IONM | .677 | .673 | 1.012 | 1 | .314 | 1.969 | .526 | 7.366 |
| Preop. DTI acquisition | 1.144 | .709 | 2.605 | 1 | .107 | 3.140 | .783 | 12.597 |
| Preop. fMRI acquisition | -1.480 | .944 | 2.458 | 1 | .117 | .228 | .036 | 1.448 |
| Preop. 3D Slicer preplanning | -.175 | .575 | .092 | 1 | .762 | .840 | .272 | 2.593 |
| Preop. KPS | -.029 | .020 | 2.000 | 1 | .157 | .972 | .934 | 1.011 |
| Preop. language deficit | -.038 | .624 | .004 | 1 | .951 | .963 | .284 | 3.269 |
| Preop. motor deficit | -.384 | .522 | .541 | 1 | .462 | .681 | .245 | 1.894 |
| Constant | 13.386 | 3.952 | 11.474 | 1 | .001 | 650628.968 | | |

Table A.11 - Binomial logistic regression analysis of preoperative covariates on “CE-tumor postoperative residual volume ≤ 2 cc” as dependent variable

A.4.7 Motor function deterioration

A binomial logistic regression was performed to ascertain the effects preoperative independent variables on the likelihood of achieving postoperative deterioration in motor function (**Table A.12**). Multicollinearity was detected between the variable *preoperative*

fMRI and *DTI acquisition* through the inspection of the variance inflation factors; due to this reason we decided, in this case, to remove *fMRI* as a predictive variable from our model since a higher trend toward statistical significance was found for *DTI* at univariate analysis ($p = 0.054$).

| Variables in the equation | B | S.E. | Wald | df | Sig. | Exp(B) | 95% C.I.for EXP(B) | |
|--|---------------|--------------|---------------|----------|-------------|---------------|--------------------|----------------|
| | | | | | | | Lower | Upper |
| Age (yrs) | -.027 | .027 | 1.002 | 1 | .317 | .973 | .922 | 1.027 |
| Sex | -.355 | .727 | .239 | 1 | .625 | .701 | .168 | 2.916 |
| WHO 2016 Grade | -.199 | .466 | .183 | 1 | .669 | .819 | .329 | 2.043 |
| Primary or recurrent tumor | -.308 | .791 | .152 | 1 | .697 | .735 | .156 | 3.466 |
| IDH-1 status | .961 | .750 | 1.641 | 1 | .200 | 2.615 | .601 | 11.383 |
| Number of brain lobes/regions involved | .335 | .764 | .192 | 1 | .661 | 1.397 | .313 | 6.243 |
| Midline / Deep location | -17.924 | 17191.438 | .000 | 1 | .999 | .000 | .000 | . |
| Tumor close to language area | -2.154 | 1.203 | 3.207 | 1 | .073 | .116 | .011 | 1.226 |
| Tumor close to motor area | 3.227 | .938 | 11.829 | 1 | .001 | 25.204 | 4.007 | 158.534 |
| Preop. FLAIR-volume (cc) | -.001 | .009 | .008 | 1 | .928 | .999 | .981 | 1.018 |
| Preop. CE-volume (cc) | -.021 | .025 | .700 | 1 | .403 | .979 | .933 | 1.028 |
| Intraop. Neuronavigation | .390 | .865 | .204 | 1 | .652 | 1.478 | .271 | 8.048 |
| Intraop. Ultrasound | .151 | .784 | .037 | 1 | .847 | 1.164 | .250 | 5.411 |
| Intraop. IONM | .624 | .885 | .497 | 1 | .481 | 1.867 | .329 | 10.590 |
| Preop. DTI acquisition | -3.540 | 1.435 | 6.089 | 1 | .014 | .029 | .002 | .483 |
| Preop. 3D Slicer preplanning | 1.056 | 1.107 | .911 | 1 | .340 | 2.875 | .329 | 25.159 |
| Preop. KPS | -.051 | .034 | 2.288 | 1 | .130 | .950 | .889 | 1.015 |
| Preop. language deficit | 1.722 | 1.323 | 1.695 | 1 | .193 | 5.595 | .419 | 74.751 |
| Preop. motor deficit | -2.222 | .994 | 4.998 | 1 | .025 | .108 | .015 | .760 |
| Constant | 3.153 | 3.890 | .657 | 1 | .418 | 23.408 | | |

Table A.12 - Binomial logistic regression analysis of preoperative covariates on “motor function deterioration” as dependent variable.

A.4.8 Language function deterioration

A binomial logistic regression was performed to ascertain the effects of preoperative independent variables on the likelihood of achieving postoperative deterioration in language function (as shown in **Table A.13**). The logistic regression model was statistically significant, $\chi^2(20) = 32.468$, $p = 0.039$. The model explained 61.9% (Nagelkerke R²) of the variance in deterioration in language function and correctly classified 98.2% of cases. Sensitivity was 33.3%, specificity was 100%.

| Variables in the equation | B | S.E. | Wald | df | Sig. | Exp(B) | 95% C.I.for EXP(B) | |
|----------------------------|--------|-------|-------|----|------|--------|--------------------|----------|
| | | | | | | | Lower | Upper |
| Age (yrs) | .016 | .060 | .071 | 1 | .790 | 1.016 | .903 | 1.144 |
| Sex | -7.080 | 4.818 | 2.160 | 1 | .142 | .001 | .000 | 10.618 |
| WHO 2016 Grade | -.582 | 1.028 | .320 | 1 | .572 | .559 | .074 | 4.194 |
| Primary or recurrent tumor | 2.562 | 2.613 | .962 | 1 | .327 | 12.965 | .077 | 2171.221 |

| | | | | | | | | |
|--|-------------|-----------|-------|---|------|----------|------|----------|
| IDH-1 status | 1.253 | 2.186 | .329 | 1 | .566 | 3.502 | .048 | 254.127 |
| Number of brain lobes/regions involved | 2.582 | 2.150 | 1.443 | 1 | .230 | 13.223 | .196 | 893.585 |
| Midline / Deep location | - 18.444 | 14392.601 | .000 | 1 | .999 | .000 | .000 | . |
| Tumor close to language area | 23.254 | 1480.999 | .000 | 1 | .987 | 1.26E+10 | .000 | . |
| Tumor close to motor area | 1.344 | 2.288 | .345 | 1 | .557 | 3.836 | .043 | 340.128 |
| Preop. FLAIR-volume (cc) | -.027 | .033 | .677 | 1 | .411 | .974 | .913 | 1.038 |
| Preop. CE-volume (cc) | -.020 | .067 | .091 | 1 | .763 | .980 | .860 | 1.117 |
| Intraop. Neuronavigation | 29.794 | 2522.216 | .000 | 1 | .991 | 8.70E+12 | .000 | . |
| Intraop. Ultrasound | 1.529 | 2.070 | .546 | 1 | .460 | 4.613 | .080 | 266.534 |
| Intraop. IONM | -.419 | 1.848 | .051 | 1 | .820 | .657 | .018 | 24.600 |
| Preop. DTI acquisition | -3.594 | 3.273 | 1.206 | 1 | .272 | .027 | .000 | 16.788 |
| Preop. fMRI acquisition | -.477 | 2.789 | .029 | 1 | .864 | .621 | .003 | 146.868 |
| Preop. 3D Slicer preplanning | .805 | 1.819 | .196 | 1 | .658 | 2.237 | .063 | 79.076 |
| Preop. KPS | -.291 | .241 | 1.464 | 1 | .226 | .747 | .466 | 1.198 |
| Preop. language deficit | .367 | 2.413 | .023 | 1 | .879 | 1.443 | .013 | 163.396 |
| Preop. motor deficit | 2.255 | 3.521 | .410 | 1 | .522 | 9.535 | .010 | 9463.216 |
| Constant | - 26.067 | 2924.856 | .000 | 1 | .993 | .000 | | |

Table A.13 - Binomial logistic regression analysis of preoperative covariates on “postoperative language function deterioration” as dependent variable

A.4.9 Karnofsky Performance Status deterioration

A binomial logistic regression was performed to ascertain the effects of preoperative independent variables on the likelihood of incurring in postoperative deterioration in KPS (as shown in **Table A.14**). The logistic regression model was statistically significant, $\chi^2(20) = 35.751$, $p = 0.016$. The model explained 28.6% (Nagelkerke R²) of the variance in deterioration in at least one clinical function and correctly classified 88.1% of cases. Sensitivity was 14.8%, specificity was 98.4%.

| Variables in the equation | B | S.E. | Wald | df | Sig. | Exp(B) | 95% C.I. for EXP(B) | |
|--|-------|-------|-------|----|-------------|--------|---------------------|---------|
| | | | | | | | Lower | Upper |
| <u>Age (yrs)</u> | .059 | .021 | 7.852 | 1 | <u>.005</u> | 1.061 | 1.018 | 1.105 |
| <u>Sex</u> | 1.429 | .527 | 7.356 | 1 | <u>.007</u> | 4.174 | 1.486 | 11.724 |
| WHO 2016 Grade | -.269 | .378 | .506 | 1 | .477 | .764 | .364 | 1.603 |
| Primary or recurrent tumor | .348 | .617 | .317 | 1 | .573 | 1.416 | .422 | 4.746 |
| IDH-1 status | -.203 | .725 | .078 | 1 | .780 | .816 | .197 | 3.382 |
| Number of brain lobes/regions involved | -.223 | .546 | .166 | 1 | .684 | .800 | .275 | 2.333 |
| Midline / Deep location | 2.203 | 1.591 | 1.916 | 1 | .166 | 9.052 | .400 | 204.835 |
| Tumor close to language area | -.073 | .677 | .012 | 1 | .914 | .930 | .247 | 3.502 |
| Tumor close to motor area | .235 | .604 | .151 | 1 | .697 | 1.265 | .387 | 4.135 |
| Preop. FLAIR-volume (cc) | .002 | .005 | .095 | 1 | .757 | 1.002 | .991 | 1.012 |
| Preop. CE-volume (cc) | .009 | .012 | .590 | 1 | .442 | 1.009 | .986 | 1.032 |
| Intraop. Neuronavigation | .590 | .597 | .976 | 1 | .323 | 1.804 | .560 | 5.817 |
| Intraop. Ultrasound | .185 | .546 | .114 | 1 | .735 | 1.203 | .412 | 3.509 |
| Intraop. IONM | -.744 | .766 | .942 | 1 | .332 | .475 | .106 | 2.134 |
| Preop. DTI acquisition | -.050 | .762 | .004 | 1 | .948 | .951 | .214 | 4.237 |
| Preop. fMRI acquisition | .251 | .998 | .063 | 1 | .802 | 1.285 | .182 | 9.086 |
| Preop. 3D Slicer preplanning | .058 | .652 | .008 | 1 | .929 | 1.060 | .295 | 3.806 |

| | | | | | | | | |
|-------------------------|--------|-------|-------|---|-------------|------|------|-------|
| Preop. KPS | -.047 | .019 | 6.044 | 1 | .014 | .954 | .918 | .990 |
| Preop. language deficit | -.607 | .744 | .664 | 1 | .415 | .545 | .127 | 2.345 |
| Preop. motor deficit | -.260 | .627 | .172 | 1 | .678 | .771 | .226 | 2.635 |
| Constant | -1.499 | 2.590 | .335 | 1 | .563 | .223 | | |

Table A.14 - Binomial logistic regression analysis of preoperative covariates on “postoperative Karnofsky Performance Status deterioration” as dependent variable

A.4.10 Deterioration in one or more functions

A binomial logistic regression was performed to ascertain the effects of preoperative independent variables on the likelihood of incurring in postoperative deterioration in at least one clinical function (as shown in **Table A.15**). The logistic regression model was statistically significant, $\chi^2(20) = 44.254$, $p = 0.001$. The model explained 29.4% (Nagelkerke R²) of the variance in deterioration in at least one clinical function and correctly classified 85.5% of cases. Sensitivity was 29.3%, specificity was 98.3%.

| Variables in the equation | B | S.E. | Wald | df | Sig. | Exp(B) | 95% C.I. for EXP(B) | |
|--|--------|-------|--------|----|-------------|--------|---------------------|---------|
| | | | | | | | Lower | Upper |
| Age (yrs) | -.016 | .016 | .920 | 1 | .337 | .985 | .954 | 1.016 |
| Sex | -.205 | .430 | .227 | 1 | .633 | .815 | .351 | 1.891 |
| WHO 2016 Grade | .041 | .273 | .023 | 1 | .879 | 1.042 | .611 | 1.779 |
| Primary or recurrent tumor | -.136 | .519 | .069 | 1 | .793 | .873 | .316 | 2.412 |
| IDH-1 status | .060 | .484 | .015 | 1 | .902 | 1.061 | .411 | 2.741 |
| Number of brain lobes/regions involved | -.033 | .457 | .005 | 1 | .943 | .968 | .395 | 2.370 |
| Midline / Deep location | 2.826 | 1.594 | 3.141 | 1 | .076 | 16.871 | .741 | 383.900 |
| Tumor close to language area | -.004 | .539 | .000 | 1 | .994 | .996 | .346 | 2.866 |
| Tumor close to motor area | 1.509 | .507 | 8.870 | 1 | .003 | 4.524 | 1.675 | 12.216 |
| Preop. FLAIR-volume (cc) | .006 | .005 | 1.519 | 1 | .218 | 1.006 | .997 | 1.015 |
| Preop. CE-volume (cc) | -.030 | .014 | 4.333 | 1 | .037 | .970 | .943 | .998 |
| Intraop. Neuronavigation | -.238 | .521 | .209 | 1 | .648 | .788 | .284 | 2.190 |
| Intraop. Ultrasound | .431 | .469 | .846 | 1 | .358 | 1.539 | .614 | 3.855 |
| Intraop. IONM | .443 | .557 | .633 | 1 | .426 | 1.557 | .523 | 4.640 |
| Preop. DTI acquisition | -2.217 | 1.008 | 4.833 | 1 | .028 | .109 | .015 | .786 |
| Preop. fMRI acquisition | .421 | 1.081 | .152 | 1 | .697 | 1.523 | .183 | 12.663 |
| Preop. 3D Slicer preplanning | .736 | .576 | 1.635 | 1 | .201 | 2.088 | .675 | 6.456 |
| Preop. KPS | -.029 | .021 | 1.907 | 1 | .167 | .972 | .932 | 1.012 |
| Preop. language deficit | -.267 | .682 | .153 | 1 | .696 | .766 | .201 | 2.914 |
| Preop. motor deficit | -2.061 | .613 | 11.316 | 1 | .001 | .127 | .038 | .423 |
| Constant | 2.089 | 2.417 | .747 | 1 | .387 | 8.080 | | |

Table A.15 - Binomial logistic regression analysis of preoperative covariates on “postoperative deterioration in one or more functions” as dependent variable

A.4.11 Improvement in one or more functions

A binomial logistic regression was performed to ascertain the effects of preoperative independent variables on the likelihood of achieving postoperative improvement in at least one clinical function (as shown in **Table A.16**). The logistic regression model was

statistically significant, $\chi^2(20) = 95.361$, $p < 0.0001$. The model explained 49.9% (Nagelkerke R²) of the variance in postoperative improvement in at least one clinical function and correctly classified 83.7% of cases. Sensitivity was 64.6%, specificity was 91.7%.

| Variables in the equation | B | S.E. | Wald | df | Sig. | Exp(B) | 95% C.I. for EXP(B) | |
|--|--------|-------|--------|----|-------------|--------|---------------------|--------|
| | | | | | | | Lower | Upper |
| Age (yrs) | .004 | .017 | .047 | 1 | .828 | 1.004 | .971 | 1.037 |
| Sex | -.608 | .428 | 2.021 | 1 | .155 | .544 | .235 | 1.259 |
| WHO 2016 Grade | .032 | .296 | .012 | 1 | .914 | 1.033 | .578 | 1.846 |
| Primary or recurrent tumor | -1.274 | .612 | 4.336 | 1 | .037 | .280 | .084 | .928 |
| IDH-1 status | -1.108 | .600 | 3.409 | 1 | .065 | .330 | .102 | 1.071 |
| Number of brain lobes/regions involved | -.161 | .433 | .139 | 1 | .710 | .851 | .364 | 1.988 |
| Midline / Deep location | -2.867 | 1.573 | 3.322 | 1 | .068 | .057 | .003 | 1.241 |
| Tumor close to language area | .012 | .509 | .001 | 1 | .982 | 1.012 | .373 | 2.741 |
| Tumor close to motor area | -.477 | .536 | .791 | 1 | .374 | .621 | .217 | 1.776 |
| Preop. FLAIR-volume (cc) | .004 | .004 | .701 | 1 | .402 | 1.004 | .995 | 1.012 |
| Preop. CE-volume (cc) | -.001 | .009 | .011 | 1 | .916 | .999 | .981 | 1.017 |
| Intraop. Neuronavigation | -.404 | .467 | .749 | 1 | .387 | .668 | .267 | 1.667 |
| Intraop. Ultrasound | .383 | .433 | .782 | 1 | .376 | 1.466 | .628 | 3.422 |
| Intraop. IONM | -.129 | .552 | .054 | 1 | .816 | .879 | .298 | 2.596 |
| Preop. DTI acquisition | 1.795 | .618 | 8.432 | 1 | .004 | 6.018 | 1.792 | 20.207 |
| Preop. fMRI acquisition | -.914 | .751 | 1.480 | 1 | .224 | .401 | .092 | 1.748 |
| Preop. 3D Slicer preplanning | .526 | .570 | .853 | 1 | .356 | 1.692 | .554 | 5.168 |
| Preop. KPS | .066 | .020 | 10.595 | 1 | .001 | 1.069 | 1.027 | 1.112 |
| Preop. language deficit | 1.480 | .569 | 6.763 | 1 | .009 | 4.393 | 1.440 | 13.400 |
| Preop. motor deficit | 3.006 | .545 | 30.421 | 1 | .000 | 20.201 | 6.942 | 58.780 |
| Constant | -8.950 | 2.381 | 14.128 | 1 | .000 | .000 | | |

Table A.16 - Binomial logistic regression analysis of preoperative covariates on “postoperative improvement in one or more functions” as dependent variable

A.4.12 Impact of preoperative variables on Overall survival

A Cox regression was performed to ascertain the effects of preoperative variables on OS (as shown in **Table A.17**). The Cox regression model was statistically significant, $\chi^2(20) = 148.9$, $p < 0.0001$.

| Variables in the Equation | B | SE | Wald | df | Sig. | Exp(B) | 95.0% CI for Exp(B) | |
|---|-------|------|--------|----|-------------|--------|---------------------|--------|
| | | | | | | | Lower | Upper |
| Age (yrs) | .029 | .010 | 8.763 | 1 | .003 | 1.030 | 1.010 | 1.050 |
| Sex | -.571 | .223 | 6.527 | 1 | .011 | .565 | .365 | .876 |
| Preop. KPS | -.010 | .009 | 1.237 | 1 | .266 | .990 | .973 | 1.008 |
| WHO 2016 Grade | 1.358 | .222 | 37.300 | 1 | .000 | 3.889 | 2.515 | 6.013 |
| Primary or recurrent tumor | 1.407 | .283 | 24.689 | 1 | .000 | 4.082 | 2.344 | 7.109 |
| IDH-1 status | -.988 | .367 | 7.269 | 1 | .007 | .372 | .181 | .763 |
| Number of brain lobes/regions involved | .489 | .214 | 5.233 | 1 | .022 | 1.630 | 1.072 | 2.477 |
| Midline / Deep location | 2.130 | .766 | 7.731 | 1 | .005 | 8.412 | 1.875 | 37.743 |
| Tumor close to language area | .651 | .280 | 5.378 | 1 | .020 | 1.917 | 1.106 | 3.321 |
| Tumor close to motor area | .121 | .268 | .204 | 1 | .651 | 1.129 | .667 | 1.910 |

| | | | | | | | | |
|--------------------------------|--------------|-------------|--------------|----------|-------------|-------------|-------------|-------------|
| Preop. FLAIR-volume (cc) | .001 | .002 | .233 | 1 | .630 | 1.001 | .997 | 1.005 |
| Preop. CE-volume (cc) | .004 | .004 | .750 | 1 | .386 | 1.004 | .995 | 1.013 |
| Intraop. Neuronavigation | -.192 | .231 | .689 | 1 | .406 | .826 | .525 | 1.298 |
| Intraop. Ultrasound | -.010 | .215 | .002 | 1 | .961 | .990 | .649 | 1.509 |
| Intraop. IONM | -.999 | .323 | 9.562 | 1 | .002 | .368 | .196 | .694 |
| Preop. DTI acquisition | -.901 | .316 | 8.131 | 1 | .004 | .406 | .219 | .755 |
| Preop. fMRI acquisition | -1.113 | .412 | 7.306 | 1 | .077 | .368 | .147 | .736 |
| Preop. 3D Slicer preplanning | .066 | .259 | .066 | 1 | .798 | 1.069 | .643 | 1.776 |
| Preop. language deficit | -.593 | .282 | 4.412 | 1 | .036 | .553 | .318 | .961 |
| Preop. motor deficit | -.079 | .232 | .115 | 1 | .735 | .924 | .586 | 1.458 |

Table A.17 - Cox-regression analysis of preoperative covariates on the dependent variable overall survival

A.4.13 Impact of postoperative variables on Overall survival

A second Cox regression was performed to ascertain the effects of postoperative variables on OS (as shown in **Table A.18**). The Cox regression model was statistically significant, $\chi^2(13) = 63.773$, $p < 0.0001$.

| Variables in the Equation | B | SE | Wald | df | Sig. | Exp(B) | 95.0% CI for Exp(B) | |
|--|--------------|-------------|---------------|----------|-------------|--------------|---------------------|---------------|
| | | | | | | | Lower | Upper |
| Postop. FLAIR-volume (cc) | .002 | .004 | .435 | 1 | .510 | 1.002 | .995 | 1.010 |
| FLAIR-tumor extent of resection (%) | .008 | .008 | 1.022 | 1 | .312 | 1.008 | .992 | 1.024 |
| Flair-tumor EOR Cutoff 75% | -.907 | .366 | 6.152 | 1 | .013 | .404 | .197 | .827 |
| Postop. FLAIR-tumor volume (5cc) | -.198 | .297 | .444 | 1 | .505 | .820 | .458 | 1.469 |
| Postop. FLAIR-tumor volume (25cc) | -.111 | .303 | .134 | 1 | .714 | .895 | .495 | 1.620 |
| Postop. CE-volume (cc) | .056 | .018 | 9.463 | 1 | .002 | 1.057 | 1.020 | 1.096 |
| CE-tumor extent of resection (%) | -.026 | .012 | 4.430 | 1 | .035 | .990 | 1.002 | 1.052 |
| CE-tumor Gross Total Resection | -.531 | .235 | 5.129 | 1 | .024 | .588 | .371 | .931 |
| Residual CE Tumor (2cc cutoff) | .137 | .268 | .263 | 1 | .608 | 1.147 | .679 | 1.938 |
| Postop. language deterioration | 2.219 | .598 | 13.779 | 1 | .000 | 9.194 | 2.850 | 29.666 |
| Postop. motor deterioration | -.074 | .515 | .021 | 1 | .885 | .928 | .339 | 2.546 |
| Postop. KPS | -.005 | .006 | .744 | 1 | .388 | .995 | .982 | 1.007 |
| Postop. worsening in at least one function | -.369 | .337 | 1.196 | 1 | .274 | .691 | .357 | 1.339 |

Table A.18 - Cox regression analysis of postoperative covariates on the dependent

A.5 Other considerations regarding the present series

A.5.1 Patients and tumors preoperative characteristics

When assessing signs/symptoms registered at hospital admission, some degree of hemiparesis was present in 35% of cases, being the most common clinical finding. Language disabilities and cranial nerve impairment (predominantly central facial nerve deficit) were present in about 20% of cases; the former were significantly associated with a worse OS at multi-variate analysis. Visual dysfunctions and sensorial impairments were present in roughly 15% of the patients. HGGs showed, in general, a rate of neurological impairment at hospital admission about two times higher than lower grade gliomas. These

findings were similar to those previously reported in other studies (Chang *et al.*, 2005; Smits & Jakola, 2019).

Median preoperative *CE-tumor* volume in WHO grade IV lesions was similar (32.5 cc) to that reported in most published series (24.9-35 cc) (Bette *et al.*, 2018; Chaichana *et al.*, 2014a; Grabowski *et al.*, 2014; Lacroix *et al.*, 2001).

Some preceding series observed a significant correlation between preoperative *CE-tumor* volume (Awad *et al.*, 2017; Bette *et al.*, 2018) and OS, although this finding was not supported by other authors (Chaichana *et al.*, 2014a). No significant correlations were found between preoperative *FLAIR-tumor* and *CE-tumor* volumes and OS in the present cohort when stratifying per WHO grade.

A higher rate of EOR and OS was found associated with frontal lobe involvement in our series; conversely, lower EOR and OS were related to occipital lobe invasion. These findings seem in contrast with other reports from the literature (Awad *et al.*, 2017), but we believe that it might be explained by the fact that, in the present cohort, cases with frontal lobe involvement had a lower median and mean *CE-* and *FLAIR-tumor* volume and were mostly (69%) limited to a single lobe, a status positively correlated with OS. Conversely, when the occipital lobe was involved a simultaneous invasion of multiple lobes (≥ 2 in 89% and ≥ 3 in 27%) was predominant, and mean and median *FLAIR-tumor* and *CE-tumor* volumes were the highest registered in the series. Tumor invading deep structures close to the midline were previously reported to entail a significantly worse neurological outcome and prognosis (Awad *et al.*, 2017; Sang *et al.*, 2018); despite the extremely low number of individuals harboring this type of lesions in our series, this finding was associated with a postoperative clinical deterioration at univariate analysis ($p < 0.001$) and a lower OS at Cox regression analysis ($p = 0.005$, HR = 8.412).

A.5.2 *Clinical outcome*

In a study founded on a prospective database of 499 glioma patients from 52 North American centers, the neurological status was found to deteriorate postoperatively in 10% of cases (Chang *et al.*, 2003), an apparently lower finding compared to the 19% rate reported in our series, although it is not clear if they considered in their analysis all the functional areas we were able to assess in the present work. They also reported a higher rate of perioperative complications and clinical deterioration among patients undergoing

redo-surgery (33% and 18%, respectively) compared to those approached by first surgical attempt (24% and 8%, respectively) (Chang *et al.*, 2003). Similar findings were identified in our series, where postoperative clinical deterioration was higher among surgery for relapsing tumors (25.5 vs. 17.5%, but not statistically significant), while the rate of postoperative clinical improvement was significantly lower in the same group (17.6 vs 32.8%; p 0.037 and $OD = 0.280$ in binomial logistic regression).

De Witt *et al.*, published a meta-analysis evaluating postoperative neurological outcomes in 6095 glioma patients from 75 different publications: neurologic morbidity of any severity was noted in over 7% of cases (De Witt Hamer *et al.*, 2021; De Witt Hamer *et al.*, 2012); a severe motor deficit was present in 4.7%, a severe language deficit in 2.4% and combined motor and language deficits in 0.6%. Severe deficits were reported to persist 3 months postoperatively in 4.6% of cases (De Witt Hamer *et al.*, 2021; De Witt Hamer *et al.*, 2012).

In the present series, motor function was improved in 18.4% of patients at hospital discharge, while it deteriorated in 7.3%; the latter results appears in the range of the 3-11% incidence reported among the largest published series (see **Table A.18**) (Bello *et al.*, 2014; Chaichana *et al.*, 2009; Duffau *et al.*, 2005; Keles *et al.*, 2004; Kim *et al.*, 2009; Li *et al.*, 2016; McGirt *et al.*, 2009; Vorster & Barnett, 1998; Zhang *et al.*, 2018).

| Authors and Year | Year | Persistent postoperative motor deficit | Study population |
|--|------|--|------------------|
| Vorster <i>et al.</i> (Vorster & Barnett, 1998) | 1998 | 4% | 207 |
| Keles <i>et al.</i> (Keles <i>et al.</i> , 2004) | 2004 | 5% | 294 |
| Duffau <i>et al.</i> (Duffau <i>et al.</i> , 2005) | 2005 | 8% | 222 |
| Chaichana <i>et al.</i> (Chaichana <i>et al.</i> , 2009) | 2009 | 4% | 648 |
| McGirt <i>et al.</i> (McGirt <i>et al.</i> , 2009) | 2009 | 6% | 306 |
| Kim <i>et al.</i> (Kim <i>et al.</i> , 2009) | 2009 | 7% | 309 |
| Bello <i>et al.</i> (Bello <i>et al.</i> , 2014) | 2014 | 3% | 591 |
| Li <i>et al.</i> (Li <i>et al.</i> , 2016) | 2016 | 9% | 1229 |
| Zhang <i>et al.</i> (Zhang <i>et al.</i> , 2018) | 2018 | 11% | 734 |

Table A.18 - Persistent postoperative motor function deterioration among published large glioma series.

Language function was found improved in 7.7% of cases at the time of hospital discharge, whereas it was deteriorated in 2.6% of patients, a finding consistent with the 2-14% range of deficit reported in the largest published series (see **Table A.19**) (Chaichana *et al.*, 2009; Duffau *et al.*, 2005; Kim *et al.*, 2009; Li *et al.*, 2016; McGirt *et al.*, 2009; Sanai *et al.*, 2008; Vorster & Barnett, 1998).

| Authors and Year | Year | Persistent postoperative language deficit | Study population |
|--|------|---|------------------|
| Vorster et al.(Vorster & Barnett, 1998) | 1998 | 2% | 207 |
| Duffau et al.(Duffau <i>et al.</i> , 2005) | 2005 | 5% | 222 |
| Sanai et al.(Sanai <i>et al.</i> , 2008) | 2008 | 2% | 250 |
| McGirt et al.(McGirt <i>et al.</i> , 2009) | 2009 | 2% | 306 |
| Chaichana et al.(Chaichana <i>et al.</i> , 2009) | 2009 | 4% | 648 |
| Kim et al.(Kim <i>et al.</i> , 2009) | 2009 | 14% | 309 |
| Li et al.(Li <i>et al.</i> , 2016) | 2016 | 6% | 1229 |

Table A.19 - Persistent postoperative language function deterioration among published large glioma series.

In the formerly cited meta-analysis, other low-frequency deficits were also mentioned, comprising: hemifacial paresis, visual field deficit, somatosensory hemisyndrome, parietal syndrome, and deficit of other cranial nerves (De Witt Hamer *et al.*, 2021; De Witt Hamer *et al.*, 2012). It is not clear if these deficits actually entail a low occurrence or are rather not thoroughly investigated and therefore mostly neglected (De Witt Hamer *et al.*, 2021; De Witt Hamer *et al.*, 2012). In our series, a postoperative visual function deficit was reported in 5.6% of cases, while the incidence of the remaining symptoms ranged between 0 and 3.4%.

The same meta-analysis reported that the use of intraoperative stimulation mapping (IONM) was able to lower the rate of persisting serious deficit from 8.3% (with no IONM) to 3.4% (with IONM adoption) (De Witt Hamer *et al.*, 2021; De Witt Hamer *et al.*, 2012). In our series we did not note significant disparities in clinical postoperative deterioration at uni- and multi-variate analysis, but probably because IONM was specifically selected in those cases harboring the highest risk of clinical deterioration due to the extreme proximity to eloquent areas, representing a clear bias in our analysis. Nonetheless, IONM

turned out significantly associated with a better OS at both uni- and multi-variate analysis ($p = 0.002$, HR 0.368).

Tumor proximity to eloquent areas was identified as the most relevant variable to determine the risk of postoperative morbidity occurrence in a published series of 400 patients (Sawaya *et al.*, 1998), whereas its clear association with shorter OS was pointed out in a different study (Lacroix *et al.*, 2001). Thus, when assessing a relation between OS and glioma surgery, it is pivotal to take into account tumor location, particularly in relation to critical functional and anatomical areas (Sawaya *et al.*, 1998). In our series the proximity to motor or language functional areas (among all included gliomas) were related to a significant reduction of *FLAIR-tumor* volume EOR (median 74.9 vs. 83.8%), a non-significant reduction of *CE-tumor* volume EOR (median 98.5 vs. 99.5%) and a higher (although not significant) risk of motor (9 vs. 4.5%) language (4.1 vs. 0%) and any clinical deterioration (22.1% vs. 14.6%). These differences were even more pronounced (and statistically significant for “motor function” and “any clinical” deterioration: $p = 0.015$) when considering HGGs alone. At multi-variate analysis, proximity to motor functional areas was also related to a higher likelihood of deterioration in at least one clinical function ($p = 0.003$, OR 4.524), while proximity to language functional area had a higher likelihood of shorter OS ($p = 0.020$, HD = 1.917).

Most published investigations on glioma surgery assessed the activity of daily living and performance status, pre and postoperatively, using the KPS, and to a lesser extent with the ECOG score (De Witt Hamer *et al.*, 2021). In the present series 26 patients (11.1%) overall reported a worsening (≥ 10) in the KPS at hospital discharge compared to their preoperative status and our data seemed to be comparable to those reported in other large glioma series (see **Table A.20**). No significant preoperative variable was identified in logistic regression as affecting postoperative KPS status apart from its preoperative score and patient’s age and sex, whereas a higher preoperative KPS score was significantly ($p = 0.001$) associated with the chance of postoperative clinical improvement.

| Authors and Year | Year | Study population | Postoperative KPS decline | Postoperative KPS improvement |
|---|------|------------------|---------------------------|-------------------------------|
| Chaichana et al.(Chaichana <i>et al.</i> , 2014a) | 2014 | 292 | 5% (≥ 20 points) | N/A |
| Awad et al.(Awad <i>et al.</i> , 2017) | 2017 | 330 | 24.1% | 53% |
| Frey et al.(Frey <i>et al.</i> , 2014) | 2014 | 250 | 13% | 13% |

Table A.20 - Karnofsky Performance Status outcomes reported in large series.

A.5.3 Extent of resection

As reported in **Table A.21** and **Table A.22**, several EOR cut-offs have been proposed in the past years as significantly affecting OS, but the level of evidence remains, to date, close to “expert opinion” for most of them (Chaichana *et al.*, 2014b; de Leeuw & Vogelbaum, 2019; Duffau, 2016, 2019; Eyupoglu *et al.*, 2016; Fujii *et al.*, 2018; Incekara *et al.*, 2020a; Keles *et al.*, 2006; Li *et al.*, 2016; Marko *et al.*, 2014; Molinaro *et al.*, 2020; Nuno *et al.*, 2013; Oppenlander *et al.*, 2014; Orringer *et al.*, 2012; Pessina *et al.*, 2017; Sales *et al.*, 2019; Sanai *et al.*, 2011; Smith *et al.*, 2008; Stummer *et al.*, 2008; Wijnenga *et al.*, 2018). The previously identified thresholds were also investigated in the present study.

A.5.4 FLAIR-tumor EOR and postoperative residual volume

The region of hyperintensity on T2/FLAIR MR images, has been shown to comprise a variable composition between tumor infiltration and edema, especially among HGGs (Kelly *et al.*, 1987). However, its relevance, proper timing for its delineation and ability to predict prognosis is still debated (Grabowski *et al.*, 2014): preoperative mass effect on surrounding tissues, along with intraoperative manipulation of brain tissue encompassing the surgical corridor and cavity can generate an anomalous, edema-related T2/FLAIR signal that endures for days to weeks after the procedure (Vogelbaum *et al.*, 2012). Therefore, a tumor resection calculated merely on this area might either over- or underestimate the real tumor extension from case to case. Grabowsky *et al.* demonstrated a significant association between *FLAIR-tumor* EOR and OS at multivariate analysis, but

they were not able to identify any specific cutoff (Grabowski *et al.*, 2014). Smith and Wijnenga proposed a residual *FLAIR-tumor* volume ≤ 5 cc (Smith *et al.*, 2008; Wijnenga *et al.*, 2018) as significantly improving OS in WHO grade II tumors, whereas Fujii *et al.* proposed a residual *FLAIR-tumor* volume ≤ 25 cc (Fujii *et al.*, 2018) as significantly improving OS in higher grade (WHO III) tumors. The aforementioned cutoffs were validated as significantly correlated with a positive OS also in our series, together with an EOR over 75% in both LGGs and HGGs; the latter was found significant ($p = 0.013$, HR 0.404) also at Cox regression analysis.

| | FLAIR-tumor resection in WHO II-III gliomas | | | | Supra-maximal |
|-------------------|---|---|---|--|---|
| | Partial 1-39% | Partial $\geq 40\%$ | Near total $\geq 90\%$ | Complete 100% | |
| Series | Fuji, 2018 (Fujii <i>et al.</i> , 2018) | Fuji, 2018 (Fujii <i>et al.</i> , 2018) Smith, 2008 (Smith <i>et al.</i> , 2008) Wijnenga, 2018 (Wijnenga <i>et al.</i> , 2018) | Keles, 2006(Keles <i>et al.</i> , 2006) Smith, 2008 (Smith <i>et al.</i> , 2008) Wijnenga, 2018 (Wijnenga <i>et al.</i> , 2018) | Smith, 2008 (Smith <i>et al.</i> , 2008) Nuno, 2013 (Nuno <i>et al.</i> , 2013) Wijnenga, 2018 (Wijnenga <i>et al.</i> , 2018) | Duffau, 2016 (Duffau, 2016) Duffau, 2019 (Duffau, 2019) de Leeuw, 2019 (de Leeuw & Vogelbaum, 2019) |
| Level of evidence | IV | IV | IV | IV | IV |

Table A.21 - FLAIR-tumor EOR cut-off in WHO grade II and III gliomas, proposed over the years by different studies as significantly affecting overall survival.

A.5.5 CE-tumor EOR and postoperative residual volume

A slightly higher level of evidence has been reported in the literature for gross total (IIB) and supra-maximal (III) resection of contrast/enhancing areas when considering the impact on OS in glioblastomas. In our series, the degree of *CE-tumor* EOR was found significantly correlated with OS at multivariate analysis. However, when assessing different EOR cutoffs, only the obtaining of a GTR was found statistically significant at both Log-Rank and Cox-regression analysis ($p = 0.024$, HR = 0.588).

Most studies analyzing *CE-tumor* EOR in HGGs comprise a significant number of cases harboring lesions where extensive resection cannot be safely attained, as in the case of eloquent and/or deep-seated location (Chaichana *et al.*, 2014a; Lacroix *et al.*, 2001; Orringer *et al.*, 2012; Sanai *et al.*, 2011). This mixed population, including heterogeneous neoplasms with different molecular characteristics, treatment status (primary surgery or secondary treatment after recurrence), surgical goals, risks and expected outcomes makes it difficult to identify if higher EORs are independently associated with prolonged OS

(Chaichana *et al.*, 2014a). In addition, a significant part of the patients in many studies pre-dated the inclusion of temozolomide as a standard of care, adding another possible confounding factor (Chaichana *et al.*, 2014a).

| | CE-tumor resection in contrast enhancing high grade gliomas. | | | | | | |
|--------------------------|--|---|---|---|--|--|---|
| | Subtotal ≥78% | Subtotal ≥80% | Subtotal ≥90% | Near total ≥95% | Near total ≥98% | Complete 100% | Supra- maximal |
| Series | Sanai, 2011 (Sanai <i>et al.</i> , 2011) | Oppenlander, 2014 (Oppenlander <i>et al.</i> , 2014) Chaichana, 2014 (Chaichana <i>et al.</i> , 2014b) Sales, 2019 (Sales <i>et al.</i> , 2019) | Orringer 2012 (Orringer <i>et al.</i> , 2012) | Chaichana, 2014 (Chaichana <i>et al.</i> , 2014b) Marko, 2014 (Marko <i>et al.</i> , 2014) Molinaro, 2020 (Molinaro <i>et al.</i> , 2020) Incekara, 2020 (Incekara <i>et al.</i> , 2020a) | Lacroix 2001 (Lacroix <i>et al.</i> , 2001) Grabowski, 2014 (Grabowski <i>et al.</i> , 2014) | Stummer, 2008 (Stummer <i>et al.</i> , 2008) Sanai 2011 (Sanai <i>et al.</i> , 2011) Marko 2014 (Marko <i>et al.</i> , 2014) Molinaro 2020 (Molinaro <i>et al.</i> , 2020) Lacroix (Lacroix <i>et al.</i> , 2001) Brown, 2016 (Brown <i>et al.</i> , 2016) | Li, 2016 (Li <i>et al.</i> , 2016) Eyupoglu, 2016 (Eyupoglu <i>et al.</i> , 2016) Pessina, 2017 (Pessina <i>et al.</i> , 2017) Molinaro, 2020 (Molinaro <i>et al.</i> , 2020) |
| Level of evidence | IV | IV | IV | IV | IV | IIB | III |

Table A.22 - CE-tumor EOR cut-offs in contrast enhancing high grade gliomas, proposed over the years by different studies as significantly affecting survival.

Most of the studies were focused on WHO grade IV tumors.

Some authors believe that since EOR mainly depends on the preoperative tumor volume, a survival analysis based on this independent variable might carry a bias; for instance, a near-total resective surgery of a sizeable lesion may leave a larger residual mass compared to a subtotal removal of a small one (Bette *et al.*, 2018; Grabowski *et al.*, 2014). Since tumor recurrence (and potential malignant degeneration) clearly depend on the number of vital tumoral cells remaining, an analysis on postoperative volume (rather than EOR rate) has been suggested as more appropriate. The following cutoffs have been reported significantly associated with OS in multivariate analyses from previous works: 2 cm³ (Chaichana *et al.*, 2014a; Grabowski *et al.*, 2014) and 2.66 cm³ (Bette *et al.*, 2018).

In our series, a *postoperative CE-tumor burden smaller than 2 cm³* was found significantly associated with a longer OS at Log-rank testing, but not at cox-regression analysis; however, the latter multi-variate statistical test confirmed that a higher postoperative *CE-tumor residual volume* was significantly associated with a shorter OS (p = 0.002, HR = 1.057).